Dublin City University
Ollscoil Chathair Bhaile Átha Cliath

THE PREPARATION OF MAGNETIC NANOPARTICLE ASSEMBLIES FOR BIOMEDICAL APPLICATIONS

by

Swapankumar Ghosh, B. Sc., M. Tech.

Thesis submitted for the Degree of Doctor of Philosophy

Supervisor:
Dr. Dermot F. Brougham

School of Chemical Sciences
Dublin City University

January 2006

Declaration

I hereby certify that this material, which I now submit for assessment on the programme of study leading to the award of PhD, is entirely my own work and has not been taken from the work of others save and to the extent that such work has been cited and acknowledged within the text of my work.

Signed: Swapankumar Ghosh (Candidate)

ID No.: 52142850

Date: January 12, 2016

Dedication

To my father

Acknowledgements

First and foremost I would like to express my gratitude towards my supervisor, Dr. Dermot Brougham who introduced me to the wonderful and equally challenging area of NMR and its applications in the emerging area of magnetic nanomaterials. The years that I have worked with him will always be very memorable as my most productive years scientifically, as he provided me with the perfect balance of research independence and support. He was always very approachable at any point of time. I am grateful for his thorough and methodical approach to any scientific problem (probably true of any genuine Physical Chemist's way), the ideas, help, advice and encouragement all the time.

I would like to thank Eoin Murray, Sarah Kebbell, Carla Meladandri, Dr. Darren Carty and Martina O'Toole for their constant help by means of productive discussions, showing me how to improve the presentation of my work, and mostly for their company and support over the years I have been here. I would like to also thank Dr. Michael Gottschalk, who worked in our group, for his ideas, cooperation and many fruitful discussions.

I wish to thank all the technicians for their constant help, guidance and training on different instrumentation (Vincent Hooper, Damien McGuirk, Ambrose May, Mick Burke, Maurice Burke, John M^{c}Loughlin, Veronica Dobbyn, Mary Ross and Ann Corcoran). I have found all the staff to be very helpful and approachable and I am indebted for their help during my time at DCU. It was a great pleasure to work here and I wish to thank all the staff members of the School of Chemical Sciences.

My postgraduate research in DCU was definitely enriched by the availability of materials and different instrumental techniques through collaboration with the Department of Chemistry, Trinity College Dublin. I am grateful for the help of Ms. Serena Corr, Dr. Yurii Gunko and Dr. Sivakumar, B., at TCD for getting our TEM and Raman spectra done at the shortest of notice and also for their useful suggestions and discussions at different stages of my research.

My first few months in Ireland proved difficult personally, being away from my wife and children. I am indebted to Dr. Wasim Basir for his friendship, company and help when I

Table of Contents

Abstract

The Preparation of Magnetic Nanoparticle Assemblies for Biomedical applications

Magnetic nanoparticles and their assemblies are subjects of considerable scientific interest for basic research, but also for applications as contrast agents in magnetic resonance imaging (MRI) and for hyperthermia. Such applications depend on the production of stable suspensions of the particles, it is important therefore to characterise the particles in suspension. In this work photon correlation spectroscopy was used to measure of the hydrodynamic size of the particles. NMR techniques were used to determine the stability and to quantify the contrast efficiency (relaxivity) of the suspensions. This work has also provided insight into the nature of the nanoclusters in suspension and into the mechanisms of their growth.

In the first part of this thesis the synthesis, stabilisation and magnetic properties of aqueous magnetite nanocomposite suspensions which are formed in the presence of fatty acids or DNA are presented. For fatty-acid stabilised nanocomposites the NMR response is sensitively dependent on the method of preparation, which cab result in magnetically blocked or superparamagnetic nanoclusters. In the case of the DNA nanocomposites, the biomolecule acts as a template for the preparation of low dimensional assemblies, or magnetic nanowires, whose suspensions exhibit high relaxivity at low magnetic field.

In this second part the synthesis, stabilisation and magnetic properties of magnetite nanoparticle suspensions formed in organic solvents in the presence of long chain surfactants are presented. The influence of nanoparticle size on the magnetic properties is discussed in detail. The NMR response of the particles in non-aqueous suspension is shown to conform to a model previously developed for aqueous suspensions of magnetite. Studies of the controlled clustering of the nanoparticles in organic solvents are presented. The mechanism and kinetics of nanocluster growth are discussed.

Chapter 1

Introduction

1.1 Thesis overview

Chapter 1 of this thesis is an introduction to the field of magnetic resonance and to the current *state-of-the-art* in the preparation and applications of magnetic nanoparticle dispersions. In the first section of the chapter the principles underpinning NMR and MRI are described. As the thesis focuses on the application of magnetic nanoparticles in MRI, the different classes of magnetic materials are then summarised. In the following two sections the stabilisation and synthesis of magnetic nanoparticles are reviewed. In the final literature sections, the current applications of stable suspensions of magnetic nanoparticles, with an emphasis on the biomedical field, are reviewed.

In Chapter 2 the main experimental techniques employed throughout the thesis are described. These include nuclear magnetic resonance dispersion, NMRD, and photon correlation spectroscopy, PCS. Experimental details specific to individual chapters are described as they arise.

In Chapter 3 the preparation and characterisation of aqueous nanoparticle suspensions is described. Three types of materials are presented; uncoated magnetic nanoparticles, DNA- stabilised nanoclusters synthesised *in situ*, and fatty acid stabilised nanoclusters. The temperature and pH dependence of the relaxation mechanisms are presented and the data interpreted in terms of the effective particle size and magnetic state of the suspended nanoparticles or nanoclusters. It is found that the uncoated nanoparticles disperse, but when surface active molecules are used at least under the conditions described, stable clusters of nanoparticles are invariably formed. Despite their small primary particle sizes these clusters are not superparamagnetic, except in the case of the double-stranded DNA stabilised magnetic fluids, and then only partially.

The synthesis *in situ* coating and characterisation of fatty-acid bilayer stabilised magnetic fluids is described in Chapter 4. Efforts are described to synthesise smaller nanoparticles by increasing the ionic strength during coprecipitation. Most of the suspensions conformed to superparamagnetic relaxation theory, however large hydrodynamic sizes showed that they were not dispersed. This approach therefore produces stable superparamagnetic nanoclusters. The effects of change in pH and temperature on the stable magnetite suspensions are presented. NMRD characterisation was also performed on aqueous precipitated magnetite with a single surfactant phase transferred into heptane.

The relaxation behaviour of the coated magnetite suspension was also studied as a function of chain length of the fatty acid.

In Chapter 5 the synthesis of stable ultra-fine iron oxide particles, in the size range 4-11 nm, by a non-aqueous method are discussed. A series of experiments were conducted to investigate the effect of the experimental conditions on the size of the magnetite nanoparticles produced. Selected NMRD data was fitted using superparamagnetic relaxation theory. This procedure gave information on the particle size dependence of the materials, which is discussed in the light of the current literature.

In Chapter 6, studies on stimulated nanocluster growth from previously stable non-aqueous magnetite suspensions are presented. The use of alkyl-grafted porous silica powder was shown to mediate nanocluster growth. Experiments were conducted to investigate the mechanism of precipitation of surfactant coated magnetite, from heptane suspension, onto the silica surface.

1.2 Nuclear magnetic resonance techniques

1.2.1 Principles of nuclear magnetic resonance

The pioneering work of Felix Bloch and E. M. Purcell in 1946 [1-4] demonstrated that when certain nuclei were placed in an external magnetic field, they absorbed energy in the radiofrequency range and re-emitted the energy when the radiation was switched off. This discovery of nuclear magnetic resonance, NMR, seemed to be of academic interest initially. However, it was soon realised that the technique had tremendous potential applications. In particular, Proctor and Dickinson [5, 6] observed the chemical shift phenomenon in 1950 and proved that the resonance frequency is dependent on the chemical environment of the nuclei. The field of structural analysis was subsequently revolutionised, as NMR spectroscopy was developed into a powerful analytical tool.

The existence of nuclear spin had been first suggested by Pauli in 1924 [7]. Electrons have a spin 'I' of $^1/_2$. Many nuclei also possess spin. The simplest nucleus is of hydrogen, which consists of only one ^{1}H nucleus, it has I = $^1/_2$. For other nuclei the spin angular momentum is the sum of all individual spins of nucleons. For example, nuclei with both even mass and charge numbers have zero spin (e.g. ^{4}He, ^{12}C, ^{16}O etc). Nuclei with odd

mass numbers have half-integral spins {e.g. ^{1}H, ^{15}N ($I = {}^{1}/_{2}$), ^{17}O ($I = {}^{5}/_{2}$)} and nuclei with even mass number but odd charge numbers have integral spins {e.g. ^{2}H, ^{14}N ($I = 1$), ^{10}B ($I = 3$)}. The most commonly used nuclei for *in vivo* NMR are ^{1}H and ^{31}P, both of which have $I = {}^{1}/_{2}$. These two isotopes have natural abundance of nearly 100%, and are present in detectable quantities in all parts of human body.

In the vector model of NMR ^{1}H nuclei in a magnetic field have magnetisation, due to their nuclear spin, and acts like tiny precessing tops. ^{1}H nuclei spinning around their own axis will generate electromagnetic fields due to their inherent charge and will posses a characteristic dipolar magnetic moment (μ). The associated spin angular momentum (I) is related by the equation in classical terms

$$\mu = \gamma I \qquad (1.1)$$

where γ is a constant called the gyro-magnetic ratio, related to the charge and mass number of the nuclei, it determines the resonance frequency of the nucleus. The rate of precession is the resonance or Larmor frequency, ν_L.

$$\nu_L = \gamma B_0 / 2\pi \qquad (1.2)$$

In the earth's weak magnetic field, the spins of a nucleus are randomly oriented so that the net magnetisation (M), the net sum of the individual magnetisation vectors, is virtually zero. When a sample containing non-zero spins is placed in an external magnetic field, referred to as B_0, the spins align in $(2I + 1)$ different orientations (Zeeman splitting), each labelled by magnetic quantum number M_I. = -I, -I+1, ...I-1, I. In the case of the ^{1}H nucleus, $I = {}^{1}/_{2}$, so there are two orientations. The moments are either in the lower energy α-state, $M_I = +{}^{1}/_{2}$, with the moment aligned with the magnetic field, or in the β-state, $M_I = -{}^{1}/_{2}$, aligned against the B_0 field. The relative populations of the states are given by the Boltzmann distribution

$$\frac{n_{+\frac{1}{2}}}{n_{-\frac{1}{2}}} = e^{h\gamma B_0 / 2\pi kT} = e^{\Delta E / kT} \qquad (1.3)$$

Where h is Planck's constant, k is the Boltzmann constant, T is temperature in Kelvin, γ is the gyro-magnetic ratio of the nucleus and ΔE the difference in energy between the states. The relative populations of spins in the two possible energy levels are shown in

the diagram below (Figure 1.1). As the energy difference is very low, c.10^{-25}J, at thermal equilibrium the lower level is only slightly more populated. N_α/N_β is c 1.000007 for attainable fields at room temperature. In a system with many non-synchronised spins, the component of average spin vector in the xy-plane is zero. So given the small population

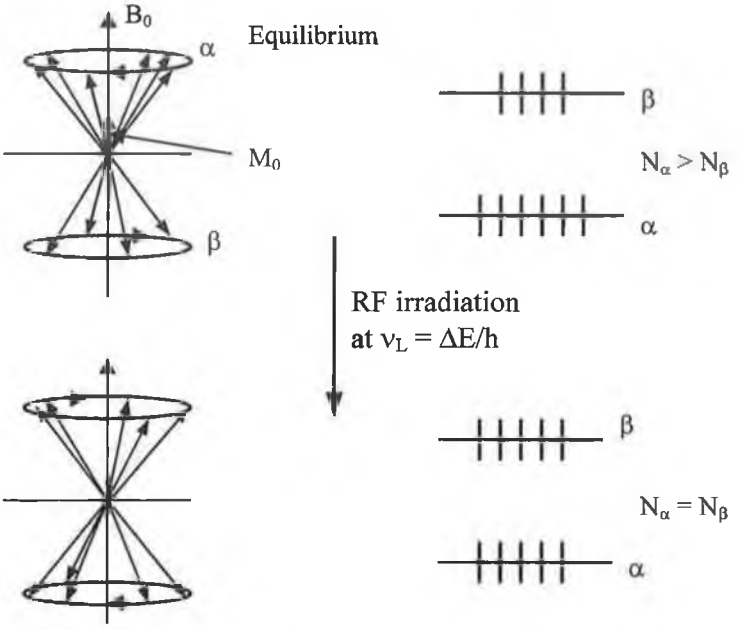

Figure 1.1. Equilibrium distribution of H nuclear spins under magnetic field and on RF radiation

difference there is a weak net magnetisation vector M_0, the sample magnetisation, along the field direction. As this magnetisation is small, NMR is an intrinsically insensitive technique and there is ongoing interest in attaining higher external fields. The current *state-of-the-art* is of the order of 20 T, corresponding to a Larmor frequency of 1 GHz for ^{1}H. When the nuclei are exposed to RF radiation (B_1 field) at the Larmor frequency, $\alpha \rightarrow \beta$ and $\beta \rightarrow \alpha$ transitions are stimulated, causing the net magnetisation to spiral away from the B_0 field and to lie in the transverse xy-plane. It is in this position that the net magnetisation can be detected. The angle that the net magnetisation vector rotates is commonly called the 'flip' or 'tip' angle. At angles greater or less than 90° there will still be a small component of the magnetisation in the xy-plane, which can therefore be detected.

The magnetisation at thermal equilibrium is chosen to be parallel to the positive z-axis. The manipulation of spin distribution by RF radiation results in rotation of the

magnetisation towards xy-plane and if radiation continues to be supplied to the system, towards negative z-axis. The RF pulse synchronises the spins, resulting in phase coherence and the net transverse magnetisation, M_{xy} rotates around the z-axis at the Larmor frequency. It is convenient to switch the coordinate system from the laboratory frame to a frame rotating around z-axis at the Larmor frequency, so that the on-resonance transverse magnetisation becomes stationary. Whenever there is net transverse magnetisation in the xy-plane, the NMR signal can be detected through induction of current to an RF coil tuned to the frequency of oscillation. The process of tilting the magnetisation from the z-axis to the xy-plane is called "excitation" whereupon the spins are said to have received a "90° pulse". An inverting "180° pulse" tilts the spin so that magnetisation is left along the negative z-axis. Following such a perturbation, the magnetisation starts to return towards its equilibrium state through relaxation. At the same time, the precessing magnetisation in the xy-plane induces current flow into the receiver coil, producing the measured signal, the free induction decay (FID). By the time $t = T_1$ where T_1 is the spin lattice relaxation time, the difference in spin population has grown to 63% of its value at thermal equilibrium (Figure 1.2). The signal behaviour as determined by the relaxation process is one of the key sources of contrast in MRI.

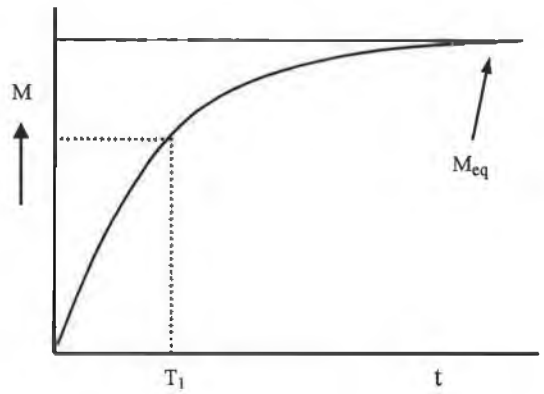

Figure 1.2. Recovery of magnetisation under field B_0 after application of a 90° pulse, after $t = 5T_1$, the magnetisation has grown to more than 98% of its equilibrium value, M_{eq}.

The perturbed state of magnetisation is thermodynamically unstable and thus, magnetisation "relaxes" back to thermal equilibrium with characteristic time coefficients. Due to the large magnetic moments of electrons (658 times greater than that of ^1H nuclei), the moment associated with the superspin in the case of superparamagnetic particles, absorb energy from the ^1H spin system, thereby inducing relaxation. The characteristic time over which the magnetisation returns to equilibrium along the

direction of the applied field, is the spin-lattice or longitudinal relaxation and is defined by the longitudinal relaxation time, T_1 (the longitudinal relaxation rate, $R_1 = 1/ T_1$). The relaxation process, T_1, by which the excess energy is dissipated into the lattice is a random process. Thus the magnetisation recovery is exponential with time, τ, and is described by;

$$M_z = M_o(1 - e^{-\tau / T_1}) \tag{1.4}$$

To obtain a quantitative NMR spectrum a time delay between successive RF pulses of the order of 5 times T_1 must be applied.

The characteristic time with which the phase coherence of the transverse magnetisation, M_{xy}, decays to zero is defined by the spin-spin or transverse relaxation time T_2, or transverse relaxation rate ($R_2 = 1/T_2$), which is also a random process.

$$M_y = M_o e^{\tau / T_2} \tag{1.5}$$

In the true T_2 process spin-spin relaxation occurs when spins in the high and low energy states exchange energy, thus the energy of the spin system is unchanged. The phases are lost, hence the driving force for the loss of the transverse magnetisation is entropic in nature. In pure water the T_1 and T_2 relaxation times are equal, and typically of the order of 2 to 3 seconds. In case of solids or semi-solids such as biological systems, T_2 can be considerably shorter than T_1.

In aqueous solution, in the absence of any paramagnetic relaxation enhancement, the mechanism for spin-lattice relaxation is the modulation of the intra- and intermolecular ^{1}H-^{1}H dipolar interaction brought about by molecular tumbling [8]. This occurs because the dipolar interaction is dependent on the angle, θ, the ^{1}H-^{1}H vector makes with the external field, B_0. Thus fluctuations in the dipolar interaction due to molecular tumbling are most efficient at stimulating relaxation when $\omega_L \tau_r = 1$, where ω_L is the Larmor frequency and τ_r is the rotational correlation time for tumbling.

The fact that T_1 is often of the order of seconds, while τ_r, for water is of the order of picoseconds, demonstrates that the system is in the weak collision limit, i.e. the spins are

not strongly coupled to the lattice. It can be shown that for a single motional process which modulates the dipolar interaction between a pair of spins that the ^1H T_1 is given by

$$\frac{1}{T_1} = \frac{9}{8}\left(\frac{\mu_0}{4\pi}\right)^2 \gamma^4 \left(\frac{h}{2\pi}\right)^2 \frac{1}{r^6}\left[\frac{4}{15}J_m(\omega) + \frac{16}{15}J_m(2\omega)\right] \qquad (1.6)$$

Where r is the distance between the ^1H nuclei, μ_0 is the vacuum permeability and $J_m(\omega)$ is the *spectral density* for the motion at the Larmor frequency (ω is the angular frequency in radians s^{-1}).

$$J_m(\omega) = \int_0^{\alpha} G_m(t) e^{i\omega t} dt \qquad (1.7)$$

The spectral density is the fourier transform of $G_m(t)$, the time autocorrelation function for the dynamic process of interest. The subscript m corresponds to the different transitions between energy states. For random rotational motions, the correlation function is exponential in time, this is often assumed to be the case in interpreting NMR relaxation data. The frequency spectrum of intramolecular magnetic interactions, modulated by molecular tumbling, should resemble one of the curves drawn in Figure 1.3. $J(\omega)$ can be thought of as being proportional to the probability of finding a component of the random motion at a particular frequency.

The characteristic time τ_c, the *rotational correlation time* is the average time taken to tumble through an angle of about 1 radian, τ_c^{-1} must be approximately the root-mean-square rotational frequency (in radians s^{-1}). τ_c is the average time taken for the root-mean-square deflection of the molecules for ~1 radian. If the dynamic process is random, then Gm(t) is exponential, as the spectral density $J(\omega)$ is the fourier transform of the correlation function, it has a lorentzian form:

$$J(\omega) = \frac{2\tau_c}{1 + \tau_c^{\,2}\omega^2} \qquad (1.8)$$

The integral of $J(\omega)$ over all frequencies is a constant, independent of τ_c. The frequency dependence of $J(\omega)$ is governed by τ_c, in fact the tumbling rate, τ_c^{-1}, can be extracted

directly from the half-width of the spectral density function. For smaller molecules, less viscous solvents, or higher temperatures the correlation time is shorter (faster tumbling) and the spectral density extends to higher frequencies, as shown in Figure 1.3 for three different τ_c values. As the relaxation rates depend on the ratio between the Larmor

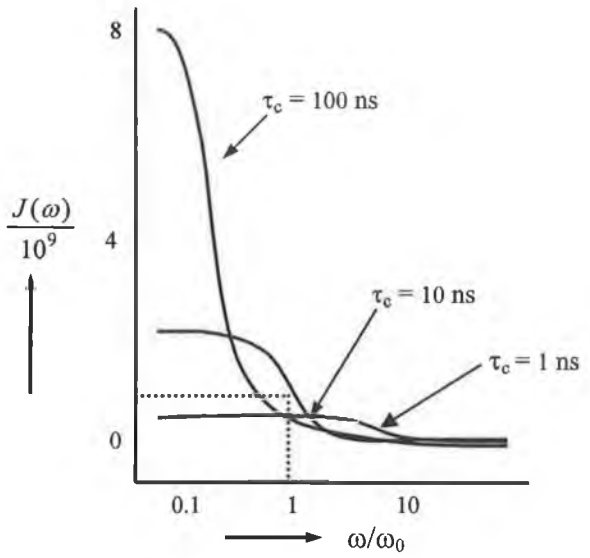

Figure 1.3. Spectral density function $J(\omega)$ drawn for three values of rotational correlation time τ_c.

frequency and the correlation time, it is useful to study the relaxation as a function of B_0. In addition it is not always the case that there is only one motional process modulating the dipolar interaction, or that the dynamic process is random. Field-cycling relaxometry is the only NMR technique that permits measurements of T_1 over several decades of the frequency with the same instrument and is one the most powerful tool for the identification and characterisation of molecular dynamics in complex systems [9]. Field-cycling NMR relaxometry [9] is also referred to as nuclear magnetic relaxation dispersion (NMRD). The NMRD technique maps out the spectral density functions. So in a system with only one rotational correlation time, the NMRD profile is a single Lorentzian. However, if there are distributions of barrier heights and hence of correlation times a "stretched" lorentzian can be applied [10]. In a similar way, when the relaxation mechanism is due to paramagnetic interactions, the NMRD technique can allow measurement of the strength of these interactions and of the dynamic processes that modulate them. This will be discussed in detail in the section below.

1.2.2 Principles of magnetic resonance imaging

The discovery of x-rays at the end of nineteenth century revolutionised medical diagnostics especially for the study of inside of a human body. However, the scientists and doctors soon learned of the destructive effects of X-ray on tissues. Today's X-Ray techniques, although much more safe and sophisticated than before, still employ ionising radiation and constitute the same kind of health risks as years ago.

The work of Paul C. Lauterbur [11] in 1972 demonstrated image formation by reconstruction from a number of NMR measurements, each taken in the presence of a linear field gradient applied in different directions. This was the real foundation of a new non-invasive technique called magnetic resonance imaging, MRI, which produces images of the body in thin slices. Since the first crude images in early 1970s, the hardware and imaging experiments have vastly improved. MRI scanners have grown in number and become indispensable diagnostic tools in almost all the major research and medical institutions in the world. In MRI substances are irradiated with low intensity radiofrequency electromagnetic radiation while placed in a strong magnetic field. Both the magnetic field and the radiofrequency radiation have proved, so far, to be harmless to the living tissues.

The technique maps the spatial distribution of ^1H signal, the intensity of which depends on the amount of water in the scanned volume and on the NMR relaxation times. MRI is essentially spatially resolved ^1H NMR. As in NMR, ^1H nuclei are excited with short pulses of radiofrequency radiation. By the application of magnetic field gradients during and after the radiofrequency pulses, spatial information is encoded both in the resonance frequencies and relative prescessional phases of the spins. The free induction decay generated as they relax is measured and deconvoluted by means of a Fourier transform, which provides an image of the tissue that corresponds to ^1H density [12]. Regions of high ^1H density, usually in the form of water or lipid molecules, have a strong signal and appear bright. Regions of bone or tendon, which have a low ^1H density because of the lack of water and lipids, have a weak signal and appear dark. The signal intensity also depends on the NMR relaxation times T_1 and T_2 which in turn are influenced by a range of factors [12, 13]. Controlling these factors to maximise the information content of the image is the ultimate goal of the radiologist trying to diagnose by analysing an MRI image.

1.2.3 Contrast agents in MRI

Paramagnetic species called "contrast agents" can be administered to the subject to alter selectively the image intensity of a particular anatomical or functional region. Contrast agents can considerably reduce the spin-lattice relaxation time T_1, the spin-spin relaxation time T_2 as well as T_2^*, the dephasing time in the presence of field inhomogeneities. Reducing T_1 leads to increase in signal intensity in the region containing the agent, when the image is recorded under T_1-weighted conditions (rapid scanning). On the other hand, reducing T_2 produces much broader lines which results in decreased signal intensity [14]. The net result is a nonlinear relationship between signal intensity and the concentration of the contrast agent [15]. It is often found that at low concentrations, an increase in contrast agent provides an increase in signal intensity, due to the T_1 effect, until the optimal concentration is reached. Further increase in concentration reduces the signal because of the T_2 effect.

Positive contrast agents (appear bright in MRI) are typically low molecular weight complexes containing as their paramagnetic element gadolinium, manganese or iron. Gd^{3+} is preferred as it contains 7 unpaired electrons and hence its complexes can have high relaxivity, which make them good T_1 relaxation agents.

The relaxation enhancement or efficacy of an agent for MRI is quantified by a concentration independent parameter called the relaxivity, r_1. The observed relaxation rate is given by;

$$R_{1,obs} = R_{1solvent} + R_{1enhancement}$$
$$\frac{1}{T_{1,obs}} = \frac{1}{T_{1,solvent}} + r_1[Fe] \qquad (1.9)$$

where $R_{1,solvent}$ is the observed rate at zero concentration, which is usually given in mM. Both r_1 and r_2 relaxivities can be determined experimentally at any given field. Relaxivity is quoted in units of $s^{-1}mM^{-1}$, for nanoparticulate agents, the total iron concentration is used. Typical values of r_1 for nanosuspensions are 10-20 $s^{-1}mM^{-1}$ at clinical fields of 60 to 100 MHz.

High relaxivity means that the clinical dose can be reduced, this is relevant for gadolinium, in particular, as the free ion is toxic. Thus successful gadolinium-based contrast agents are invariably highly stable chelates. In most cases the coordination sphere includes an exchangeable water molecule with the exchange lifetime optimised to maximise the bulk water relaxation (inner-sphere effect) [12]. Some typical contrast agents include gadopentetate dimeglumine, gadoteridol, and gadoterate meglumine, which can be used for imaging the central nervous system or the complete body. Mangafodipir trisodium is specially used for lesions of the liver and gadodiamide for the central nervous system.

Negative contrast agents (appear dark in MRI) are usually small particulate aggregates often termed small particles of iron oxide (SPIO). These agents produce predominantly spin-spin relaxation effects, but particles smaller than 100 nm also produce substantial T_1 relaxation. These particles are called ultrasmall particles of iron oxide (USPIO). This T_1 effect, along with the high potential relaxivity, and interesting pharmacokinetics, provide the motivation for substantial ongoing research worldwide into nanoparticulate contrast agents, aspects of which will be discussed in detail in later sections [12].

1.3 Magnetism and magnetic materials

Magnetic materials are classified by virtue of their response to an externally applied magnetic field. The orientations of the magnetic moments in a material help to identify different forms of magnetism observed in nature. If a magnetic field H induces magnetism M in a material, the material is said to possess a magnetic susceptibility

$$M = K H$$

$$\text{or} \qquad M = \chi H / V \qquad (1.10)$$

where K is the susceptibility, which is dimensionless, or χ is the volume susceptibility, units m^3kg^{-1}. In the SI system M and H are measured in units of Am^{-1}, where 1 Am^{-1} = $4\pi/10^3$ Oe. On a microscopic level the magnetism arises due to the presence of magnetic moments, a single unpaired electron has a moment of 1 μ_B, a bohr magneton, where 1 μ_B = $9.27402x10^{-24}Am^2$. The magnetisation per unit mass, σ_m is also sometimes of interest, it is derived from the magnetism by dividing by the density, and so has units of Am^2kg^{-1}, note that 1 Am^2kg^{-1} = 1 $emug^{-1}$.

1.3.1 Magnetic classification of matter

There are two main sub-classes of magnetic materials; those that possess randomness or short-range order and those that possess long-range order. The former are easily disturbed by thermal agitation and hence have zero magnetisation in zero external field, the latter have very strong quantum mechanical forces ordering the magnetic moments over large distances and consequently have properties which are less temperature dependent, and can exhibit memory (hysteresis) of previous magnetic field exposure. Ordered materials are also usually magnetically anisotropic. This means that some of their fundamental magnetic properties are dependent upon crystallographic direction.

A complete discussion of the theories behind the different classes of magnetism materials is beyond the scope of this dissertation. But some appropriate fundamentals will be provided to address the magnetisation in ferrimagnetic nanoparticles and their dispersions. The magnetic behaviour of materials can be classified into five major groups:

1.3.1.1 Diamagnetism

All atoms are intrinsically diamagnetic. Diamagnetism is an atomic manifestation of the Lenz effect. Lenz's law states "in electromagnetism, an induced electric current flows in a direction such that the current opposes the change that induced it" in a magnetic field, atomic currents are set up to oppose the applied field, hence dia- (opposed to) magnetism. Diamagnetic substances are composed of atoms which have no net magnetic moments (i.e., all the orbital shells are filled and there are no unpaired electrons). This is a weak temperature dependent fundamental property of all materials, in which a material acquires a small magnetic moment, μ, proportional to, but opposite in direction to, the applied field.

1.3.1.2 Paramagnetism

Paramagnetism, a slightly stronger effect, occurs in the direction of the applied field. Paramagnetism is still however a weak effect as it arises in disordered magnetic phases. In this class of materials, some of the atoms or ions in the material have a net magnetic moment due to unpaired electrons in partially filled orbitals such as Fe^{2+}, Fe^{3+}, Ni^{2+},

Mn^{2+} etc. However, the individual magnetic moments do not interact magnetically, and like diamagnetism, the magnetisation is zero when the field is removed. However, in the presence of a field, there is a partial alignment of the atomic magnetic moments in the direction of the field, resulting in a net positive magnetisation and positive susceptibility

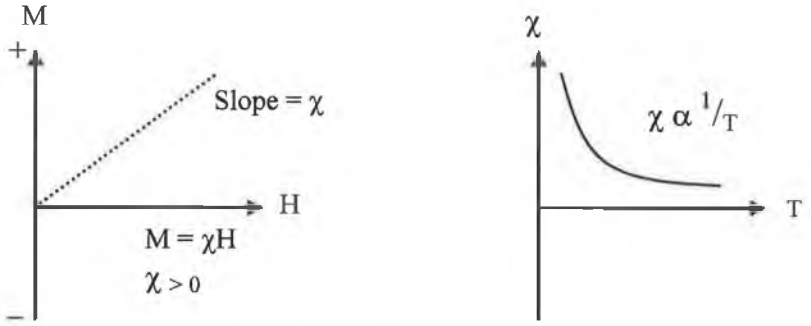

Figure 1.4. Schematic representation of paramagnetism.

The efficiency of the field in aligning the moments is opposed by the randomising effects of temperature. This results in a temperature dependent susceptibility, given by the Curie Law;

$$M = CB/T \qquad (1.11)$$

where M is the magnetisation per unit volume, B is the magnetic flux density and C is the Curie constant.

At normal temperatures and in moderate fields, the paramagnetic susceptibility is small, but larger than the diamagnetic contributions. Unless the temperature is very low (<<100 K) or the field is very high, paramagnetic susceptibility is independent of the applied field. Under these conditions, paramagnetic susceptibility is proportional to the total content of the paramagnetic species. Many iron-bearing minerals are paramagnetic at room temperature. Some examples with magnetisation per unit mass, σ_m in units of 10^{-8} m^3/kg, include; montmorillonite clay (13), nontronite (Fe-rich) clay (65), biotite mica (79), siderite (carbonate) (100) and pyrite (30) [16].

1.3.1.3 Ferromagnetism

The molecular theory of ferromagnetism was first suggested by Weiss in the early 1900's, which sufficed as a semi-quantitative description. The theory is based on the assumption that each atomic dipole is subject to a local field that is proportional to the magnetisation summed over all the other dipoles in the material [17-19].

Ferromagnetic materials exhibit long-range ordering at the atomic level which causes the unpaired electron spins to line up parallel with each other in a region called a domain (clusters of 10^{17} to 10^{21} atoms). Within a domain, the magnetic field is intense, but in a bulk sample the material will usually be unmagnetised because the domains, and hence the moments are randomly oriented with respect to one another. Ferromagnetism manifests itself in the fact that a small, externally applied, magnetic field can align the magnetic domains so the material is magnetised. This adds to the applied magnetic field by a factor, which is usually expressed as a relative permeability of the material. Ferromagnetism is extremely strong in metallic elements of the transition metals; Fe, Ni, and Co and at low temperatures in the rare earth and lanthanide elements.

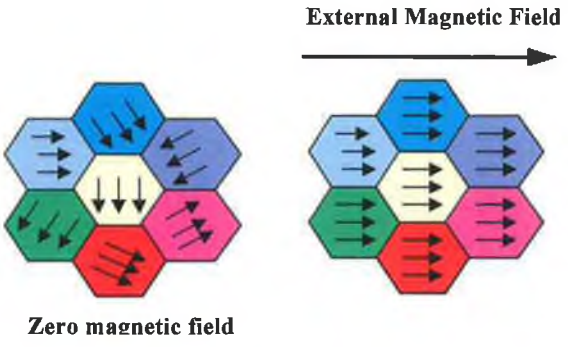

Figure 1.5. Schematic representation of the magnetic ordering in ferromagnetic materials

Two distinct characteristics of ferromagnetic materials are; (i) spontaneous magnetisation, and (ii) the existence of a magnetic ordering temperature.

The spontaneous magnetisation is the net magnetisation that exists inside a uniformly magnetised microscopic volume in the absence of a field. The magnitude of this magnetisation, at 0 K, is dependent on the spin magnetic moments of electrons. A related property is the saturation magnetisation, which can be measured in the laboratory. The saturation magnetisation is the maximum induced magnetic moment that can be obtained in a magnetic field (H_s), at higher fields no further increase in magnetisation occurs.

Saturation magnetisation (M_s) is an intrinsic property, independent of particle size, above the nano-range, but dependent on temperature. The fraction of the saturation magnetisation, which is retained when the driving field is removed, is called the remanence (M_r) of the material, and is an important factor in permanent magnets.

All ferromagnets have a maximum temperature where the magnetism disappears as a result of thermal agitation. This temperature is called the Curie temperature (T_c). Below the Curie temperature, the ferromagnet is ordered and above it, disordered. The saturation magnetisation goes to zero at the Curie temperature. In addition to the Curie temperature and saturation magnetisation, ferromagnets will tend to stay magnetised to some extent after being subjected to an external magnetic field.

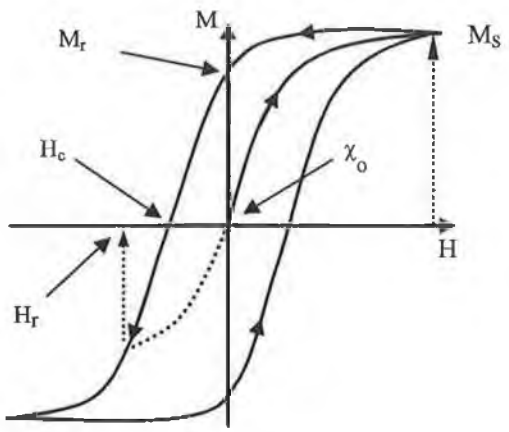

Figure 1.6. A typical hysteresis loop for a ferromagnetic material where magnetisation (M) in the sample is driven by the external magnetic field strength (H).

The fact that the properties are dependent on the magnetic history is called hystereis, and is shown in Figure 1.6, where χ_o is the initial susceptibility, and H_c is the coercivity. The reversed field required to reduce *M* to zero from remanence is called the coercive field or coercivity (H_c). The various hysteresis parameters are not solely intrinsic properties but are dependent on grain size, domain state, stresses, and temperature. Because hysteresis parameters are dependent on grain size, they are useful for magnetic grain sizing of natural samples.

1.3.1.4 Antiferromagnetism

Antiferromagnetism is a phenomenon in some magnetically ordered materials in which there is an anti-parallel alignment of the spins of two interpenetrating structures so that the material do not exhibit any overall bulk magnetisation. The moments of sublattices are exactly equal but opposite, the net moment is zero. This type of magnetic ordering is called antiferromagnetism. This spontaneous antiparallel coupling of atomic magnets is disrupted by heating and disappears entirely above a certain critical temperature, called the Néel temperature (T_N). Above T_N, the susceptibility obeys the Curie-Weiss law for paramagnets but with a negative intercept indicating negative magnetic exchange interactions. Hematite crystallizes in the corundum structure with the oxygen ions in a hexagonal close packed framework. The magnetic moments of the Fe^{3+} ions are ferromagnetically coupled within a given c-plane, but are antiferromagnetically coupled between the planes. Above -10°C, the spin moments lie in the c-plane but are slightly canted. This produces a weak spontaneous magnetisation within the c-plane (M_s = 0.4 Am^2/kg). Below -10°C, the direction of the antiferromagnetism changes and becomes parallel to the c-axis; there is no spin canting and hematite behaves as a perfect antiferromagnet.

1.3.1.5 Ferrimagnetism

In ionic compounds, such as oxides, more complex forms of magnetic ordering can occur as a result of the crystal structure. A simple representation of the magnetic spins in a ferrimagnetic oxide is shown below. The magnetic structure is composed of two magnetic sublattices (called A and B) separated by oxygen ions. The exchange interactions are mediated by the oxygen anions. When this occurs, the interactions are referred to as indirect or superexchange interactions. The strongest superexchange interactions result in an antiparallel alignment of spins between the 'A' and 'B' sublattice. In ferrimagnets, the magnetic moments of the A and B sublattices are not equal and result in a net magnetic moment. Ferrimagnetism is therefore similar to ferromagnetism.

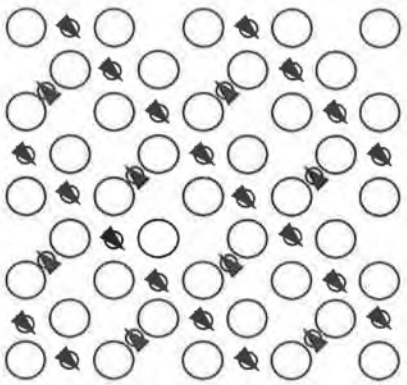

Figure 1.7. Distribution of two magnetic sub-lattices separated by oxygen in ferromagnetic materials.

It exhibits all the hallmarks of ferromagnetic behaviour; spontaneous magnetisation, Curie temperatures, hysteresis, and remanence. However, ferromagnetic and ferrimagnetic materials have very different magnetic ordering.

Magnetite, Fe_3O_4, or more properly $(Fe^{2+}O)(Fe^{3+}{}_2O_3)$ is a good example of a ferrimagnetic material. The moments on the Fe^{2+} and Fe^{3+} sites (of inverse spinel structure) are opposite and unequal. Indeed, magnetite was considered a ferromagnet until the 1940's, when Néel provided the theoretical framework for understanding ferrimagnetism. Magnetite, Fe_3O_4 crystallises with the spinel structure, in which the tetrahedral and octahedral sites form the two magnetic sublattices, A and B respectively. The spins on the 'A' sublattice are antiparallel to those on the B sublattice. The two crystal sites are very different and result in complex forms of exchange interactions of the iron ions between and within the two types of sites. Ferrimagnetic oxide materials typically have values of M_s of half to a quarter of their pure metal counterparts. They are however of great commercial importance because of their stability to oxidation, relatively simple and cheap commercial preparation and low biological toxicity [20].

1.3.2 Magnetic anisotropy

Magnetic materials are very often anisotropic, in that there is a preference for the magnetisation to point along one direction as opposed to others. In a single domain particle, all the individual (atomic) magnetic moment are ferro or ferrimagnetically coupled in the whole volume, so that the magnetization of the entire particle can be described by one magnetic moment. The anisotropy energy, E_a, may be defined by

$$E_a = KV\sin^2\theta \qquad (1.12)$$

where K is the magnetic anisotropy (volumic) density, V the particle volume and θ the angle between the easy axis and the magnetic moment directions. K is also sometimes called anisotropy constant which varies drastically with temperature [21].

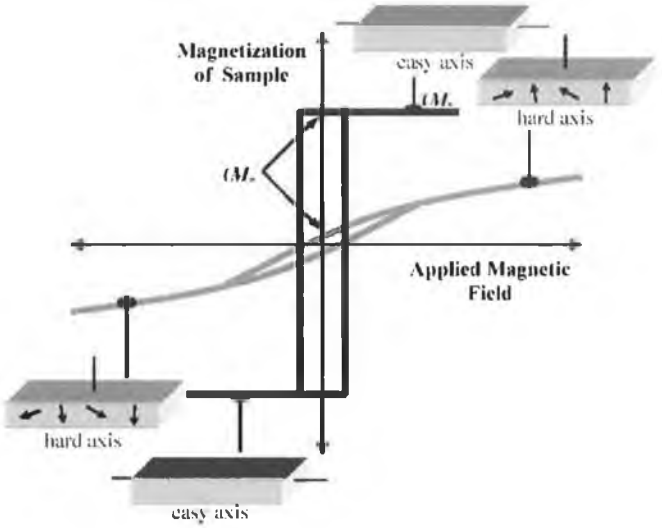

Figure 1.8. The hysteresis loop where magnetisation (M) in the sample is shown against the external magnetic field strength (H) with easy and hard axes of magnetisation.

The difference between the response of a material along an easy axis and the response along a hard axis is illustrated in the hysteresis loop shown in Figure1.8. In the curve shown in black, a low applied field is required, it is "easy", to drive all of the moments to point along a particular direction. Upon reducing the field to zero, the magnetisation remains constant since the moments are quite content to point along this axis. The grey curve in the figure shows that it is "hard" to saturate the moments along the direction perpendicular to easy axis. At a relatively large applied field, it is still the case that not all of the moments have been forced to align. Unlike the behaviour observed along the easy axis, the magnetisation decreases quite significantly as the applied field is reduced to zero. It is energetically less favourable for the moments to point along the direction in which the field was applied. The horizontal segments of the black hysteresis loop correspond to situations in which every moment in the sample has been forced to point to the left or to the right, as shown in the small drawings in the figure. When all of the moments in a magnetic sample are forced to point in the same direction, it is said that the sample has reached its saturation magnetisation (M_s). Above this field no further

magnetisation can be acquired. The remanence is much smaller in the case of the hard axis loop than it is when the field is applied along the easy axis.

1.3.3 The structure of magnetite

Iron oxide is found in nature in a variety of chemical compositions with different magnetic properties. The structural chemistry of iron oxy(hydroxi)des is very rich and diversified and more than a dozen structural types exist for ferrous, ferric and mixed valent compounds [22]. Among them the oxides such as maghemite, magnetite and oxides of the formula $MO.Fe_2O_3$ (where M is Mn, Co, Ni or Cu) are considered important because their stable ferrimagnetism and reduced sensitivity to oxidation make them suitable in magnetic applications [23]. Magnetite (Fe_3O_4) and maghemite (γ-Fe_2O_3) are the most intensely investigated iron oxides. The mixed-metal/valent $MO.Fe_2O_3$ ferrites also constitute a very important class of materials because of their unique physicochemical properties and applications in electronics.

Magnetite (Fe_3O_4) is a common magnetic iron oxide that has a face centered cubic inverse spinel structure of type AB_2O_4 where A signifies a divalent, and B a trivalent iron. It is more conveniently expressed in the formula $FeO.Fe_2O_3$. The unit cell is composed of 56 atoms, 32 O^{2-} anions, 16 Fe^{3+} cations and 8 Fe^{2+} cations. The ferrimagnetism in magnetite is due to the interpenetrating sublattices aligned antiparallel with unequal moments [23]. Fe cations occupy interstitial tetrahedral and octahedral sites and oxygen forming a fcc close packing along the [111] axis [24]. The Fe^{3+} ions occupy vacancies in both the octahedral and tetrahedral sub-lattices, with the moments in each type aligned anti-parallel. While the Fe^{2+} ions occupy vacancies or holes in the octahedral metal sub-lattice only [25]. The magnetic moment arises due to the Fe^{2+} cations only. Each Fe^{2+} is high spin so it contributes 4 unpaired electrons. The moment, and as a result the easy axis of the resulting magnetite crystal, is aligned along the cube edge. The saturation magnetisation can be calculated from

$$M_s = (n_B \mu_B) / V \qquad (1.13)$$

Where n_B is the number of Bohr magnetons per unit cell = 32, $\mu_B = 9.2704\times10^{-24}$ Am^2/Bohr magneton, and V is the volume of the unit cell, $5.906\times10^{-28}m^3$. Thus Ms = $5.0x10^5 Am^{-1}$. By dividing by the density (ρ = 5207.42 kgm^{-3}), the mass magnetisation

can be obtained, $\sigma(Fe_3O_4) = 96\ Am^2kg^{-1} = 96\ emu\ g^{-1}$. Values which can be verified for bulk magnetite (Table 1).

The spins of 3d electrons in the two interpenetrating sublattices in the octahedrally coordinated Fe^{3+} and Fe^{2+} "are coupled ferromagnetically via a double-exchange mechanism associated with inter-ion electron transfer" [26]. In other words, the electrons can hop between Fe^{2+} and Fe^{3+} ions in the octahedral sites at room temperature, rendering magnetite a unique class of half-metallic materials [27].

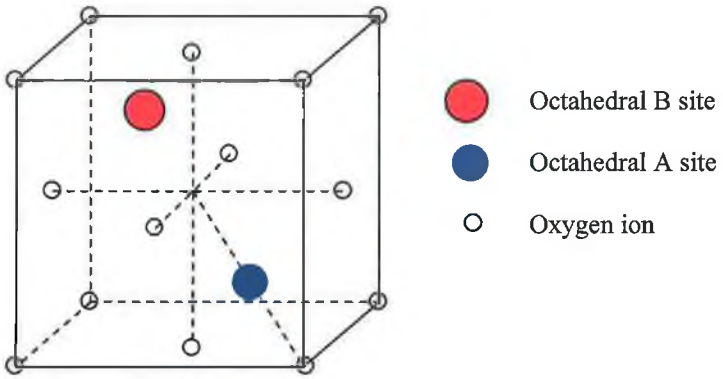

Figure 1.9. The inverse spinel structure of crystalline magnetite

Magnetite, Fe_3O_4, and maghemite, γ-Fe_2O_3, are similar materials, with closely related crystallographic structure. In magnetite iron ions are distributed into the octahedral (Oh) and tetrahedral (Td) sites of the fcc stacking of oxygen according to $[Fe^{3+}]_{Td}[Fe^{3+}Fe^{2+}]_{Oh}O_4$ whereas distribution of Fe^{3+} in maghemite may be expressed as $[Fe^{3+}]_{Td}[Fe^{3+}_{5/3}V_{1/3}]_{Oh}O_4$ where V stands for a cationic vacancy [28]. In freshly synthesised magnetite sample, the main peak in the X-ray diffraction pattern is centred at $2\theta = 41.39°$ (2.18 Å), while for powder kept under ordinary laboratory conditions after a month is at $2\theta = 41.62°$ (2.17 Å). This shift in the maximum is attributed to the oxidation of the Fe_3O_4 to γ-Fe_2O_3 nanoparticles [29]. The crystalline anisotropy constant (K) for magnetite is 1.4×10^5 erg/cm^3 and the superparamagnetic maximum critical size is for the crystal, estimated from KV ~ 25kT, is ~25 nm. Magnetite has slightly higher saturation magnetisation than maghemite. A few physical properties of the three main crystalline phases are given in Table 1.1 below [23, 30]. Magnetite is stable but slowly oxidises to maghemite in the presence of air and oxidises to hematite (α-Fe_2O_3) at temperature greater than 300°C.

Table 1.1. Magnetic and mineralogical data of few selected forms of iron oxides [31].

Mineral	Crystal family	Cell parameters (nm)	Density (g/cm^3)	Colour	Magnetisation Ms (emu/g)	Curie temp (K)
Magnetite	cubic	a=0.839	5.18	black	90-98	848-858
Maghemite	cubic or tetragonal	a=0.834	4.87	reddish brown	76-81	820-986
Hematite	trigonal	a=0.5032 c=1.3737	5.27	steel-grey to black	0.4	948

1.3.4 Magnetic properties of small nanoparticles: Single domain particles

A magnetic domain is region in which all of the atomic dipoles are coupled together in a preferential direction. Thus, for instance, ferromagnetic materials have magnetic properties, not only because their atoms possess a magnetic moment, but also because the material is made up of small regions known as magnetic domains. Within a domain large numbers, typically 10^{12}-10^{18}, of atomic moments are aligned.

The thickness of a domain wall is a function of the magnetocrystalline anisotropy, the exchange energy and lattice spacing of the crystal structure. The domain wall is a few hundred angstroms thick [32, 33]. As the particle size decreases, the number of magnetic domains per particle decreases down to the limit where it is energetically unfavourable for a domain wall to exist [34, 35].

Table 1.2. Estimated maximum single-domain size for spherical particles with no shape anisotropy [18, 36].

Material	D_S (nm)
Fe	14
Co	70
Ni	55
Fe_3O_4	128
γ-Fe_2O_3	166

In this critical size range such nanoparticles are single domain materials. In the presence of an applied magnetic field, the spins orientation and subsequent magnetic saturation is achieved with lower field strengths than with the analogous bulk materials. The magnetic moment of each particle is ~ 10^5 times larger than for transition metal ions and saturation magnetisation is reached at applied magnetic fields as low as 1 kOe [37].

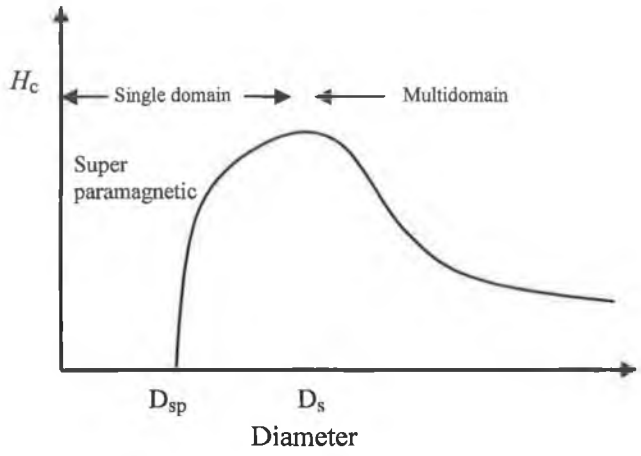

Figure 1.10. Coercivity as a function of particle size, D_{sp} is the superparamagnetic size and D_s is the single domain particle size.

When the field is decreased, demagnetisation is dependent on coherent rotation of the spins, which results in large coercive forces [36]. The large coercive force in single domain particles is due to magnetocrystalline and shape anisotropies for nonspherical particles.

Nanoparticles of iron oxide normally have lower magnetisation than the bulk materials due to the structural disorder in small crystal. For example, a magnetite sample of about 5 nm diameter will have about 110 unit cells, while a 3 nm particle will only contain 10 unit cells, resulting in a decrease in magnetisation [29, 38]. The saturation magnetisation of magnetite nanoparticles is reported in the literature in the range 30-60 emu/g where as bulk magnetite can have magnetisation as high as 92 emu/g [39, 40]. Morales *et al.* [38] studied the nanoparticle size of iron oxide prepared through coprecipitation of mixed valent iron salts by NH_4OH and KOH as well as by laser pyrolysis of $Fe(CO)_5$. They observed a strong structural relationship with the size and magnetic properties of the nanoparticles. A linear correlation was observed between the particles size with the magnetisation as shown in Figure 1.11.

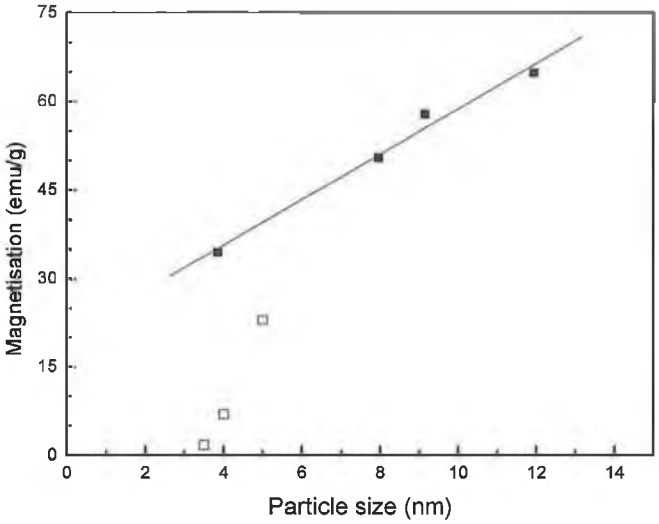

Figure 1.11. Variation of the saturation magnetisation at room temperature with particles size for different samples prepared though (■) precipitation and (□) by pyrolysis [38].

The structural aspects were investigated by XRD and FTIR. The very fine particles were found to be maghemite and their saturation magnetisation deviated from the linear relationship observed for larger particles. The superlattice reflections were found in the range 10-30° (2θ) for maghemite crystals. Crystals of size smaller than 5 nm were extremely difficult to characterise, due to their low scattering intensity and high surface area. The very low magnetisation obtained for the 4 nm maghemite particles was unexpected and could be due to surface defects and structural order-disorder [38].

1.3.5 Superparamagnetism

Superparamagnetism is a phenomenon which is exhibited by small particles made out of ferromagnetic material such as iron oxide. For very small ferromagnetic particles the magnetic anisotropy energy (responsible for keeping the magnetisation oriented in certain directions) is comparable to the thermal energy (kT). When this happens, the particles become superparamagnetic; as thermal fluctuations randomly flip the magnetisation direction between parallel and antiparallel orientations [37]. Below approximately 100 nanometers, such particles are so small that the cooperative phenomenon of ferromagnetism is no longer observed and no permanent magnetisation remains after the particles have been subject to an external magnetic field. However, the particles still exhibit very strong paramagnetic properties (hence the name of the phenomenon) with a very large susceptibility below the Curie or the Néel temperature. The magnetic anisotropy, which keeps a particle magnetised in specific direction, is

generally proportional to the volume of a particle. As the size of the particle decreases, the energy associated with the uniaxial anisotropy (K) decreases until thermal energy is sufficient to overcome any preferential orientation of the moment in the particle.

Superparamagnetism is dependent on the sample rapidly reaching magnetisation equilibrium at experimental temperatures [34, 41]. When superparamagnetic particles are placed in an external magnetic field, their magnetic moments align by particle rotation and on removing the field, they relax back to equilibrium by two different mechanisms. The first mechanism is Brownian relaxation, which is accomplished by bulk rotational diffusion of the particle within the carrier liquid, with a relaxation time,

$$\tau_B = 3V'\eta/kT \qquad (1.14)$$

where V' is the hydrodynamic volume of the particle (includes surfactant), η the dynamic viscosity of the carrier liquid, k is Boltzmann's constant and T is the absolute temperature The second mechanism is Néel relaxation, i.e. rotation of the internal magnetisation vector inside the particle, with a time constant of

$$\tau_N = \tau_0 \exp(\Delta E/kT) \qquad (1.15)$$

where $\Delta E = KV(1 - h)^2$, and where τ_0 is usually approximated as 10^{-9} s. ΔE is the energy barrier assuming uniaxial noninteracting particles, $h = H/H_k$ is the reduced magnetic field and H_k is the internal field due to anisotropy [42].

Particles with diameter larger than the critical values (Table 1.2) are said to be blocked [42]. The blocking temperatute (T_B) of a material is given by

$$T_B = \frac{KV}{25k} \qquad (1.16)$$

Below T_B free movement of the moment is blocked by the magnetic anisotropy. The particle is free to align its moment in an applied field above T_B and becomes superparamagnetic [18].

At thermal equilibrium the moments of paramagnetic particles will be distributed according to Boltzmann distribution law along the direction of magnetic field and the orientations are described by the Langevin function

$$m_{av} = m\left(\coth \alpha - \frac{1}{\alpha}\right) \quad \text{where} \quad \alpha = \frac{mH}{kT} \qquad (1.17)$$

Where m_{av} is the average magnetic moment, k is Boltzmann's constant and T is the absolute temperature [34]. This is very similar to the classical treatment of paramagnetism with the atomic moment replaced by the single domain particle moment, hence the name 'superparamagnetism' [43]. The moment of an individual superparamagnetic particle is given by $M = n\mu_{av}$, where n is the number of particles per volume.

In a recent review article by R. H. Kodama [44], the principles of superparamagnetism were discussed and relations between the chemistry of magnetic nanomaterials and their magnetic properties demonstrated. It is well known that the magnetic rotational energy is determined by the magnetocrystalline, magnetoelastic, and shape anisotropy of these particles. This may restrict such particles in two or more metastable orientations, giving rise to hysteresis in the moment versus applied field. Recent studies of ferrite nanoparticles [41, 45, 46] and Fe nanoparticles coated with magnetic oxides [47] presented a more complex picture, where the surface spins are disordered, and the exchange coupling between the surface and core gives rise to a variety of spin distributions within a particle which is well within the single-domain size regime. The 'surface spin states' can result in high field hysteresis and relaxation of the magnetisation due to irreversible reorientations of the surface spins.

Thus there are challenges ahead for both theory and experiment to understand how microscopic modes such as spin waves and phonons couple to the particle moment in the approach to thermal equilibrium [44]. It should be noted that the same issues are necessarily ignored in the theory for water relaxation in the presence of superparamagnetic particles, see below. As a result that theory is strictly applicable only to particles smaller than 20 nm.

1.4 Stabilisation of magnetite nanoparticles in suspension

1.4.1 The stability of magnetic fluids

Ferrofluids contain surfactant coated magnetic particles in appropriate (usually non-aqueous) carrier liquids. The particles are usually superparamagnetic magnetite (Fe_3O_4) of mean diameter of about 10 nm. Such a material can be considered to consist of single domain particles [48, 49]. Under the normal gravitational field it will remain dispersed, as it should not sediment due to random thermal motions, and should not aggregate due to the magnetic dipole interaction. However, coagulation due to van der Waals attraction is still possible. The particles are coated with long chain fatty acid surfactants to provide stability due to steric and/or electrostatic stabilisation [50]. So dispersion relies on the balancing of the gravitational, magnetic, and van der Waals forces.

The attractive magnetic energy between two magnetic dipoles is a function of the dipole moments μ_1 and μ_2 and the distance between the particles given by Equation 1.18;

$$E_A^{Mag} = \frac{1}{4\pi\mu_0 r^3}\left[\overline{\mu_1}\,\overline{\mu_2} - 3\left(\overline{\mu_1}\cdot\bar{r}/r\right)\left(\overline{\mu_2}\cdot\bar{r}/r\right)\right] \qquad (1.18)$$

where **r** is the vector between the centres of the two dipoles and μ_0 is the permeability of space [34]. The magnetic dipole of a single domain particle is $\mu = I_0V$ where I_0 is the magnetisation per unit volume of the particle and V is the volume of the particle. The interaction energy increases as the distance between the particles decreases and aggregation may occur unless prevented by a repulsive force. The attraction energy can also be expressed in the following form;

$$E_d = -\frac{\pi M_s^{\,2} d^3}{9\mu_0 (l+2)^3} \qquad (1.19)$$

where M_S is the saturation magnetisation and μ_0 is the magnetic permeability, s is the distance between the spherical surfaces, d is the diameter of the particles and l = 2s/d. The magnetic energy of the system is small when the particles are superparamagnetic, as the energy is proportional to volume, and so is overcome by thermal fluctuations resulting in colloidal stability. The factor l expresses the importance of the volume fraction in determining stability.

The relative importance of the gravitational force can be assessed from the ratio of the gravitational energy to the attractive magnetic energy, which is given by;

$$\frac{Gravitational.Energy}{Magnetic.Energy} = \frac{\Delta\rho gL}{\mu_0 MH} \tag{1.20}$$

where $\Delta\rho$ is the difference in density of the solid and the liquid, L is the height of the suspension and g is the gravitational constant. Using common values for the parameters it is found that the gravitational effect on nanoparticle stability for typical magnetite fluids is insignificant [50].

The van der Waals forces are the result of spontaneously induced polarisability of fluctuating electric dipole-dipole forces and are a relatively weak distance dependent interaction. The energy due to the van der Waals force, which arises due to fluctuating dipoles energies for equal sized spheres is given by the Hamaker expression shown in Equation 1.21,

$$E_i = -\frac{A}{6}\left(\frac{2}{l^2+4l} + \frac{2}{(l+2)^2} + \ln\frac{l^2+4l}{(l+2)^2}\right) \tag{1.21}$$

where A is the Hamaker constant (approximately 10^{-19} N.m for Fe_3O_4, γFe_2O_3 and Fe) [50], and $l = 2s/d$ where s is the distance between the sphere surfaces, d is the diameter of the particle. So the interaction energy increases as two particles come closer. The van der Waals attractive forces are a significant factor and must be countered with a repulsive force to maintain a stable colloidal suspension.

Electrostatic and steric repulsions are two forces which balance the attractive forces between among the colloidal particles. The electrostatic stabilisation is induced by charge, and so it is pH sensitive. The particles repel each other when they go closer than a certain distance. Steric repulsions are normally achieved by using a long chain fatty acid surfactant.

1.4.2 The surface chemistry of magnetite

The aqueous chemistry of metal cations is extremely complex and diverse and it is possible to control many characteristics of oxide nanoparticles in particular the

crystalline structure and its surface characteristics including particle size and shape [51, 52]. The surface chemistry of magnetite may be controlled during the synthesis by the experimental conditions e.g., chemical reagents, their purity and stoichiometry, pH, temperature of reaction, ionic strength of the medium etc. The surface iron atoms which are not chemically bound to oxygen atoms act as Lewis acids and therefore coordinate with molecules that donate electrons, Lewis bases. In aqueous suspensions, surface iron atoms coordinate with water which leaves hydroxyl groups attached to the iron oxide surface. The iron oxide surface is thus hydrophilic [53] and reacts with both acids and bases. It is well known that the surface charge in oxides is largely dependent on the pH of the suspension, the surface is amphoteric in nature. The pH of zero surface charge, pH_{pzc}, or isoelectric point, is at pH 6.8 for magnetite. Iron cations form hexacoordinated aquo complexes, $[Fe(H_2O)_6]^{z+}$ in water in which the polarisation of coordinated water molecules is strongly dependent on the formal charge (oxidation state) and size of the iron cation. This makes the ferric aquo complexes more acidic than ferrous complexes. The hydroxylation of the cations occurs in very distinct ranges of pH (at $pH \geq 1$ for the ferric and pH~6 for the ferrous polycation) [28]. Hydroxylated complexes condense mainly via olation mechanism, with the elimination of water and formation of hydroxo bridges. During precipitation, the aquo hydroxo zero-charge complex forms which is the precursor of the solid [52].

One of the major issues in synthesising stable magnetic nanoparticle suspensions is to prevent agglomeration during synthesis and the coating process. This is consistent with the size-dependent balance between van der Waals and magnetic dipole-dipole interactions [54]. Fine magnetite nanoparticles have a large ratio of surface-area to volume and tend to agglomerate, due to strong magnetic dipole-dipole attractions between particles, during synthesis as this reduces their surface energy (>100 dyn/cm) [55].

Aggregation due to attractive forces associated with magnetite nanoparticles can be prevented by applying an electrostatic double layer, or by use of a surfactant functioning as a steric stabiliser [53]. Ionic surfactants prevent agglomeration due to the repulsive forces originating from the proximity of like charged particles approaching each other. Electrostatic stabilisation is a pH sensitive method. Close to the pH_{pzc} [56] the net surface charge density is zero and the interparticle electrostatic repulsions are not sufficient to

prevent the particles van der Waals attractive forces from causing flocculation. The bare magnetite particles can be peptised at pH above 10 [57]. The isoelectric point of magnetite can be shifted to pH 2-4 by applying a silica coating on magnetite and thus coated magnetite particles are stable in suspension above pH 4. Phosphate and carboxylate functional groups are known to bind to the surface of magnetite particles [23, 58].

Weakly polarising, positively charged ions, such as the $N(CH_3)_4^+$ ion of tetramethylammonium hydroxide (TMAOH) are also known to stabilise the magnetite particles [59].

1.4.3 Steric or entropic stabilisation

Stabilisation by steric repulsion is normally achieved by applying a surfactant to the magnetite surface. Usually the surfactant molecules have a long chain amphiphilic (fatty) molecule with a polar head group which binds onto the magnetite surface either chemically or physicochemically. Particles stabilised in this way can be dispersed in nonpolar hydrocarbon solvents, such as hexane, with the readily solvated hydrophobic surfactant hydrocarbon chains extending from the particle surface [60]. The surfactant thickness must be such that the sum of the energy of van der Waals (E_i, equation 1.21) and magnetic attractive forces (E_d, equation 1.19) is less than or equal to the thermal energy or Brownian motion of the particle system (equation 1.22) [61, 62].

$$\left|E_i + E_d\right| \leq kT \qquad (1.22)$$

The stabilisation mechanism can be explained in two ways. When two particles each containing an adsorbed surfactant layer of thickness δ approach to a distance of separation h, where $h \leq 2\ \delta$, repulsion occurs as a result of two main effects: (i) unfavourable mixing of the stabilising chains of the adsorbed layers. (ii) When the particles approach one another the surfactant tails interpenetrate creating an osmotic pressure and a repulsive force because of an increase in configurational entropy as the surfactant chains begin to compress one another. This is referred to as elastic (entropic) interaction.

Mackor proposed a model for particle-particle collisions where the surfactant tails compress and repel one another [50]. Rosenswieg *et al.* modified the Mackor expression

for the repulsive forces based on a flat surface model to an integrated expression for two approaching nanospheres

$$\frac{E_r}{kT} = 2\pi d^2 \xi \left[2 - \frac{l+2}{t} \ln\left(\frac{1+t}{1+l/2}\right) - \frac{l}{t}\right] \qquad (1.23)$$

where ξ is the concentration of adsorbed surfactant molecules on magnetite particle surface, and again d is the particle diameter, s = surface to surface separation, l = 2s/d, t = 2δ/d, k is Boltzmann's constant, T is the absolute temperature.

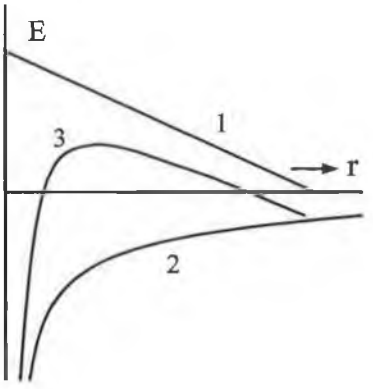

Figure 1.12. The potential energy diagram for steric stabilisation where 1 represents repulsive force due to surfactant, 2 attractive energies of magnetite nanoparticles and 3 net energy.

The surfactant coated nanoparticles will not agglomerate as long as the net energy is positive. A long carboxylic acid chain creates a potential barrier of ~ 25 kT that is an order of magnitude greater than the thermal energy for each particle and under this condition it is unlikely the particles will coalesce [50].

1.4.4 Stabilisation by long chain surfactants

The steric stabilisation of fatty acid coated magnetite nanoparticles in nonpolar and aqueous carrier liquids has been reported. The carboxylic head group of the primary fatty acid layer is chemisorbed onto the magnetite surface, see Figure 1.13 [58].

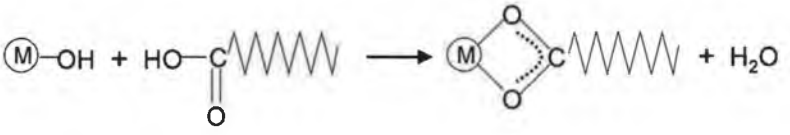

Figure 1.13. Chemisorbed carboxylic acid group on magnetite particle M [58].

The steric stabilisation of fatty acid coated magnetite nanoparticles in nonpolar and aqueous carrier liquids is shown schematically in Figure 1.14. The carboxylic functional group is indicated by the small circles at the surface of the magnetite particles in Figure 1.14b and 1.14c and the hydrophobic tail of the surfactant extends out into the nonpolar solvent in Figure 1.14b as a curved line.

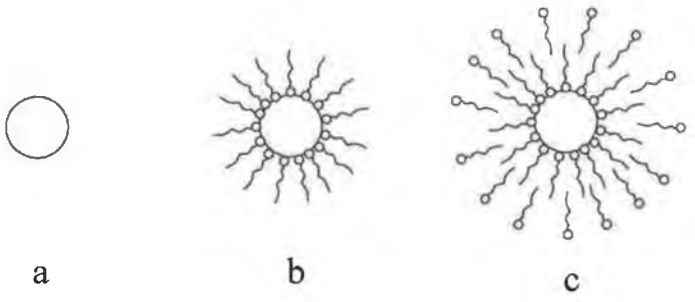

Figure 1.14. Schematic diagram of a) uncoated magnetite particle, b) monolayer surfactant coated in nonpolar solvent and c) bilayer stabilised in aqueous suspension.

For fatty acid stabilised nanoparticles in water, partially stable suspensions are obtainable using a bilayer surfactant coating, [63] with the same or similar surfactants in the outer physisorbed layer. The second fatty acid layer is then attached to the primary chemisorbed layer with their hydrophilic carboxylic groups oriented towards the dispersion medium and it is covered with hydrated NH_4^+ ions. Consequently, the degree of stability of water based magnetic fluids depends on the pH value of the medium and the stabilisation mechanism is specific only to water as carrier liquid.

Khalafalla *et al.* emphasised the importance of the hydrophilic-lipophilic balance (HLB) number which must be greater than 12 [64]. The HLB number characterises the ratio of water-loving and oil-loving portions of a surfactant molecule, respectively, in an arbitrary range of 1- 40. The authors also report that fatty acids with chain length C10 to C15 can form water dispersible coated magnetite suspensions [64] and that they are superior to oleic acid for aqueous suspensions. Wooding *et al.* [58] note that saturated fatty acid molecules (C9-C15) can also successfully stabilise the suspensions in water. The quantity of the surfactant in the primary layer was determined for C_{10}–C_{18} and the surface area occupied per molecule of surfactant was found in the range to be ca. 21 and 38 Å with highly organised surfactant bilayer structures [58]. The mean diameter of the particles was in 7 to 9 nm range. Differential scanning calorimetry indicated the presence

of a phase transition for the bilayer-coated particles that suggesting partial interpenetration of the hydrocarbon tails of the primary and secondary surfactants [65, 66].

One limitation of these water based fluids is their instability against dilution with pure water beyond the CMC (critical micelle concentration) of the surfactant [67]. The secondary surfactant layer is weakly attached (physisorbed) to the chemisorbed primary surfactant. Dilution can result in stripping the physisorbed secondary surfactant from the particle surfaces. Upon loss of the stabilising secondary surfactant, the hydrocarbon tails of the primary surfactant are exposed to the surrounding water, and the resulting incompatibility causes the magnetic particles to agglomerate and ultimately precipitate from solution when the aggregates grow sufficiently large.

Several authors have used oleic acid as a surfactant in their investigation in steric stabilisation of magnetite particles [58, 65]. The double bond in the hydrocarbon chain of oleic acid seems to play an important role for an effective stabilisation of iron oxide [68]. This is also the case for suspensions in nonpolar liquids. It is accepted that efficient packing of adjacent hydrocarbon tails, due to the 'kink' in the chain caused by the unsaturation, facilitates the formation of a stable primary layer [68].

Other surfactants have been used by some investigators. Phosphate containing surfactants including alkyl phosphate, dodecylphosphonic acid (DDP), hexadecyl phosphonic acid (HDP) and hexadecyl phosphate (DHDP) [69] have been used for nonpolar magnetite dispersions. Surfactants with bifunctional head groups like, dodecyldimethylammonium bromide (DDAB) have also been used.

1.4.5 Clustering and aggregation in aqueous suspension

It has been reported recently that water-based magnetic fluids consist of a considerable fraction of non-superparamagnetic particles at room temperature [70]. The presence of a large number of inherent clusters in the range of 200 nm the in the water-based fluids, as compared to hydrocarbon based or ionic fluids, may be due to differences in the preparation technique, which assists the formation of aggregates. It was reported that at zero field, the formation of rings was favoured over chains for all clusters large enough

to contain more than three particles due to the strong dipole–dipole interaction between particles in the aqueous system.

Avdeev *et al.* [71] investigated the effect of the magnetic particle concentration on the structure of magnetite based ferrofluid and by means of small-angle neutron scattering. The suspension was stabilised by oleic acid surfactant dispersed in deuterated benzene. The authors proposed a model of noninteracting spherical particles covered by a homogeneous shell which fits experimental data well at magnetite concentration up to 19 vol% revealing a significant decrease in the thickness of the shell with an increase in the magnetite concentration [71]. The results were interpreted as indicating the interlacing of surfactant tails in the layer caused by the interparticle interactions.

Static light scattering has been used to provide useful insights into the nature of the aggregates formed in hydrous ferric oxide flocs. The assembly of particles appear to exhibit fractal properties over a significant size range. The aggregates tend to break easily by agitation resulting in breakup and/or restructuring to denser assemblages [72].

Dynamic light scattering studies of paramagnetic particles containing 67% magnetite (Fe_3O_4) coated with polymer latex showed that the magnetite forms many tiny ferrimagnetic crystallites of size ~5 nm which are uniformly dispersed in the latex spheres. The experimental scattering intensity and auto-correlation function, $g(t)$, of the materials were examined and compared with those from calculations on isotropic and anisotropic dielectric particles. This demonstrated that the magnetic dipole radiation of the paramagnetic particles is unusually large and is approximately equal to one third of the electric dipole radiation of the particles. Dynamic light scattering measurements showed that the measured $g(t)$ for the depolarised scattering is strongly influenced by the size distribution of the particles. This is because the large paramagnetic particles contain more magnetite (are more magnetic) and hence weigh more in the depolarised scattering. Simple sedimentation methods were found to be effective in size separating the particles of different sizes to obtain relatively monodispersed scattering samples [73].

1.5 Synthesis of magnetite nanoparticles

The synthesis of magnetic nanoparticles of controlled size has long been of scientific and technological interest. Stable suspensions of magnetic fluids were first synthesised in

1964 by Papell [74]. There are many synthetic procedures reported in the literature for preparing nanosized crystalline magnetite. Reported procedures for the synthesis of magnetite and maghemite are different. However, in practice mixtures of the two are often obtained even when a high level of care is taken experimentally. The sensitivity to reagent stoichiometry and a large number of other reaction parameters often complicate the ability to obtain pure magnetite crystalline structures. The review given here is mainly focussed on the literature on magnetite. Due to the similarity of their magnetic properties, and of the synthetic procedures some references on maghemite are included. The synthetic procedures for magnetite can be broadly classified into three groups: aqueous precipitation, thermal decomposition of carbonyl complexes/chelates and high temperature alcohol reduction of Fe^{3+} chemical precursor, usually in non polar solvents.

1.5.1 The synthesis of magnetic nanoparticles by alkaline coprecipitation

Magnetite synthesis by the aqueous precipitation of mixed Fe^{3+} and Fe^{2+} salts has been known since early 1900s [75]. The molar ratio of Fe^{3+} and Fe^{2+} salts used in the synthesis is 2:1 as the magnetite can be described as $FeO.Fe_2O_3$ [58, 65]. As the Fe^{2+} ion is prone to oxidation, researchers emphasised the use of closed reactors for magnetite synthesis with nitrogen or argon gas purging through the reaction mixture. Some authors used the iron salts with Fe^{3+}/ Fe^{2+} ratio greater than 2 due to the oxidative instability of Fe^{2+} ion [64, 76]. The complex mechanism of inverse spinel magnetite formation is not well understood. A very general mechanistic agreement on the formation of magnetite through aqueous precipitation is that the Fe^{2+} precursor hydrolyses to $Fe(OH)_2$ and consequently reacts with other hydrous oxides to form magnetite [77]. Farley *et al.* proposed that the formation of oxides occurs via surface adsorption of cations especially when the bulk solution concentration is below saturation with the solid phase [78]. There is general agreement [53, 79] that the process starts with the nucleation of magnetite followed by crystal growth to obtain monodisperse particles [23]. The sequence of magnetite formation from the hydrated ferrous and ferric oxides during alkali precipitation may be given as [79]

$$[Fe_2(OH)_3]^{3+} + FeOH^+ + 2OH^- \rightarrow Fe_3O(OH)_4^{2+} + H_2O \qquad (1.24)$$

$$Fe_3O(OH)_4^{2+} + 2OH^- \rightarrow Fe_3O_4 + 3H_2O \qquad (1.25)$$

Magnetite nucleates when the concentration of ions becomes supersaturated, from that point the experimental conditions control the crystal growth process. Once the of Fe^{3+}/ Fe^{2+} ratio corresponds to the stoichiometry of magnetite, the mean particle size is determined in the range 2–12 nm by the conditions; the medium, pH and ionic strength, I, imposed by a salt ($8.5 \leq pH \leq 12$ and $0.5 \leq I \leq 3$ mol.L^{-1}) [80]. It is known that acidity and ionic strength, which are responsible for the protonation–deprotonation equilibria of surface hydroxylated groups, determine the electrostatic surface charge. At higher pH and ionic strength changes in the chemical composition of the interface, result in a decrease of the interfacial tension, γ. As stated by Gibbs's law, $d\gamma = -\Gamma_i \, d\mu_i$, where Γ_i is the density of adsorbed species 'i', which increases with pH, of chemical potential μ_i. As the free enthalpy for the formation of particles is defined by $dG = \gamma dA$, where dA is the change in surface area, reduced interfacial tension is consistent with a spontaneous increase in the system surface area [80].

Kim *et al.* [81] describe an interesting study of the effect of pH on the Fe-Cl-H_2O system. They detail the operating conditions for co-precipitation of the precursor where it can be protected from undesired critical oxidation during the synthesis.

1.5.1.1 The effect of oxidation, ionic strength and pH

Complexing agents are also frequently used in magnetite synthesis, but they mostly affect the morphology of the particles. Such methods raise difficulties in getting particles free from polymer, surfactant, or ligands [80]. Ammonia precipitation is of special interest because the resulting particles are free from the organic impurities introduced in other techniques [82]. Magnetite particles formed under normal kinetically controlled ammonia precipitation can grow in size, by Ostwald ripening, during ageing [83]. Researchers [30, 56, 80] have observed no particle growth with time when synthesis is carried out at high ionic strength. The saturation magnetisation of such small magnetite nanoparticles prepared with 1.0 M ionic strength with NaCl are lower (63 emu/g) than those prepared in NaCl free solutions (71 emu/g) [30]. Jolivet observes that the particles are smaller when precipitation takes place at pH above the isoelectric pH [56]. Wu *et al.* [84] published a similar finding in 2001. TEM micrographs of the particles that were formed in these reactions showed aggregation at a pH of 12.49.

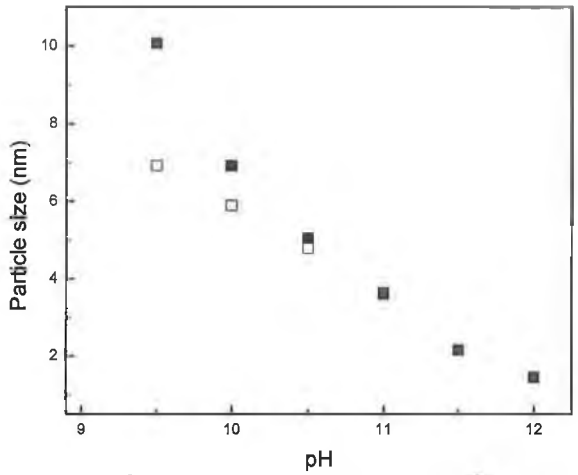

Figure 1.15. Mean diameter of magnetite particles as a function of the pH, (□) freshly precipitated and (■) after 8 day ageing in suspension, ionic strength 3 (M) $NaNO_3$ at 25°C [56].

However, when the particles were formed at a pH of 13.98, they were spherical and discrete. Most researchers who describe magnetite synthesis in the laboratory do not report altering the ionic strength of the reactant suspension. For synthesising magnetite in the laboratory, the base is added to the mixed iron salts under vigorous stirring conditions until precipitation is complete at a pH in the range 9-14. However, Gribanov *et al.*, [85] reversed the process by adding the iron salt solution to the base and described the limiting concentration of the reactants to be ~0.1 M for producing finest magnetite particles. The author indicated that the high concentrations limit the mobility of hydrated trivalent and divalent Fe ions and hence their ability to polycondense via the olation mechanism. It is also stated that the base should be added to the iron salts rapidly (in 1-2 s) with vigorous stirring, as slow addition creates inhomogeneity in the regions of hydrated iron species leading to polydispersity in the magnetic properties of the particles [85].

1.5.1.2 The effect of temperature and the base

Gribanov *et al.* investigated the effect of the nature of the cation on the magnetic properties of product magnetite [85]. The saturation magnetisation increased in nanoparticulate magnetite in the order KOH > NaOH > LiOH > NH_4OH. However, X-ray examination showed the presence of non-magnetic species when KOH and NaOH are used. Whereas magnetite particles produced between pH 8.5 to 10 using NH_4OH did not show the presence of nonmagnetic materials in the product. Bizdoaca *et al.* produced

monodisperse magnetite particles of ~10 nm diameter by aqueous coprecipitation using tetrabutylammonium hydroxide [86]. There are many articles regarding the ammonia coprecipitation of mixed iron salts to crystallise nanosized magnetite. Most of the researchers report injecting ammonia into deaerated solutions of iron chlorides at 60-80°C [58, 65, 69]. Some authors have precipitated magnetite at room temperature [55, 87] though Kim *et al.* used NaOH base for their synthesis [55, 81]. Dresco *et al.* carried out chemical coprecipitation in a similar way at low temperature (4-6°C) under vigorous stirring at pH 9-9.5 and produced small magnetite crystals (5-15 nm) [48]. Several researchers report the importance of elevated temperature for to obtaining optimum crystal properties. If the magnetite is prepared at temperatures below 60°C the final iron oxide formed predominated by α− or γ−FeOOH forms. Magnetite dispersions prepared above 60°C displayed saturation magnetisations of ~52 emu/g and XRD confirmed the magnetite crystal structure [84]. Gribanov *et al.* investigated the formation kinetics of magnetite crystal as a function of temperature (Figure 1.16). The rate of formation of magnetite increases with increase in temperature. However, the authors report that a reaction temperature of greater than 343K adversely affects the quality of crystal [85].

Goetze *et al.* report the synthesis of very small (2–30 nm) magnetite particles by variations of the concentration of reactants, temperature, reaction time, pH and the electrolyte concentration. Smaller particles were obtained by coprecipitation in diluted solutions or by coprecipitation at low temperature for a reaction time of few seconds [88].

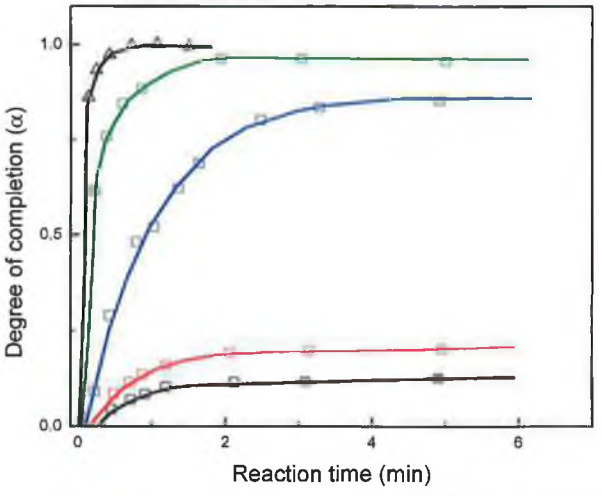

Figure 1.16. Plot of magnetite output (α) versus precipitation time (min) at (□) 268, (□) 283, (□) 290, (□) 307 and (Δ) 316K [85].

Wooding *et al.* [58] observed micelle formation which prevented complete dispersion of magnetite by stearic acid and myristic acids, this was overcome by introducing the acid in several portions.

1.5.2 The synthesis of magnetic nanoparticles by other methods

Other aqueous precipitation methods include: oxidation of Fe^{2+} [89-92], reduction of Fe^{3+} salt followed by precipitation [93], precipitation through water-in-oil microemulsions [48, 94-97], vesicles [98] and liposomal preparations [99].

The experimental parameters control the size of these particles and the resulting physical and chemical properties. A wide range of techniques have been exploited in order to improve the control of the size distribution of magnetic nanoparticles [100-102].

1.5.2.1 The synthesis of magnetic nanoparticles by oxidation

Domingo *et al.* demonstrated that [90] the mechanism of formation of magnetite from an aqueous alkaline slurry of $Fe(OH)_2$ involves the sequence of dissolution, oxidation, nucleation on $Fe(OH)_2$, and finally growth of Fe_3O_4. The dependence of the size and shape of the particles on experimental conditions is also discussed. Strable *et al.* [91] described the formation and stabilisation of ferrimagnetic iron oxide nanoparticles. Oxidation of Fe(II) at slightly elevated pH and temperature resulted in the formation of highly soluble nanocomposites of iron oxides which are stable under a wide range of temperatures and pH's. Deng *et al.* described the synthesis of magnetite by the hydrolysis and precipitation of $FeSO_4$ solution with NaOH. Hydrogen peroxide oxidation produces nanoparticles of size ~20 nm at pH 13 in presence of surfactant [89]. While in another method [92] described the synthesis of ultrafine (8-10 nm) magnetite particles by the precipitation of ferrous hydroxide from $Fe(NH_4)_2(SO_4)_2.6H_2O$ with excess NaOH. Hydrogen peroxide was used to oxidise the resulting green precipitate, in the presence of oleic acid and a commercial NNO surfactant at 60-70°C.

1.5.2.2 The synthesis of magnetic nanoparticles by reduction

Qu, S. C. *et al.* [93] successfully synthesised 3 to 10 nm magnetite particles by reduction of ferric chloride by Na_2SO_3 before precipitating with ammonia. The authors emphasised

the importance of Fe^{3+}/SO_3^{2-} ratio and the initial concentration of Fe^{3+} ion in determining the particle size and surface properties of the magnetite. The researchers report that the most appropriate ratio is 3:1, and that the magnetite particle diameter decreased from ca. 11 to ca. 3 nm with a decrease of the concentration of aqueous ferric chloride from 0.45 to 0.075 $molL^{-1}$. The advantage of this method lies in the fact that precipitation is done at the end of reduction process, and so precautions to prevent oxidation, e.g. by purging nitrogen or argon, are required.

1.5.2.3 The synthesis of magnetic nanoparticles by water-in-oil methods

A range of techniques where particle growth is limited by precipitating Fe^{3+} and Fe^{2+} ions in microemulsions, vesicles, polymer solutions, or gels have been reported [29, 103]. Water-in-oil (w/o) microemulsions are created by amphoteric surfactants. Water forms a microdroplet surrounded by a monolayer of surfactant molecules organised with their polar heads toward the aqueous core, known as the water-pool, and the hydrophobic tails in contact with the bulk nonpolar solvent [104]. With appropriate surfactant, chemical composition and concentration, such micellar cores can serve as nanoreactors for the coprecipitation of aqueous iron salts. Ionic surfactants successfully used include sodium bis(2-ethyl hexyl sulphosuccinate) (AOT) [105-108] and cetyltrimethyl ammonium bromide (CTAB) [98, 109].

Water-in-oil microemulsion techniques involving non-ionic surfactants have been reported [96, 110]. These are simpler techniques in that the surfactant is not also the complexing species in the synthesis of magnetite.

1.5.2.4 Magnetoliposomes

Magnetoliposomes are phospholipid stabilised magnetic iron oxide particles [99]. Synthetic liposomes are aqueous bodies stabilised with phospholipid bilayers. These vesicles can also be used as reactors to synthsise small magnetite nanoparticles [111]. Alternatively magnetoliposomes can be prepared by exposing fatty acid stabilised nanoparticles to lipids in solution. The lipids rapidly displace the fatty acids in a process analogous to phosphatising in metallurgy [111]. The surface of magnetoliposomes is partially compatible with biological membranes, and so they have immense potential for site specific drug targeting and other biomedical applications. Vesicles have also been

prepared containing didodecyl methyl ammonium bromide, containing an ionic magnetic fluid [112].

1.5.2.5 The synthesis of magnetic nanoparticles by thermal decomposition

Sapieszko *et al.* prepared magnetite by the thermal decomposition of alkaline solutions of Fe^{3+} chelates in the presence of hydrazine [113]. Vijayakumar and co-authors prepared pure magnetite crystals with particle size 10 nm by sonochemical decomposition of hydrated Fe(II) acetate salt under argon atmosphere [114]. Mild thermal treatment increased the proportion of the magnetite phase, as characterised by X-ray diffraction. Rockenberger *et al.* [115] demonstrated a new non aqueous approach for synthesising dispersible nanocrystals of iron oxide by the thermal decomposition of iron cupferron complexes in octylamine in presence of hot trioctylamine surfactants. The reaction produces γ-ferrite with a narrow size distribution around 6-7 nm.

Prozorov *et al.* reports [116] iron oxide nanoparticles synthesis using sonochemical radiation of $Fe(CO)_5$ at 30°C in presence of oleic acid. TEM expertiments showed that nanoparticles in fresh liquids were round-shaped and had almost uniform particle size distribution centred around 10 nm. Magnetisation measurements demonstrated the change of magnetic signal with time, as compared to the fresh ferrofluids, it was suggested that this was due to changes in the ordering of the magnetic clusters.
Gunko *et al.* [117] prepared both magnetite and maghemite by the hydrolysis of the metallorganic precursor $Fe(OBu^t)_2$-$(THF)_2$ followed by ultrasound and thermal treatment. The maghemite nanoparticles (9 ± 2 nm) were superparamagnetic with needle-like assemblies whereas the Fe_3O_4 (19 ± 2 nm) formed plate-like 10 μm thick aggregates.

1.5.2.6 Non aqueous synthesis

The disadvantages of the aqueous precipitation method is that the pH value of the reaction mixture has to be adjusted in both the synthesis and the purification steps and efforts to produce smaller (<10 nm) monodisperse nanoparticles have had very limited success. Specifically, in all of the reports which quote the preparation of sub 6 nm particles characterisation of the preparations was in the solid state only. There is no precedent for the preparation of stable suspensions of such small particles. Organic solution phase decomposition of the iron precursor at high temperature had been widely

used in iron oxide nanoparticle synthesis. Recent advances in the synthesis demonstrated that direct decomposition of $Fe(CO)_5$ followed by oxidation [118] can lead to high quality monodisperse γ-Fe_2O_3 type of nanoparticles.

In a recent article, Sun et al. demonstrated a high temperature (265° C) reflux method for synthesising suspension a of 4 nm monodispersed superparamagnetic magnetite particles. The nanoparticles were characterised by high resolution TEM and X-ray diffraction which indicated single crystal magnetite nanoparticles with very tight size distribution. In this method iron acetyl acetonate was refluxed in phenyl ether in presence of alcohol, 1,2 hexadecanediol and mixed surfactant oleic acid and oleyl amine [24].

1.6 Applications of magnetic fluids

1.6.1 Superparamagnetic nanoparticles in nanotechnology

The last decade has seen intense research on nano-magnetic materials due to the novel properties exhibited by these materials of quantum dimensions. Their sizes fall between the limits of atoms and bulk solids and can produce physical and chemical properties different from their atomic and bulk counterparts [55]. Due to their size superparamagnetic nanoparticles have unique physical, tribological, thermal, and mechanical properties and offer a high potential for several applications in different areas such as ferrofluids, colour imaging, magnetic refrigeration, detoxification of biological fluids, magnetically controlled transport of anti-cancer drugs, magnetic resonance imaging contrast enhancement and magnetic cell separation [39, 119-121].

In materials science, magnetic nanoparticles are the active components of recording tape, and flexible disk recording media [41]. Magnetite particle dispersions have been used as ferrofluids in, for example, rotary-shaft sealing, oscillation damping and position sensing [122] in bearings [61], actuators [123], as magneto-fluidic seals for moving parts in vacuum systems, fluid film bearings for computer hard disks, damping and cooling agents in audio speakers [124].

Surfactant coated micron scale magnetite dispersions are used as magnetorheological fluids (MR fluid). The most attractive feature of MR fluids is that several properties, such as viscosity, magnetic susceptibility, and optical characteristics, can be rapidly

manipulated by adjusting the strength and direction of the externally applied magnetic field. To add reversible properties to magnetic suspensions, surfactants are introduced into the liquid. Because of the acid-base behaviour of the ferric oxide surface, these particles have cationic surface charges in acidic aqueous solution. These charges ensure electrostatic repulsions between grains, which can be dispersed in water to obtain stable acidic suspension called ferrofluid [57]. Magnetic fluids comprise dispersions of magnetisable particles (magnetorheological fluids) and of dipolar particles (ferrofluids) [57]. The possibility of creating chains and controlling their spacing by applying magnetic fields, introduces the possibility of using these fluids in optical applications such as colour displays or controlled diffraction gratings [125].

Much attention has been focused on magnetic recording media materials, due to the demands for further miniaturisation of devices [37] and increased need for high memory density. Efforts to reduce the anisotropy energy per particle continue with a view to stretching to the so-called "superparamagnetic limit" in recording media [126-128]. Incorporating these materials into thin films enables the fabrication of a recording media by using a recording head, which can flip the magnetic spin of metal oxide by either a magnetic or an electric field [127].

Magnetite nanoparticles (Fe_3O_4)-cross-linked polyaniline with both conducting and ferromagnetic properties are also extremely useful due to their unique properties and potential applications as batteries, electro-chemical display devices, molecular electronic, non-linear optics, sensor, electrical-magnetic shields and wave-absorbing materials [89].

Biological applications of magnetic nanoparticles include their use as cell separators in biological/medical processes [129], for targeted drug delivery, and in tissue engineering. The use of properly coated magnetite nanoparticles in clinical medicine has also intensified. Stable water-based suspensions of magnetite nanoparticles [87] can interact with external magnetic fields, and be positioned in the body, facilitating magnetic resonance imaging for medical diagnosis [130] and AC magnetic field assisted cancer therapy [131]. These medical applications, which will be discussed in detail below, require firstly that the nanoparticles are superparamagnetic with sizes smaller than 20 nm, that the particle size distribution is narrow so that the particles have uniform physical and chemical properties, and finally that a suitable surfactant coating is present to maintain an electrostatically stable suspension.

1.6.2 Magnetic nanoparticles as mediators for magnetic hyperthermia.

Hyperthermia is a type of cancer treatment in which body tissue is exposed to high temperatures. It is also called thermal therapy or thermotherapy. Heat was proposed as a potential treatment for breast cancer more than 5000 years ago [132]. For treatment of surface tumours devices like heating rods, thermal blankets, or microwave, radiofrequency and ultrasound radiation can be applied to the body. For internal treatment substances called pyrogens are administered to the patient in order to induce fever evoking a febrile response from the patient's immune system.

Research has shown that high temperatures can damage and kill cancer cells, usually with minimal injury to normal tissues [133]. By killing cancer cells and damaging proteins and structures within cells [134], hyperthermia may shrink tumours.

Today, hyperthermia remains a promising form of cancer therapy aside from the well-known methods of surgery, chemotherapy and radiotherapy. Two kinds of heating treatments are currently available; (mild) hyperthermia refers to temperatures between 41 and 46°C, which stimulates the immune response for non-specific immunotherapy of cancers, while thermoablation, which refers to temperatures from 46 to 56°C, leads to tumour destruction by direct cell necrosis, coagulation or carbonisation [131]. Clinical experiments taking advantage of the higher sensitivity of tumour cells, to temperature in the range of 42–45°C than normal tissue cells were reported in the 1970s [135]. It is thought that, in such a temperature range, the function of structural and enzymatic proteins within the cells is modified, which in turn alters cell growth and differentiation and can induce apoptosis [136]. The synergistic effects of (mild) hyperthermia combined with radiation have been studied the most. Hyperthermia has been used for the treatment of resistant tumours of many kinds, with very good results. Combined hyperthermia and radiation have been reported to yield higher complete and durable responses than radiation alone in superficial tumours [137].

Recently devices for clinical hyperthermia based on either focused ultrasound or electromagnetic radiation have become commercially available. However these devices are not able to accurately deliver high heat energy to deeply situated cancers without destroying the surrounding normal tissues. Thus there is interest in developing technologies based on inserted heating sources.

Biomaterials, called mediators can convert the electromagnetic energy into heat when exposed to an external electrical or magnetic field. In this method suspensions of magnetic nanoparticles are injected at the site of the tumour. The tissue is then heated either by capacitive applicators, which are designed to maximise the electric component of electromagnetic fields (E-field), or by inductive applicators where the magnetic component is maximised (H-field) [138]. For capacitive hyperthermia, mediators are made from materials with high electric conductivity, as the heating is *via* eddy currents. While for inductive hyperthermia the materials must be magnetisable. Capacitive applicators may lead to uncontrolled heating of the body because of the tissue's intrinsic electrical conductivity and/or to electrical field heterogeneities due to differences in tissue dielectrical permeabilities. Therefore inductive mediators are currently of greater interest as tissues do not contain intrinsic magnetic materials. Nevertheless, it is impossible to completely prevent tissue heating by eddy currents, since the E-field component is never equal to zero. Therefore, for patient comfort, it was found that the product $H\nu$ (where H is the amplitude and ν the frequency of the AC magnetic field) should be lower than 4.85×10^8 $Am^{-1}s^{-1}$ for a treatment duration of one hour [139]. Moreover, the frequency must be above 50 kHz to avoid neuromuscular electrostimulation and lower than 10 MHz for appropriate penetration depth of the rf-field [140].

1.6.3 Magnetic nanoparticles as contrast agents for MRI

Ultra small (superparamagnetic) particles of iron oxide (USPIO) have been evaluated in multicentre clinical trials for lymph node MR imaging and MR angiography, with the clinical impact currently under discussion [141]. In addition, a wide variety of vector and carrier molecules, including antibodies, peptides, proteins, polysaccharides, liposomes, and cells have been developed to deliver magnetic labels to specific sites. Technical advances in MR imaging will further increase the efficacy and necessity of tissue-specific MRI contrast agents.

Superparamagnetic contrast agents usually change the rate at which ^1H nuclei decay from their excited state to the ground state, allowing more effective decay through energy transfer to a neighbouring nucleus, by the spin-spin or T_2 effect. As a result, regions containing the superparamagnetic contrast agent appear darker (negative contrast) in an

MRI than regions without the agent. For instance, when superparamagnetic nanoparticles are delivered to the liver, healthy liver cells can uptake the particles; diseased cells cannot. Consequently, the healthy regions are darkened, although the diseased regions remain bright [142].

Superparamagnetic Fe_3O_4 nanoparticles in suspension are useful as magnetic resonance imaging (MRI) contrast agents [143]. Their applications rely on the stability of magnetic order of the nanoparticles and suspensions over time [124]. Superparamagnetic particles have many advantages over other contrast agents. Compared with other magnetic contrast agents (e.g., gadolinium chelates), they are much more potent (as much as 50 times more effective per mole) [144]. Unlike agents such as perfluorochemicals, oils, and fats, superparamagnetic particles are miscible with aqueous systems, which means they can mix with material in the bowel and be used in small volumes. This miscibility also allows them to be used intravenously. Another advantage is that the particles do not pass the blood-brain barrier; thus, they are well suited for tracking blood flow in the brain [145]. Immiscible agents must be used in sufficient quantity to displace intestinal matter [146].

1.6.4 The NMR relaxation mechanism in aqueous magnetic fluids

The relaxation mechanism of water ^1H nuclei in presence of superparamagnetic iron oxide contrast agents is based on the original theory developed for paramagnetic molecules. In aqueous solutions there are two types of interactions or ^1H-electron couplings: intramolecular and intermolecular. These are modulated by molecular rotation and diffusion, for the intramolecular and intermolecular interactions respectively. These interactions are weak in pure water and hence the T_1 values are relatively large (>2 s). However, in the presence of paramagnetic molecules of high anisotropy energy, the relaxation times are significantly reduced.

The longitudinal (R_1) and transverse (R_2) relaxation rates of water ^1H nuclei diffusing past unpaired electrons are well predicted by outer sphere relaxation theory [147]. The interaction between the ^1H nuclear spin and the particle moment is a dipolar interaction, scalar coupling is not possible as there is no direct contact between the ^1H nuclei and the paramagnetic ions. The interaction is modulated by the diffusion of the water molecules τ_D and the electronic relaxation of the spin of the ion, τ_{s1}.

The field dependence of the water ^1H relaxation rates in aqueous suspensions of superparamagnetic iron oxide particles is due to so-called Curie relaxation [148] which dominates essentially in the high magnetic field part (> 0.02 T) of a nuclear magnetic relaxation dispersion (NMRD) profile. These profiles show an inflection point (high field maximum) where the total energy E, (sum of the Zeeman, E_Z and the anisotropy, E_A energies) of the system satisfy the condition $E \times \tau_c = \hbar$. τ_c is the correlation time for the energy fluctutations. This is the familiar $\omega\tau_c = 1$ relationship, it holds for small superparamagnetic crystals where the energy is mainly due to Zeeman contributions.

On the other hand, inner-sphere effects arise from the direct exchange of energy between the ^1H nuclei and the electrons, when the nucleus is located in the hydration sphere of a paramagnetic ion. There are both dipolar and scalar couplings involved, but the dipolar component dominates and is determined by the exchange rate with the bulk water in the hydration sphere of the paramagnetic ion. If the electronic fluctuations are slow, the ^1H nucleus experiences a constant electronic field and undergoes effective dipolar coupling with the electron spin. If the fluctuations are fast, then ^1H nuclei experience fluctuating electron fields and the dipolar coupling may be limited. The modulations of the dipolar couplings may be described by a correlation time τ_c by the relation

$$1/\tau_c = 1/\tau_r + 1/\tau_m + 1/\tau_{s1} \qquad (1.26)$$

where τ_r is the rotational correlation time of the paramagnetic centres, τ_c the exchange rate of water molecule in and out of the hydration sphere and τ_{s1} the electron relaxation of the electronic spin of the paramagnetic ion [149, 150]. So the fastest modulation or the highest value for $1/\tau$ will dominate the equation 11 above and will influence maximum on the correlation time τ_c. For most gadolinium chelates the limiting factor is molecular rotation, hence a new generation of contrast agents has recently been developed where the chelate is bound to serum albumins to slow down the molecular tumbling. This increases the magnetic interaction and results in faster water relaxation.

Nuclear magnetic relaxation dispersion (NMRD) profiles are used to estimate the spectral density functions which reflect the correlation between the Larmor frequency and the electron-^1H nuclei exchange modulation expressed as the ^1H relaxation rates R_1 and R_2. The relaxation rates in the NMRD profile reflect the averages of all the

mechanisms that drive the relaxation of water ^1H nuclei. The inflection points of the spectral density functions give some additional features. NMRD profiles of superparamagnetic magnetite suspensions (particle size > 15 nm) are normally recognised by two inflection points. In the outer sphere, diffusion dominated high frequency region, the inflection occurs at the precession frequency of the ^1H nucleus (when $\omega\tau_c = 1$). While the inner sphere mechanism operates in the low frequency region at the precession frequency of the electron (when $\omega\tau_c = 1$).

Many authors proposed simplified equations [149-151] to describe the relaxation rates in the inner sphere and outer-sphere regime. While these equations are relevant for low molecular weight iron complexes, such as ferritin, the simplified models do not accurately describe the relaxation for superparamagnetic iron oxide. Most of the theories do not take into account the Curie contribution which is prevalent in the high field and the anisotropic energy that modulates the relaxation at the low field. Finally Alan Roch and Muller proposed a successful model in 1999 [152] that describes the ^1H relaxation by magnetic particles at all Larmor frequencies. Importantly, they also succeeded in accounting for the behaviour of aqueous suspensions of magnetite, including some commercial contrast agents, by applying the theory and using reasonable values for the physical parameters.

All the NMRD profiles of USPIO have a common feature, after the low field plateau, there is a inflection downwards, the so-called low-field dispersion, before a sharp increase with a maximum in the high field region (high-field dispersion) and finally a

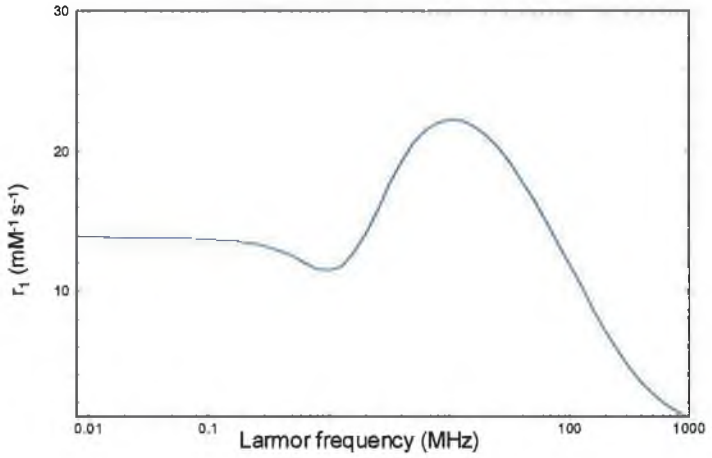

Figure 1.17. Simulated NMRD dispersion curve, using Muller's theory [152], showing the characteristic features for USPIO, the low field plateau and inflections at high field due to outer-sphere relaxation and c. 0.8 MHz due to the Néel process. Note clinical MRI fields are typically 60–100 MHz.

decrease to zero. The transverse relaxation profiles are essentially of the same shape except for the fact that they do not go to zero at the high field limit. An increase in the anisotropy energy attenuates the low-field dispersion, until it disappears and the same effect is produced by an increase of the particle size. The anisotropy energy is also increased when smaller crystals become agglomerated, as intercrystal interactions produce a high anisotropy field. Thus the low-field dispersion vanishes when the small nanocrystals become agglomerated.

At intermediate fields the relaxation is modulated by both the spectral density functions. The mean magnetisation at any frequency can be described by the equation 1.27.

$$\mu_C = < \mu_Z > = L(\alpha).\mu \qquad (1.27)$$

Equation 1.27 is very similar to the Langevin function discussed before (equation 1.17). However, the average magnetisation $< \mu_Z >$ takes care of all possible fluctuations of the magnetic moment due to anisotropy. This is critical in the mid-field range where the magnetic field is not strong enough to orient all the spins parallel to the field. The amount of spins will increase according to Boltzmann statistics until the applied field is strong enough to align and lock them. At high field, the magnetisation is locked parallel to the applied field (no Néel relaxation) so that the relaxation values reflect the influence of the diffusional interaction only. The Néel correlation time characterises the rate at

which the magnetisation flips from one easy axis of magnetisation to another. For a uniaxial single domain particle, this motion is between two antiparallel directions.

Muller and Roch formulated their theory in a fortran program which they have made available to our group. Thus it is possible for us to illustrate the effect of the parameters of the model on the predicted NMRD profiles. The program is also used in this thesis to fit some of the NMRD profiles. The parameters of the model include; the temperature,

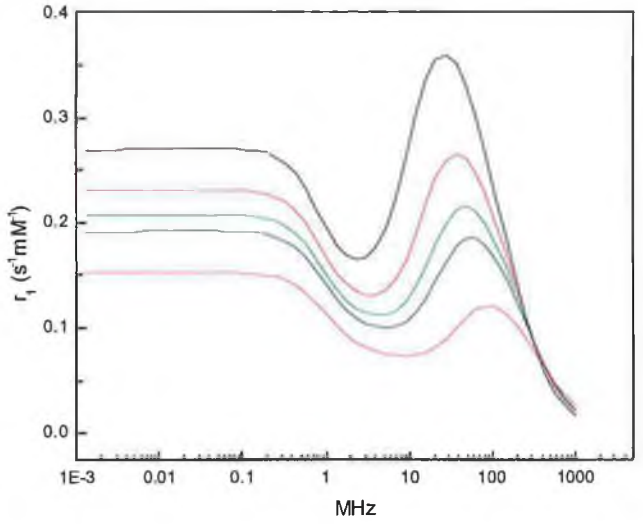

Figure 1.18. Simulated NMRD dispersion curves, showing the effect of increasing the particle size, the diameter of the particles are (—) 8, (—) 7, (—) 6.4, (—) 6 and (—) 5 nm. The other parameters are M_s = 26 Am^2kg^{-1}, D = 4.7x10^{-6} cm^2s^{-1}, τ_N=7×10^{-9} s, ν_{anis} = 1 GHz.

the diffusion coefficient of the medium, the concentration of iron, the radius of the magnetite core, the anisotropy energy (expressed as a frequency ν_{anis}, in GHz), the Néel correlation time, τ_N and the saturation magnetisation, M_s. The major experimental observation for USPIO is that reducing the core size moves the high field maximum to higher frequency. This trend is predicted by the theory.

The effect of increasing the saturation magnetisation, M_s, is, as expected, to increase the relaxivity. Note, applying Muller's convention, the "Ms" value has been expressed in the units of mass magnetisation, Am^2kg^{-1}, where 1 Am^2kg^{-1} = 1emg g^{-1}. The scaling is close

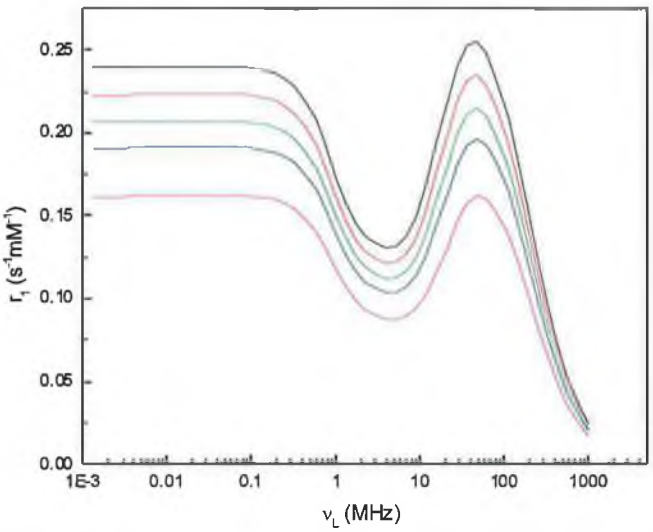

Figure 1.19. Simulated NMRD dispersion curves, showing the effect of increasing the saturation magnetisation, the values used are (—) 28, (—) 27, (—) 26, (—) 25 and (—) 23 Am^2kg^{-1}. The other parameters are D_{core} = 6.4 nm, $D_{eff} = 4.7\times10^{-6}$ cm^2s^{-1}, $\tau_N = 7\times10^{-9}$ s and ν_{anis} = 1 GHz.

to being linear over a small range. However as the anistropy energy is inversely related to M_s, there is some alteration to the shape of the profile at low field.

The effect of increasing the Néel correlation time, τ_N is to attenuate the low field

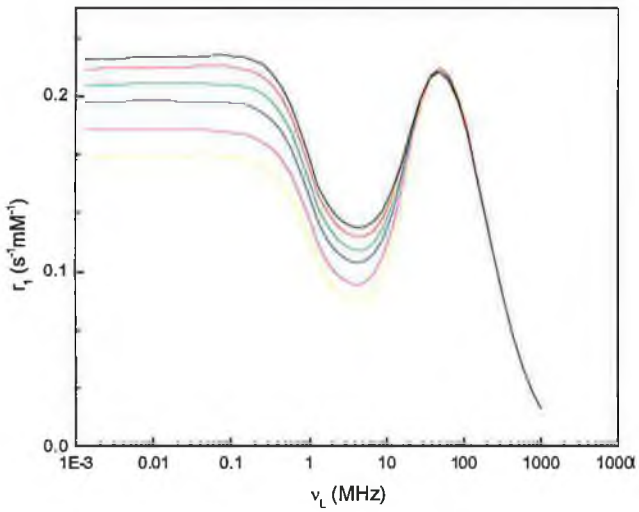

Figure 1.20. Simulated NMRD dispersion curves, showing the effect of increasing the Néel correlation time, τ_N, the values are (—) 13, (—) 10, (—) 7, (—) 5, 3 (—) and (—) 2 ns. The other parameters are D_{core} = 6.4 nm, M_s = 26 Am^2kg^{-1}, D = 4.7×10^{-6} cm^2s^{-1}, τ_N=7x10^{-9}s, ν_{anis} = 1 GHz.
dispersion and increase the relaxivity of the low-field plateau.

Finally, the effect of increasing the anisotropy frequency, ν_{anis}, is similar to the effect of altering τ_N. The relaxivity of the low field dispersion is reduced. There are also

significant changes in the shape of the mid-field minimum. It should also be pointed out that the anisotropy frequency, and the Néel correlation time are related, by the Arrhenius, or a similar, law. However, the simulation below is useful as it illustrates the general behaviour predicted by the model.

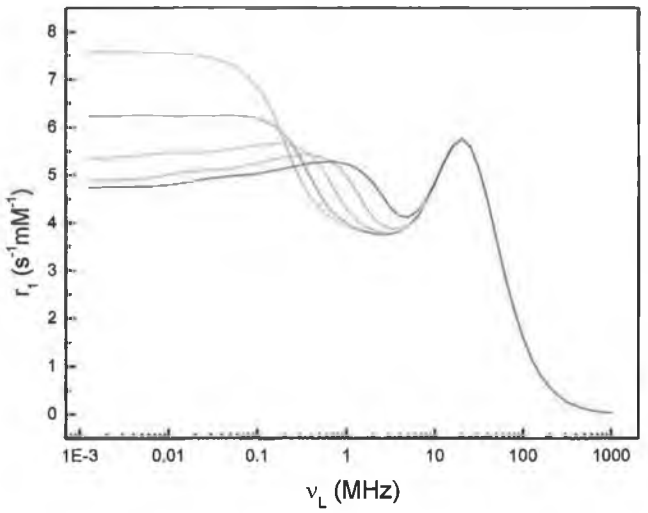

Figure 1.21. Simulated NMRD dispersion curves, showing the effect of increasing the anisotropy frequency, ν_{anis}, the values used are (—) 5, (—) 2, (—) 1, (—) 0.5 and (—) 0.25 GHz. The other parameters are D_{core} = 6.4 nm, M_s = 26 Am^2kg^{-1}, D = 4.7×10^{-6} cm^2s^{-1}, τ_N=$7x10^{-9}$ s.

While the mathematical details of SPM theory are beyond the scope of this thesis, it is worthwhile drawing the analogy to relaxation by modulation of the dipolar interaction due to molecular motion, as described earlier in this introduction. The relaxation is dominated at high field by the rapid diffusional process, resulting in a high field dispersion. There is a second dispersion in the low MHz range when $\omega\tau_c$=1 for the slower, Neel process, i.e. in the range where relaxation is due to the motion of the nanoparticles magnetic moment.

Finally, it important to mention the limitations of the model. The major problem is that the theory only predicts the NMRD profile due to single-sized spherical particles, while invariably there is some polydispersity in the nanoparticle sizes. This problem is compounded by the fact that the predictions of the theory are size-dependent, and indeed many of the parameters, for example the anisotropy energy are also size dependent. Thus the theory is only applicable to reasonably monodisperse suspensions. It is also assumed that there is no "inner-sphere" interaction.

The theory is limited to particles of less than 20 nm. This is because it is assumed that the crystals magnetic moment is a "superspin" and the exchange interactions are ignored. Magnetic measurements in the solid state indicate that for larger particles the existence of spin waves should become important. It is also assumed that the Néel correlation time is much shorter than the particle rotation correlation time ($\tau_N << \tau_R$), so the particle can be regarded as static. However, the Néel relaxation time is an exponential function of the particle volume while the rotational correlation time varies linearly with volume. So the assumption that the particle is static breaks down for magnetite cores of diameter greater than about 20nm. Lastly, it is assumed that τ_N is the same irrespective of the electronic spin energy level. This is reasonable if the populations of all such levels are the same, i.e. if the anisotropy energy is small, which again is the case for small crystals.

Despite these difficulties SPM theory does reproduce the relaxation profiles of aqueous suspensions of superpramagnetic iron-oxide. The parameters extracted by fitting the theory to experimental data can be useful, though they do need to be treated with some caution. In this thesis SPM theory is used firstly to interpret the relaxation profiles of aqueous suspensions of iron-oxide nanoparticles stabilised with bio-polymers which show some degree of clustering. Secondly, the theory is extended to interpret, for the first time, the profiles of non-aqueous suspensions of dispersed nanoparticles.

Chapter 2

Experimental Section

2.1 Introduction

In this section the experimental techniques which are applied throughout the thesis will be described. The thesis is based on characterisation of surfactant coated and uncoated magnetite nanoparticles with a view to assessing their suitability for use as MRI contrast agents. Uncoated magnetite nanoparticles were synthesised in Trinity College by our project partner and most of the monolayer and bilayer coated particles were synthesised in DCU. Details of the syntheses are given in the relevant chapter. Methods of application of surfactants on uncoated dry magnetites are also discussed in their respective section (Section 3).

NMRD and hydrodynamic size measurements by photon correlation spectroscopy are the two most widely used techniques and are described in detail in this section. Also included are analytical methods which were used for materials analysis; atomic absorption for estimation of iron, permanganetometry for estimation of Fe^{2+} and gas chromatography for oleic acid estimation. Brief descriptions of the techniques of Transmission and Scanning electron microscopy and Raman spectroscopy are also included.

They include fast field cycling NMR, photon correlation spectroscopy and the analytical techniques used in materials analysis. All the NMRD profiles were taken using a Stelar SPINMASTER-FFC 2000 relaxometer.

2.2 Fast field cycling NMR

2.2.1 Historical development of the technique

Fast Field cycling relaxometry is a preferred [153-155] method for measuring the dependence of NMR relaxation times on the magnetic field strength. It is also known as nuclear magnetic relaxation dispersion (NMRD). Since the very beginning of Nuclear Magnetic Resonance there had been great interest in relaxation phenomena and their field dependence [156-161]. Both T_1 and T_2 vary with field-strength, more so in the case of T_1. The mechanism of field strength dependence is complex and it is difficult to extrapolate measured relaxation times from one field to another. Thus, in field cycling relaxometry the dependence is measured directly using a single spectrometer. Field dependent

information can be obtained by using multiple spectrometers each operating at a fixed field, but the number of fields required make this approach prohibitively expensive.

In field cycling a high magnetic field (polarisation field) is applied to pre-polarise the sample in order to boost signal intensity. Thereafter, the sample is allowed to relax in a second field (relaxation field) which can be set to any desired value, including zero. The signal remaining after this relaxation interval, which is determined by T_1 at the relaxation field and the time spent at that field, is detected in a field of fixed flux density B_{acq}, which again is as high as possible. By measuring the dependence of the recovered magnetisation on the time spent at the relaxation field, T_1 can be determined. The signals are acquired with a radio frequency (RF) unit tuned to a predetermined field (frequency) irrespective of the relaxation field chosen. As the shortest measurable T_1 is directly dependent on the field switching time, fast electronic methods for switching the magnetic field are applied. This requires the development of low-inductance, air-coil magnets and power supplies capable of switching the field electronically to any desired value in a matter of milliseconds while, at the same time, maintaining the high field stability and homogeneity required by NMR. Despite this, it is not possible with current technology to obtain the field homogeneity required to perform spectroscopy. This approach, known as fast field cycling, has been tried with success in several laboratories [162].

The field cycling NMR technique was developed in 1953, within a few years of the first NMR experiments, by Packard and Varian [163]. They used a rudimentary field cycling device to observe nuclear magnetism in the earth's field. In the late 1950's Abragam and Proctor were responsible for introducing the technique in France, while studying the concept of spin temperature. In this case, the magnetic field cycle was effected by extracting the sample from the magnet by hand. The relaxation times of the studied samples had to be extremely long (of the order of minutes to hours).

In 1959 A. G. Anderson [161] used a field cycling apparatus to study the absorption of audio frequency radiation by local fields. A magnetic field cycle was required to achieve a suitable spin polarization before switching down the field for the irradiation step. The design was based on relays, batteries, capacitor banks and variable resistances.

In Germany during the 1960's, Friederich Noack introduced the concept of "relaxation spectroscopy" through his Ph.D. thesis at University of Stuttgart. The first electronically

field cycled NMR instrument in Europe was constructed by Reiner Kimmich in Noack's laboratory in the late 1960's. The nested solenoid design of the magnet was originally due to Noack and Schweikert, where each coil is cut from a single cylinder of metal with a variable step of the helix [164]. Since then development has progressed along two principal paths; switching the field while keeping the sample in place (usually referred to as fast field cycling) and combining two magnets and shuttling the sample between them. The main advantage of the latter technique is that the detection magnet can have high sensitivity and resolution comparable to a modern fixed field spectrometer, from which they are usually constructed. However, this approach is limited to samples with long T_1 values and the accessible temperature range is severely restricted.

The use of field cycling was limited to research groups able to build their own field cycling instruments. An Italian company Stelar SRL started a project to develop a commercial Fast Field Cycling instrument for NMR relaxometry studies in 1994. In the recent years fast field cycling instruments have become available commercially through Stelar. It is now possible to measure relaxation times in the entire range from 10 kHz to 40 MHz [165]. Another advantage with field cycling is that the measurements can be automated, it is often, but not always, possible to set up the experiment at the highest field and then automatically step down to the lowest frequency. This provides an essential gain in time compared to a conventional field variable magnet where all fields have to be set manually. The development of field cycling devices has not stopped; however, new magnets continue to emerge [166]. In addition, the field cycling technique is versatile [165, 167] and not limited to what is often referred to as relaxometry i.e. the measurement of T_1. Inversion recovery experiment as well as spin echo like sequences are also possible with the fast field cycling technique [165, 167].

2.2.2 The field cycling experiment

One of the pulse sequences is the *prepolarised sequence,* which is composed of a *polarisation* time (approximately 5 times the relaxation time) in a relatively high field (typically 10-14 MHz) to obtain reproducible initial magnetisation, followed by an *evolution* time where the sample is left to relax in the actual field of interest and finally a *detection* time with a relatively high field (typically 9.25 MHz) when a 90° detection pulse is applied and subsequently the sample magnetisation from the free induction decay

(FID) is detected in the xy-plane. The sequence is outlined in Figure 2.1 below. Even with this sequence some residual effects of the field switch can influence the signal, it may be necessary to omit short *evolution* times. As the detection field is reproduced in subsequent cycles phase sensitive detection is feasible. This 'quadrature' detection allows further compensation for the effects of the field switch by using the magnitude for evaluation of the magnetisation intensity. It also means that signals can be accumulated to improve the sensitivity [168].

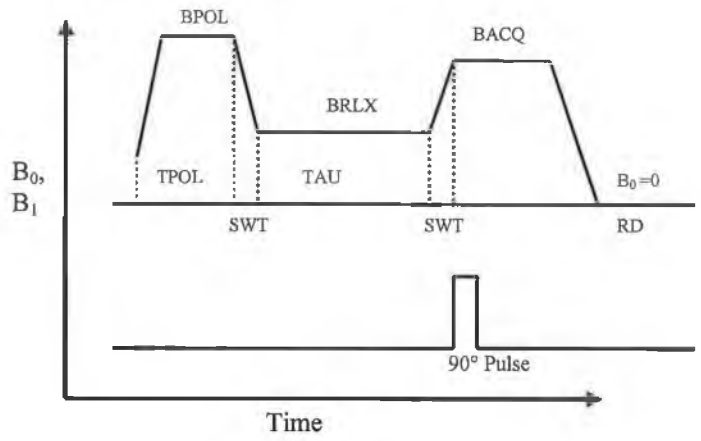

Figure 2.1. The basic pre-polarised pulse sequence in NMRD experiment.

The pre-polarised sequence can be used to measure T_1, by repeating the sequence and varying the time τ. When τ is short the intensity of the magnetisation will reflect the polarisation period, when τ is long compared to T_1 at B_{rlx}, the intensity of the magnetisation will reflect the equilibrium magnetisation at B_{rlx}. So from the dependence of the magnetisation on τ, the value of T_1 can be extracted by least squares fitting of an exponential decay function. Typically 16 values of τ are chosen, ranging from 1ms to $5xT_{1est}$, where T_{1est} is an estimate of T_1. In this thesis the magnetisation recovery of the magnetic fluids studied was invariable mono-exponential. This was confirmed from time to time by recording recovery curves at a given filed, but using upwards of 30 τ values. The data was always followed a single exponential recovery. In order to get good statistics, typically 16 scans were required.

The pre-polarised sequence is not always suitable for measuring the T_1, when the *evolution* and *polarisation* field become close, the difference in initial (short τ) and final (long τ) magnetisation in the exponential decay curve becomes small and it becomes

difficult to obtain an accurate value for T_1. Therefore the *zero or non-polarised* method is employed in this regime (typically ≥ 6 MHz). One of the central blocks of this sequence is outlined in Figure 2.2. This technique maintains significant difference between the

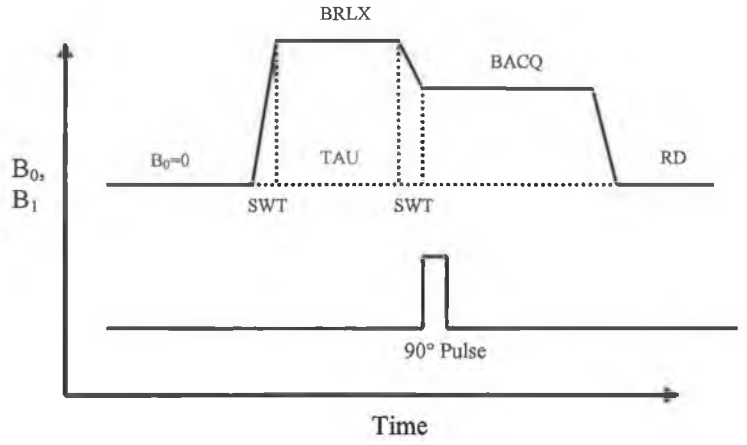

Figure 2.2. The zero or non-polarised pulse sequence in NMRD experiment.

magnetisation observed between short and long delays, at high B_{rlx}. Balanced sequences with an array of evolution times are employed for the actual T_1 measurement exactly in both the pre-polarised and non-polarised sequences.

One of the crucial limitations of field-cycling applications is the signal-to-noise ratio. However, averaging a number of transient measurements, as is standard in high-resolution NMR spectroscopy may conflict with the limited stability intrinsic to field-cycling systems [9]. The signal-to-noise ratio can be expressed by [169-171].

$$S/N \propto Bo\ \xi \sqrt{\frac{\eta Q V_S}{k_B T}\left(\frac{\nu_o}{\Delta\nu}\right)} \qquad (2.1)$$

where η is the filling factor of the RF coil, Q is the quality factor of that coil, V_S is the sample volume, k_B is the Boltzmann constant, T is the absolute temperature, $\nu_0=\gamma B_0/2\pi$ is the Larmor frequency, $\Delta\nu$ is the bandwidth of the receiver filtering and amplification system, and $\xi < 1$ represents the reciprocal of the noise level of the receiver electronics. This equation indicates that the *S/N* ratio increases proportional to $B_0^{3/2}$. On the other hand, the use of high polarisation and detection flux densities, large samples, high Q coils, low-noise receivers and narrow RF filters are all employed to maximise the sensitivity of the instrument. Despite this the sensitivity is poor, errors in T_1 of less than

1% can be achieved for water suspensions. However when detecting the solute, the best achievable concentration is c. 5M for ^{1}H in the solution state, with errors at 3-5%. The situation is worse for solids than liquids, due to shorter T_2, and worse again for nuclei other than ^{1}H. Profiles can be obtained for ^{19}F [172] and isotropically enriched ^{2}H and ^{17}O.

2.2.3 Practical considerations

Samples are maintained at a constant temperature during the NMRD experiments. The Spinmaster Variable Temperature Controller attached to the Stelar FFC allows setting of the sample temperature between −140 and 140°C with control of about 0.1°C. Most of our measurements were carried out, unless stated otherwise, at sample temperature of 24°C.

The cooling pump for the B_0 magnet and rf transmitter are turned on. Then the sample, in a 10 mm diameter NMR tube, is placed in the probe. The measurement starts with the setting of acquisition frequency (B_{ACQ}) normally 9.25 MHz. The probe is tuned to be resonant at 9.25 MHz. Optimal acquisition parameters are found by trial and error, typical values for the samples studied in this thesis are:

RF attenuator = 35
AF Gain = 1
EXP = PP
Recycle delay = 0.2
TPOL = 0.2
Switching time= 0.003
TAU = 0.001
BRLX = 0.1
Block size = 256
Sweep width = 500000
FLTR = 270000
Max. Scans = 4
Dummy Scan = 0
PW90 = 7
RINH = 16

The signal intensity after the application of the 90° pulse is recorded as a function of the *evolution* time. The intensities are then fitted to a decay exponential curve to obtain the

actual T_1. The signal intensity is detected as the first points on the FID, after some clipping to remove instrumental artefacts including magnet settling and probe ringing. This immediately points at one of the difficulties with fast field cycling. In order to get reliable results the signal must be kept on resonance frequency for all evolution times. When a high current passes through the magnet coils during the experiment, the resulting heat causes a change in the geometry of the magnet coil due to thermal expansion that shifts the magnetic field produced. The magnet temperature may fall as much as 20-30° C between *polarisation* and evolution for long time pulses. This is compensated for by a circuit that senses the magnet temperature and adds a current proportional to the temperature increase to stabilise the magnetic field, this is referred to as *temperature compensation* and is one of the set up variables in an FFC experiment. The cooling-heating cycle is normally less than couple of seconds due to an efficient cooling system. With varied evolution times, as in a typical T_1 experiment, the magnet will have different temperatures for different evolution times, which will produce small variable field offsets. To remove this one may introduce a so-called *balanced multiblock sequence* [164] as the one employed in Stelar FFC relaxometer consisting of typically 16-32 evolution times (τ).

To record an NMRD profile successive T_1 measurements as a function of field are performed using a macro on which most of the parameters are preset. The general procedure is:

- The sample temperature is set
- Using NP sequence all the parameters concerning the magnet cycle (switching time, slew rate, pre-scan delay etc.,), RF (90° pulse width, receiver gain etc.) and acquisition (scan size, spectral width, etc.) at the maximum desired Larmor frequency of the profile are optimised and fixed.
- An appropriate magnet temperature compensation factor is chosen.
- The maximum expected T_1, polarisation time, pre-scan delay are then set in the loaded NP/S sequence (normally for the profile range 20 to 0.01 MHz). T_1 is measured and saved in a pre defined data and results file.
- When all these parameters are optimised, the macro is started to acquire the NMRD profile automatically.

Some parameters, e.g. the estimate for T_1 which determines the range of τ values used, are updated after each field.

For the samples prepared in this project, as there is the possibility of some precipitation due to the applied field, after completing a profile the first (highest field) point was always re-measured, to check the stability of the suspensions.

2.3 Photon correlation spectroscopy

2.3.1 Principles of the technique

Photon correlation spectroscopy (PCS) or dynamic light scattering (DLS) is a technique used for particle sizing of samples, typically in the sub-micron range. The technique measures time-dependent fluctuations in the intensity of light scattered by colloidal particles in suspension. In the fields of electronics, biotechnology, and materials [173] nanoparticle size distributions are usually determined, after drying, by electron microscopy. However, this method cannot be used to characterise particles in suspension.

The modern roots of the PCS technique date from the early 1960's [174, 175]. Since that time PCS has been used to investigate a wide variety of colloidal suspensions [176, 177]. A low intensity laser beam is scattered by particles in suspension. The diffusion of particles causes rapid fluctuations in backscattered intensity around a mean value at a certain angle. The instrument determines the particle size by measuring the rate of fluctuations in the scattered laser light. The time scale of the fluctuations depends on the particle size [177]. The experimental scattering time autocorrelation function is directly obtained from the measurement. This is then fitted to a calculated function and the diffusion coefficient of the particles obtained. For a given temperature and viscosity the particle size can be determined.

Despite its practical success, standard PCS techniques are limited to very dilute (single scattering) samples. This makes it impossible to apply the technique to study the particle dynamics of a wide range of naturally occuring colloidal suspensions without dilution. The advantages are that PCS is a non-destructive method and it can measure in-situ average particle size [178] in a range between 0.6 and 6000 nm. In addition to giving information on the average hydrodynamic diameter, the technique also provides a measure of the width of the distribution, called the polydispersity index (PDI).

All reliable methods for interpreting the experimental time autocorrelation function are based on the assumption that the particles under consideration are spherical and are based on the established data on the interaction between the spherical particles and its surroundings, i.e. the particle is assumed to tumble freely in suspension without interacting with other particles [179]. There are some models for dealing with PCS data from anisotropic particles, like rods and disks [180] and non-spherical or even cluster-like particles [181]. The results obtained are invariably very sensitive to the shape information built into the model. Shape information can more reliably be obtained from static light scattering approaches [182], where the intensity is measured as a function of the scattering angle. However limitations remain and the static scattering techniques are not suitable for particles of size close to or below 100 nm.

From PCS analysis the particle size is given as diameter, in this case the hydrodynamic diameter. This is the true particle size only when the particles measured are spherical. For non-spherical particles, the technique does not provide any information about the actual particle shape but rather indicates the "equivalent spherical diameter", the diameter of an imaginary sphere of the same volume [180].

A correlation function can be used to determine the correlation or relationship between the measurements of a fluctuating signal. An example of the intensity autocorrelation function due to the diffusional motion is shown in Figure 2.3 below.

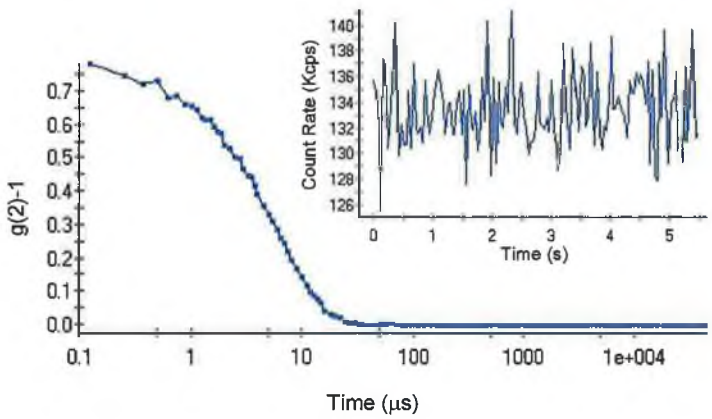

Figure 2.3. The intensity autocorrelation function of the counts trace which shown in the inset. The sample is 1:10 diluted 10.25 nm magnetite in heptane.

The electric field correlation function, $g_1(t)$ which is directly related to the dynamics of the scatterers may be defined as;

$$g_1(t) = \langle I(t)I(t+\tau) \rangle \qquad (2.2)$$

where I is the intensity, τ is delay time, the angle brackets denote the time averaging. The normalised intensity autocorrelation function $g_2(t)$ is related to the field correlation function by the relation [177].

$$g_2(t) = 1 + \sigma \left| g_1(t) \right|^2 \qquad (2.3)$$

where σ is an instrumental coherence factor mainly determined by the number of coherence areas exposed on the detector. The coherence area is defined by

$$A_{coherence} = \frac{\lambda^2 R^2}{\pi a^2} \qquad (2.4)$$

where R is the distance between the detector and the scattering volume of radius a, λ being the wavelength of the incident light. The optics of the PCS spectrometer are designed so that σ is close to the ideal value of one. The 'R' in Malvern HPPS spectrometer is in the range from –3.5 mm to 5 mm.

Brownian motion can be used to obtain information about the dimensions of the solvated particles. For a monodisperse system in Brownian motion, the random diffusion of the particles causes the intensity autocorrelation equation to decay exponentially. The Stokes-Einstein equation for the diffusivity of particles of radius r in a liquid defines the diffusion coefficient, D, of the particles as

$$D = \frac{k_B T}{6\pi\eta r} \qquad (2.5)$$

where k_B is Boltzmann's constant, T is the temperature in Kelvin, η is the viscosity of the liquid in which the particles are suspended. Since the fluctuation of the intensity signal is caused by the motion of particles, those particles that diffuse more quickly are characterized by a smaller fluctuation time. As seen in equation 2.4, the diffusion coefficient is inversely proportional to the size of the particles, and, consequently, the smaller the particle, the shorter the fluctuation time. For a monodisperse suspension the autocorrelation function is a single exponential and may be expressed as;

$$g_1(t) = \exp(-t\,\Gamma) \qquad (2.6)$$

where $1/\Gamma$ is the characteristic time constant of the correlation function. It is related to the diffusion coefficient by $\Gamma = Dq^2$, and the scattering vector, q, is given by

$$q = \frac{4\pi n}{\lambda_o} \sin\left(\frac{\theta}{2}\right) \qquad (2.7)$$

in which n is the index of refraction of the liquid medium, θ is the scattering angle and λ_0 is the laser wavelength in air. Geometrically, the scattering vector is defined as the difference between the scattered wave vector and the incident wave vector. By combining equation (2.5) and the equation for the linewidth, Γ, an equation for the radius of the scattering particle is obtained as

$$r = k_B T q^2 / 6\pi\eta\Gamma \qquad (2.8)$$

Using equation (2.8) the size of the scattering particles can then be determined if the temperature and viscosity are known. When the logarithm of the autocorrelation function is graphed versus time, the slope of the resulting line is the linewidth, Γ.

2.3.2 Practical considerations

All measurements were done on a Malvern High Performance Particle Sizer at 25°C. Aqueous samples were taken in standard (12.5 × 12.5 × 45 mm) disposable cuvettes and loaded in the press-fit sample chamber in the machine. For heptane suspensions UV-VIS spectroscopic (200-3800 nm) quartz cuvettes were used. The temperature of the sample was maintained constant with an internal heating system attached in the instrument. A low power (60 mW) He-Ne laser, with λ= 632.8 nm is used as a light source and the measurements were made at a detection angle of 7° (backscatter). The scattered light is detected by the photomultiplier tube and the signal is then converted into digital pulses by a pulse amplifier discriminator (PAD). The output, a stream of digital pulses, is then fed to the correlator which calculates the normalized autocorrelation function of the incoming pulses, i.e. the detected intensity. The laser power is automatically attenuated so that the count rate from the sample, especially high scattering samples, is within acceptable limits. An attenuation index of 11 denotes no attenuation (full laser power), while 0 denotes full attenuation (total laser block). The measurement position within the

cuvette was automatically determined by the software to allow a large range of sample concentrations to be measured. Lower range of numbers indicates that the measurement position is closer to the cuvette wall (when sample is turbid).

The results of the measurement are available based either on intensity, volume or number. The results section gives three pieces of information as shown in Figure 2.4.

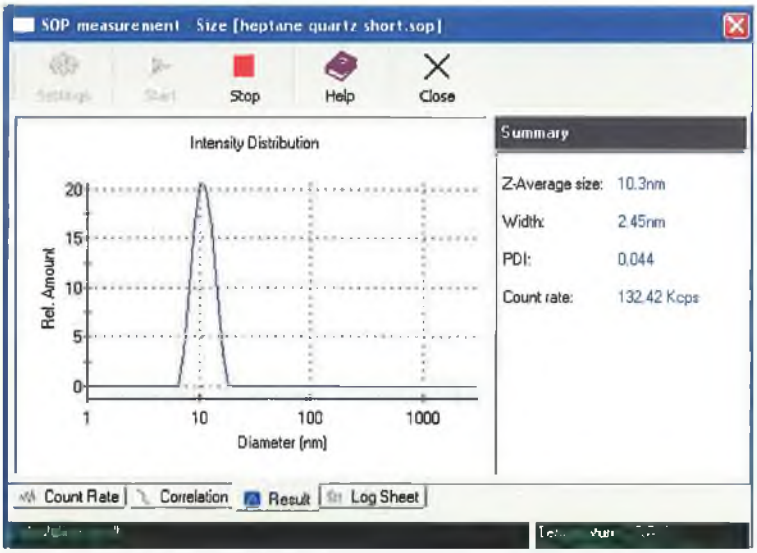

Figure 2.4. The HPPS results window indicating the Z average, PDI, width and count rate for the same 10.25 nm superparamagnetic magnetite particle.

The z-average diameter, also known as the "cumulants mean", is the mean diameter based on the intensity of scattered light and is sensitive to the presence of aggregates and/or large particles. This is the size to use if a number is required for quality control purposes. It will only be comparable with other techniques if the sample is monomodal (i.e. only one peak in the size distribution), spherical and monodisperse (i.e. there is no width to the distribution), and the sample is prepared in the correct dispersant.

For a monodisperse suspension $g_1(t)$ is a single exponential. For all practical samples the size distribution is multimodal or at least has some polydispersity. So $g_1(t)$ is not of singly exponential. There are many methods available for "inverting" such data to get distribution of characteristic times (Laplace inversion etc.). One of the methods, which is implemented in the HPPS software is cumulants analysis. This gives two values, a mean value for the size, and a width parameter known as the polydispersity index (PDI). It is important to note that the mean size (often given the symbol Z or z-average) is an intensity mean. It is not a mass or number mean because it is calculated from the signal

intensity. The scattering intensity is approximately proportional to the volume of the scattering particle.

The cumulants analysis is a fit of a polynomial to the log of the g_1 correlation function (equation 2.8).

$$Ln[g_1] = a + bt + ct^2 + dt^3 + et^4 + \ldots\ldots\ldots \quad (2.9)$$

The value of b is known as the second order cumulant, or the z-average diffusion coefficient. This is converted to a size using the dispersant viscosity and some instrumental constants. Only the first three terms a, b, c are used in the standard analysis to avoid over-resolving the data; however this does mean that the Z-average size is likely to be interpreted incorrectly if the distribution is very broad (i.e. has a high polydispersity).

The polydispersity index, PDI, is defined as equal to $2c/b^2$ [183]. Note that unlike the *polydisperity* familiar from polymer science, a PDI value close to zero is indicative of a monodisperse suspension and a larger PDI is indicative of a broader distribution. A PDI value of 1 indicates the later term 'c', in the cumulants expansion is of more importance than the term 'b'. This situation corresponds to a very broad, or, more commonly, a multimodal distribution. PDI 'values' above 1 are is reported as 1.0 by the software.

The software also displays the size and percentage by either intensity, volume or number for up to three peaks within the result. The cumulants analysis gives a good description of the size that is comparable with other methods of analysis for spherical, reasonably narrow monomodal samples, i.e. with polydispersity below a value of 0.1. For samples with a slightly increased width, the Z-average size and polydispersity will give values that can be used for comparative purposes, as they reasonably represent the distribution. For broader distributions, where the polydispersity is over 0.5, it is unwise to rely on the Z-average mean, and a distribution analysis should be used to determine the peak positions.

2.4 Other analytical techniques

2.4.1 Atomic absorption spectroscopy

Accuracy, precision and long term reproducibility in the determination of iron in the magnetite suspensions is required to assess the relaxivity (relaxation rate per mMol of Fe) of the nanoparticles. The analyst must have the knowledge of limitations of different methods and be aware of sources of error, which may be introduced. The accuracy of a determination may be defined as the concordance between it and the true or most probable value. Iron content with less than 1% random error can accurately be determined by both colorimetric and spectrophotometric methods.

In 1955 the Australian physicist Alan Walsh reported the first application of atomic absorption spectra to chemical analysis [184]. Atomic absorption spectroscopy (AAS) is employed in the determination of metals (in soluble form) in liquid samples. Metals include Fe, Cu, Al, Pb, Ca, Zn, Cd and many more [185]. The flame atomic absorption spectroscopy (FAAS) technique is used by many researchers for determining Fe at milimolar levels [185-187]. The technique of flame atomic absorption spectroscopy (FAAS) requires a liquid sample to be aspirated, aerosolised, and mixed with combustible gases, such as acetylene and air or acetylene and nitrous oxide. The mixture is ignited in a flame whose temperature ranges from 2100 to 2800 ^{o}C.

During combustion, atoms of the element of interest in the sample are reduced to free, unexcited ground state atoms, which absorb light at characteristic wavelengths. The characteristic wavelengths are element specific and accurate to 0.01-0.1 nm. For iron estimation Fe-cathode lamp is used whose characteristic wave length is 248.3 nm. A light beam from a lamp whose cathode is made of iron is passed through the flame. A device such as photomultiplier can detect the amount of reduction of the light intensity due to absorption by the analyte, and this can be directly related to the amount of the element in the sample. The sample in aqueous solution is aspirated into the flame through a device called the 'atom cell'. The atom cell has two major functions, nebulisation of the sample solution into a fine aerosol and dissociation of the analyte elements into the free gaseous ground state form. As the sample passes through the flame, a beam of light passes through it into a monochromator. The monochromator isolates the specific spectrum line emitted by the light source through spectral dispersion, and focuses it upon a

photomultiplier detector whose function is to convert the light signal into an electrical signal. A computer data system converts the change in intensity into an absorbance.

For determining iron in the iron oxide sample, calibration data was generated by aspirating into the flame samples of solutions containing known concentrations of iron (typically 0.5, 1.0, 1.5, 2.0 and 2.5 mM Fe), and measuring the absorption of each solution. At least five solutions were used covering the absorbance range 0.02 to 0.2 as it is found that the calibration curve is not linear beyond this absorbance rage (fitting error < 0.99). A blank (Milli q water used in all preparation and dilutions) was also included in the standards for 'zero' ppm iron. Special care was taken in preparing and diluting the test solutions using Gilson pipettes. The values of absorbance were plotted against the Fe^{3+} concentration in ppm. A straight line fit through the data could then be used to determine the iron concentration of a solution from the absorbance of this solution. One of the calibration curves for the estimation of iron in magnetite samples is given in Figure 2.3 below.

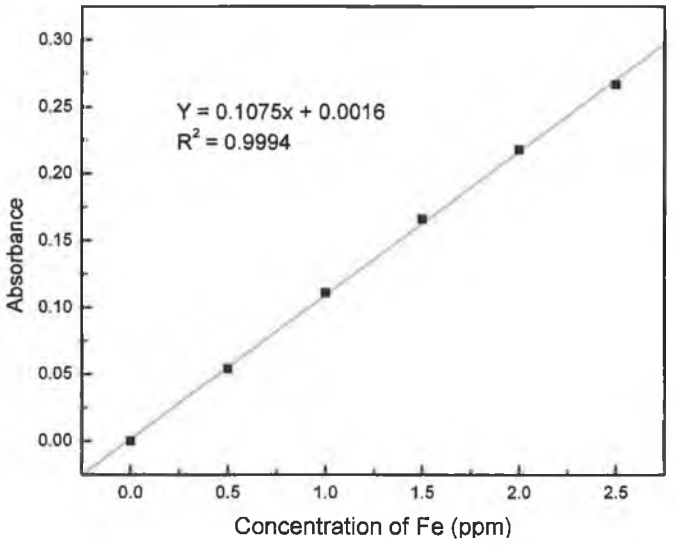

Figure 2.5. A standard calibration curve for iron using solutions with known concentration of Fe in the range 0.5 to 2.5 mM by AAS.

To produce a sample for estimation 0.3-0.5 ml aliquots were removed from the NMR tube after the NMRD profile had been recorded. The Atomic absorption spectra were taken on a Varian SpectrAA Spectrometer. Thus given the initial iron content, the sample was already in the T_1 range conveniently measurable with the NMRD instrument (T_1 = 5-200 ms). Five drops of 6N analar grade hydrochloric acid were then added and the solution boiled on a hot plate with 1 mL of deionised water (in a fume hood). The heating

was continued until the solution reduced to a couple of drops. 25 mL of Milli-Q water was added and the solution heated to boiling. The solution was then cooled to room temperature, transferred to a 100 mL flask and diluted to the mark with Milli-Q water. To produce a sample solution in the range of our standard calibration curve (iron of ~0.5-3 ppm), these solutions were further diluted as necessary.

2.4.2 Redox distribution of iron in iron oxide samples

The oxidation states of iron in magnetite synthesised in two sets were evaluated by estimating the Fe^{2+} and Fe^{3+} iron with standard potassium permanganate. For this purpose a small aliquot (0.5 ml) of magnetite suspension in heptane was digested in 10 drops of 1:4 hydrochloric acid by slowly boiling it. The digested mass was carefully dried taking care that the dried mass is not overheated. The dried solid was redissolved and boiled again by adding about 20 ml water. The solution was cooled and the volume was adjusted to 100 ml in a volumetric flask. Aliquots of 10 ml were lifted for estimating the Fe^{2+} present by titrating (oxidising) it with 0.1 M standard potassium permanganate from purple to colourless end point.

For estimating the total iron (Fe^{2+} and Fe^{3+}), 10 ml aliquot was boiled with 1ml 1M sulphuric acid and a pinch of granular zinc for about 5 minutes. The solution was filtered and washed to remove the unreacted zinc after cooling. All the washings and filtrate were collected in the same container (100 ml conical flask) and titrated against same standard potassium permanganate for quantitative estimation of total iron. The difference of these two data gives the amount of iron in the Fe^{3+} state and the results are given in table 5.6 in chapter 5.

2.4.3 Fatty acid determination

Gas chromatography is a chromatographic technique that is generally used to separate organic compounds that are volatile. The organic compounds are separated due to differences in their partitioning behaviour between the mobile gas phase and the stationary phase in the column.

Fatty acid quantification is commonly investigated by gas chromatographic analysis of their methyl ester derivatives. Methyl esters offer increased volatility and sensitivity, while eliminating the problem of fatty acid adsorption on the injector [188, 189]. Oleic

acid, both free in suspension and chemisorbed on magnetite particle surfaces were analysed by gas chromatography. The derivatisation process was performed by a reflux with a BF_3-methanol complex reagent, and the resulting methyl esters were extracted into n-hexane. For quantification purposes, five standard solutions of oleic acid methyl ester were prepared in a concentration range of 2-10 mM.

Samples were analyzed on a Varian Star 3400 CX Gas Chromatograph. The oven temperature was isothermal at 230°C and nitrogen was employed as the carrier gas at a flow of 1.0 mL/min. The injector temperature was set to 260°C and the oven temperature was 300°C. The split ratio was set at 1:33 and the injected volume was 1μL. A standard curve of peak area versus concentration was prepared, allowing for the determination of oleic acid concentrations in chemisorbed magnetite samples.

2.4.4 Raman spectroscopy of iron oxide samples

Raman spectra were recorded with a Renishaw 1000 micro-Raman spectrometer. The excitation wavelength was 514.5 nm from an Ar^+ Ion laser (Laser Physics Reliant 150 Select Multi-Line) with a typical laser power of ~20 mW in order to avoid excessive heating. The incident and scattered beams were focussed using a Leica microscope with 100× objective and a laser spot of approximately 4-5 μm diameter. All measurements were carried out at room temperature. The spectra are presented in figure 5.10 and 5.11.

2.4.5 Electrn Microscopy

Scanning electron microscopy, SEM, was performed on a general purpose Hitachi S-3000N Scanning electron microscope. Powder samples were mounted on an adhessive carbon film fixed on a specimen stub. Magnetite suspensions were mounted by drying a drop of stable suspension of magnetite on the carbon film. High magnification SEM pictures were taken with a typical acceleration voltage of 20KV and suitable filament current/ emission. Special care was taken to avoid any stigmation in the image.

Transmission electron microscopy, TEM, was performed on a 125 kV Hitachi H7000-H7110 Transmission electron microscope.

Chapter 3

Preparation and characterisation of aqueous magnetic fluids

3.1 Introduction

In the first part of this chapter attempts to prepare stable aqueous suspensions from dry precipitated uncoated magnetic nanoparticles are described. For this purpose a few commonly used surfactants i.e., sodium oleate, sodium stearate, NNO surfactant and gelatin were selected. The preparations in sodium oleate and gelatin are described in particular. The surfactants were applied to the nanoparticle surface using different methods, and in different ratios to the iron oxide.

In the second part the characterisation of some dry samples and suspensions prepared by our project partner are described. In particular the temperature and frequency dependence of the relaxation times of the suspensions were investigated. The characteristics of the resulting nanoclusters are investigated. Finally, some data for DNA stabilised suspensions are presented.

3.2 Experimental

3.2.1 Uncoated nanoparticles suspended in water

3.2.1.1 Aqueous suspensions of uncoated maghemite

A magnetic fluid (~ 5 mM of iron) was prepared by suspending fine maghemite (γ-Fe_2O_3) particles [190] in 10 ml water and ultrasonicating the suspension at 50°C in an ultrasonic bath for 30 min. The maghemite powder was synthesised by hydrolysis of the metallorganic precursor, $Fe(OBu^t)_2$-$(THF)_2$, followed by ultrasound treatment. Drying the washed powder in air oven at 200°C yielded maghemite (γ-Fe_2O_3) [117]. It was found that less than 50% of the solid could be brought into suspension. Pure Milli-Q water was used in all the laboratory preparations.

3.2.1.2 Aqueous suspensions of uncoated magnetite

The magnetite powder (Fe_3O_4) used in this experiment [190] was prepared through a non-aqueous route giving crystalline particles in the size range 12 to 25 nm as characterised by TEM, Figure 3.1. The particles were synthesised by the procedure mentioned above for maghemite, except that the product powder was dried in vacuum for 3 h at room temperature [117].

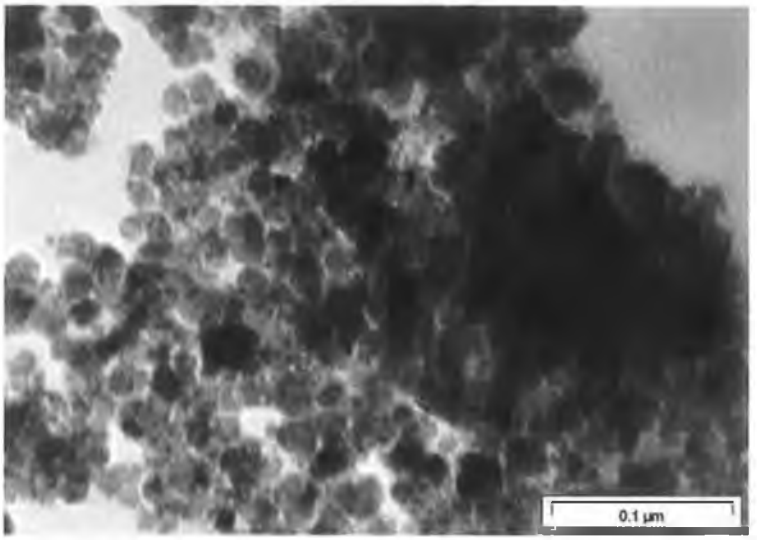

Figure 3.1. TEM micrograph of uncoated magnetite (sample no-2) showing agglomerated primary particles of size 12-25 nm.

Accurately weighed magnetite powder was added to 10 ml of water so as to make a ~10 mM of iron solution. The suspension was sonicated in a 440W ultra sonic bath for 30 minute at 50°C.

3.2.1.3 Stability of the suspensions

The magnetic fluids were kept sealed in 10 mm diameter NMRD sample tubes for evaluation of T_1 relaxation time over time. The measurements were performed at 25°C, over the frequency range 10 kHz to 20 MHz, which are the standard NMRD operating conditions throughout the thesis.

3.2.2 DNA stabilised magnetic suspensions

Magnetite nanoparticles were prepared by the collaborators [190] by coprecipitation of a mixture of ferrous (2×10^{-2} $molL^{-1}$) and ferric (1×10^{-2} $molL^{-1}$) chlorides with ammonia. The precipitation was carried out, at room temperature, in presence of either natural, double-stranded, or heat induced denatured, substantially single-stranded, herring or salmon sperm DNA (hs-DNA, ss-DNA) of concentration 1.7×10^{-3} $molL^{-1}$ [191]. The DNA coated nanocomposites were then characterised by XRD, IR, TEM and NMRD.

Similar to the fatty acid suspensions, after some months the suspensions mature. Before this stage the R_1 values decrease as precipitation continues. After maturation there is no

observable precipitation, indeed on maturing, the R_1 values also increase slightly and remain stable from that point. The suspensions which were somewhat opaque rust coloured, clarify although the colour does not change. All the data reported is for mature suspensions.

This ageing behaviour is somewhat different for the fatty acid stabilised suspensions, presented below. The fatty acid stabilised materials continue to precipitate until after some months, when the precipitation, and associated decrease in R_1, almost cease. For the fatty acid stabilised suspensions, after some months a fatty layer forms on the surface, the suspension immediately re-homogenises on exposing to the NMRD field and the R_1 values recover to their former values.

3.2.3 Surfactant coated nanoparticle suspensions in water

3.2.3.1 Ultrasonication with surfactant

All the experiments described in this section were carried out using the same sample of spherical magnetite nanoparticles, in the size range 12-25 nm [190]. The magnetic fluids were prepared by suspending magnetite nanoparticles in water using gelatin powder (>98%, Riedel-de Haen) or sodium oleate (Sigma-aldrich ~99%) as surfactants. Experiments were conducted to investigate the effect of magnetite/surfactant ratio on the stability the suspensions. The same mass, 4mg, of magnetite powder was added to 5 ml water in all the preparations, to produce c. 5 mM Fe. Different amounts of gelatin or sodium oleate were added to the suspension to generate different Fe:surfactant ratios. The weight ratios (iron oxide: surfactant) used in these experiment were 1:1.5, 1:1, 1:0.5, 1:0.25 and 1:0.125. The mixtures were sonicated at 50°C for 2 h. The stability of the fluid was monitored by measuring transmittance at 540 nm using a UV-Visible spectrometer over two months as well as by NMRD.

3.2.3.2 Wet grinding in agate mortar

The possibility of making stable aqueous magnetic fluids by grinding magnetite powder with an agate mortar and pestle (agating) in presence/absence of sodium oleate with few drops of water was explored. In a typical experiment 8 mg of dry magnetite was agated with a few drops of water either with and without surfactant, in the ratio of magnetite/ surfactant 1:1.5. The agated mass was diluted to 10 ml with Milli-Q water followed by

sonication in an ultrasonic bath maintained at 50°C for 2 h. The concentration of Fe in the suspension was ~ 4 mM. The surfactant was added either during the sonication after the grinding or was added prior to the wet grinding. NMRD characterisation of the fluids produced by agating with and without the surfactant, showed that they displayed very similar characteristics and changes with ageing to the fluids prepared purely by ultrasonication. After some months, the agated (both types) and the sonicated suspension stabilise, with mM concentrations of Fe present. The NMRD profiles of the suspensions are very similar and will be discussed below.

3.3 Results

3.3.1 Uncoated aqueous nanoparticle suspensions

3.3.1.1 Stability of the uncoated nanoparticle suspensions

For the maghemite suspension NMRD profiles recorded over a period of 10 days indicate slight precipitation, Figure 3.2. The suspensions are quite stable in spite of the fact that these maghemite particles are not coated with surfactants. The high field maximum at 7.36 MHz in the profile may be correlated with an average primary particle size of ~ 11.2 nm in accordance with Muller's theory [152]. A scaled simulated NMRD profile is included in the figure for comparison.

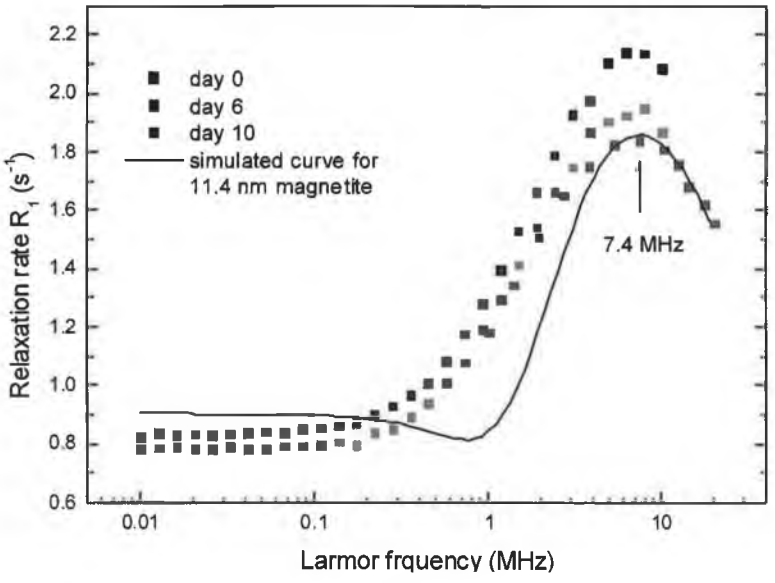

Figure 3.2. NMRD profiles for the maghemite suspension recorded on day 0 (■), day 6 (■) and day 10 (■). The solid line (—) is the simulation for an 11.2 nm magnetite core, scaled by an arbitrary concentration to match the data.

At the time of this experiment a method for the estimation of iron was not available. From the amount of precipitate, we roughly estimate that the concentration was 1mM. This would correspond to an initial approximate r_1 of 2.1 s^{-1} mM^{-1} at 7.4 MHz and 0.8 s^{-1} mM^{-1} at 0.01 MHz. These values are lower than expected. According to Muller [152], superparamagnetic magnetite particles of size 11.4 nm should have a relaxivity of ~12 $s^{-1}mM^{-1}$ on the low field plateau, and of ~21 $s^{-1}mM^{-1}$ at the high field maximum at 7.4 MHz.

The magnetite suspension was found to be less stable than that of maghemite, as evidenced by gradual precipitation over time (Figure 3.3) The precipitation is due to strong dipolar interactions among fine magnetite particles leading to aggregation [60, 86].

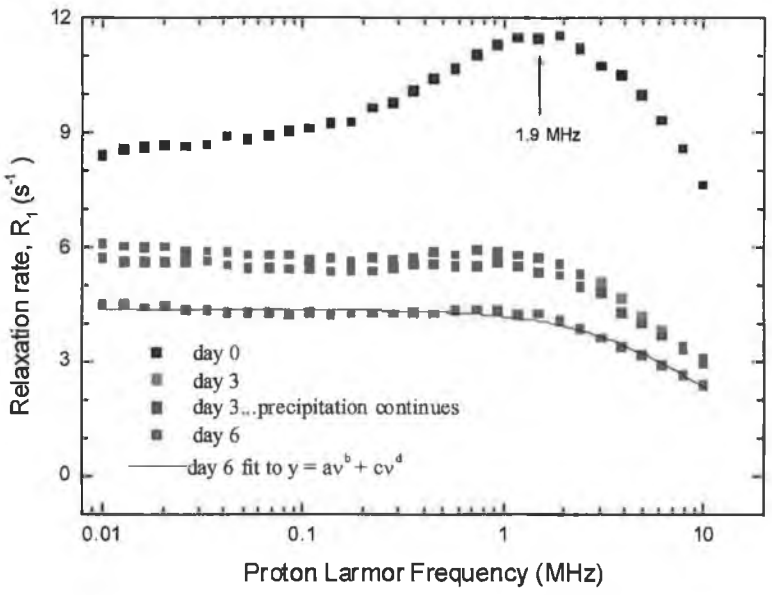

Figure 3.3. NMRD profile of magnetite suspension in water over time where (—) is the fit to the equation, $y=av^b + cv^d$ where a=0.228, b=-0.00233, c=0.0116, d=1.24.

There is a distinctive high field maximum in the NMRD profile from day 0. This is probably due to presence of a superparamagnetic fraction. In the case of the other profiles (day 3-6), the data can be fitted to a dual power law dependence of the relaxation rate on frequency. The curves above (for day 3-6) are fitted to the function $y = av^b + cv^d$. One of the fits to the data from day 6 is included. Within the error there is no change in the powers between day 3 and day 6. The data suggests that the superparamagnetic fraction precipitates first and that the residual fraction, which gives rise to the dual power law frequency dependence continues to precipitate up to day 6. We will demonstrate later that

the observed frequency dependence of the relaxation rate is characteristic of nanoparticle clusters of high effective magnetic anisotropy.

3.3.1.2 Effect of pH on the uncoated nanoparticle suspensions

Dilute hydrochloric acid (0.1 M) was used to adjust the pH of the maghemite suspension. NMRD profiles for the maghemite suspension were recorded at two different pH values. The pH of the water used was 6.5. The pH of the suspension was not raised above 7. The NMRD data (Figure 3.4) in high field region was poor with relatively high errors.

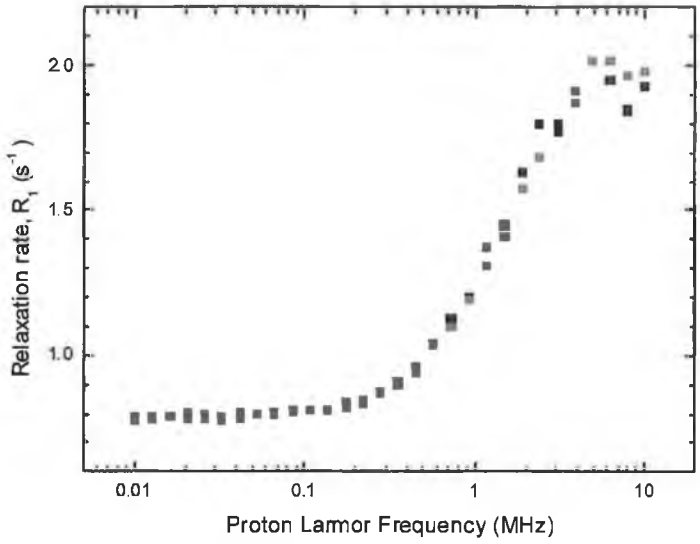

Figure 3.4. The NMRD profiles of the maghemite suspension at room temperature. Profiles were recorded at pH 7 (■) and 3.5 (■).

The longitudinal relaxation time T_1 was comparatively long. It is likely that the concentration of particles in suspension was low. The surface charge of the sample determines the stability, but this is sensitive to the preparation and is not known for this sample. Apparently there was no effect of pH on the relaxation mechanism of γ-Fe_2O_3 in the complete frequency range and the suspension was stable after changing the pH in this range. The initial precipitate was examined under SEM for its morphology and sizes.

Tightly packed large aggregates of 100 to 150 nm primary particles with amorphous surfaces were seen under scanning electron microscope (Figure not presented). The magnetite suspension after day 6, was acidified to a pH of 4.9 see Figure 3.5.

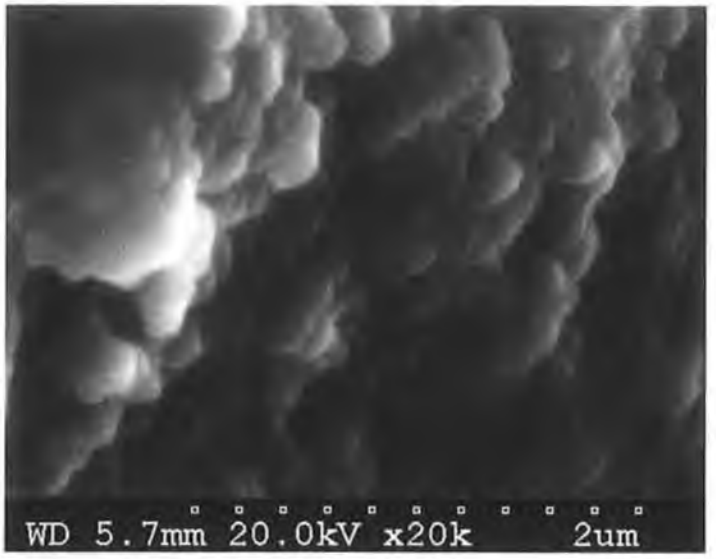

Figure 3.5. Scanning electron microscope image of maghemite precipitate (uncoated) while making the suspension.

The resulting NMRD profiles, shown in Figure 3.6, indicate that on lowering the pH the contribution from the superparamagnetic fraction to the water relaxation decreases and the fraction exhibiting a dual power law dependence on frequency increases, in a manner similar to the changes observed on ageing the suspension. The reversibility of this change was not tested, as there was visible precipitation of the sample. NMRD experiments that will be described later demonstrate that pH stability can be achieved when the magnetite sample is coated with surfactants.

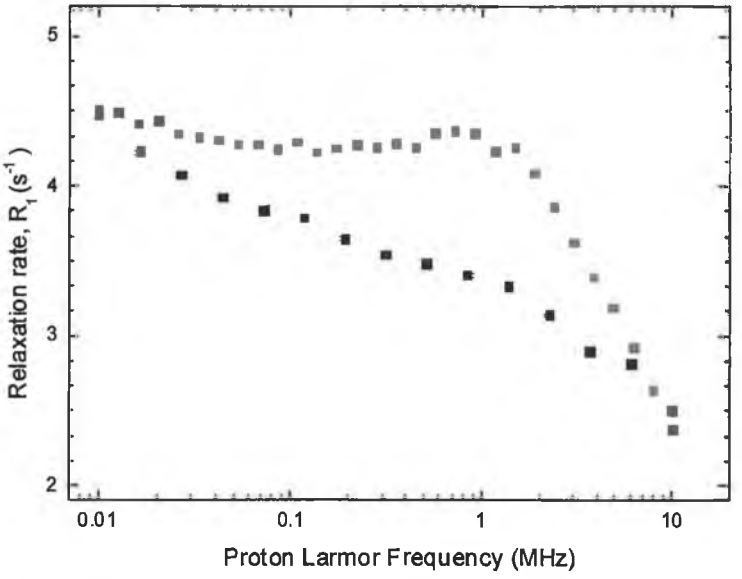

Figure 3.6. Relaxation profiles for the uncoated magnetite suspension in water at pH 7 (■) and 4.9 (■).

The natural pH of the suspension was 6.5. This is explained by the fact that the pH of Milli-Q water used in the experiment is ~6.5 and the pH of zero surface charge (pH_{pzc}) for magnetite is 6.53 [192]. Pure magnetite nanoparticles prepared by ammonia coprecipitation are expected to have a slightly electron deficient core with a net negative electrostatic charge on the surface [56] and so are acidic in nature. Due to the magnetic interactions and very high surface area, the fine magnetite particles have a tendency to agglomerate to reduce the surface energy.

3.3.2 DNA stabilised magnetic suspensions

NMRD profiles for two samples of double stranded (DS) herring and salmon sperm DNA stabilised magnetic fluids were recorded, the data is given in Figure 3.7. The magnetite suspensions were stable without any loss of particles by precipitation over a year. Both types of DNA surfactants have produced fluids with very similar profiles. There is apparent mixed behaviour of superparamagnetism and large magnetic clusters in suspension. The Z-average size by PCS was about 115 nm with PDI 0.2. The suspensions have broadly the same relaxivities and the profiles have very similar shape. The frequency of the high field maximum corresponds to magnetite cores of about 17 nm, according to Muller [152].

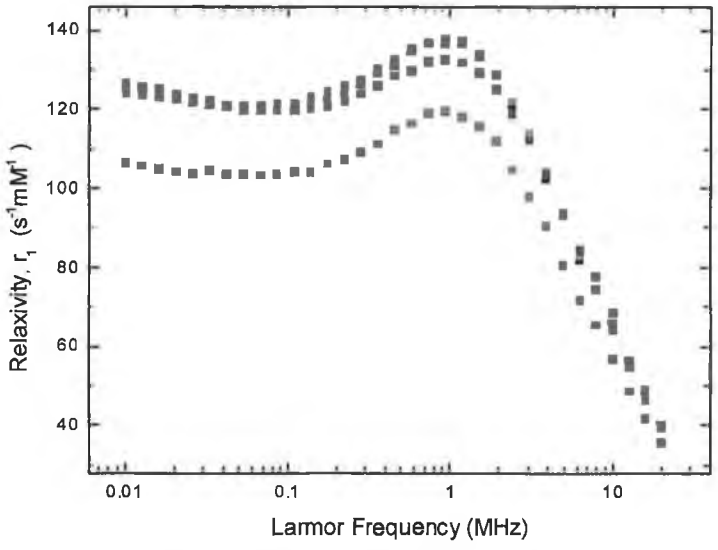

Figure 3.7. NMRD profiles of double stranded salmon sperm DNA (■) and (■), and double stranded herring sperm DNA (■) and (■) stabilised magnetic suspensions.

A transmission electron microscopy (TEM) image of DS herring sperm DNA coated magnetite is given in Figure 3.8. The 100 particle average size for the nanoparticles was 7-11 nm by TEM. Size analyses from TEM are not very authentic for coated nanoparticles. During the drying the test suspension on TEM copper mesh grid, there may be artefacts caused by drying induced aggregation during the TEM sample preparation [121].

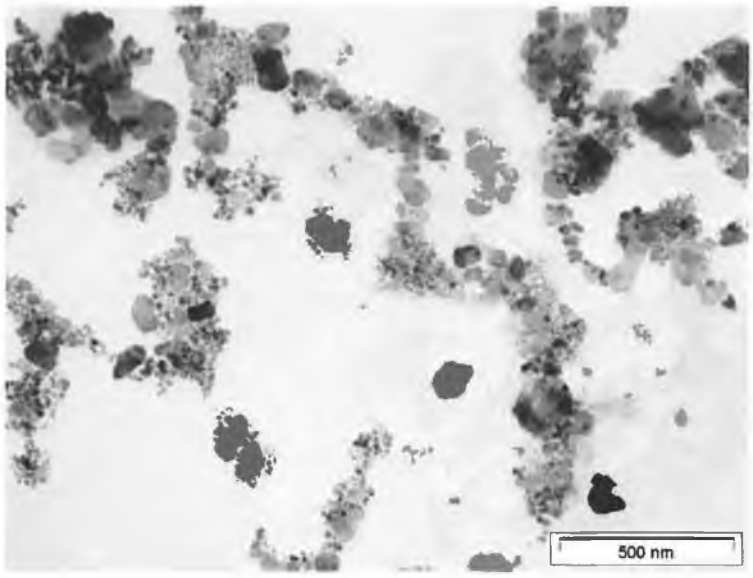

Figure 3.8. TEM image of double stranded herring sperm DNA coated magnetite particles showing entangled chains of a network structure.

Conversely there may be experimental effects on the particle size such as shrinkage under the electron beam [193] during TEM analysis. But there was a general trend that denatured double-stranded hs-DNA magnetite samples have particles in distributed entangled chains.

NMRD profiles for two samples of single stranded herring sperm DNA stabilised magnetic fluids were recorded, the data is given in Figure 3.9. The magnetite suspensions were stable without any loss of particles by precipitation over a year.

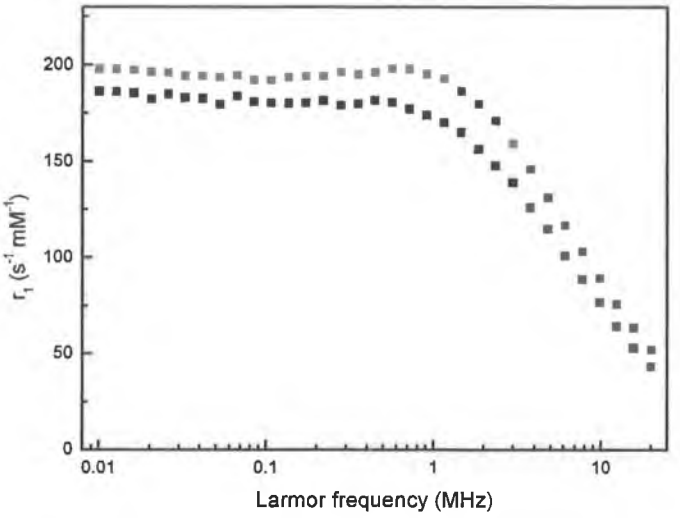

Figure 3.9. NMRD profiles of two single stranded SS herring sperm DNA stabilised magnetic suspensions.

These two preparations also show reasonable reproducibility and have profiles of very similar shape. The profiles can again be fitted to a dual power law dependence of relaxation rate on Larmor frequency. However the low frequency power is much lower in this case than was observed for the fatty acid stabilised fluids. For the single stranded preparations the Z-average size by PCS was typically around 75-80 nm with slightly higher PDI of 0.3.

3.3.3 Surfactant coated nanoparticle suspensions in water

3.3.3.1 Stability of the suspensions

For the gelatin stabilised suspensions the transmittance data is presented in Figure 3.10. The transmittance increased significantly during the first week due to precipitation. After about 10-12 days equilibrium was reached and there was almost no further loss of particles from the suspensions, as indicated by a plateau in the transmittance. The stable magnetite suspension was more translucent than the initial turbid suspension. The net transmittance increased for samples where more surfactant was used, with the exception of ratio 1:0.125.

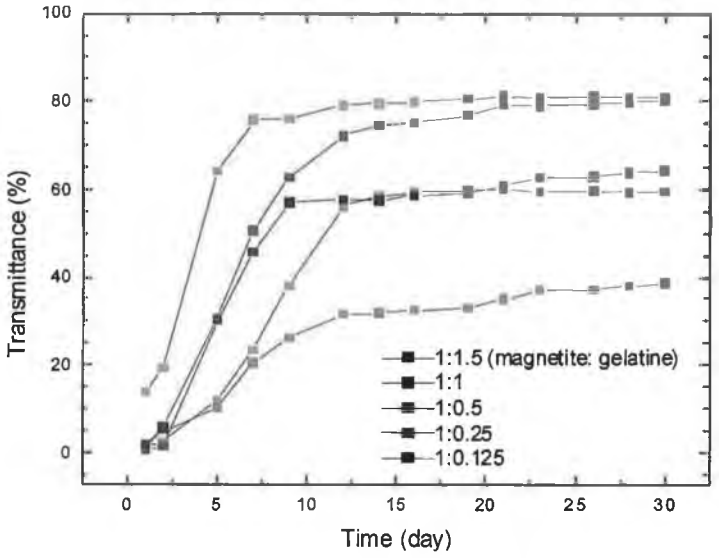

Figure 3.10. Transmittance data of gelatin coated magnetite suspension through ultrasonication against time. The magnetite:gelatin ratio used were (■) 1:1.5, (■) 1:1, (■) 1:0.5, (■) 1:0.25 and (■) 1:0.125. Transmittance values were recorded for at 540 nm.

The most stable suspension, or at least the one of highest transmittance, with a ratio of 1:1.5. The most stable suspension (1:1.5) was examined by scanning electron microscope.

A drop of the suspension was spread and dried slowly over an adhesive carbon film on a standard SEM stub and the micrograph is shown (Figure 3.11). Clusters of size 0.3 to 1 μm were observed to be homogeneously distributed in all fields of view, for example in Figure 3.11. The clusters were large and of irregular three dimensional shape with 30-50 nm primary particles, although features of this size are at the limit of resolution. Given the magnification (60,000) of the image and the amount of signal, it was not possible to observe the gelatin coating on the magnetite surface.

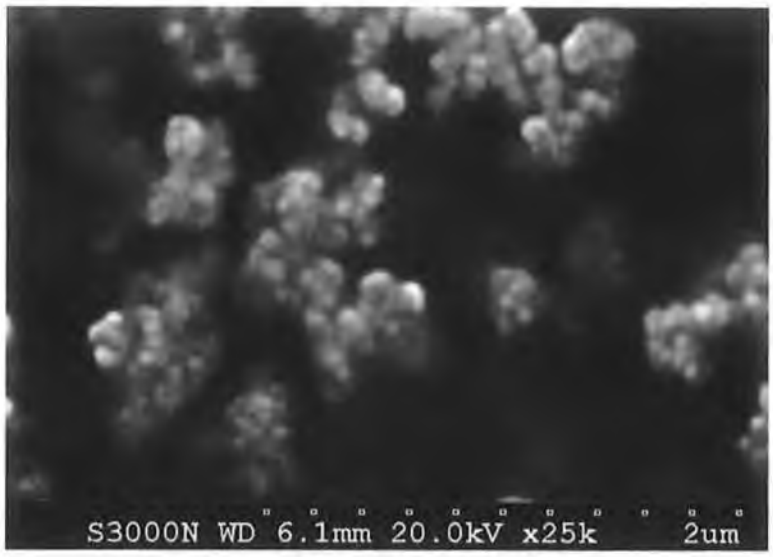

Figure 3.11. SEM micrograph of gelatin coated magnetite (sample No. 2) in stable suspension

The transmittance data for the magnetite suspensions surfacted with sodium oleate is given in Figure 3.12. The different ratios of Fe_3O_4/sodium oleate used in this experiment were the same as used in the gelatin experiment in the previous section. The loss of material from the suspension continued for somewhat longer than for the other surfactants (about 15 days). A very similar trend of stabilising effects was observed. An iron:surfactant ratio of 1:1.5 again produced the most stable suspension.

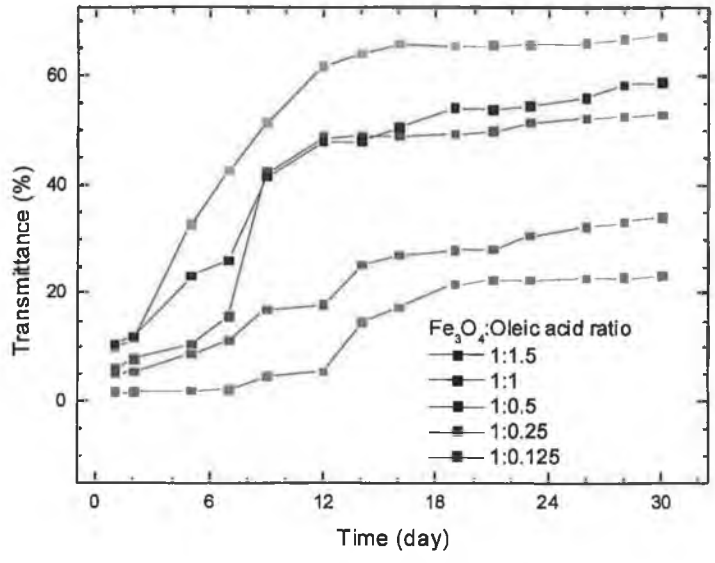

Figure 3.12. The UV transmittance data of sodium oleate coated magnetite suspension. The different ratios of magnetite to surfactant ratio are given in the legend.

Ultrasonication of magnetite with gelatin or sodium oleate surfactant produced magnetic fluids. However sodium oleate was found to be more effective in making a concentrated

fluid. The precipitation of the coated nanoparticles is more in case of gelatin addition. The net transmittance at the plateau for sodium oleate fluid is much less (~20% for the ratio 1:1.5) than in the case of gelatin surfactant (~30-35% for the same ratio) which indicates the presence of more nanoparticles in the oleate suspension. Sodium oleate was more effective in stabilising uncoated magnetite particles in all the ratios used in the sonication experiments.

3.3.3.2 NMRD characterisation

The suspensions of magnetite coated with gelatin (1:1.5) by ultrasonication were characterised by NMRD. Profiles were recorded for the suspensions over a period of nearly 2 months to monitor precipitation and magnetic changes. The NMRD data for gelatin stabilised magnetite suspensions are presented in Figure 3.13. The dual power law fit to the frequency for the day 55 data is also included in the figure.

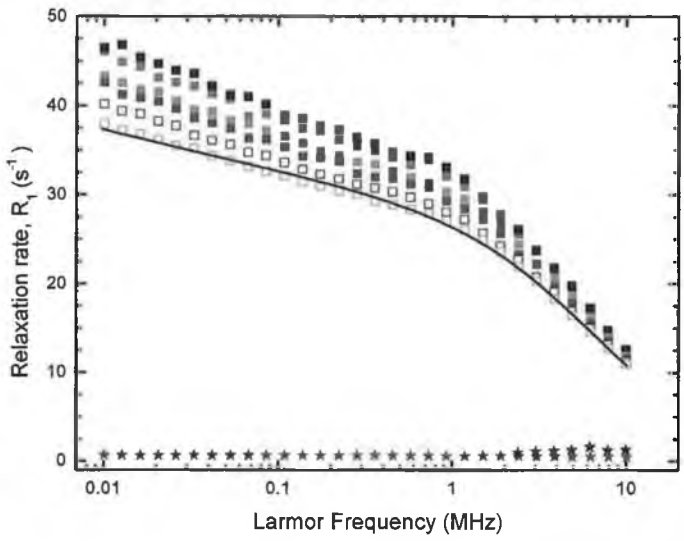

Figure 3.13. NMRD profiles of gelatin coated magnetite in the ratio 1:1.5 prepared by sonication after (■) day 0, (■) day 1, (■) day 6, (■) day 13, (□) day 28, (□) day 55. The continuous line (—) is an example of the fit to a dual power law. Profiles for the ratio 1:0.125 are also shown as (★) day 0 and (★) day 7.

Although the UV transmittance measurements indicated that the suspension with ratio 1:1.5 was stable after about 15 days, NMRD demonstrates that the suspension continued to change even after 55 days. The observed decrease in R_1 over this period of time is not simply due to the loss of magnetite by precipitation. The R_1 value at 10 MHz is almost unchanged over 55 days, while there is a 21% decrease in R_1 at 10 kHz. A dual power law dependence of R_1 on frequency was again observed, on this occasion the shape of the profiles changed with time. Interestingly the suspension with surfactant ratio 1:0.125,

which was stable during the transmittance measurements, precipitated completely during the NMRD experiments, where the field reaches 0.5 T.

The sodium oleate surfactant coated magnetite suspensions were also characterised by NMRD. Profiles recorded over a period of over 4 months are presented in Figure 3.14 below. The surfactant ratios selected for this study were 1:1.5 and 1:0.125 as was selected in gelatin study. Although it was found that sodium oleate surfactant in the ratio 1:1.5 were stable after 18 days, there was ongoing slight precipitation as indicated by NMRD and continued even after 143 days.

Again the changes are unlikely to be due to precipitation, the relaxation rate at 0.01 MHz fell by about 11% in the between day 0 and day 53. For the gelatin coated suspensions processed under the identical conditions R_1 reduced by about 21% over a similar time (55 days). The magnetite suspension with a Fe_3O_4/surfactant ratio of 1:0.125 which were stable for the UV transmittance study again precipitated when exposed to magnetic field of the NMRD experiment.

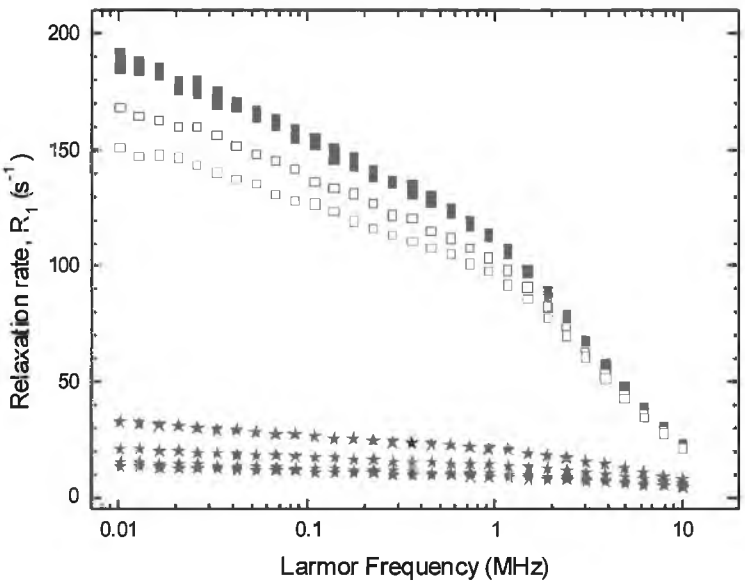

Figure 3.14. NMRD data for sodium oleate coated suspension (ratio 1:1.5) by ultrasonication. The data with Fe/surfactant ratio 1:1.5 is shown as (■) day 0, (■) day 7, (■) day 16, (■) day 26, (□) day 53 and (□) day 143. NMRD profiles for the ratio 1:0.125 are shown as (★) day 0, (★) day 7, (★) day 17 and (★) day 30.

3.3.3.3 Temperature dependence of the NMRD profiles

Experiments were conducted to study the effect of temperature on the relaxation rates operating in the NMRD frequency range. Relaxation data on sodium oleate coated magnetite [190], by wet grinding in agate mortar followed by sonication is given in Figure 3.15. The profiles were recorded in the temperature range of 19.4 to 33.4°C. The monolayer surfactant coated magnetite suspension was very stable. There was no change in the relaxation rates with temperature, in the high frequency region (>1 MHz). The change in T_1 in the low frequency regime was completely reversible, indicating the stability of the suspensions in this temperature range.

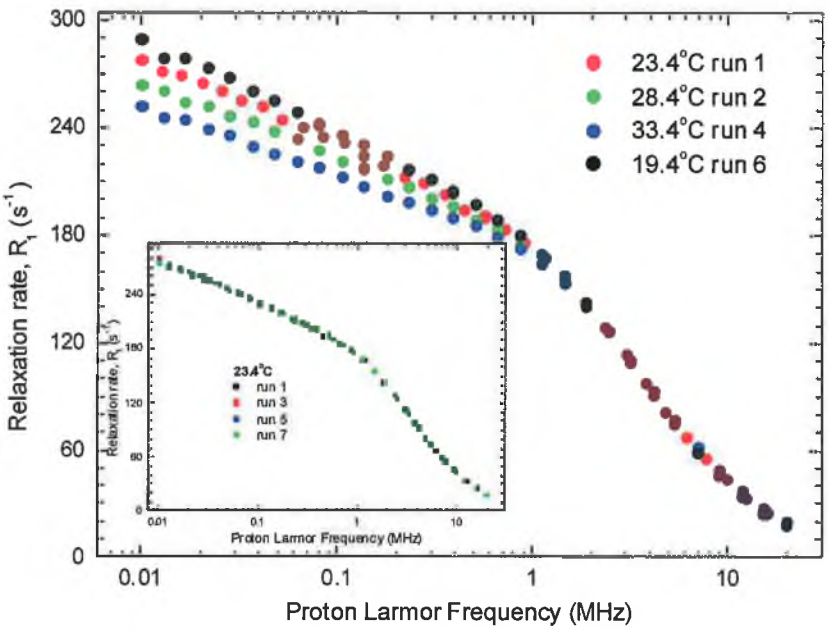

Figure 3.15. Effect of temperature on the relaxation rates of a magnetite suspension agated with sodium oleate. The insert shows successive profiles recorded at 23.4°C.

3.3.3.4 pH dependence of the NMRD profiles

Experiments were conducted to study the effect of pH on the relaxation rates operating in the NMRD frequency range. Relaxation data on a sodium decenoate stabilised suspension is shown below (Figure 3.16). The sample was stable in the range studied. The PCS size was 100 nm.

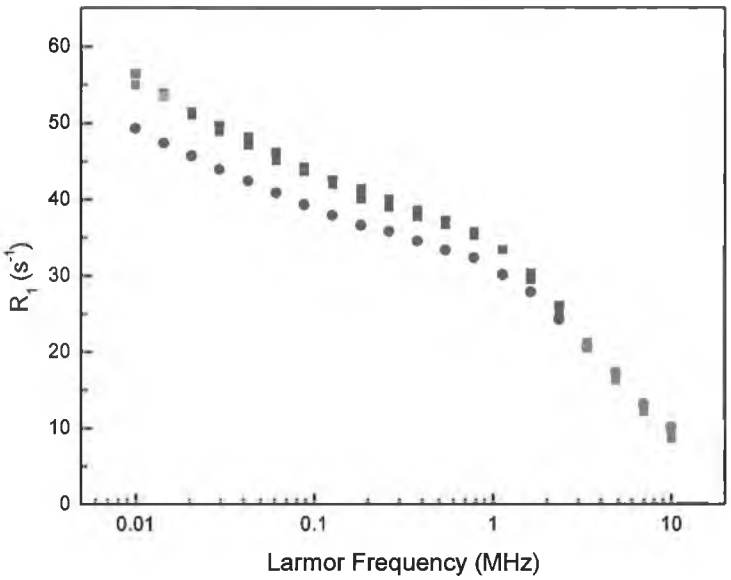

Figure 3.16. Effect of pH on the relaxation rates, at 23.4°C, of a magnetite suspension agated with sodium decenoate. The pH cycle was pH 6 (●) initial, pH 4.9 (●), pH 6 (●), pH 4.9 (●) final.

3.4 Discussion

3.4.1 Uncoated aqueous nanoparticle suspensions

It is clear that maghemite nanoparticles produce more stable suspensions than magnetite. Despite the similarity of the two phases it is likely that this is due to a difference in surface chemistry. Maghemite suspensions have been shown to be more stable to acidification. This observation is also consistent with the presence of a passivated surface layer in maghemite [29, 38], which would be expected to reduce the attractive magnetic interactions between the particles in suspension. For both types of suspension there is strong evidence for the presence of two phases or magnetic fractions; a magnetically dispersed, superparamagnetic, phase and a phase which does not have the NMRD signature of superparamagnetism. For this phase, or fraction, of the iron-oxide it is reasonable to assume that random re-orientation of the magnetic moments is blocked, due to dipolar particle-particle interactions, which effectively increase the magnetic anisotropy.

3.4.2 DNA stabilised magnetic suspensions

3.4.2.1 Double- and single-stranded DNA stabilised suspensions

The NMRD curves obtained for both DNA composites differ dramatically from that expected [12, 194] for a purely superparamagnetic dispersed magnetite sample, Figure 3.17. In particular the relaxivity at low field in both cases but especially for the single stranded sample, is extraordinarily high. The denatured DNA nanocomposites show dual power law dependence of T_1 on frequency, which is not consistent with the predictions of outer sphere theory [147]. In the figure below typical data for single stranded and double stranded preparations using herring sperm DNA, are overplotted. Also included is the simulated [152] response for a population of polydisperse superparamagnetic magnetite nanoparticles.

The simulation shown was generated by simulating the profiles of a range of particle sizes, corresponding to the TEM particle size distribution of the double stranded DNA sample whose profile is shown in the figure. Only the core size was adjusted, with reasonable values chosen for the other parameters. The individual simulations were scaled by their weights in the particle size distribution, which is centered at 9 nm, and the results were added to give the final simulation. Thus there were no free parameters used to generate the simulation.

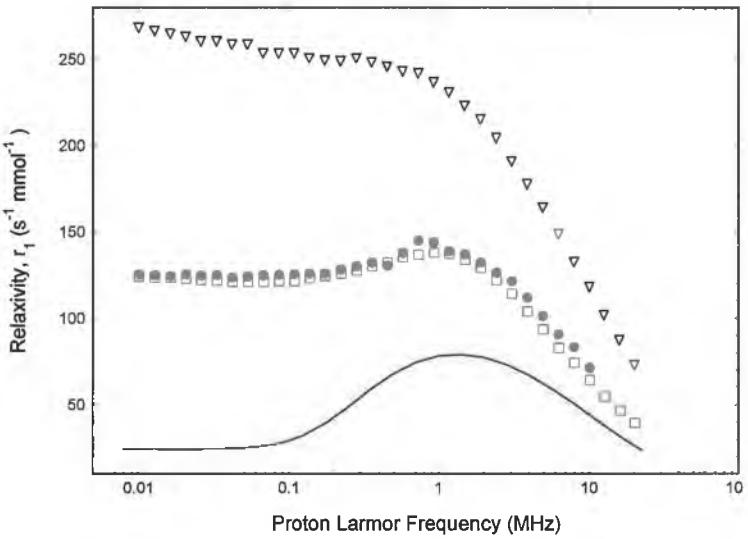

Figure 3.17. NMRD profiles for (▽) denatured hs-DNA-magnetite nanocomposites, (●) double-stranded hs-DNA-magnetite nanocomposites; (□) double-stranded salmon sperm-DNA-magnetite nanocomposites. (—) simulated curve for a distribution of superparamagnetic particles of magnetite.

For complex particulate systems, there is precedent that the contributions to the overall relaxivity from magnetic material in different components of the suspension is additive [195]. In such cases the paramagnetic contribution to the relaxivity is given by equation 3.1.

$$r_{1,obs} = \sum_i x_{1i}\, r_{1i} \qquad (3.1)$$

We propose that the behaviour of the two different DNA-stabilised systems (Figure 3.18) can be explained on the basis that the denatured DNA material is composed of 'magnetically aggregated' particles of relaxivity r_{1agg} while the double-stranded DNA composite also contains 'magnetically dispersed' superparamagnetic particles. The solid curve in blue in Figure 3.18 below, is a fit to the data for the double stranded hs-DNA sample based on equation 3.1. Assuming a two-phase system, using r_{1spm} from the simulated NMRD response (Figure 3.18, solid line in black) and r_{1agg} from the denatured DNA nanocomposites and further postulating that the relaxation due to the magnetically dispersed and aggregated populations is additive, one can obtain the mole fractions x_{spm}= 0.59 and x_{agg}= 0.41, by fitting the ds-DNA data.

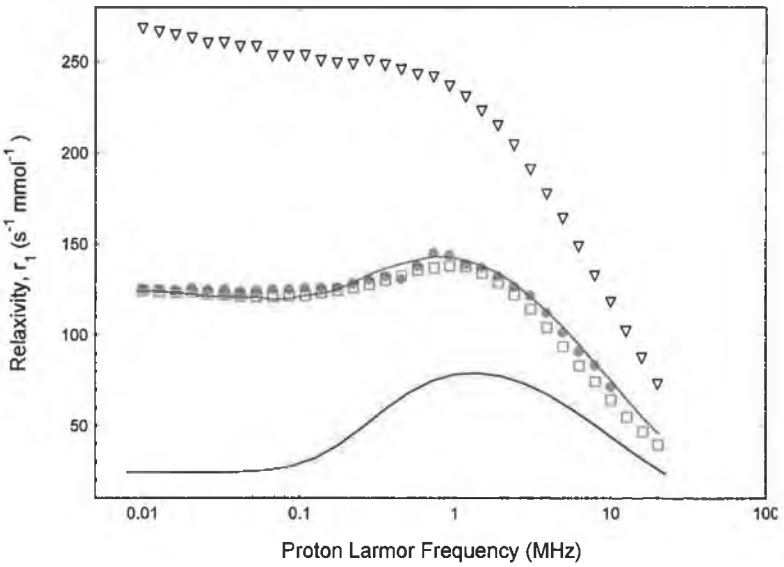

Figure 3.18. NMRD relaxation curves for the DNA-magnetite nanocomposites, the simulated curve (—) for a two component system calculated from the sum; 0.59*(—) + 0.41*(∇) data.

The differing behaviour of the two types of DNA samples may be attributed to the greater binding efficiency of the single stranded segments of the denatured DNA which results in a higher concentration of the magnetite particles. As a result, for the single

stranded nanocomposites in particular, there are stronger blocking magnetic interactions between particles, equivalent to a higher magnetocrystalline anisotropy, and hence very high relaxivity at low field.

3.4.2.2 Effect of magnetic fields on structural ordering in DNA nanocomposites

In a recent paper [191] communicating the findings of our research on DNA magnetic nanocomposites, including the NMRD studies summarised here, we noted that on drying in the presence of a 7T magnetic field, there is reorientation and controlled alignment of the DNA nanocomposites. We investigated the effect of the magnetic field on the magnetic clustering, as indicated by the NMRD response, to establish whether a similar effect is observed in suspension.

NMRD profiles were recorded in two ways. In this first method the data for a fresh sample was recorded from 2.87MHz (c.0.06T) down, without exposing sample to a field greater than 2.87MHz. Then mid frequency part of the profile, up to 7.9MHz, was acquired using a polarisation field of 7.9MHz. Then high frequency part of the profile up to 20MHz (0.5T), was acquired field by field. Then the profile was acquired in the normal way, using a high polarisation field throughout.

This experiment and other related variations were undertaken on several samples. In all cases the profiles were superimposable. Typical data is shown for salmon DS DNA coated magnetite suspension in Figure 3.19 below. It can be concluded that there is no magnetic alignment of the nanocomposites in suspension during the NMRD experiments. Or, alternatively, that the samples do align and that a field of 0.06T is sufficient to accomplish this, and it is irreversibly. This is unlikely given the high magnetic field that was required to align the drying samples.

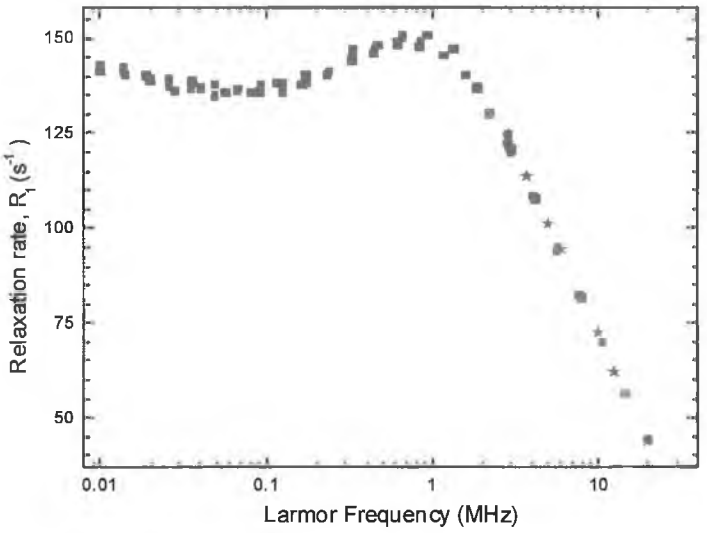

Figure 3.19. Magnetisation studies on the second sample of salmon sperm DNA-magnetite suspension, (■) profile with Bpol=2.87 MHz, (■) profile with Bpol = 7.9 MHz, (■) profile Bpol = 18 MHz and (★) R_1 at 2.87 to 20 MHz with repetitions at 2.87 MHz.

3.4.3 Coated nanoparticle suspensions in water

3.4.3.1 Presence of nanoclusters in suspension

The first observation is that the addition of a surfactant has significantly improved the stability of the magnetic fluids relative to the uncoated nanoparticles. It is difficult to assess the exact nature of the coating, but given the surface activity of the stabilising agents, it is likely that a partial monolayer has been formed on the surface of some or all of the nanoparticles.

The PCS size, at 25°C, of the suspension also characterised by NMRD, was 100 nm with PDI 0.2. The PCS measurements were then made at a temperature of 35°C. The Z-average size did not change, within the measurement error. Two days later, the PCS measurement at 25°C was then repeated, on the same sample. Once again there was no change in the size and distribution of the particles in the suspension, as indicated in Figure 3.20.

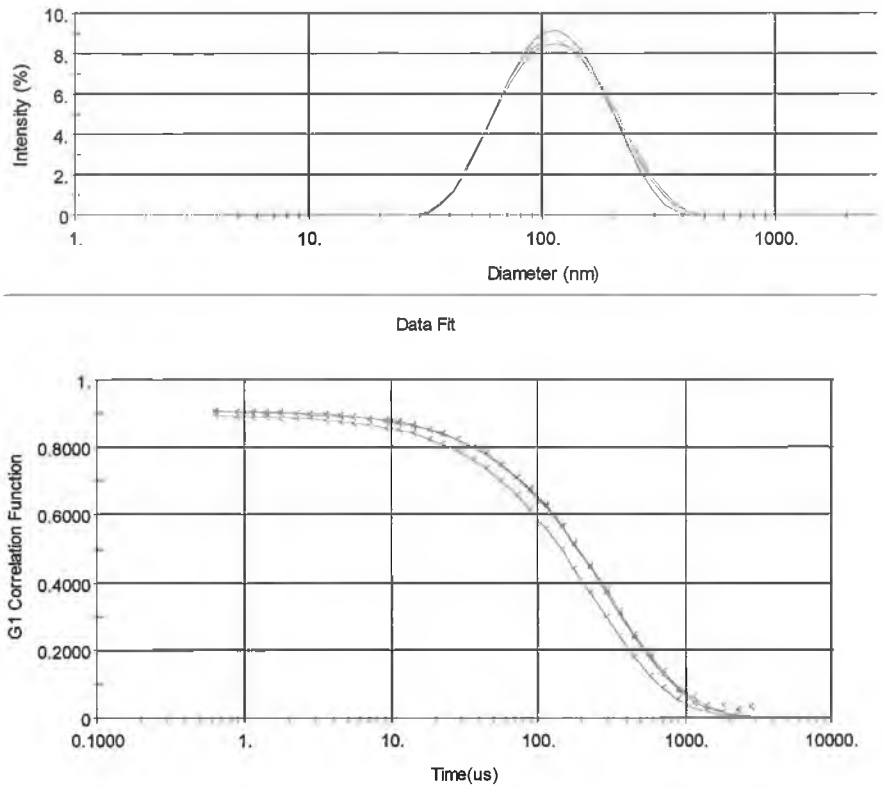

Figure 3.20. The intensity distribution and actual correlation data fit for the suspension at 25°C (—) Z-average=100.4nm (PDI =0.2). At 35°C (—) on the same day, Z-average=99.4nm (PDI =0.21), and at 25°C (—) two days later, Z-average=98.2nm (PDI =0.19).

The appropriate solvent viscosity for 35°C was used in the calculation and the same Z-average and PDI were obtained as at lower temperature. The correlation function measured at 35°C decays slightly faster, as is expected given the change in viscosity with temperature. The correlation functions also strongly indicate that there are no dispersed primary nanoparticles in suspension at 25 or 35°C. The suspensions are stable to dilution with water and with 5, and 25, mM aqueous solutions of sodium oleate.

3.4.3.2 Ageing of the suspensions studied by NMRD

The NMRD profiles show that the suspensions are not superparamagnetic, the expected maximum in the low MHz range is not observed. However the relaxation of the water ^1H nuclei is greatly enhanced by the suspended magnetic particles, R_1 = 0.39 s^{-1} for pure water. The NMRD data for both the gelatin and sodium oleate stabilised suspensions fitted well to a dual power law dependence of the relaxation rate on Larmor frequency.

$$R_1 = a\upsilon^b + c\upsilon^d \qquad (3.2)$$

The changes in the values for the intercepts, a and c, with time are given for the two suspensions in Figure 3.21 below.

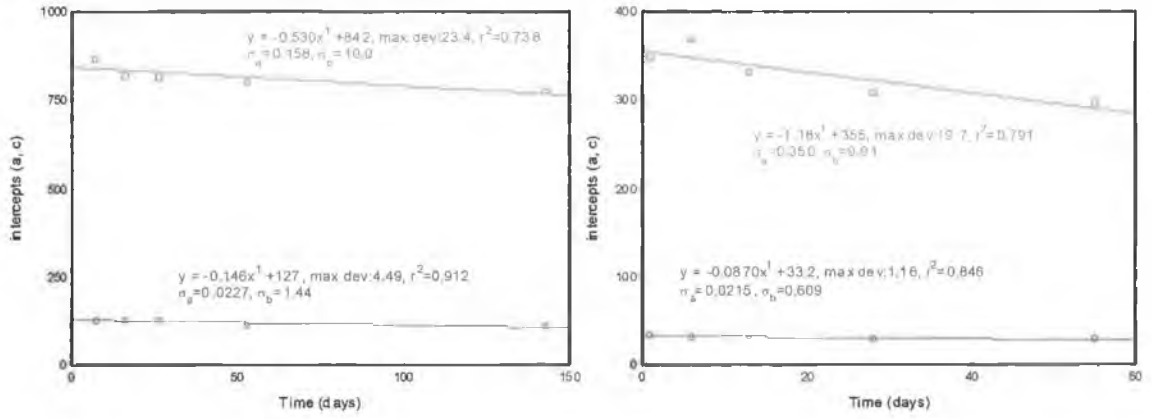

Figure 3.21. Left hand side, change in the high frequency (□), and low frequency (O), intercepts with time for the sodium oleate stabilised suspension. Right hand side, the equivalent data for the gelatin stabilised suspension.

If the changes in the profiles were due to precipitation of some of the suspended iron oxide, a proportionate change in the high and low frequency intercepts would be expected. This figure suggests that there is some reorganisation of the nanoclusters as they age. To gain insight into the changes, attempts were made to fit the high frequency data, only, to outer-sphere theory [147]. This was unsuccessful, as there are difficulties in obtaining good results without treating the whole profile and applying sophisticated interpolation for the mid-field region. This was the approach adopted by Roch, Muller et. al. [152] in successfully formulating superparamagnetic relaxation theory. The changes in the powers, b and d, are given for the two suspensions in Figure 3.22.

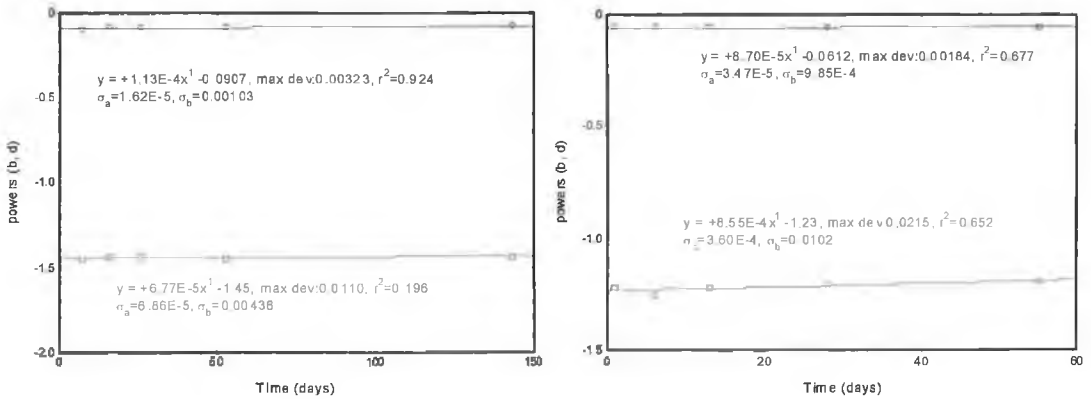

Figure 3.22. Left hand side, change in the high frequency (□), and low frequency (O), powers with time for the sodium oleate stabilised suspension. Right hand side, the equivalent data for the gelatin stabilised suspension.

There is no significant change in the powers with time, for either of the suspensions. The clearly observable changes in the NMRD profiles with ageing are largely due to a decrease in the value of high field intercept. Somewhat counterintuitively, because of the additive nature of the high and low frequency relaxation mechanisms, this appears as a greater change in the low field part of the profiles. The effect is greater in the case of the gelatin-stabilised suspension. The explanation for this is not known.

3.4.3.3 Temperature dependence of the NMRD profiles

The NMRD profiles recorded at different temperatures show the same dual power law behaviour. They also suggest, as is the case for superparamagnetic relaxation, that there are different relaxation mechanisms at high and low field. For superparamagnetic particles, it has been shown that the high field relaxation arises from diffusion of water close to the magnetic moment of the particle, and that this mechanism is insensitive to temperature change. The shape and temperature dependence of the profiles for the coated nanoparticle suspensions, at high field, is consistent with the predictions of Freeds outer-sphere model. Therefore it is reasonable to assume that the high field relaxation mechanism, for the magnetic nanoclusters is outer-sphere.

Assuming that this is true it is then reasonable to assume that the low field relaxation mechanism for the magnetic nanoclusters is inner-sphere in nature. Again by analogy with superparamagnetic relaxation, supporting evidence comes from the fact that the relaxation rates decrease strongly temperature in the low frequency region. It will be shown in the next chapter that for superparamagnetic relaxation the relaxation rate also decreases with temperature in the low field range, but the profiles have quite different shape and remain parallel as the temperature changes. For the coated nanocluster suspensions reported here, for which the primary particle size is in the superparamagnetic range, the low field relaxation can be fitted to a power law dependence on Larmor frequency, and the power decreases as the temperature is increased.

Thus there are similarities and differences between the low field relaxation in dispersed superparamagnetic nanoparticles and in magnetic clusters reported here. It is highly likely that the mechanism remains modulation of the magnetic interaction between the water exhanging close to the nanocluster and the surface of the nanoparticles. The

modulation is likely to be due to a non-diffusional motional process on the nanosecond time scale. There are two possibilities: Either the motions of the magnetic moments are only partially blocked, in which case one would expect to see a profile resembling superparamagnetic relaxation. Alternatively, motion of the water molecules penetrating the nanocluster, or exploring its surface, may be responsible for the relaxation profile observed. Motion of water about the nanocluster would occur on the appropriate time-scale, water tumbling in free solution occurs on the picosecond timescale.

If one assumes this to be the mechanism then the accessible surface of the nanocluster is acting as a relaxation sink to the water molecules. Several spectral density functions have been shown to be applicable for surface relaxation over fractal geometries [9, 196]. In the most common formulation it has been shown that the spin lattice relaxation time can be expressed as:

$$R_1 = a\upsilon^{-\left(\frac{d_f}{2}-1\right)} + b \qquad (3.3)$$

Where, R_1 is the relaxation rate, a, b are constants, ν is frequency and d_f is the dimensionality or fractal dimension of the clustered mass and $-\left(\frac{d_f}{2}-1\right)$ equates to the power obtained from least squares fitting of the profile. Thus the T_1 profile maps out the dimensionality of the cluster, as probed by the water. The results of such an analysis for the low field relaxation of the coated nanoclusters are shown in the Figure 3.23 below.

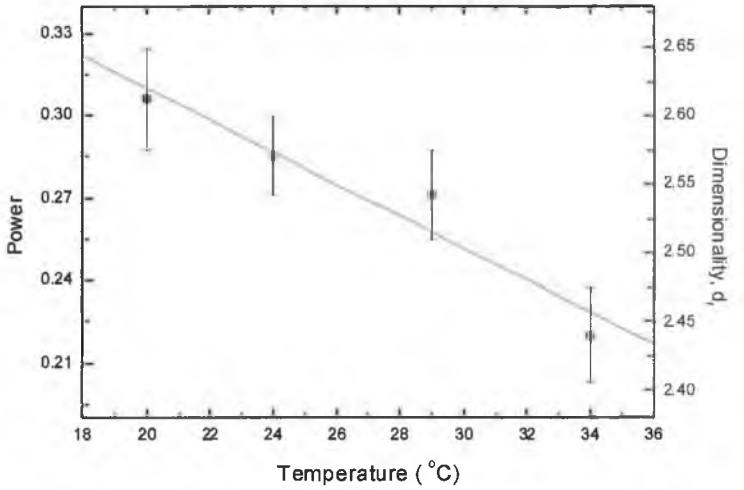

Figure 3.23. The dimensionality of clusters in aqueous suspension of magnetite sample agated with sodium oleate at different temperatures.

The implied dimensionality of the magnetite suspension was in the range of 2.40 to 2.65 in the experimental temperature range. The suggestion that the fractal dimensions of the

clusters decreases with temperature is consistent with the exclusion of water as the loose fatty acid tails become more mobile.

For the DNA stabilised nanocomposites the low field power was invariably lower, and was sometimes very close to zero, within the error. This suggests a lower dimensional cluster for the DNA nanocomposites as is expected and indeed observed by TEM. It should be noted that the hydrodynamic size, from PCS, of about 85 nm for the single stranded DNA nanocomposites represents the equivalent sphere diameter. The suspended object may still be very elongated.

Investigations are ongoing in the group, with the aim of obtaining complementary structural information on the fatty acid and DNA stabilised nanoclusters. From the angular dependence of the scattering, static light scattering may provide the volume fractal dimension of the cluster. This work has been hindered by the weak scattering obtained, as most SLS equipment is optimised for um scale materials. Alternatively, from the concentration dependence of the DLS back-scattered intensity it can be possible, using the dynamic Zimm approach, to determine the effective mass of the cluster and hence its density. This approach is also yet to produce good results, monodisperse suspensions are required, and the high masses of the nanoclusters are pace the close to the measurable limit.

3.4.3.4 pH dependence of the NMRD profiles

The NMRD profiles recorded at lower pH indicate that in the low frequency region the relaxation is enhanced. This also supports the suggestion that the high field relaxation is outer-sphere and the low field relaxation is inner-sphere. The mechanism by which the enhancement occurs is interesting. PCS measurements have shown that protonation doe not alter the size of the cluster. The low frequency power is not affected, which indicates that the topology of the cluster is also unchanged. Our interpretation agrees with that proposed by Muller for dextran coated magnetite particles [197], that the surface becomes partially protonated on lowering the pH, and the presence of suface protons amplifies the dipolar interaction between the particle and the solvent ^1H nuclei, see Figure 3.24 below.

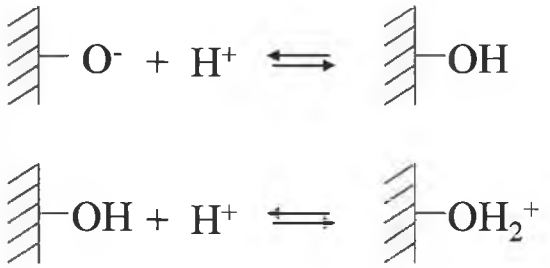

Figure 3.24. Protonation of the surface of magnetite, may occur at several sites, all of which increase the surface proton density.

This effect cannot be achieved by the ^1H of the carboxylate chains as they are futher away from the surface and are more mobile. The implication of this interpretation is that the surface is not fully coated with fatty acid.

3.5 Conclusion

It is possible to produce semi-stable suspensions of magnetite and maghemite in water without any surfactant, though the amount of solid that remains in suspension is small. It was shown to be possible to produce more stable suspensions of coated nanoclusters by applying surfactants either *in situ*, in the case of the DNA stabilised fluids, or to the uncoated particles by ultrasonicating and/or agate grinding the mixtures.

Two types of stable DNA-magnetite nanocomposites were studied. Single stranded DNA produced a material with very high low-field relaxivity, $r_1 > 150\ s^{-1}mM^{-1}$. The relaxivity

was more normal in the current clinical MRI range, 80-100MHz. Although with the advent of remote detection for NMR and MRI [198], such materials may eventually find applications. The NMRD profiles indicated that the material was not superparamagnetic, as the profile could be fitted to a dual power law dependence of r_1 on Larmor frequency. Double stranded DNA produced a material with two magnetic phases, or fractions; a superparamagnetic fraction and a magnetically clustered fraction analagous to that observed for the single stranded DNA nanocomposites.

For the fatty acid stabilised nanoclusters dual power law dependencies of r_1 on Larmor frequency were also observed. Changing the pH was found to alter the NMRD response in the low frequency region, due to a reversible inner-sphere effect. While the high frequency relaxation was unaffected by pH, indicating that the relaxation mechanism is outer-sphere in nature. Temperature dependent NMRD measurements confirm that there are separate high and low field relaxation mechanisms operating and that the high field relaxation mechanism is outer-sphere.

The low field relaxivity of fatty acid stabilised nanocluster suspensions was again very high. The NMRD profiles can be interpreted as being due to motion of the water around the nanocluster. It is suggested that the dimensionality of the nanocluster is mapped onto the spectral density function that determines the shape of the profile. The implied dimensionality of the magnetic nanoclusters varied from 2.42 to 2.6 in the experimental temperature range, a range in which there was no change in hydrodynamic diameter as measured by PCS. These are relatively high values, indicating a dense cluster, as $d_f = 2$ for a plane, and $d_f = 3$ for a solid.

Chapter 4

Alkaline coprecipitation of surfactant stabilised magnetic nanoparticles and their characterisation in suspension

4.1 Introduction

Magnetite nanoparticles in the size range of 2 to 12.5 nm can be synthesised by ammonia coprecipitation of Fe(II) and Fe(III) salts [80]. Fine particles have a tendency to undergo grain growth due to the very high surface energy due to the high surface area to volume ratio. Magnetite particles undergo spontaneous changes in their surface properties during the synthesis depending on the preparation conditions of pH and ionic strength. In addition, uncoated fine particles in suspension can undergo spontaneous growth during ageing (Ostwald ripening) [56]. Coprecipitation at pH well above the pH_{pzc} and at high ionic strength [30, 56, 199] produces smaller nanosized magnetite particles. Under these conditions the electrostatic surface charge is high and with short crystallisation times, further growth can be avoided.

Application of a fatty acid surfactants chemisorbed onto the magnetite surface during precipitation is one of the methods used to isolate the particles and to prevent both grain growth, and later, ripening. For the purposes of this discussion the fatty acids will be described by two numbers, the chain length and number of unsaturations, so for instance decanoic acid, $C_9H_{19}COOH$ is denoted [10:0]. Application of a further surfactant, as a solution of the fatty acid salt, results in a second physisorbed layer, with the fatty tail attached to the first layer and hydrophilic head group projecting outwards. This makes the magnetite particles relatively stable in aqueous suspension due to the electrostatic repulsions of the charged cloud.

The synthesis and characterisation of magnetite nanoparticles coated with two layers of fatty acid is described in this chapter. The common ammonia coprecipitation technique is adopted at a slightly elevated temperature to precipitate iron oxide. A primary surfactant is introduced in situ while a second layer is applied later to add stability in aqueous suspension. Attempts to synthesise smaller nanoparticles by increasing the ionic strength with the addition of sodium chloride during precipitation, are described. The magnetite suspensions are characterised by photon correlation spectroscopy and NMRD. The effect of change in pH and temperature on the stability of the suspensions is also studied.

The magnetite nanoparticles produced by aqueous coprecipitation, prior to the application of a second layer can be phase transferred into heptane quite easily. In heptane the particles are stabilised by a chemisorbed monolayer only. The surfacted

nanocrystals can be phase transferred into nonpolar solvents due to strong solvation of the fatty acid tails of the surfactants. This process was undertaken in order to assess the effect the relaxation enhancement due to the nanoparticle of the chain length of the fatty acid in the primary layer. It is generally found that the NMRD response is less preparation sensitive in heptane suspension. Agglomeration is also less of an issue, as a result the PCS and NMRD particle sizes can be correlated.

It has also been shown to be possible, though far more difficult, to resuspend monolayer coated particles, from a high temperature non-aqueous synthesis, into water after the application of a second layer.

4.2 Experimental

4.2.1 Ammonia coprecipitation of Fe(II) and Fe(III) salts

Stable magnetic fluids were synthesised by a sequential process involving the *in situ* coating by the surfactant decanoic acid (C10:0) during chemical coprecipitation of Fe(II) and Fe(III) salts with ammonium hydroxide by following a modification of the method of Shen *et al.* [65]. Which was itself a modification of Wooding's method [58]. A mixture of iron(III) chloride hexahydrate (99.0%, Riedel-de-Haën Chemicals) and iron(II) chloride tetrahydrate (≥99.0%, Fluka Chemicals) in the molar ratio of 2:1 (typically 0.5 and 0.25 mmol) were dissolved in 20 ml deoxygenated water. The solution was heated slowly to 80°C with very strong magnetic stirring and maintained for 30 minute at that temperature. One fifth of the total of 0.4 mmol of primary surfactant was added to the solution at this time followed by immediate addition of the required volume 0.5 ml of 33% ammonia. The remaining surfactant (0.32 mmol) was then added to the mixture in five parts over five minutes; stirring was continued for another 15 min at 80°C, the typical volume after all the additions is about 21ml. Several syntheses were undertaken with a reduced reaction time of 5 minutes instead of the normal 15 minutes, after the addition of complete surfactants. It was observed that maintaining the temperature at 80°C for some time was essential for producing fine, stable, coated magnetite particles. 30 minute stirring at 80°C was found to be optimal. The suspension was then cooled naturally to room temperature and precipitated in one step by the sequential addition of equal volumes of acetone (25 ml) and methanol (25 ml). A black precipitate was separated by using a strong bar magnet to hold the solids and washing them alternately

with acetone and methanol (polar organic solvents) five times to remove all surfactants, except that part directly bonded to the particle surface. Such washed particles disperse readily in nonpolar organic solvents to produce concentrated dispersions whereas, for dispersion in water, a secondary surfactant layer of the same or different surfactant is required [59].

The primary layer coated ultra fine nanoparticles were redispersed in water and the temperature of the suspension was raised to 60°C with strong stirring. The second surfactant (0.25 mmol), usually lauric acid (C12:0) as its ammonium salt (pH ≥10) was then added drop-wise to the suspension. This procedure produced magnetite (Fe_3O_4) nanoparticles stabilised against agglomeration by bilayers of n-alkanoic acids with 9-13 carbons. The nanoparticle suspensions were characterised by PCS, NMRD and in some cases TEM. All dilutions for the NMRD experiments were performed with 25 mM of the ammonium salt of the secondary fatty acid. The effect of pH and temperature on the relaxation behaviour was also studied.

4.2.2 Sodium chloride assisted coprecipitation

Magnetite nanoparticles were also synthesised by ammonia precipitation of mixed Fe^{3+}/ Fe^{2+} salts as described above but at higher ionic strength. Sodium chloride was dissolved in the mixed Fe^{3+}/Fe^{2+} solution to adjust the ionic strength of chloride to 0.25M. All other steps were repeated exactly as in the previous section.

4.2.3 Phase transfer from aqueous suspension into heptane

Nanosized magnetite was synthesised by coprecipitation from a mixture of ferrous/ferric nitrate, hexahydrate salts by ammonia in a modification of Shen's method [65]. In a typical synthesis to obtain 0.1 g of Fe_3O_4 precipitate, 0.870 mmol of iron(III) chloride hexahydrate (99.0%, Riedel-de-Haën Chemicals) and 0.435 mmol iron(II) chloride tetrahydrate (≥99.0%, Fluka Chemicals) were dissolved in 20 ml deaerated water. The reaction mixture was heated at 80 °C on a sand bath for 30 min with vigorous stirring. Nitrogen was purged through the mixture throughout the reaction. A large excess of about 0.5 mmol oleic acid surfactant was then added, followed by the addition of 2.5 ml of concentrated ammonia solution. In-situ oleate coated magnetite was precipitated as black particles at this stage. A total of 2.5 mmol surfactant was added immediately drop-

wise over 5 minutes to the freshly precipitated suspension. The temperature was maintained at 80 °C for 15 minutes to complete crystallisation and then the mixture was cooled slowly to room temperature. The suspension was flocculated with a 1:1 mixture of acetone and methanol and separated by a strong bar magnet. The precipitate was washed four times, alternately with acetone and methanol and finally once with ethanol. A part of the washed precipitate was suspended in about 20 ml heptane containing 0.25 mmol (12.5 mM) of the same surfactant. The suspension was again precipitated with ethanol. The separated solid was resuspended in heptane. The suspension was centrifuged at 15700 rcf for 40 minutes to remove any large particles. The coated magnetite suspension in heptane was characterised by PCS and NMRD. The second part of the precipitate was coated with a second surfactant, as its ammonium salt, as described before, for the purpose of comparison.

4.2.4 Effect of chain length on relaxivity in heptane suspension

The procedure stated above was followed to introduce different fatty acid surfactants. The carboxylic acids of saturated hydrocarbon chain length, from 6 to 18, were used to study the effect of chain length on the PCS size and relaxivity of the magnetite suspension. Sodium chloride was dissolved in the solution of iron chloride salt mixture before it was heated to 80°C. An ionic strength of 0.25 M concentration of NaCl was maintained in every case. Except for nonanoic acid (C9:0), which is a liquid at room temperature (25°C) all other surfactants were added as solids to the reaction. The final magnetite suspension was characterised by PCS and NMRD.

4.2.5 Phase transfer from non-aqueous suspension into water

2-3 mls of a moderate sized monodisperse nanoparticle suspension in heptane, sample N7, with hydrodynamic diameter of the magnetite particles 11.5 nm, PDI 0.04, synthesised as described in the following chapter, was typically used. The particles were precipitated with a volume of ethanol of about 1.5 times the volume of the suspension. The precipitate was washed with methanol and resuspended in water with vigorous stirring, while the temperature of the suspension was raised to, and then maintained at, 65°C for 30 minutes. A solution of 10 mM ammonium laurate was then added to the stirred suspension drop-wise over 5 minute, stirring was continued for 25 more minutes.

The bilayer surfactant coated magnetite was then sonicated for 30 minute at 50°C. The suspension was held over a strong bar magnet and the upper liquid decanted for use. The efficiency of the phase transfer process was low, and it was quite difficult to reproduce the phase transfer.

4.2.6 Uncoated nanoparticles in organic solvents

Uncoated magnetite nanoparticles in the size range 12-25 nm, synthesised in Trinity College by the project partner, were used as the magnetite precursor. Typically 4 mg of the sample was agate ground in an agate mortar in presence of 1:1.5 by mass oleic acid. The ground paste was transferred to a glass bottle with a 5 ml heptane, it was shaken well and then ultrasonicated for no more than 1 minute, to avoid heating. The large particles in the suspension were removed by centrifugation at 15700 rcf for 30 minutes. The resulting fine magnetite suspension was characterised by PCS and NMRD.

A suspension was also prepared from the same magnetite source by agate grinding with 1:1 oleic acid and sodium oleate and suspending the paste in water. The paste was ultrasonicated at 50°C for 30 minutes. The results for this preparation in water were also compared with those for the heptane suspension.

4.3 Results

4.3.1 Ammonia coprecipitation

The water relaxivity data for a group of repeat syntheses are shown in Figure 4.1. The results indicate good reproducibility for a synthesis involving many steps conducted over two days. The variation of r_1 (at 0.01 MHz) is no worse than ± 7%. Using SPM theory [152], to which the data conforms, the average high field maximum of the relaxation profiles suggests a primary particle size of about 20 nm. The saturation magnetisation is 28 emu/g, which is significantly less than for bulk Fe_3O_4, but is in the right range for nanoparticles of this size [29, 38]. The dependence of the saturation magnetisation on nanoparticles size will be discussed in detail in Chapter 5 of this thesis.

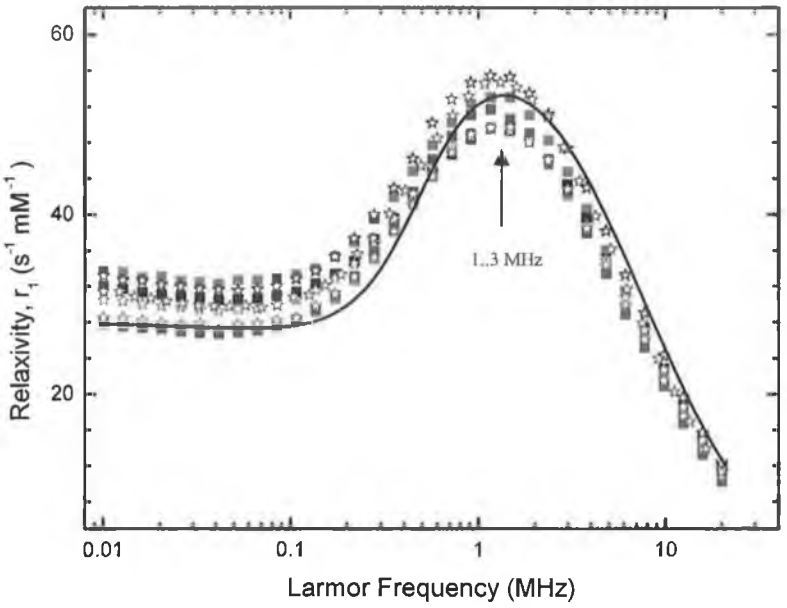

Figure 4.1. NMRD relaxivity profiles in water for eight syntheses with (C10:0) as the primary layer and (C12:0) second surfactant showing reasonable reproducibility. The simulated pattern (—) using Muller's theory for magnetite nanoparticle of 20 nm diameter fits the data reasonably well.

However, transmission electron microscopy of fine particles from two of these preparations indicated an average size of between 8 and 10.5 nm. The TEM sample was prepared by drying a drop of magnetite suspension over the TEM copper mesh grid. A typical micrograph, of C10:0/C12:0 coated magnetite particles, is shown in Figure 4.2. Analysis of the micrograph indicates a range of sizes from 5-25 nm in segregated clusters of size 80-150 nm containing 50-150 particles.

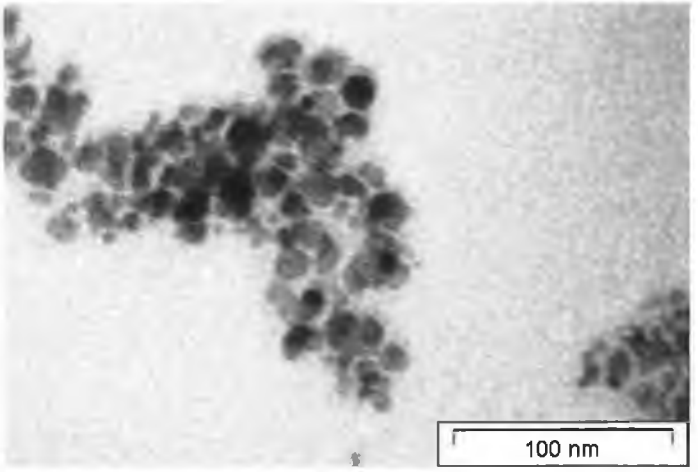

Figure 4.2. Transmission electron microscope image of magnetite particles from the synthesis given in Figure 4.1. The 100 particle average diameter is ~10.5 nm.

The hydrodynamic diameter was measured by photon correlation spectroscopy (PCS) and was in the range 80-100 nm (Figure 4.2). The actual fit and the PSD distribution of two of such coprecipitated samples are given in Figure 4.3 below. The distributions are unimodal, and all the suspensions had PDI values of less than 0.2.

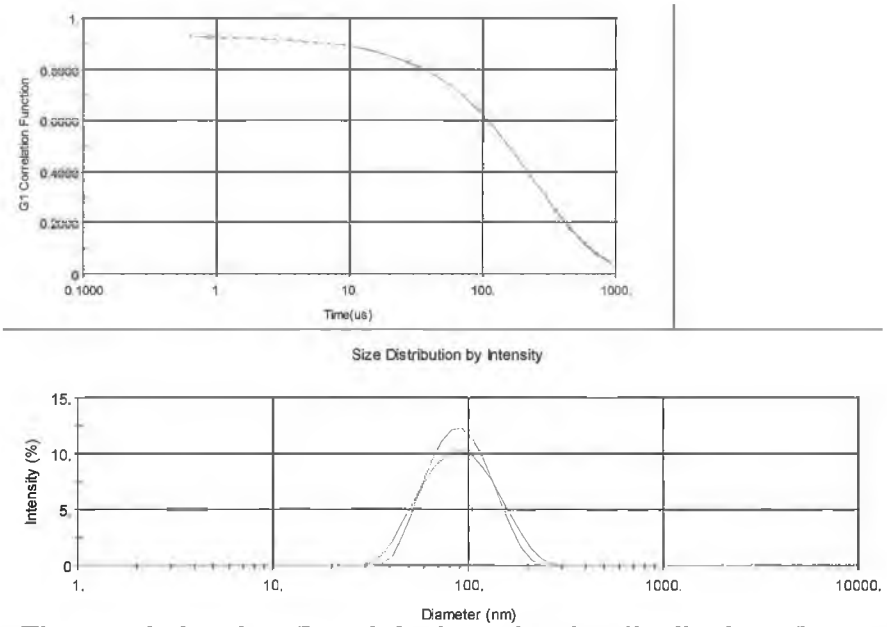

Figure 4.3. The correlation data fit and the intensity size distribution of two samples out of those eight given in Figure 4.1. The data (—) has Z-average 82.5 nm with a PDI=0.15 and (—) PCS size of 84.2 nm with PDI= 0.11.

The 5 minute reaction time suspensions gave contrasting results (not presented here). The size from the high field maximum indicated a 21 nm core, whereas the relaxivity was lower than for the longer reaction time products. It is likely that during the 5 minute preparations there was insufficient time for the magnetite particles to crystallise into a good magnetite core.

4.3.2 Effect of pH on the NMRD response

The relaxation profiles of a bilayer (C10:0/C12:0) surfactant coated magnetite suspension recorded at different pH value are shown in Figure 4.4. The natural pH of the suspension was about 10.1. The relaxation rates of water were unaffected at higher frequency (> 2 MHz) for all pH values, but there was an increase in the R_1 at low field with decrease in pH of the suspension. The effect was almost reversible with a loss of $R_1 \leq 2$ % after completing the pH cycle. There are some minor changes to the shape of the profile, which may be consistent with some slight agglomeration of the particles, however as

these changes are relatively minor they are difficult to quantify. It is interesting to note that there is almost no change in R_1 with pH in the high field region, where the relaxation mechanism is outer-sphere and is driven by diffusion. On lowering the pH further the suspension precipitates, this is presumably due to the protonation of the physisorbed fatty acid layer.

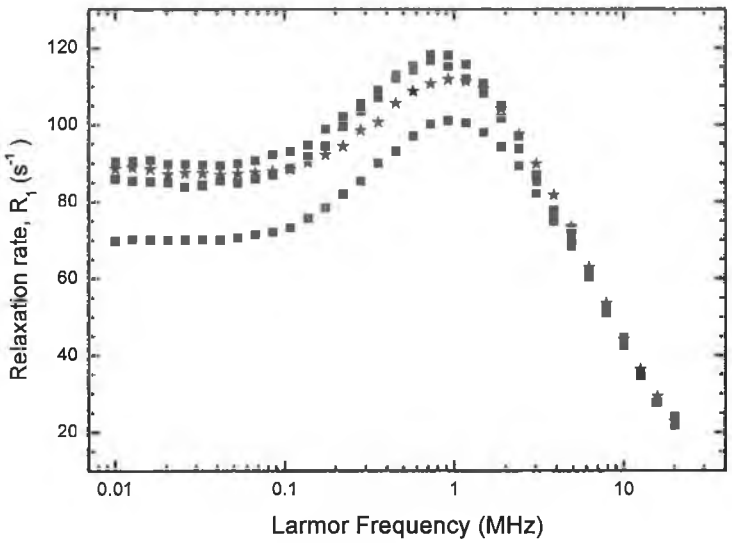

Figure 4.4. Relaxation rates of a bilayer surfactant coated magnetite suspension in water at pH (■) 10.1, (■) 9.2, (■) 11 and back to (★) 10.1 again. The natural pH for the fluid was 10.1.

4.3.3 Effect of temperature on the NMRD response

The effect of temperature on the NMRD profile for one of the stable bilayer surfactant stabilised suspensions of is shown in Figure 4.5. The changes are completely reversible as was also the case for monolayer surfactant coated magnetite suspension. The relaxation rates at higher magnetic field are not affected by change in temperature up to 35°C, which is similar to the effect of pH.

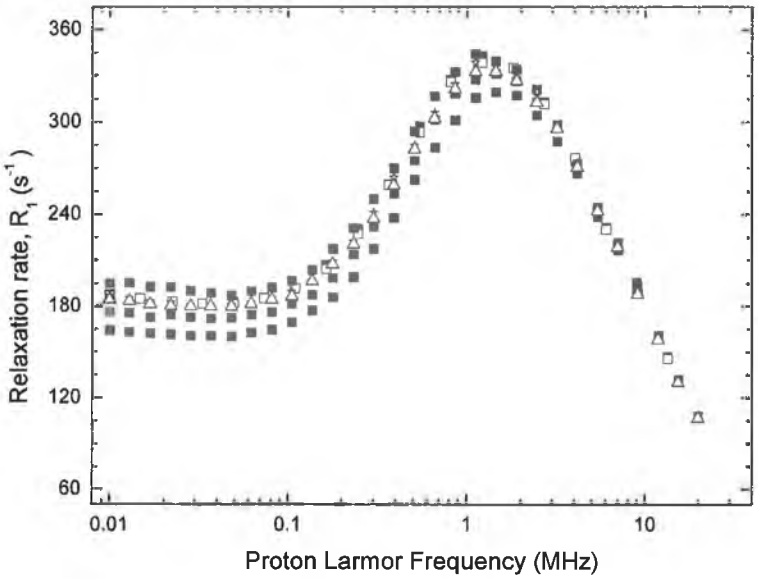

Figure 4.5. The reversible effect of temperature on relaxation rates on the NMRD response of a C10:0/C12:0 bilayer stabilised aqueous magnetite suspension. The sequence of the temperature cycle was 24°C (■), 20°C (■), 24°C (□), 29°C (■), 24°C (★), 34°C (■) and 24°C (Δ).

All the data recorded at 24°C, which are shown in black in the figure, overlap perfectly. This demonstrates the stability of the suspension over this relatively narrow temperature range. R_1 decreased as the temperature increased in the lower frequency range (<2 MHz).

4.3.4 Sodium chloride assisted coprecipitation

The NMRD results for aqueous suspensions of magnetite nanoparticles coprecipitated at higher ionic strength (0.25M NaCl) are shown in Figure 4.6. The effect of increasing the ionic strength is evident from the relaxivity results. The major difference is that the relaxivity at 0.01 MHz is below 30 $mM^{-1}s^{-1}$ (average 28 $mM^{-1}s^{-1}$) for all the suspension with a maximum error of ~3.4 % where as the average relaxivity for the bilayer C10:0/C12:0 stabilised suspension without NaCl was about 31 $mM^{-1}s^{-1}$. The high field maximum in the sodium chloride assisted syntheses is at a slightly higher frequency of 1.58 MHz which represents a magnetite core size of about 18.5 nm, though this interpretation is at the limits of resolution.

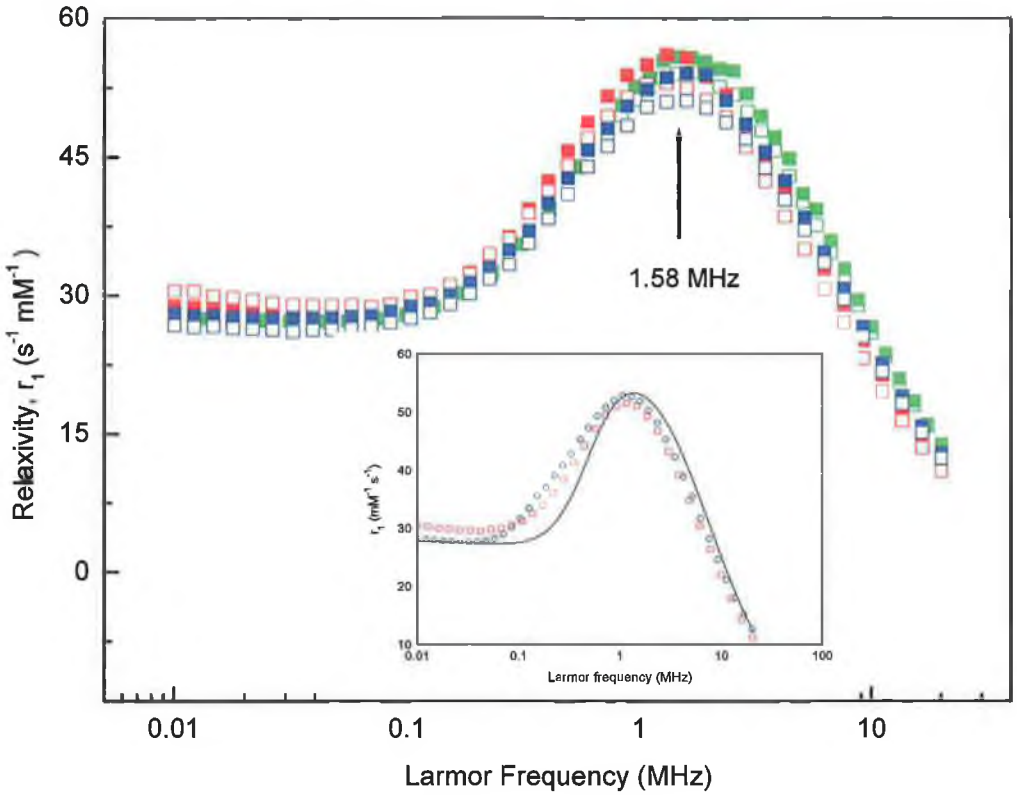

Figure 4.6. Relaxivity profiles of six identical syntheses in presence of 1 M sodium chloride by ammonia precipitation of mixed valent iron chloride salts. The insert shows the average relaxivity for the preparations with and without NaCl (see Figure 4.1).

4.3.5 Effect of chain length on relaxivity in heptane suspension

In a first series of experiments, nanoparticles were prepared in aqueous suspension, in the presence of 0.25M NaCl, using the saturated C6 to C18 carboxylic acids. The suspensions were then transferred into heptane. The recovery of precipitate from the suspension was very high for the C10 and C12 surfactants and was in the order C10~C12>>C9>C16. Palmitic acid C16:0 produced a visibly porous gel structure on adding ethanol to the surfactant coated magnetite during the first precipitation, this could be broken by shaking but the resulting yield was low. Stearic acid (C18:0) did not produce nanoparticles, in the presence of NaCl, it formed a soapy solid during the attempted coprecipitation.

In a second series of experiments, nanoparticles were prepared in aqueous suspension, without adding NaCl, using the saturated C6 to C18 carboxylic acid surfactants. The suspensions were then transferred into heptane. A different trend of stabilisation was observed.

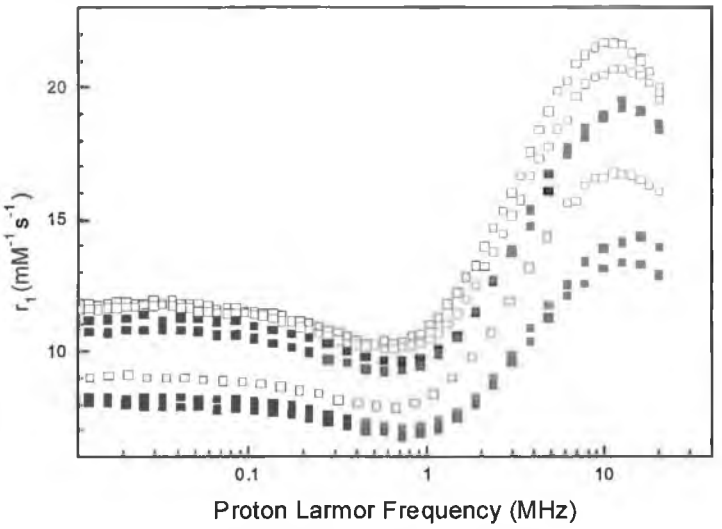

Figure 4.7. The relaxivity profiles of the aqueous ammonia coprecipitated magnetite transferred into heptane. The sodium chloride assisted products are shown as C9 (■), C10 (■), C12 (■) and C16 (■). The products without sodium chloride are C12 (□), C16 (□) and C18 (□).

It was possible to stabilise magnetite with stearic acid (C18:0), while this was no longer possible with nonaoic acid (C9:0). The recovery decreased in the order C12>C16>C18>>C10. With the yield for the C12 preparation less than half that obtained in the comparable NaCl assisted precipitation. The NMRD results for both series of experiments are summarised in Figure 4.7.

4.4 Discussion

4.4.1 Sodium chloride assisted and non-assisted coprecipitation

The stability of bilayer surfactant coated aqueous suspensions was found to be dependent on many factors. It was observed that a stirring time of at least 30 minutes for the mixed-valent iron precursor was necessary at the reaction temperature (80°C) to produce iron aquocomplex. The transparent suspension turned opaque during this time with clear indication of formation of partially hydrolysed hydration complex of iron. It is known that Fe^{3+} forms hexacoordinated aquo complex in water and condenses from fairly acidic conditions (pH $\geq$ 1) and Fe^{2+} only precipitates above pH 6 [28]. Thus the pH is maintained at a high value during the aqueous coprecipitation to precipitate the iron and to deprotonate the oleic acid (during formation of the primary layer).

After the coprecipitation is complete it is likely that a partial second layer of deprotonated fatty acid is physisorbed onto the primary layer. The nanoparticles from the original suspension are usually then precipitated and washed with acetone and methanol, to remove all unwanted reaction products from the suspension. These solvents wash away, or protonate and then wash away, the non-chemisorbed fatty acids, which are presumably responsible for the stabilisation of the monolayer coated nanoparticles in highly alkaline solution [200]. Magnetite precipitates immediately as a cluster of sticky, fatty mass because of phase separation. On washing the precipitate five times the pH is reduced closer to neutral. A second surfactant can then be applied, normally as the ammonium or sodium salt of the same, or a different, fatty acid, to form a physisorbed layer. Strong stirring during the coating process at 65°C and subsequent sonication at 50°C were found to be effective conditions for producing stable suspensions.

The NMRD profiles recorded as a function of pH and temperature, are in agreement with the predictions of SPM theory. Firstly there is almost no change in relaxation with pH in the high field region where the relaxation mechanism is 'outer-sphere' and is driven by diffusion. Similarly, there was no change in R_1 with temperature in the high frequency range. This is as expected, diffusion is a very fast process, with a low activation barrier. The limiting factor for high field relaxation is not the rate of diffusion, but the weak magnetic interaction between the core and the diffusing water molecule, so raising the temperature by this small amount is not expected to alter R_1.

In the low frequency range the relaxation is due to the motion of the magnetic moment relative to a static water molecule. The changes in R_1 with pH and temperature confirm the 'inner sphere' nature of the relaxation. It is likely that, as was the case for the 'monolayer' coated suspension in Chapter 3, lowering the pH increases the number of protons on the surface of the magnetite. Such ^1H nuclei would have dipolar coupling with the nearby water ^1H nuclei, which could amplify the interaction between the moment of the nanoparticle and the water ^1H nuclei. Alternatively, lowering the pH could neutralise some of the electrostatic charge by protonation of a second layer of surfactant molecules, but this would probably occur below pH 9 [197]. The fact that the relaxivity is pH dependent indicates that the surfactant coating does not form a complete monolayer, or at least that the surface is still partially accessible, which is surprising given that it is accepted that full layers are formed for particles stabilised in this way [65]. The changes

in R_1 with temperature are as expected for a process which is in the fast exchange limit, increasing the temperature reduced the relaxation rate, in the lower frequency range (<2 MHz).

The NMRD results indicate that the primary core sizes are in the range of 20 nm, as the data fit SPM theory quite well. The main feature in the measured profiles, a maximum in r_1 in the low MHz range, was observed to be broader than predicted, indicating some polydispersity in the core size distribution. The hydrodynamic sizes were much larger, in a range centered around 84 nm. The TEM results were not inconsistent with the presence of 50-150 nm clusters, which are themselves composed of primary nanoparticles in the superparamagnetic size range. In suspension the clusters are observed to be stable to dilution with water and with solutions (25mM) of the ammonium salt of any fatty acid, or with 25mM sodium oleate (C18:1). In contrast to the clusters described in the preceding chapter, these are not magnetically 'blocked', and so are similar in nature to the USPIO contrast agents typically found on the market today. These consist of multiple superparamagnetic cores dispersed in a larger shell of highly water permeable dextran [12, 65].

The observation of stability to dilution with water of these suspensions is in disagreement with the observations of Shen-Laibinis *et. al.*, [60] who observed the growth of 500 nm nanoclusters. This was ascribed to the loss of the physisorbed layer on dilution below the CMC of the secondary surfactant (C12:0).

The NMRD profiles for the NaCl assisted preparations show small systematic differences with the non-assisted equivalents. During the coprecipitation, the NaCl salt fully dissociates in suspension. It is likely that the magnetite core coordinates with hydroxyl ions immediately after formation, with a more loosely bound shell of hydrated sodium cations surrounding the hydroxides. Electrostatic repulsion between the magnetite particles, as a result of ion coordination, keeps the particles apart and they are inhibited from further growth, in the short time prior to surfaction. The slightly lower relaxivity at low field and the slight shift of high field maximum towards higher magnetic fields, apparent in Figure 4.6, suggest that the magnetite cores, from the syntheses at higher ionic strength, are slightly smaller and have higher anisotropy energy. It has been speculated [201] that large, highly hydrated Na^+ ions surround the hydroxides which are

coordinated to the surface of the magnetite crystallites soon after nucleation, suppressing growth, which results in smaller nanoparticles.

4.4.2 Coprecipitated magnetite in heptane

The PCS analysis of the suspension transferred into heptane showed a Z-average of 13.4 nm with PDI ~0.06. The NMRD profile of the suspension dispersed in heptane is presented in Figure 4.7 below. The high field maximum in the profile corresponds to a ~10.8 nm magnetite core. A simulated pattern for 10.8 nm magnetite particles fits approximately through the data indicating the thickness of the surfactant is about 1.3 nm. The parameters used for the simulation are very close to those reported for crystalline magnetite except the diffusion coefficient used D = $2.4*10^{-5}$ cm^2s^{-1}, which is slightly less than the reported value of about $3.5*10^{-5}$ cm^2s^{-1}. The simulated curve indicates that the measured r_1 maximum is broader than anticipated. The obvious explanation, that this is due to a distribution of particle sizes, is probably not the case given the low PDI. The cores may have lower anisotropy energy than is normally anticipated for cores of this size. In any case, it is apparent that the phase transfer procedure produces dispersed suspensions of magnetic nanoparticles in heptane.

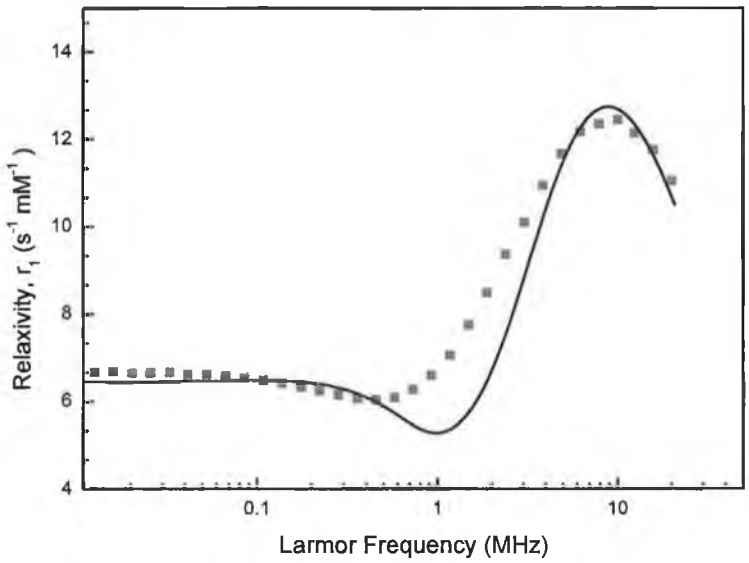

Figure 4.8. Relaxivity profile of a magnetite suspension prepared through the aqueous route suspended in heptane (■),a simulated profile (—) for a 10.8 nm particle using the parameters, M_s = 30 emu g^{-1}, τ_N =10 ns, ν_{anis}= 1 GHz.

4.4.3 Effect of chain length on relaxivity in heptane suspension

From the frequency of the r_1 maximum, in the NMRD profiles, an estimate of the particle size can be obtained. This has been done for the NaCl assisted and non-assisted series of preparations using the saturated C6 to C18 carboxylic acids, see Figure 4.7. The NMRD analysis, a summary of the preparation details and of the PCS analysis is presented in Table 4.1 below. The centrifuged fine fraction in stable suspension was used to calculate the yield. In the NaCl assisted series the hydrodynamic sizes of the C9, C10 and C12 coated suspensions are almost the same (~11 nm), while the C9 suspension had higher relaxivity, which indicates that the chain length does not determine relaxivity. The results have been shown to be reproducible, with a maximum variation of 7% from 15 preparations. The C16 coated suspension from this series was anomalous, the difference between its hydrodynamic and PCS size was greater than 3 nm. It also gave a higher PDI value, which could account for this difference.

Table 4.1. Aqueous coprecipitation synthetic parameters and properties of the resulting magnetite suspensions in heptane [202].

Saturated FA (pK_a, I = 0)	Ionic strength	Z-av nm	PDI	NMRD		r_1 at plateau $s^{-1}mM^{-1}$	Approx yield %
				r_1 max. MHz	Size nm		
C6 (4.83)	0.25 M NaCl	-	-	-	-	-	0
C9 (4.95)		11.3	0.11	12.4	9.1	11.2	4.1
C10 (5.3)		10.8	0.06	15.8	8.3	8.2	21
C12 (5.3)		11.2	0.10	12.4	9.1	8.0	17
C16 (9.85)		13.7	0.2	12.4	9.1	10.8	2.8
C18 (10.15)		-	-	-	-	-	0
C9	No NaCl	-					0
C10		17.5	0.25	-	-	-	~0
C12		15	0.14	11.1	9.5	9.0	8.0
C16		13.1	0.05	9.8	10.0	11.8	5.2
C18		13.2	0.06	11.0	9.5	11.7	4.2

For the NaCl assisted series, the hydrodynamic sizes were generally larger than anticipated from the NMRD results. More interestingly, the relaxivity of the suspensions in this series was always higher, by about 20-30%, indicating more magnetic cores.

The clearest observation from the two series of preparations is that at higher ionic strength shorter chain carboxylic acids work as efficient surfactants, forming stable magnetite dispersions. Saturated fatty acids with more than 15 carbons (pKa > 8) form monolayers on magnetite surfaces at a lower ionic strength [202]. Palmitic (C16:0) and stearic (C18:0) acids were only successfully used as the surfactant for synthesising stable magnetite suspensions in absence of any salt. Given the conditions of high pH and temperature it could be assumed that the fatty acids, of all chain lengths, are deprotonated during coprecipitation. Although at higher ionic strength the C16 and C18 carboxylates are visibly not well solvated and hence not very surface active. Alternatively, it could be speculated that on the presence of NaCl that the (C18:0) fatty acid is a stronger base than ammonia, hence the lack of reaction. Looking at the shorter chain fatty acids, as the chain length gets shorter the molecule becomes a weaker surfactant. However in the presence of NaCl the cut-off is for shorter chains, i.e. a suspension was produced with nonanoic acid (C9:0), albeit with lower yield.

The aim of the chain length study was to investigate the factors which influence the relaxivity of the suspensions. It was anticipated that reducing the size of the hydrocarbon shell would alter the low field relaxivity substantially. In fact changes in relaxivity were observed over the full frequency range. While core size strongly influences the profile, for these suspensions the differences also arise from other factors. For instance C16 from the non-assisted, and C12 from the NaCl assisted series, have high field maxima at the same frequency, but exhibit quite different relaxivity. In fact the profiles in Figure 4.8 overlap quite well indicating that the relaxivity differences arise in this case from differences in the crystallinity of the core, which is reflected in the saturation magnetisation, M_s.

4.4.4 Non aqueous magnetite suspended in aqueous suspension

The NMRD data for a sample of magnetic suspension (suspension N7) phase transferred from heptane to water, by the application of a second surfactant of ammonium laurate is given in Figure 4.9. The magnetite had a Z-average size of 11.7 nm with PDI 0.03 in heptane.

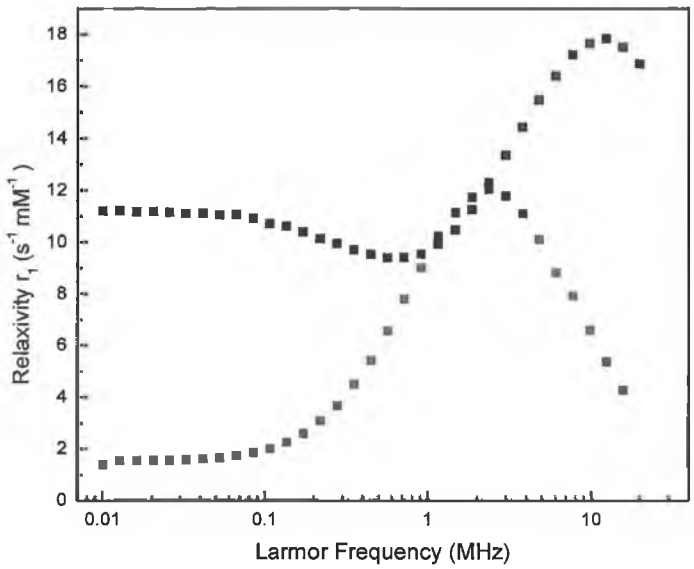

Figure 4.9. The relaxivity profile of non aqueous synthesised magnetite N-7 (■) with a PCS size 11.7 nm, PDI= 0.03 in heptane. The same magnetite phase transferred into water (■) with application of a second layer on ammonium laurate.

The water suspended magnetite from this procedure had an exceptionally low relaxivity. The suspension was not stable for a long time in water, with the r_1 value changing with time. The relaxivity value is questionable, as some precipitate, which would not influence the relaxivity, may have been included in the Fe determination. However, the shape of the profile is more reliable.

For this reason NMRD characterisation was undertaken in water and heptane for a sample synthesised by aqueous coprecipitation. The aqueous coprecipitated magnetite suspended in heptane was centrifuged at 13000 rpm for 30 minute before analysing by PCS. The Z-average diameter was 15.6 nm with PDI 0.11 for the monolayer of oleic acid coated magnetite.

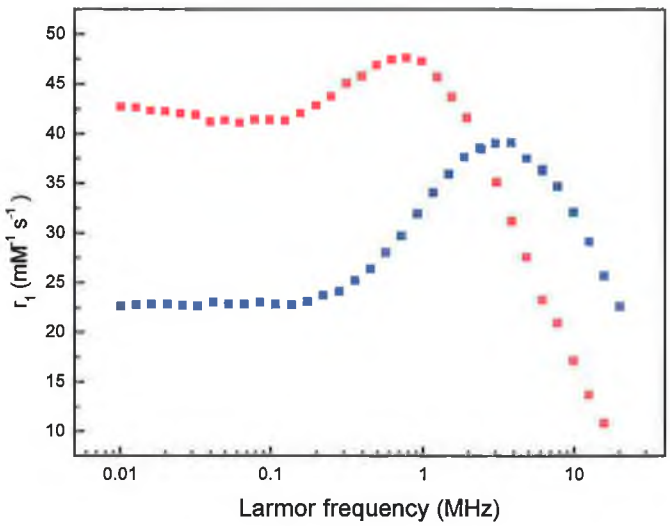

Figure 4.10. NMRD data for aqueous coprecipitated magnetite nanoparticles dispersed in heptane stabilised by an oleic acid monolayer (■), and the same preparation stabilised in water after the addition of a second layer of ammonium laurate (■). Both suspensions were stable for many days and the data is reproducible.

When the same magnetite particles were applied with a second layer of ammonium laurate and dispersed in water, the PCS size of aqueous clusters was found to be 173 nm with PDI 0.17. NMRD of the heptane suspension shows the high field maximum is at 3.8 MHz which corresponds to a magnetite core of ~14 nm which is in very good agreement with the PCS size of 15.6 nm, which includes the chemisorbed oleate layer. The NMRD and PCS results for the aqueous suspension are very typical of bilayer stabilised magnetite. The high field maximum in the NMRD profile is at 0.77 MHz which is equivalent to a magnetite core of 23 nm. However this value is not reliable due to the presence of a significant non-superparamagnetic fraction. The higher relaxivity in the low field region is also indicative of the presence aqueous clusters.

4.4.5 Uncoated magnetite in water and heptane

The NMRD data on the magnetite prepared in Trinity [190] suspend by agate grinding in heptane as well as in water are given in Figure 4.11 below. The oleic acid coated magnetite produced a stable suspension in heptane with a Z-average size of 41 nm (PDI=0.17).

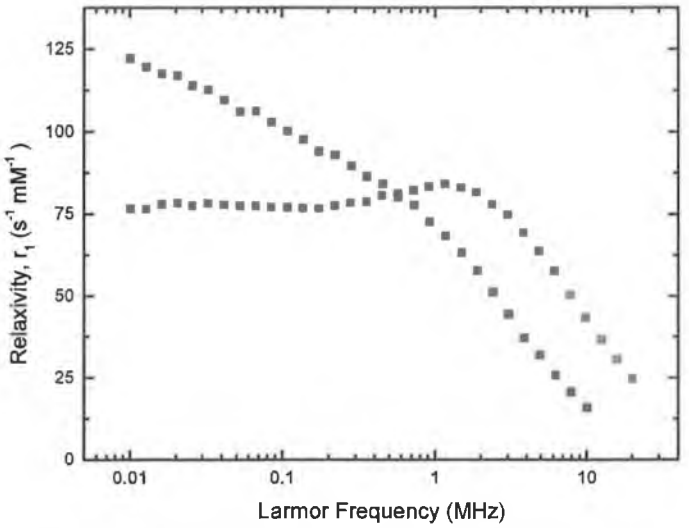

Figure 4.11. Uncoated magnetite (no-2) coated with monolayer of oleic acid in heptane (■) and with oleic acid/sodium oleate surfactant in water (■).

The same magnetite was wet ground with oleic acid and sodium oleate (1:1) as mentioned previously and was transferred in required volume of water. The aqueous suspension was then sonicated for 30 min at 50°C which produced a stable suspension. The PCS size for the aqueous suspension was 113 nm with PDI 0.25.

This experiment again demonstrates how the state of the surface coating alters the magnetic nature of the resulting suspension. In the case of agating in heptane, the surfactant binds more efficiently to the surface, resulting in a significant proportion of the magnetic nanoparticles displaying superparamagnetic behaviour in suspension, i.e. more magnetically dispersed clusters were generated. When water was used there was no evidence of a maximum, indicating a magnetically 'blocked' suspension. These observations are consistent with those of the preceding chapter.

4.5 Conclusion

The synthetic method of coprecipitation of mixed Fe^{3+}/Fe^{2+} salts was found to produce smaller particles when synthesised at a relatively high pH (pH>12) and ionic strength ($\geq$ 0.25 M). The NMRD response of the bilayer stabilised magnetite suspensions showed no dependence on temperature or pH dependence at high field, confirming the relaxation mechanism. The low field relaxation on the other hand is found to be inner sphere in nature and shows the expected dependence on temperature or pH.

Using surfactants of different chain lengths produces moderate effects on the relaxivity of the suspensions, in heptane. The saturated acids with chains of more than 15 carbons were found not to be effective at coating magnetite at higher ionic strength. Decanoic and dodecanoic acid were found to be the most effective fatty acids tested for producing manolayer stabilised magnetite suspensions in heptane. Efforts to produce systematic changes in relaxivity by altering the fatty acid surfactant have been thwarted by the complexity of the synthetic procedure, the number of variables involved, and probably also by the fact that the crystallisation process is probably under kinetically control. A simpler synthetic procedure would be required to exert such control on the outcome.

Chapter 5

The preparation and characterisation of non-aqueous magnetic fluids

5.1 Introduction

In a recent article, Sun and Zeng [24] reported a method involving high temperature reflux for synthesising suspensions of 4 nm monodispersed superparamagnetic magnetite particles. The nanoparticles were characterised by high resolution TEM and X-ray diffraction which indicated crystalline magnetite with a very tight size distribution. In this method iron acetylacetonate (2 mmol) was refluxed in diphenyl ether (20 ml) in presence of alcohol, 1,2 hexadecanediol (10 mmol) and surfactant oleic acid (6 mmol) and oleyl amine (6 mmol).

Given the attractive features claimed for this method, a series of experiments to investigate the effect of the experimental conditions on the size of the magnetite nanoparticles was undertaken. In particular, with a view to controlling the size to produce very small magnetic nanoparticles. Firstly, the effect of reaction time was investigated, reflux times of 1 and 15 minutes were chosen. Secondly, the effect of varying the ratio of Fe precursor to surfactant, and the iron concentration, was investigated. Thirdly, the effect of varying the overall concentration was investigated, by increasing the phenyl ether concentration from 20, to 30 to 40mls. Finally the effect of temperature; 200°C or reflux temperatures, 265°C was investigated.

The disadvantages of the aqueous precipitation method, described in Chapter 3, are that the pH value of the reaction mixture, its ionic potential, concentration of reactants, temperature all play a role in the kinetics of formation and growth of the particles. The synthesis of smaller (<10 nm) monodisperse nanoparticles through ammonia precipitation had limited success. It is very difficult to obtain reproducible relaxivities for the suspensions through aqueous synthesis because of the very complicated surface properties of magnetite in aqueous suspension and the stabilisation mechanism through the surfactant layer applied on to the surface.

In contrast the high temperature reflux method is very simple one-step process. All the chemicals are added in one step before closing the reactor for degassing by purging nitrogen. The whole process from start of nitrogen purging to heating up to crystallisation takes place anaerobically without opening the system to atmospheric oxygen with no other process variables involved. Our initial experiments indicated that the process produces very monodisperse particles of reproducible sizes.

5.2 Experimental

The reactants were added in to a 100 ml 3-necked round-bottom flask with the central neck being connected to a water cooled condenser. Oleic acid (≥99.0%, Fluka Chemicals) and oleylamine (≥70.0% GC, Fluka) were first weighed in the reactor, the appropriate amount of 1,2 hexadecandiol (Technical grade 90%, Aldrich) and iron acetylacetonate (99.9%, Aldrich) were then weighed in a weighing boat. The solids were transferred into the reactor through the central neck and required amount of diphenyl ether (99%, Aldrich) was then added as the last reagent. Nitrogen gas was purged through the suspension for 20 min through a glass pipette. A 350°C thermometer was connected to the remaining neck using a thermometer pocket. The flask was then heated on a heating mantle at full power (60 W). About 15 min was required for the vessel to reach reflux temperature (~265° C). There was no stirring used during the reaction. The temperature of the liquid was monitored by the thermometer. The solid Fe precursor and alcohol dissolved at about 100° C producing a wine red transparent colour which slowly turned into dark red at ~125° C followed by orange till the mixture started boiling at ~ 260° C. At this point the colour of the mixture rapidly turned dark.

The mixture was allowed to reflux for 15 min for magnetite crystals to grow. During the reflux there suspension would 'bump' strongly on occasion. In some cases this dislodged one of the thermometer pockets connected or the top of the reflux condenser could be thrown off. A slight positive pressure of nitrogen was maintained in the reactor throughout the reflux, in any case. At the end of the reflux, a vigorous reaction with frothing was observed and the suspension turned black which is probably the indication of formation of magnetite crystals. The reactor was then lifted off the mantle and allowed to cool naturally to room temperature.

The nanoparticles were precipitated from this dark suspension by adding ethyl alcohol (about 60 ml) and leaving overnight. The upper liquid was decanted and the precipitate was redispersed in 20 ml heptane in the presence of about 20 % of the original amount of both oleic acid and oleyl amine. The final magnetite particles were reprecipitated with ethanol, separated and redispersed in about 20 ml heptane to produce the final magnetic fluid. 10 mmol of 1,2 hexadecandiol was used in all the preparations. The details of synthesis parameters and the corresponding sample identifiers are given in Table 5.1.

Table 5.1. The synthetic parameters; amount, ratio of reactants and the corresponding preparation labels for the first series of preparations.

Sample name	Reaction temp (°C)	Phenyl ether used (ml)	Reaction time (min)	Fe source used (mmol)	Total surfactants used (mmol)	Surf/ Fe ratio
N3	reflux	20	15	2.00	12.00	6.00
N6	reflux	20	15	0.40	12.00	30.00
N7	reflux	20	15	4.00	12.00	3.00
N8	reflux	30	15	2.00	12.00	6.00
N9	reflux	40	15	2.00	12.00	6.00
N10	reflux	20	15	2.00	2.40	1.20
N11	reflux	20	15	3.50	12.00	3.43
N11a	reflux	20	15	2.00	6.86	3.43
N12	reflux	20	15	0.55	12.00	22.00
N14	reflux	20	15	0.86	12.00	14.00
NL	200	20	1	0.20	12.00	
N2	~260	20	1	2.00	12.00	
N4	~267	20	1	0.20	12.00	
N5	~265	20	1	0.40	12.00	

All the preparations were repeated to check the reproducibility of the synthetic procedure. The 1 min reactions were not repeated as they did not produce monodisperse nanocrystals. All the repeated preparations will be denoted by a prefix 'R' before the name given in Table 5.1. For example N3 in the repeat product is denoted as RN3.

The magnetic fluids were centrifuged to remove any remaining large particles or clusters. All centrifugations were carried out with a tabletop Eppendorf Centrifuge 5415 D at the speed 13000 rpm (rcf ~15700) for 30 minutes. The stable magnetic fluids in heptane were characterised by PCS at 25°C and by NMRD at 24°C, as described in Chapter 2.

5.3 Results

5.3.1 General observations

Below are the representative PCS data for all the samples. The diameter is selected on the basis lowest Z-average and the best correlation time fits.

Table 5.2. The average PCS size and polydispersity index of first series of preparations.

Sample	Surf/ Fe ratio	Reflux time (min)	Dilution factor for PCS	Count	Z-ave (nm)	PDI	Peak 1 intensity (nm)	Peak 2 intensity (nm)
N3	6	15	2	92	7.12	0.071	7.72	0
N6	30	15	2	268	8.91	0.078	9.52	0
N7	3	15	6	23	10.54	0.036	11.90	0
N8	6	15	2	178	6.42	0.072	7.03	0
N9	6	15	3	125	6.44	0.106	7.28	0
N10	1.2	15	5	391	8.50	0.035	9.18	0
N11	3.43	15	10	110	8.44	0.043	11.50	0
N11a	3.43	15	4	202	8.4	0.031	8.93	0
N12	22	15	4	230	7.30	0.066	12.18	0
N14	14	15	3	38	8.01	0.035	8.72	0
N2	2	1	6	246	6.57	0.127	7.57	0
N4	0.2	1	0	165	27.07	0.392	43.77	1613
N5	0.4	1	2	397	14.89	0.078	16.21	0

It is evident from this data that all the suspensions, except for N4, contain monodisperse particles, as the PDIs are low. Sample N4 has a Z-average (average size) ~ 27 nm with a few large clusters in the micrometer range.

The results of the repeat preparations shown below in Table 5.3 are slightly different from those of the original preparations. There are only two compositions (N6 and N10) where there is a decrease in the hydrodynamic size of the magnetite particles prepared in the second set (RN6 and RN10). The magnetite particle size in N6 decreased from 8.9 nm to 8.4 nm in the repeat (RN6). A reduction in size of about 0.6 nm was found from N10 (8.5 nm) to RN10. The compositions N7 and N11a had no change in their magnetite crystal size as found by PCS measurements (Table 5.2 and 5.3).

Table 5.3. PCS size data, including dilution, for the repeat series of preparations.

Sample	Surf/ Fe ratio	Reflux time (min)	Dilution factor for PCS	Count	Z-ave (nm)	PDI	Peak 1 intensity (nm)	Peak 2 intensity (nm)
RN3	6	15	4	170	7.9	0.03	8.49	0
RN6	30	15	3	225	8.4	0.004	8.74	0
RN7	3	15	6	170	10.5	0.031	11.21	0
RN8	6	15	5	57	7.5	0.04	8.22	0
RN9	6	15	3	240	7.2	0.04	7.61	0
RN10	1.2	15	7	163	7.9	0.03	8.31	0
RN11	3.43	15	10	110	10.4	0.05	11.5	0
RN11a	3.43	15	3	147	8.4	0.047	9.28	0
RN12	22	15	3	65	7.8	0.018	7.62	0
RN14	14	15	6	157	7.9	0.04	8.43	0

The other interesting point to note that the largest increase in hydrodynamic size (0.8 to 1.1 nm) was observed in the three formulations (N3, N8 and N9) with the molar ratio of reactants (Fe:surfactant:1,2 hexadecanediol = 2:12:10), as used by Sun *et al.* [24].

5.3.2 The effect of temperature on the reaction

A synthesis was attempted (suspension NL) with 0.2 mmol of Fe precursor, while limiting the temperature of the reaction mixture to 200°C. At 200°C the purging nitrogen flow momentarily increased which caused the suspension to 'bump', as was observed during synthesis under normal reflux conditions. The suspension was then cooled. A greenish yellow solid was formed on first precipitation with ethanol in presence of surfactants. During the second precipitation the whole suspension agglomerated into a rubbery solid mass, which was not suspendable in heptane. It is clear that a reflux temperature is required for the reaction to start.

5.3.3 The effect of concentration on the PCS analysis

It was observed that dilution of the neat magnetite suspension with heptane was necessary to arrive at a monodisperse reproducible distribution of sizes. The Z-average (hydrodynamic diameter) value is indicative of a unimodal distribution when the polydispersity index (PDI) of the PCS measurement is below 0.2 and preferebly around

0.1. The Z-average and PDI decrease with dilution, from neat, 0, to a factor of ~5. The PCS data obtained for the neat fluids, in which the magnetite concentration is ~75-100 mM, do not represent the true particle size. The detailed analysis of PCS data on sample N8 is given in Table 5.4 below. The concentration of Fe in the neat sample was ~ 84 mM. A X5 dilution with pure heptane was found to produce a suspension with monodisperse size distribution around ~6.4 nm, with a reasonably small PDI of about 0.072 and with a better fit to the correlation time functions. There was no change in Z-average on further dilution. The volume fraction of magnetite nanoparticles in heptane is ca. 0.003 (the volume ratio of heptane to magnetite is ~335) is quite high in the neat suspension. At this high volume fraction, there may be interactions between the surfactant-coated particles which restrict their diffusion, leading to a systematic overestimate of the PCS diameter [203].

Other possible explanations include multiple scattering due to high volume fraction of magnetic nanoparticles, or the high magnetite concentration may cause particle clustering due to the interlacing of surfactant tails caused by the interparticle interaction [71].

Table 5.4. The effect of dilution of sample N8 on the PCS size and polydispersity index

Dilution factor to neat	Mean Count Rate (kcps)	Z-Ave. (nm)	PDI	Peak 1 size (nm)	Peak 2 size (nm)	Peak 1 area	Peak 2 area
1	331	14.16	0.311	14.2	1561	86	13
2	34	8.51	0.274	9.8	1949	92	7
3	65	7.05	0.188	8.2	2002	97	2
3	67	6.85	0.203	8.5	0	100	0
3	104	6.54	0.091	7.2	0	100	0
3	104	6.58	0.077	7.2	0	100	0
5	151	6.47	0.102	7.3	0	100	0
5	178	6.42	0.072	7.0	0	100	0

Irrespective of the cause, it is clear that an approximate Fe concentration of no more than 10-15 mM is necessary to obtain stable and representative PCS results for heptane suspensions. The histogram describing the distribution of sizes of N8, for both nest and diluted suspensions is presented in Figure 5.1. The finest magnetite suspension (N8, neat) in the first set of preparations had a Z-average size of over 14 nm with poor PDI=0.3 when measured by PCS. The same fluid displayed a Z-average size of 6.42 nm with

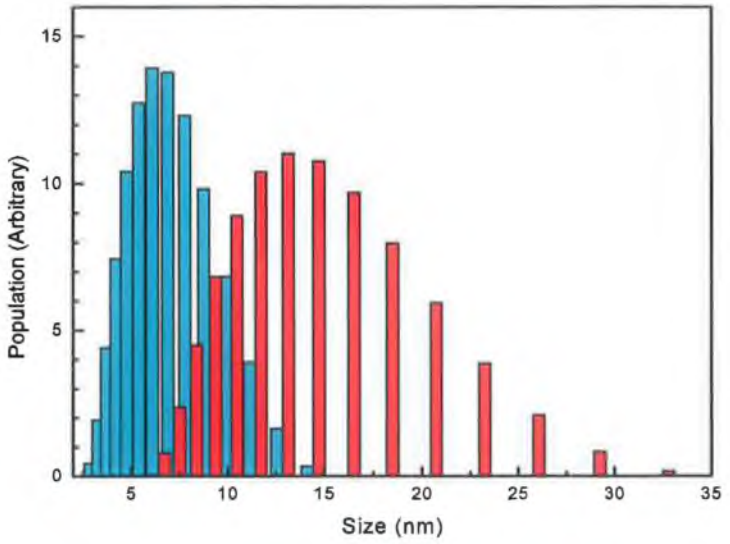

Figure 5.1. The PCS size distribution of neat (■), and X5 diluted suspension (■), of preparation N8.

PDI =0.072 when diluted ×5 with heptane. The raw correlation data fit by the Malvern software is presented in Figure 5.2. The fit in Figure 5.2 is through all the data points in the graph and so is the very low polydispersity (PDI 0.07).

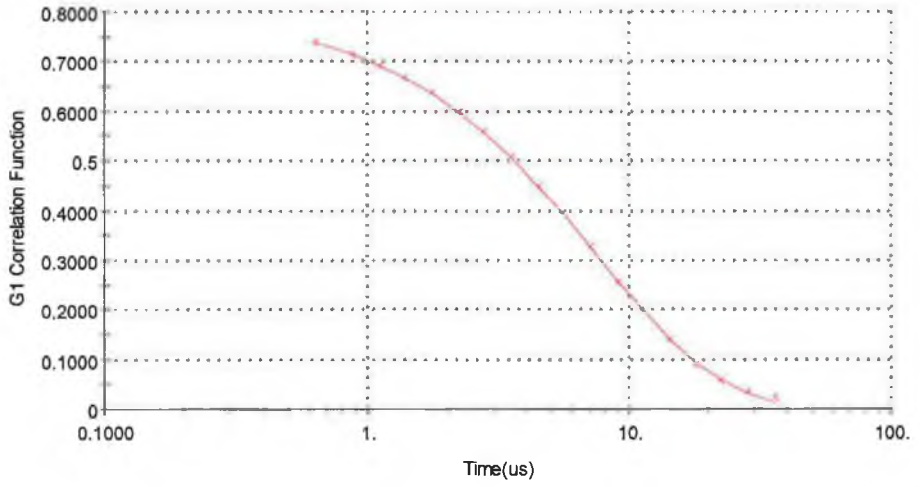

Figure 5.2. The raw PCS data, including the fit to the correlation function (G1) for the X5 diluted sample from preparation N8.

The PDI for most of the preparations refluxed for 1 minute was poor. The actual fit of the correlation function for sample N4 for a dilution X4 with heptane is given in Figure 5.3 below. The fit does not pass through all the data points, which corresponds to a high polydispersity (PDI).

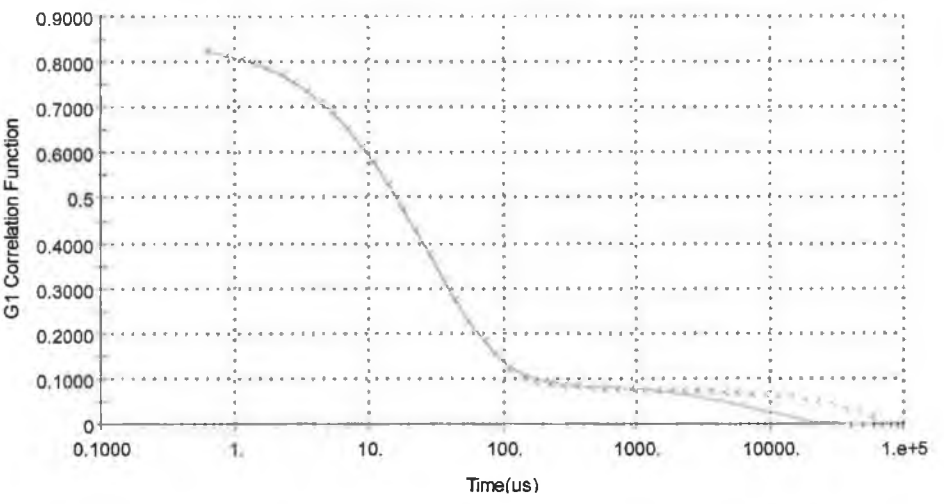

Figure 5.3. The correlation data fit for X4 diluted suspension of N4 showing a 'poor' fit.

5.3.4 NMR relaxation rate measurements

The NMRD results will be discussed in detail below. The relaxation rate data for the sample containing the largest nanoparticles, N7, in the first set of preparations is presented in Figure 5.4 below. The general shape is similar to that observed for aqueous suspensions of magnetite. The magnetite in the suspension is superparamagnetic as is clear from the low field dispersion as predicted by Roch *et al.* [152]. A high field maximum in R_1 is observed in the frequency range 10 to 20 MHz. A slight precipitation of nanoparticles was observed as a decrease in R_1 over a few days.

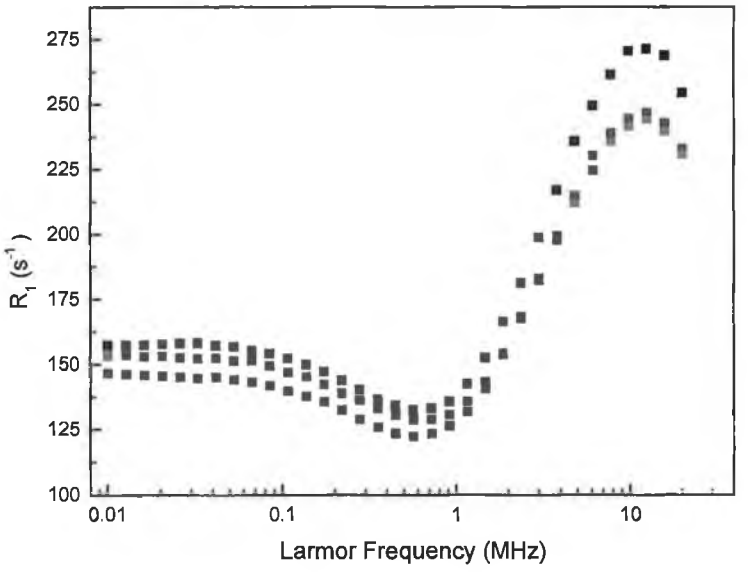

Figure 5.4. The relaxation rate data for N7 (Z-average=11.2 nm) against frequency over 6 days. The data in black represents day 0, in red is day1 and blue data represents day 6.

An interesting point to note is that the relaxation rates for the suspension on day 6 started with a marginal drop in R_1 (precipitation) in the high frequency side in the profile. But at about 3.5 MHz the R_1 increased and remained high in the rest of the profile in the low frequency range. This may due to clustering of finer magnetite particles in N7 in an analogous fashion to that observed for aqueous suspensions.

5.3.5 The effect of concentration on the NMRD analysis

The characterisation of non-aqueous magnetic fluids by NMRD is without precedent in the literature. While it is apparent that the profiles have the same general shape as those observed for aqueous suspensions of magnetite nanoparticles, it is important to establish that the relaxation of the heptane ^1H resonance is due to paramagnetic relaxation enhancement of the magnetic particle. The enhancement is given by

$$R_{1,obs} = R_{1,solvent} + R_{1enhancement}$$

$$\frac{1}{T_{1,obs}} = \frac{1}{T_{1,solvent}} + r_1[Fe] \qquad (5.1)$$

where, $R_{1,obs}$ is the observed relaxation rate ($R_{1,obs}$=1/ $T_{1,obs}$), $R_{1,solvent}$ is the R_1 for the solvent protons, $T_{1,obs}$ is the measured relaxation time, r_1 is the concentration independent relaxivity ($s^{-1}mM^{-1}$) and [Fe] is the concentration of iron in the magnetite suspension.
Profiles recorded for sample N2 at different concentrations are shown below in Figure 5.5. It is seen that there is no change in the shape of the profile on dilution. The hydrodynamic size of the particles is also unchanged. It can be seen in Figure 5.5 that it is also possible to overlay the R_1, of the neat suspension with that recorded for the diluted sample scaled by the dilution factor. This clearly establishes the relaxation rate enhancement is proportional to the iron concentration. Similar experiments were undertaken for preparations N3 and N6, the results are shown in Figure 5.6. Change in

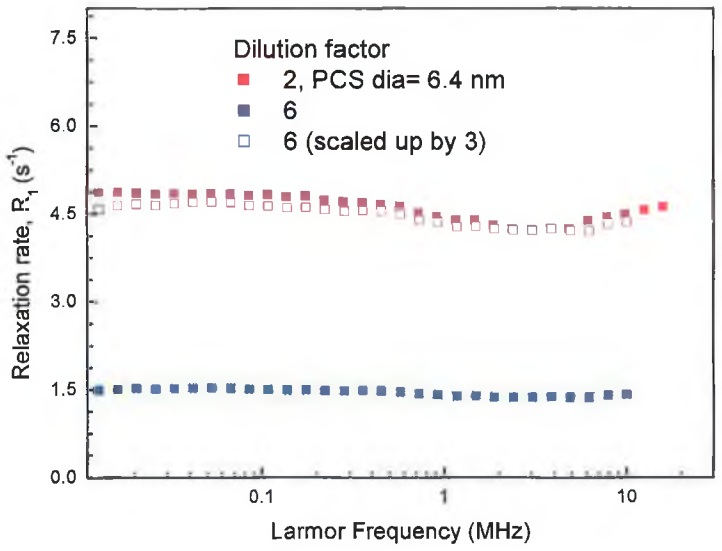

Figure 5.5. Proton relaxation rates of preparation N2 at different dilutions.

the Z-averages was observed on dilution, for the reasons discussed previously, but dilution has minimal effect on the shape of the profile.

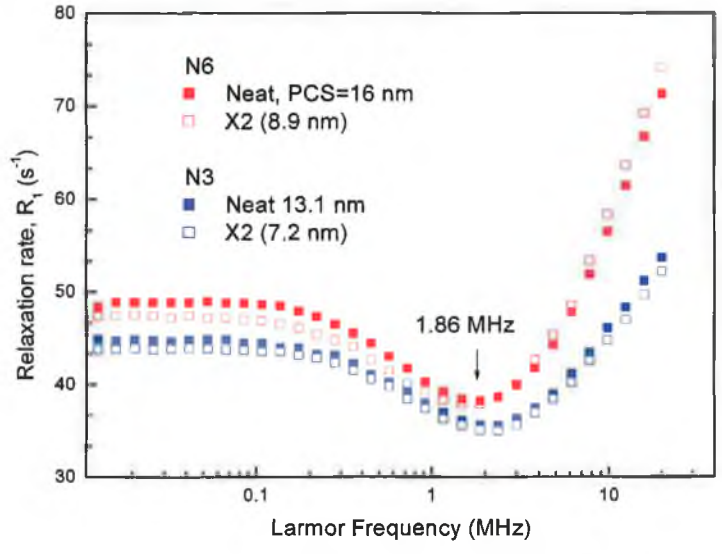

Figure 5.6. The effect of particle sizes (Z-average) on the shape of NMRD profiles for preparations N3 and N6.

It should be noted, finally, that pure water has a concentration of 55.5M, so the hydrogen concentration is 110M. Pure heptane (C_7H_{14}) on the other hand has a much lower concentration of 6.9M, which corresponds to a hydrogen concentration of 96.6M. Thus pure water contains only 1.15 times the hydrogen content, per unit volume, of pure heptane. As the paramagnetic enhancement in the case of heptane is divided over fewer hydrogen nuclei, it could be argued that the ^1H relaxivity profiles simulated using

superparamagnetic theory [152] should be scaled up by a factor of 1.15. However, given the significant assumptions required in formulating the theory and the relatively large number of fitting parameters it is perhaps best to use the output of the theory as it stands and accept an error of the order of 15% in the saturation magnetisation, M_s, of the particles, obtained from the fitting procedure. This parameter scales the simulated profiles, without altering the shape significantly.

5.3.6 The relaxivity of the suspensions:

The NMRD profiles (relaxivity) for the first set of preparations are shown below in Figure 5.7. The hydrodynamic diameter and polydispersity index data is also added in the figure legend for comparison. The two samples with the highest relaxivity are N7 and N11 which were synthesised with excess iron to change the surf/Fe ratio. Their sizes are also larger with a very narrow size distribution (PDI $\leq$ 0.05). The PCS diameter for N6 (8.9 nm) is not reflected in its relaxivity.

The finest particles in the series (N8 and N9) have low relaxivity, $r_1 < 1$ mM^{-1} s^{-1}. Another interesting point in Figure 5.7 is that the preparations (N2, N4, N5) from the short reaction time refluxes also have very low relaxivity.

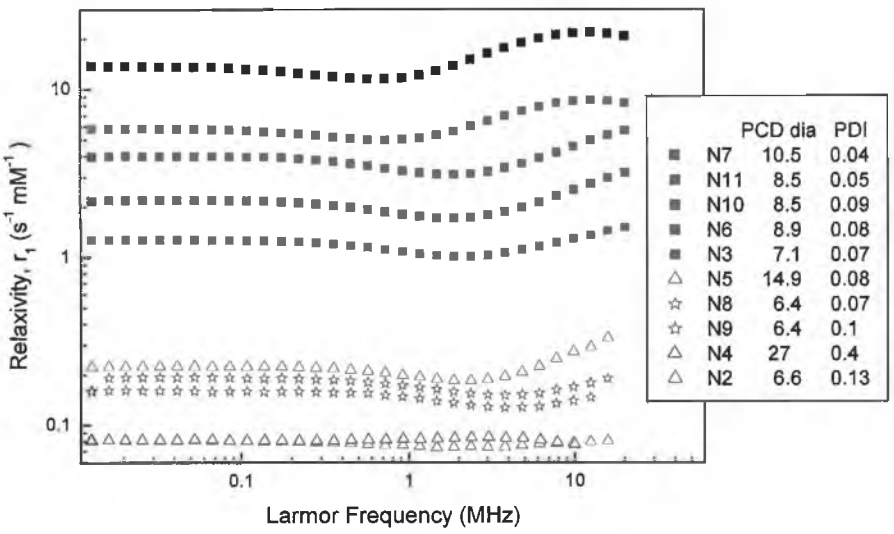

Figure 5.7. Relaxivity data for the first set of preparations as a function of Larmor frequency. Samples with $r_1 > 1$ mM^{-1} s^{-1} are given in solid squires, $r_1 < 1$ $mM^{-1}s^{-1}$ are given in unfilled stars and the 1 minute reaction products are in empty triangles. The PCS size and PDI are included in the legend.

The particle sizes from these preparations were also widely different (6.5 and 27 nm) with no correlations apparent in the NMRD results. The indication is that these preparations have different crystal properties than for instance preparation N3, which has particles of similar size.

The relaxivity data for all the repeat preps are presented in Figure 5.8 below. The reduction in the magnetite particle size in RN6 (8.4 nm) from 8.9 nm particles in N6 (Table 5.2 and 5.3) is not reflected in their relaxivity data. Rather sample N6 has slight lower relaxivity than sample RN6.

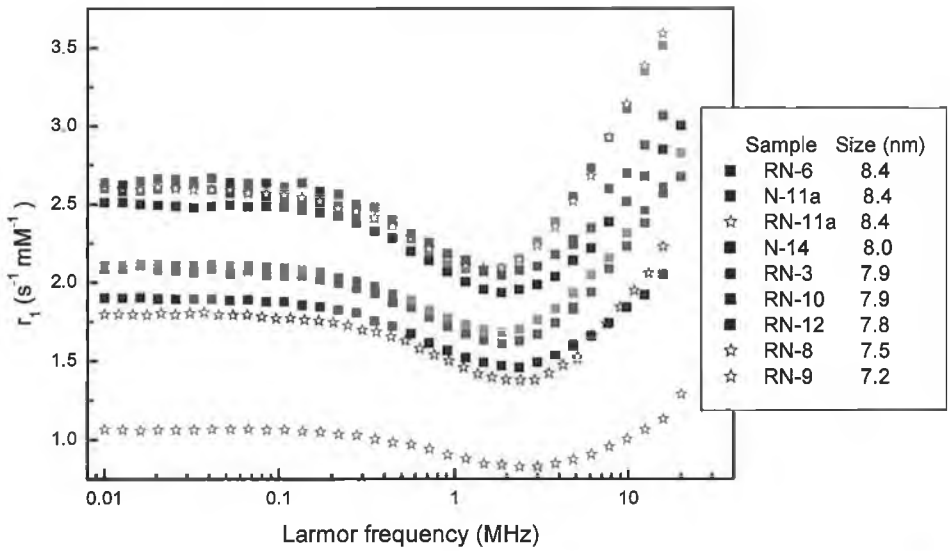

Figure 5.8. The relaxivity data for all the non-aqueous repeat sysntheses as a function of Larmor frequency. The sample names and their PCS size are indicated in the legend.

For the other sample which showed a reduction in PCS size is N10 (8.5 nm to 7.9 nm in RN10) the expected decrease in relaxivity was observed. The samples N7 and N11a had no change in their magnetite crystal size as found by PCS measurements (Table 5.2 and 5.3), this is reflected for instance in their relaxivity profiles, shown for suspensions N7 and RN7 Figure 5.9. This excellent reproducibility, is as good as could be produced in this study, was only possible with suspensions of larger particles.

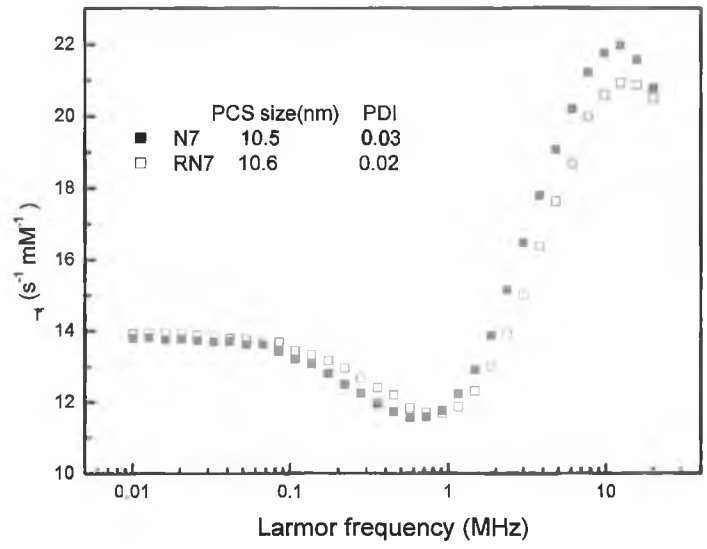

Figure 5.9. The closely matching relaxivity profiles of sample N7 and repeat sample RN7 with the same composition synthesised under identical conditions.

Samples (RN8 and RN9) were synthesised with the molar ratio of reactants Fe:surfactant: hexadecanediol = 2:12:10 (Table 5.1) as used by Sun *et al.* [24] and refluxed in diluted solutions with additional volume of diphenyl ether. They have the smallest sizes among sample in the repeat set and have low, and strikingly different relaxivity (Figure 5.7). Compared to the equivalent suspensions, N8 and N9, from the first series of preparations, which showed smaller PCS size and far lower, but reproducible, relaxivity. These results indicate that the magnetic character of the preparations reported by Sun and co-workers are questionable.

5.3.7 The effect of applying ultrasonic energy to the magnetic fluids:

It was interesting to note that oleic acid coated nanoparticles from the 1 minute reflux could be made to agglomerate on applying ultrasound energy to the suspension. A sample of suspension N2 was sonicated in a 80 W ultrasonic bath for 5 min and PCS measurements were taken immediately. The size data is given in Table 5.5. Sonication produced a suspension with very high Z-average size. The clustered particles resulted in a poor fit to the PCS data and a high PDI. This probably arose due to the formation of loose aggregates which slowly broke down to the original size on equilibrating overnight. Sample N2 was tested by PCS on the application of ultrasound energy within 7 days of synthesis. A similar observation was also noted with N4 (data not presented).

Table 5.5. The change in size and PDI of suspension N2 on ultrasonication.

Operation	Count (kcps)	Z-Ave. (nm)	PDI	Peak 1 (nm)	Peak 2 (nm)	Peak 3 (nm)
Stable suspension	246	6.571	0.127	7.570	0	0
Sonicated for 5 min	299	280.8	0.229	5.922	26.31	2671
After 150 min	286	80.84	0.115	6.47	84.23	2445
After 48 hr	248	6.631	0.197	7.315	1735	0
Centrifuged again	248	6.466	0.13	7.457	0	0

Surprisingly, when suspension N2 was resonicated after a month, no increase in Z-average was observed. Many attempts to reproduce this stimulated clustering proved unsuccessful. It was not possible to induce clustering in suspensions produced from the 15 minute reflux syntheses. These suspensions contained particles of similar size to the shorter time preparations, but they usually exhibited higher relaxivity and hence are more magnetic. It is likely that ultrasonic energy is sufficient to reorient and form aggregates for the less magnetic particles produced in the 1 minute syntheses.

5.3.8 Transmission electron microscopy results

Transmission electron microscopic images for two samples (N3 and N8) from the first set of preparations are given in Figure 5.10 and 5.11 and RN7 from the repeat series is shown in Figure 5.12. Sample N3 has a Z-average of 7.12 nm and the average TEM size (100 particles) is 5.2 nm. There is a difference of 1.98 nm between the TEM and PCS size.

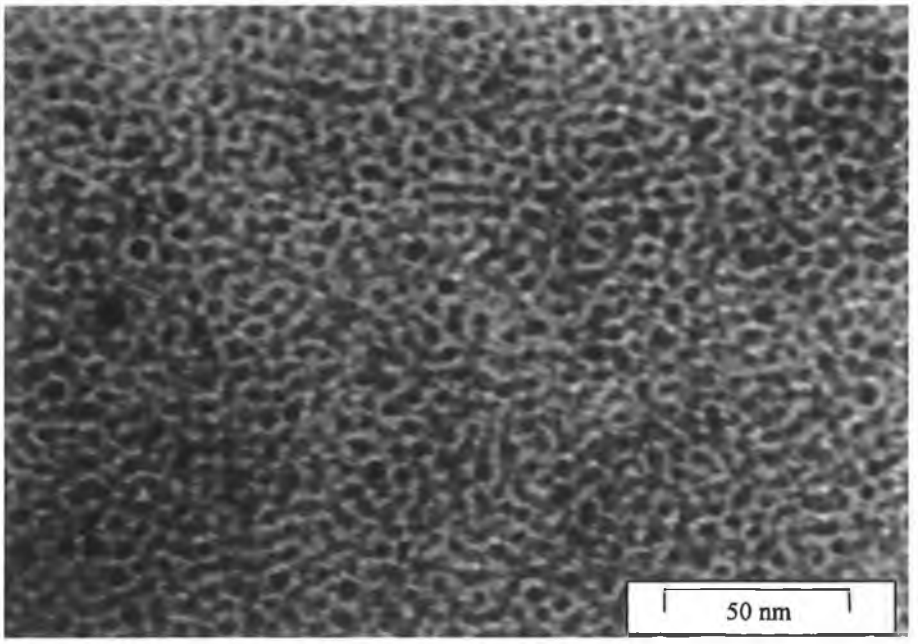

Figure 5.10. TEM image of N3 showing monodisperse particles with average size of 5.2 nm.

For suspension N8 the Z-average is 6.42 nm and the average TEM size is 4.1 nm, which gives rise to a difference of ~2.3 nm. These differences arise because TEM is sensitive to the heavier elements (iron), and so gives the core size, while PCS gives the hydrodynamic size. The difference is mainly due to the surfactant coating, a value of ~1

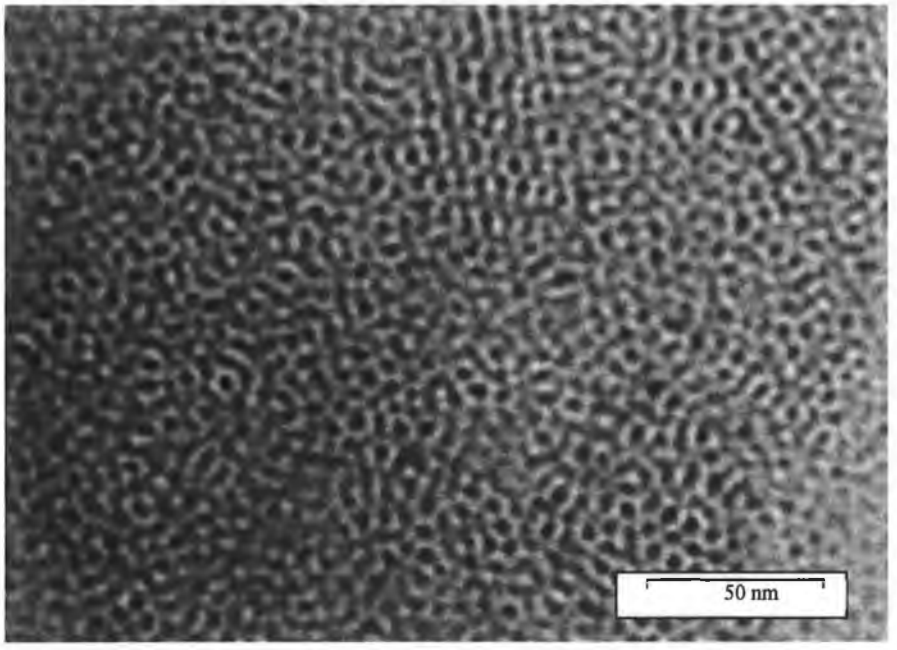

Figure 5.11. TEM image of sample N8 with standard ratio of reactants, showing very tight distribution of particles sizes with an average of 4.1 nm.

nm is very close to 0.9 nm reported by other authors [204] for the length of a C18 chain. The difference is greater for the finer particles N8 (1.15 nm), this may be due to the presence of an amorphous, non-magnetic, layer outside the magnetite core, which is supported by their low relaxivities (Figure 5.7).

5.3.9 Raman spectroscopic study of magnetite particles

Raman spectra of two samples of different sizes and relaxivities are given in Figures 5.12 and 5.13. All measurements were carried out at room temperature. Figure 5.12 shows the Raman spectrum for the finest particulate sample N8. The main features in the spectra are observed at about 226, 244, 293, 410, 495, and 611 cm^{-1}. All these features are indicative of the weakly ferromagnetic hematite phase [205, 206]. Normally magnetite, Fe_3O_4, is known to undergo a temperature induced phase transformation to maghemite (γ-Fe_2O_3) at about 200°C and then to hematite (α-Fe_2O_3) when the temperature is further increased to about 400°C. Faria *et al.* [206] observed sharp hematite Raman peaks in a magnetite sample heated at 300°C. An additional broad peak at 657 cm^{-1} is probably due to magnetite with a small shift of about 10 cm^{-1}. The observed peak at 611 cm^{-1} can be assigned to magnetite as reported by Thibeau *et al.* [207]. It can be concluded that sample N8 is a mixture composed mostly of hematite and some magnetite.

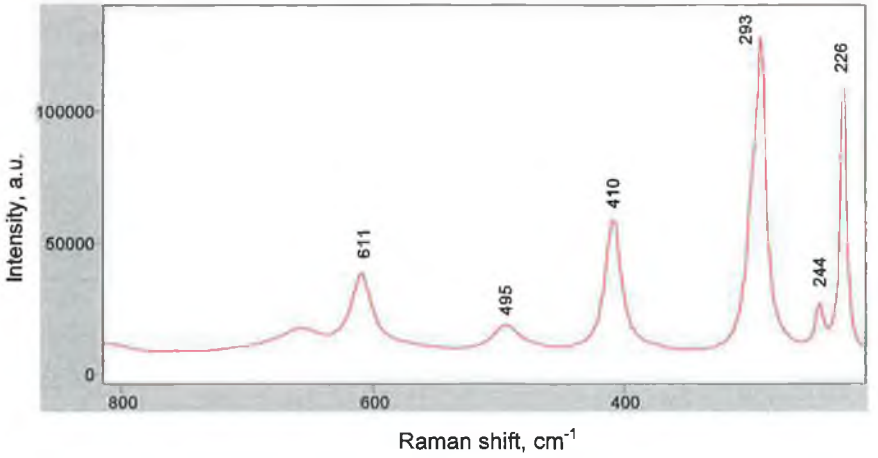

Figure 5.12. Raman spectra of dried particles from the finest suspension, N8, with average particle size of 6.4 nm.

The Raman spectra for the sample N11, a sample with Z-average size of 10.5 nm is given in Figure 5.13. This sample has completely different Raman bands, which are much broader. The spectrum also has a far higher signal to noise ratio than N8, which was acquired under very similar conditions.

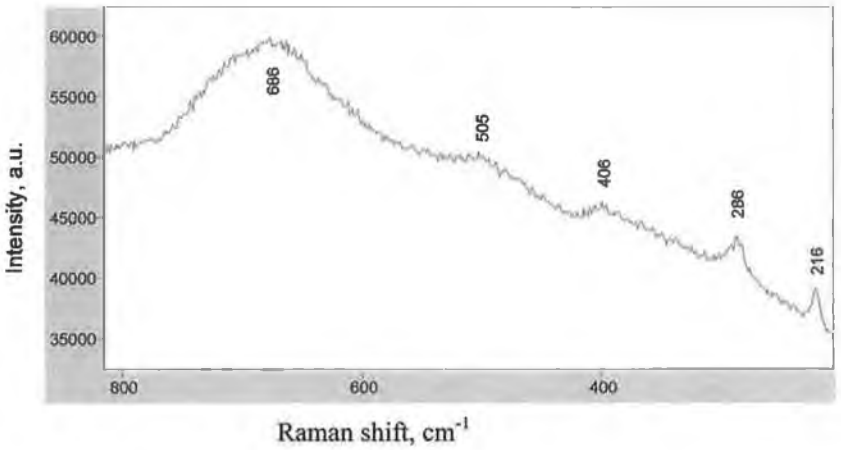

Figure 5.13. Raman spectra of dried particles from suspension N11, with an average particle size of 10.5 nm.

The weak broad features at 286, 505 and 686 cm^{-1} can be assigned to magnetite [208] with a band shift of about 10 cm^{-1}. de Faria *et al.* [206] assigned a Raman band at 680 cm^{-1} to magnetite and the broad Raman band at 505 cm^{-1} was attributed to maghemite. In contrast to hematite and magnetite, maghemite bands are not well defined due to their inherent poor crystallinity [206]. The iron oxide produced from the non aqueous method is also not very crystalline as we have seen from the poor amorphous X-ray diffraction pattern. It is evident from the references of previous workers that sample N11 is a mixture of magnetite and maghemite with slight majority of magnetite phase, however quantification is not possible from Raman spectra alone. The poor appearance of the spectrum is due to the presence of maghemite.

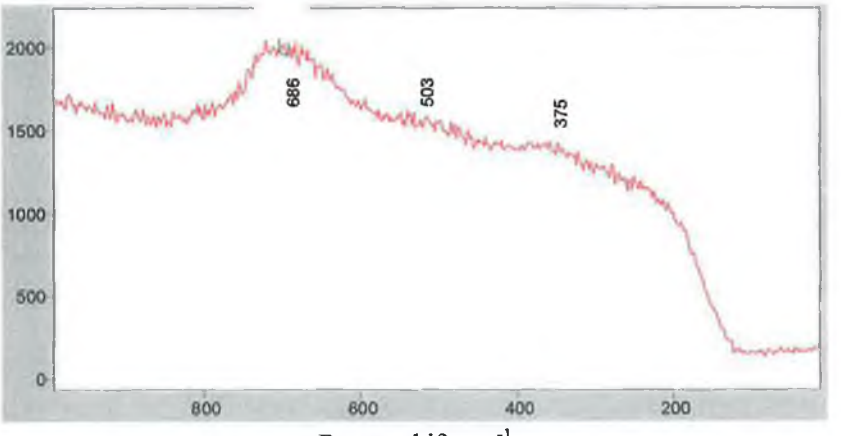

Figure 5.14. Raman spectra of dried particles from suspension N9, with average particle size of 6.4 nm.

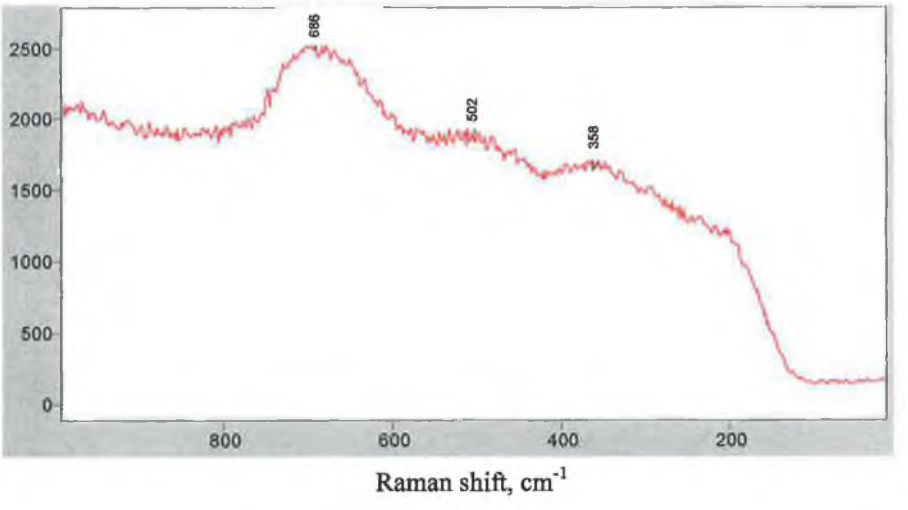

Figure 5.15. Raman spectra of dried particles from the finest RN7 sample with average particle size of 10.6 nm.

The spectra for suspensions N9 and RN7, shown in Figure 5.14, and 5.15, are very similar to suspension N11, the bands are broad and the spectra indicate the presence of a mixture of maghemite and magnetite.

Due to the presence of ferrimagnetic inverse spinel magnetite and maghemite the sample N11 is strongly magnetic as we seen from the high relaxivity of its suspension. At the same time, the poorly magnetic phase hematite (α-Fe_2O_3) is responsible for the fine iron oxide suspension N8 of its exceptionally low relaxivity (Figure 5.7). The hematite phase could not be observed by X-ray diffraction due to the extremely fine crystals in the dried suspension.

5.3.10 Redox-distribution of iron in magnetite

The oxidation states of iron in magnetite synthesised in the two series of preparations were evaluated by estimating Fe^{2+} and Fe^{3+} with standard 0.1 M potassium permanganate. Dilute sulphuric acid and a pinch of granular zinc were used as the reducing agent for estimating the total iron. The details of the procedure are given in Chapter 2. The distribution of ferrous and ferric iron of some selected samples from the first and repeat series are given in Table 5.6 below. While it is possible to determine the relative proportion of magnetite, due to their identical stoichiometry it is not possible to discriminate between maghemite and hematite, using wet chemistry methods. The data is analysed assuming, on the basis of the Raman studies and literature, that there are only two types of iron oxide present, of stoichiometry Fe_2O_3 (maghemite and hematite), and Fe_3O_4. For all samples, titrations were repeated until two values were in agreement. The error is of the order of 1-2%.

Table 5.6. The presence of Fe^{2+} and Fe^{3+} oxidation states in magnetite synthesised by high temperature reflux method.

Sample	PCS size (nm)	Fe^{2+}/Fe^{3+}	Fe_2O_3 / Fe_3O_4
N4	27	5.00	-
N7	11.4	0.18	1.8
N11	10.8	0.14	2.7
N6	8.9	0.18	1.8
N3	7.2	0.10	4.1
N8	6.4	0.45	0.11
N9	6.4	0.31	0.61
N10	8.5	0.23	1.21
RN3	7.9	0.39	0.28
RN7	10.7	0.38	0.30
RN8	7.5	0.39	0.28

The ratios of Fe^{2+}/Fe^{3+} are mostly in the range of 0.1 to over 3. For the 1 minute reaction product N4, there was very little Fe^{3+}, so the iron oxide in this low relaxivity sample is an undefined iron oxide or oxyhydroxide. For stoichiometric magnetite the ratio of Fe^{2+} to Fe^{3+} is 0.5:1.0. For the other samples the ratios obtained were lower than, this indicates the presence of maghemite (γ-Fe_2O_3) and/or hematite (α-Fe_2O_3). The excess Fe^{3+} is expressed as mole of Fe_2O_3 per mole of magnetite (Fe_3O_4) in the fourth column. It is

found that all samples from the first series of preparations contain more Fe_2O_3. N7 indicates a good core with the largest fraction of magnetite. While the preparation N3 with finer particles (Z-average size 7.2 nm) has twice the amount of magnetite. All three samples from the repeat series of preparations have high magnetite content, they also show higher relaxivity.

5.4 Discussion:

5.4.1 The synthesis of non-aqueous magnetic fluids

The mechanism for the formation of magnetite is not well established but could be due to the high temperature decomposition of acetylacetonate followed by a partial reduction of Fe by alcohol in presence of acid. The reflux temperature was about 265°C.

The amount of 1,2 hexadecandiol was kept constant in all the preparations (10 mmol). It is evident from the data in Table 5.2 that the size of the nanoscale magnetite increases when the ratio of surfactant/Fe is different from 6. This is equivalent to 80 monolayers of surfactant molecules, assuming a 6 nm magnetite core with an average foot-print of oleic/oleyl amine of 32 A^2. In case of N7 and N11 the ratio is decreased by increasing the amount of Fe, which resulted in large monodisperse iron oxide particles. In the compositions N6, N10, N11a, N12 and N14, the surfactant to Fe ratio was changed by decreasing either surfactant or Fe, keeping the other components unchanged. This also increases the size of the nanoparticles but to a much smaller extent. Increasing the amount of Fe precursor (>2 mmol) results in larger magnetite crystals, probably because the growth phase can proceed for longer at higher concentrations (N7 and N11). When the ratio is changed by decreasing the iron concentration, there is no excess iron for the nuclei to grow (in N6, N12 and N14). In the event when the ratio is altered by decreasing surfactant as in N10 and N11a, the effect was not that pronounced as in N7 and N11. This may be because the other reactants were in stoichiometric quantities, or because in this range the surfactant concentration is not strongly limiting.

In the case of the repeat preparations, the Z-average sizes do not vary as strongly with the reaction conditions as was expected, but the results are remarkably reproducible, see

Figure 5.16. The only difference between the preparations is that the second series was completed with a fresh source of diphenyl ether.

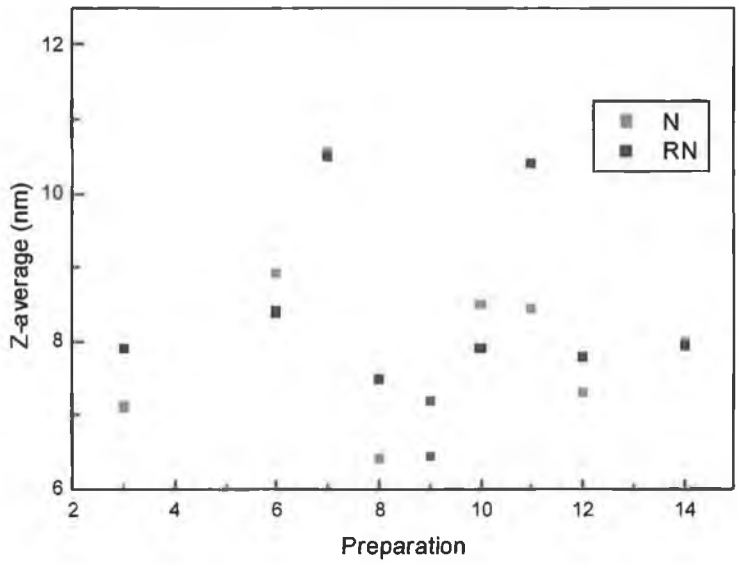

Figure 5.16. The reproducibility in average hydrodynamic size between the two series of preparations (■) first set N, and (■) second set RN.

The smallest nanocrystals were again produced in the RN9 composition with a surfactant:Fe ratio 6:1, refluxed in 40 ml phenyl ether instead of 20. The largest nanoparticles of size 10.8 nm with PDI 0.05 are produced in the RN11 preparation.

It is interesting to note that for the samples numbering 3, 8 and 9 with the reactants in exact molar ratio as used Sun and Zeng [24], the greatest change in Z-average size are observed. Also these suspensions contain the smallest nanoparticles, but the magnetic properties of these preparations are far from optimal. The best and most reproducible NMRD results were obtained for the larger particles, suspensions N11, RN11 and in particular N7, RN7.

5.4.2 NMRD characterisation of the non-aqueous magnetic fluids

Well-crystallised superparamagnetic particles of size above 10 nm are expected to produce relaxivities over 10 s^{-1} mM^{-1} as was seen in the case 11.44 nm particles in sample N7 (Figure 5.7). Very low relaxivities are indicative of low magnetic density in the crystal. The relaxivities of sample N4 were expected to be much higher as its average particles size is 27 nm. It is likely that there was not enough time for iron oxide from the high temperature decomposition of iron acetylacetonate to crystallise as N4 was prepared with a short (1 min reflux) reaction time.

The relaxivity profiles for the samples N3 and N6 are given in Figure 5.17 below, these are both the product of 15 min reflux time. N3 is synthesised by exactly following the method described by Sun *et al.* [24].

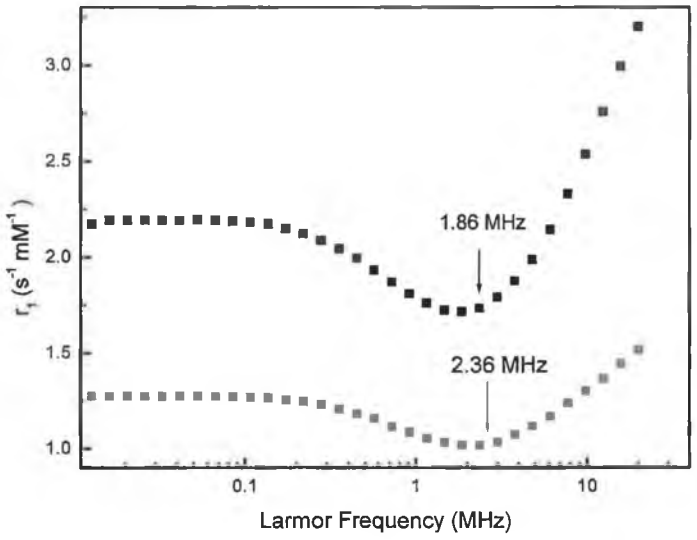

Figure 5.17. Relaxivity data for the non-aqueous prep samples N3 (■) Z-average size= 7.2 nm and N6 (■) Z-average size= 8.9 nm. The arrows in the figure are indicating the low field minimum for the superparamagnetic magnetite nanocrystals.

Suspension N6 was produced using a surfactant: Fe ratio of 30:1, by decreasing the amount of Fe precursor in the reaction mixture. The product has a slightly higher particle size of ~8.9 nm with an expected higher relaxivity. The frequency of the mid-field minimum for the two samples is also as expected. N6, a suspension with larger particles has this minimum at 1.86 MHz with respect to the same for the N3 at 2.36 MHz.

The relaxivity profile for suspension N7 is given in Figure 5.18. The relaxivity values for this suspension are much higher than for suspensions N3 and N6. This is understandable from the fact that the larger particles will have both a larger total magnetisation and higher anisotropy energy, resulting in higher relaxivity.

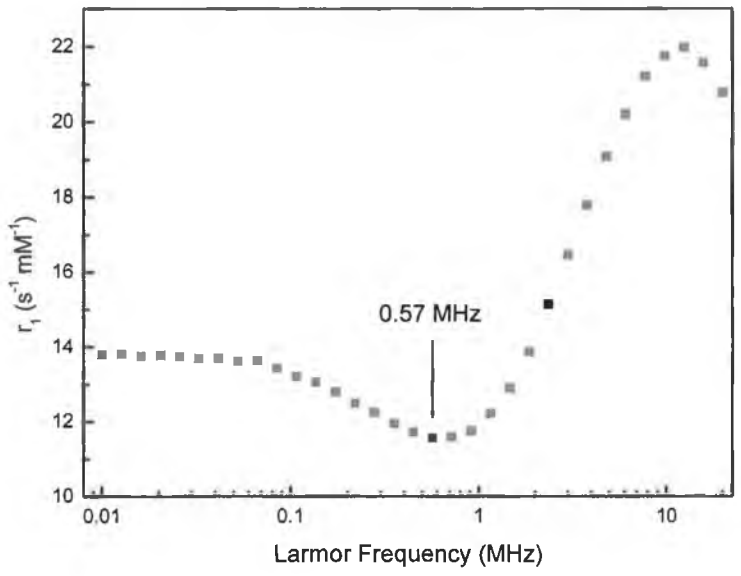

Figure 5.18. Relaxivity as a function of frequency for preparation N7. The mid-field minimum is indicated at 0.57 MHz, the PCS size is 11.4 nm.

The Z-average size for this suspension is 11.4 nm, so it is expected that the high field maximum falls into the measurable frequency range. The mid-field minimum is also at the lowest frequency among the entire first set of preparations.

It is observed that we were not able to produce smaller magnetite crystals by changing the surf/Fe precursor ratio. Smaller nanoparticles could only be produced by maintaining a standard ratio (Fe:surfactant:1,2-hexadecanediol = 2:12:10) of all reactants and diluting them by adding more diphenyl ether. N8 and N9 are the result of such an attempt, which resulted in a hydrodynamic diameter of ~6.4 nm (Table 5.2), while the relaxivity of preparation N9 was slightly lower, indicating a less magnetic core in this sample (Figure 5.19). The relaxivity profiles of sample N8 and N9 are given Figure 5.19 below, both suspensions are of very fine particles. Their PCS diameter is close to 6.4 nm with low PDI of 0.072 and 0.1 respectively. Both the samples had their mid field minimum at 3.8 MHz which is the highest field among NMRD of all the samples reported here.

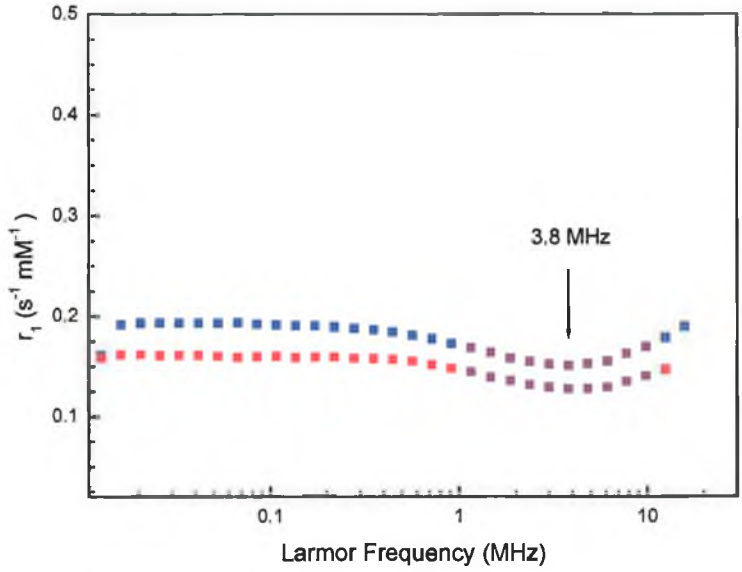

Figure 5.19. Relaxivity as a function of Larmor frequency for the samples N8 (■), and N9 (■). The mid-field minimum for both suspensions occurs at 3.8 MHz.

The NMRD profiles of N10 and N11 are presented in Figure 5.20. Preparation N11 is the second suspension for which the high field maximum was in the measurement range because of its relatively large size (10.8 nm). The mid-field minimum is also at a very low field (0.72 MHz) next to 0.57 MHz for N7. The relaxivity of the preparation N10 is lower than that of N11.

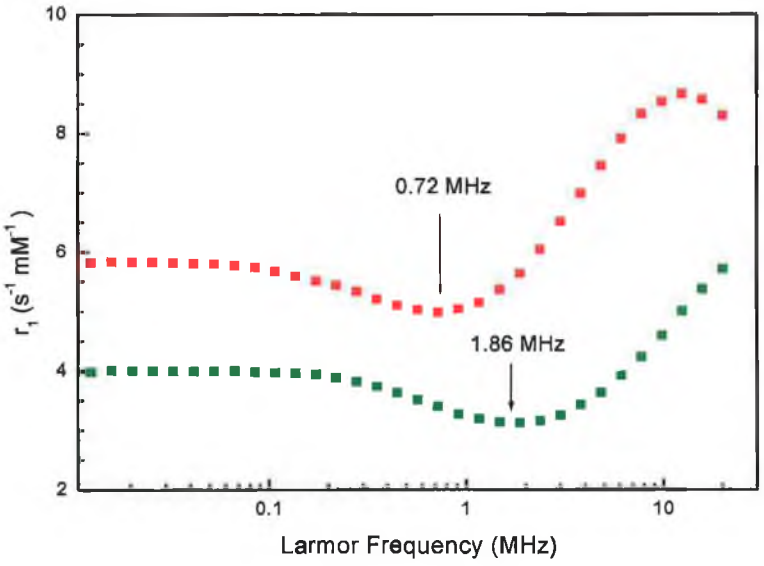

Figure 5.20. The relaxivity as a function of Larmor frequency for the sample N10 (■), and N11 (■).

Suspensions N11 and N11a (Table 5.2 and 5.3) have the same surf/Fe ratio, but N11 were produced by increasing the amount of iron precursor above 2 mmol whereas in case

of N11a the ratio was arrived at by reducing the amount of surfactant. N11a has produced in smaller nanoparticles (8.4 nm) than the N11 prep with much lower relaxivities. N11 samples had an average PCS size of 10.8 nm. RN11a is the repeat prep of N11a and the PCS size for RN11a is 8.35 with PDI=0.11 is a very close match to the corresponding size of N11a (Z-average 8.4 nm with PDI=0.04). The relaxivity data is also almost superimposable over in the full range.

All the suspensions have an expected correlation between their size and relaxivity as evident from the Figure 5.7 and 5.8. Preparation RN9 has a relaxivity of 1.1 $mM^{-1}s^{-1}$ at the plateau and its PCS diameter is 7.1 nm. Preparation N3 has a similar hydrodynamic size of about 7.2 nm and the corresponding relaxivity at the low field plateau was 1.27 $mM^{-1}s^{-1}$ which are in good agreement.

5.4.3 Consistency of the NMRD results with SPM theory

A satisfactory theory for water relaxation due to its interaction with superparamagnetic nanoparticles in known, SPM theory [152]. The NMRD profiles shown in this chapter for heptane suspensions of magnetite are consistent with the predictions of this theory. The theory was presented in detail in the introduction to this thesis. The principal observation in that for fine nanoparticles it is anticipated that the high field maximum and the mid-field minimum in the NMRD profiles move to higher frequency as the diameter of the primary iron oxide core increases. In fact the theory predicts a near exponential relationship between the crystal diameter and the frequency of the high field maximum as shown in the Figure 5.21, assuming all the other adjustable parameters are constant. As the particle sizes of our preparations were mostly below 11 nm, the high field maxima usually fell above the measurable range (>20 MHz). This makes the fitting procedure more difficult, although particle sizes from PCS could be used as a guide in many cases.

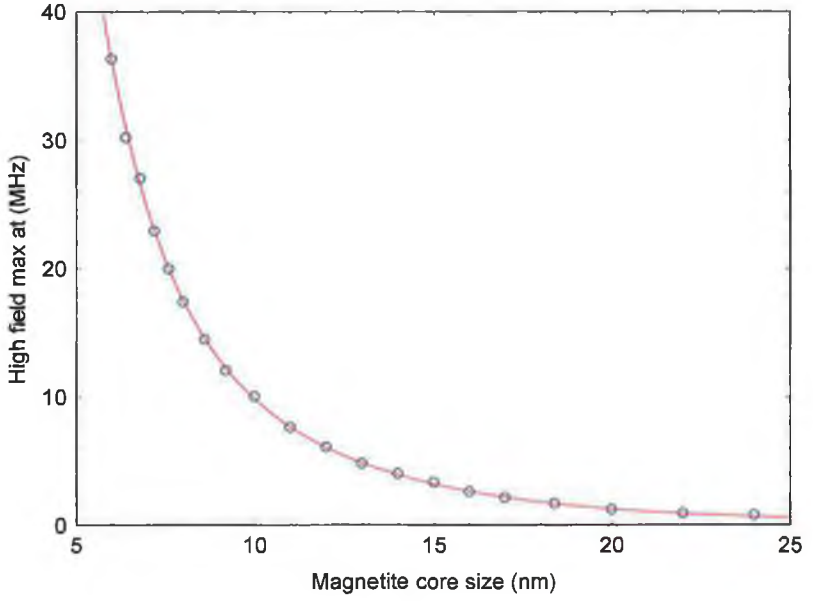

Figure 5.21. The high field maximum as a function of the size of magnetite nanoparticles simulated using the standard theory, (○) [192]. The solid line is a biexponential fit to the data, included as a guide to the eye.

A similar exponential relationship can be found from simulations of the mid-field minimum as a function of magnetite core size. The presence of this minimum is associated with the high magnetocrystalline anisotropy of the magnetic nanoparticles. A plot of the observed frequency of the mid-field minimum as a function of the hydrodynamic size for the first series of preparations is shown in Figure 5.22, again it shows the expected trend.

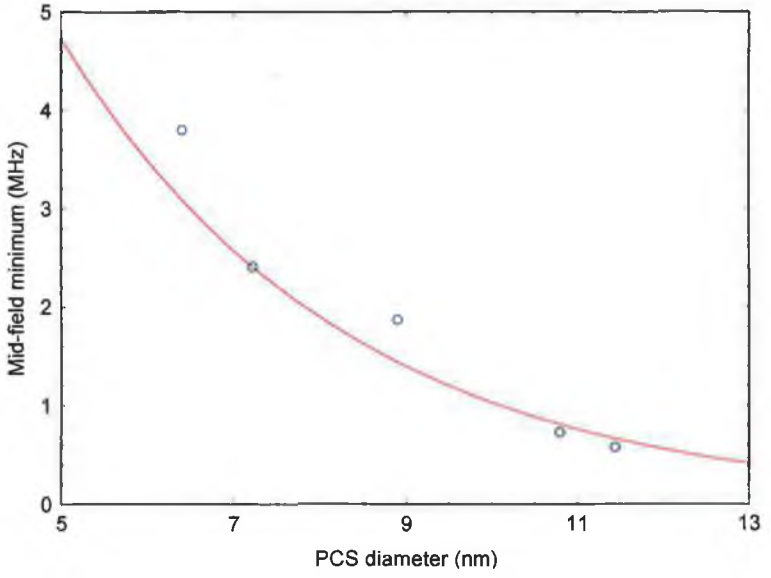

Figure 5.22. The relationship between the mid field minimum and the observed hydrodynamic size (○) as measured by PCS. The solid line illustrates the simulated behaviour using the standard theory, [152] as in the previous figure.

The mid field minimum occurred between 0.5 to 4 MHz in all cases.

The relaxivity values at 0.01 MHz for the suspensions produced from 15 minute refluxes; N3, N6, N7 and N8 (15 min reaction) are shown, plotted against magnetic particles sizes (Z-average), in Figure 5.23 below. When the hydrodynamic size was less than about 7 nm, which corresponds to a core of about 5 nm, the low field relaxivity of the magnetic colloids were found to decrease sharply.

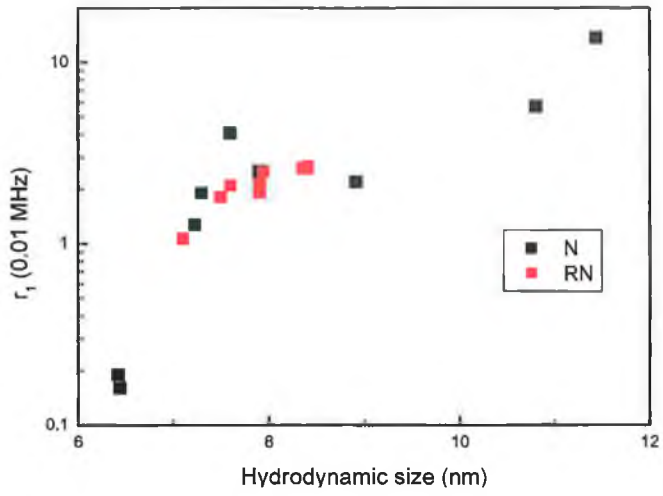

Figure 5.23. The relaxivity, at 0.01MHz, of the magnetic fluids as a function of hydrodynamic size. The (■) data mark indicates the first series of preparations, (■) indicates the second series.

5.4.4 Interpretation of the NMRD results with SPM theory

Using the published theory [152] it is possible to fit the NMRD profiles obtained for the heptane suspensions. Superparamagnetic relaxation theory is described in detail in the introduction to this thesis. One of the major problems with the theory is the number of parameters that are involved. Some of the parameters; the temperature, concentration and D_{eff}, the diffusion coefficient of the solvent, are independent of the nature the nanoparticles. The others relate directly to the core, they are; the size of the (spherical) magnetic core, the magnetisation at saturation, M_s, the Néel correlation time, τ_N, and anisotropy energy ΔE_{anis}. The anisotropy energy is often expressed as an anisotropy frequency, and is of the order of GHz. The Néel correlation time, τ_N, is of the order of ns. ΔE_{anis} and τ_N characterise the motion of the moment of the nanoparticle are usually assumed to have an Arrhenius relationship. They have a moderate effect on the high field

relaxation (ν_L > 1MHz), but affect the appearance of the profile at lower field. These two parameters are correlated and their effect on the NMRD response is subtle; thus it is difficult to obtain them quantitatively from the analysis of NMRD data. On the other hand the profiles are very sensitive to the particle size and to the saturation magnetisation, and so these parameters can be obtained with a higher degree of confidence.

In Figure 5.24 below, the fits to five of the higher relaxivity samples are shown, the quality of the fit becomes poorer as the relaxivity decreases. In all cases the fit was obtained by fixing the particle radius using the PCS Z-average, with a 1.8 nm correction for the oleate coating [204], which is assumed to be a monolayer. The temperature was 297 K and the diffusion coefficient of heptane was taken as $D_{eff} = 7.8\times10^{-5}$ cm^2s^{-1} [209].

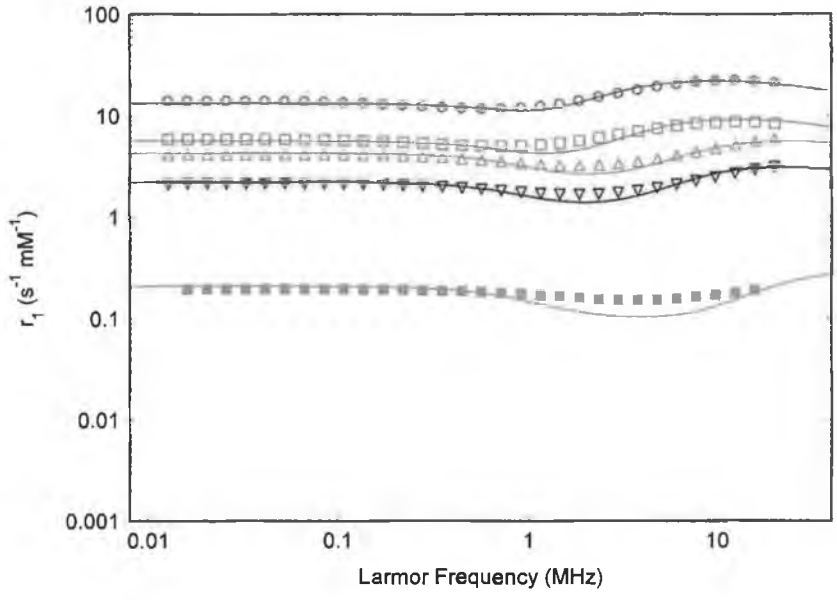

Figure 5.24. The fitted profiles for selected preparations. The samples shown are N7 (○), N11 (□), N10 (Δ), N6 (∇) and N3 (■).

The fitting parameters are summarised in Table 5.6, also included in the table is an estimate of the number of magnetite stoichiometric units that would be expected to be contained in a spherical core of the given radius, assuming the density of the cores is equal to that of bulk Fe_3O_4 = 5.18 gcm^{-3}.

Table 5.6. The summary fitting parameter for selected suspensions.

Preparation	Z-Ave, nm	Crystal radius, nm	M_s, emu/g	τ_N, ns	ν_{anis}, GHz	No. of Fe_3O_4 units
N7	11.4	4.80	66.0	10	1.0	780
N11	10.8	4.50	47.0	10	1.8	643
N6	8.9	3.55	37.5	5	4.0	316
N10	7.6	2.90	61.5	2	2.5	172
N3	7.23	2.72	38.5	3.5	8.0	142

The values of M_s obtained, are in agreement with those expected for magnetite nanoparticles of this size [29, 38]. The observed size dependence of M_s was explained as arising due to the increase in the specific surface area and/or to the presence of a surface passivated layer. The speciation results presented for our samples demonstrate that the saturation magnetisation decreases weakly as the fraction of magnetite decreases. While our observations that the particle size from the NMRD analysis matches with both the hydrodynamic size, and with the core size obtained from TEM, suggests that if there is a passive layer, it is very narrow. In Figure 5.25 below the data obtained from the NMRD analysis are overlayed with the data from the published studies.

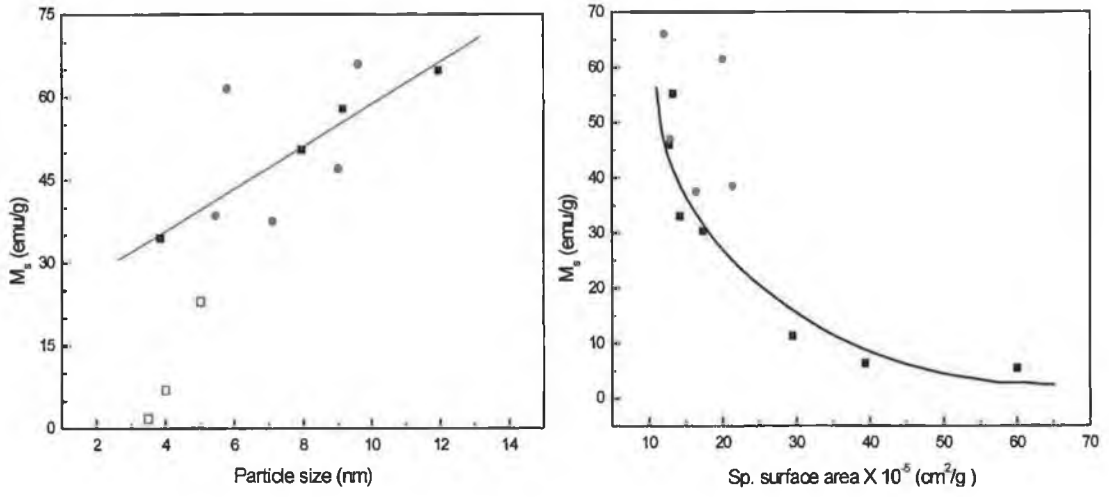

Figure 5.25. The agreement between the data from the NMRD analysis (●) and the published dependence of the saturation magnetisation on the particle size (left hand side) [38], and on the specific surface area (right hand side)[29].

The fact that the agreement is good strongly supports the validity of interpreting the other parameters obtained form the fits to the NMRD data. Perhaps the most startling

observation from Table 5.6 is that the anisotropy frequency is larger for the smaller cores. This is not surprising given the relatively large number of stoichiometric units involved in particles of this size. An increase in the anisotropy frequency is consistent with a less spherical particle, as distortions in shape will increase the barrier to the reorientation of the particle moment. We propose that this is the best interpretation of the data. Unfortunately it is not possible to access shape information from HR-TEM for particles of such small size, while light scattering techniques can only provide effective sizes once the shape is known.

5.5 Conclusions

Analysis of the particle size results shown in Table 5.2 and of the relaxivity data for all the nanoparticles reported above clearly shows a trend. All the 1 minute reflux time syntheses produced very low relaxivity samples. In this case there was not enough time for magnetite to crystallise into a crystalline core with reproducible magnetisation. Further investigation would require investigation into the reaction kinetics and the mineralogical characterisation of the product. It appears likely that the iron phase present is undefined iron oxide or hydroxide and that the resulting nanoparticles can be stimulated by the application of ultrasound to form loosely aggregated clusters that slowly break up on removing the stimulus.

The use of smaller or greater amount of Fe source than that used by Sun and Zeng [24] in this reflux method did not result in finer particles. It is also interesting to note that all preparations with 2 mmol of iron in the reaction mixture have produced 6 to 7 nm particles. A reaction time of 15 min produced very distinct dispersions in the NMRD profiles and relatively higher relaxivities, while the high field maxima in the NMRD profiles were not observable, they are expected to occur outside the measurable range.

The NMRD profiles of the suspensions conform to superparamagnetic relaxation theory, confirming the heptane tumbles isotropically in the vicinity of the suspended particles. The anisotropy energy increases significantly for the smaller particles, suggesting that they are less spherical. The magnetite nanoparticles prepared from the two series of preparations have slightly different crystal sizes, and show variation in saturation

magnetisation and relaxivity despite efforts to produce them under identical conditions. For suspension, N8, with very fine particles, it has been shown that the phase present is hematite. This probably arises because of its very small size and hence the very high surface energy. It is also interesting to note that the fraction of magnetite decreased as the crystal size decreased.

Chapter 6

The adsorption of coated magnetite nanoparticles on silica

6.1 Introduction

The process of adsorption involves separation of an atom, molecule, or particle from one phase accompanied by its accumulation or concentration on the surface of a second phase. Physical adsorption is caused mainly by van der Waals and electrostatic forces between adsorbate molecules and the atoms on the adsorbent surface. Thus adsorbents are characterised by surface properties such as surface area and polarity. A large specific surface area is preferable for providing adsorption capacity. Porous silica comes under the category of non polar adsorbents. These adsorbents have more affinity with oil or hydrocarbons than water. In this chapter an investigation into the interaction of a non-aqueous magnetite suspension with macroporous silica is described. Several types of silica sufaces were investigated including silica-C18 an octadecyl carbon loaded material, silica-CN a negatively charged cyanated silica, and an untreated silica. It was anticipated that there might be a tendency for the nanoparticles to physisorb on the silica-C18 surface. While any nanoparticles in excess of the surface capacity should remain in stable suspension.

Nanocrystalline magnetite particles stabilised by a monolayer coating of oleic acid form a very stable suspension in non-polar solvents like heptane. The carboxylic head group is chemisorbed on the magnetite surface. The hydrophobic fatty chain extending from the magnetite surface is solvated by the nonpolar hydrocarbon solvent [60]. The suspensions prepared here using a method by Sun *et al.* [24] are found to be stable for over one year. There are many theories describing the mechanisms of stability of fatty acid coated magnetite in carrier liquids. In polar media the colloidal interaction is well described by the Derjaguin-Landau-Verwey-Overbeek (DLVO) theory, which is a combination of the van der Waals type of attractive forces among the particles and the electrostatic repulsive forces due to the ionic cloud surrounding the particle [210]. However, monolayer surfactant coated magnetite nanoparticles are stabilised in non-polar solvents by steric or entropic stabilisation.

6.2 Experimental

6.2.1 Materials

The substrate used in most of the experiments, silica-C18, was silica with 60Å pores, 50μm average particle size, and endcapping coated withC18 (Octadecyl, 6% carbon load) from Alltech Associates, Deerfield, IL. Silica-CN a negatively charged cyanated silica, and an untreated silica of the same dimensions from the same source were also used.

The magnetite nanoparticles were synthesised by coprecipitation of mixed Fe^{3+}/Fe^{2+} salts with ammonium hydroxide. A monolayer of surfactant coating was applied by adding excess oleic acid during the iron oxide precipitation. The magnetite dispersion was precipitated with acetone and methanol and washed five times with acetone and lastly with ethanol. The precipitate was then phase transferred into heptane. The heptane suspension was centrifuged at 13000 rpm (~16000g rcf) for 40 min to remove any aggregated particles. Suspension H5a had a Z-average of 12.0 nm with a low PDI (0.09) and H5b had a Z-average size 11.8 nm Z-average and was also monodisperse PDI (0.07).

The relaxivity data for the two magnetite suspensions in heptane used in the adsorption study are given in Figure 6.1 below. The simulated profiles for the magnetite cores for fitting the data are also added in the figure. The simulated relaxivity profile for 9 nm magnetite cores using Muller's model [152] is also added to the same figure for comparison. The simulated profile for a 10 nm magnetite particle is almost overlaps with the NMRD profile of the 11.8 nm SPM (H5b). The high field maximum for the suspension at 14 MHz just overlaps with the simulated profile but the fit is poorer in the

Table 6.1. The fitting parameters used for the two sample suspensions used in the adsorption

Sample	Z-average (nm)	Crystal radius (nm)	M_{sat}	τ_N (ns)
H5a	11.8	4.50	27	7
H5b	12.0	4.90	40	8

mid field region (0.8-5 MHz). The temperature used in the fit is 298K and the anisotropy energy ν_{anis} is kept constant at 1 GHz in both the fits. The other fitting parameters are given in Table 6.1.

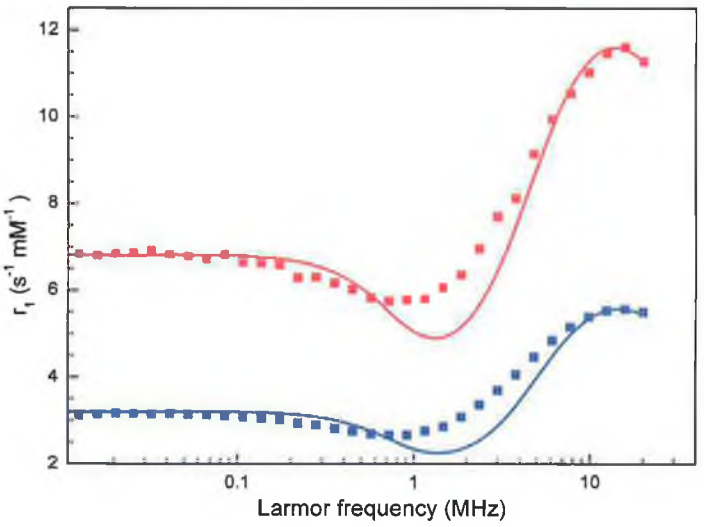

Figure 6.1. The relaxivity profiles for the two magnetite suspensions (■) H5a and (■) H5b used for adsorption experiment. The layers with solid line are the simulated curves using Muller's theory with different parameters given in Table 6.1.

The two suspensions have different magnetic core sizes of 9 and 9.8 nm, PCS diameter of about 12 nm. This indicates the monolayer oleic acid coating has a thickness slightly more than 0.9 nm, in agreement with other authors [204]. There is clearly some difference in the magnetisation of the cores, but given the variation in the NMRD profiles described in the last chapter, there is little real difference between these two samples.

6.2.2 PCS experiment

A calculated and predetermined quantity of magnetite suspension in heptane was placed over a silica substrate in the quartz cuvette for PCS analysis. The cuvette was placed in the PCS spectrometer with care to avoid any agitation. The temperature of the cuvettes was maintained at 25°C. The quantity of silica was restricted so that the incident laser light is not occluded. In effect this limited the height of the silica to <1 mm, which is equivalent to 50 mg of silica.

In a first series of experiments a quantity of magnetic fluid sufficient to cover the entire silica surface with a monolayer of nanoparticles was placed over silica-C18 powder in a

quartz cuvette. In a second series of experiments sufficient magnetite suspension was provided to produce a bilayer. The magnetite content was about 1.47 mM for sample H5a and about 1.52 mM for sample H5b. The following assumptions were made in calculating the quantities required:

1. There is no adsorption of nanoparticles into the pores on the silica-C18 surface.
2. The silica-C18 particles are spherical with diameter of 50 μm.
3. The adsorbed nanoparticles form a sheet of hexagonal closed packed spheres on the silica-C18 surface to form a uniform monolayer, and
4. A bilayer is composed of two identical monolayers.

The onset of growth/aggregation of magnetite nanoparticles in suspension was monitored by PCS spectroscopy at an interval of 30 min for 1-7 days (as long as there were particles in suspension). The standard operating procedure (SOP) used for the PCS measurements was for 200 measurements with a suitable delay such that successive measurements are separated by 30 min. Each measurement takes about 5 min which, consists of 20 runs of 10 sec each. For most experiments the cuvette position and the attenuation index remain constant throughout one experiment as all the data collected was with one SOP (standard operating procedure). Therefore the backscattered light intensity is representative of the volume weighted number of scatterers.

The change in absorbance, at a wavelength of 475 nm, of an identically prepared suspension over silica-C18 was monitored using UV visible spectrometer. The experiment was carried out with suspension H5a under identical conditions as described for mono/bilayer experiment by PCS above. For all experiments a sufficient volume of magnetite suspension was placed over 50 mg silica-C18 substrate to form a mono or bilayer, while keeping the iron concentration at 1.5mM. For the ME experiments this ws achieved by diluting 150μl of suspension with 750 μl heptane. For the BE experiments this was achieved by diluting 300μl of suspension with 1500μl heptane The absorbance of light through the magnetite suspension was recorded every 30 minutes for 2 days.

6.3 Results

It was immediately apparent that the nanoparticles were adsorbing onto the silica. Irrespective of the concentration, the suspension lost colour over a period of hours, while the white silica-C18 powder turned a chocolate brown.

6.3.1 Monolayer equivalent adsorption

6.3.1.1 Suspension H5a

In the first set of experiments one monolayer equivalent (ME) of magnetite suspension (H5a) was placed over silica-C18 and the Z-average particle size monitored over time, the data is presented in Figure 6.2 below. The observed increase in size as a function of time shown in Figure 6.2 is converted into change in spherical volume, and is shown as an insert in the figure. The growth of the clusters followed linear progress until about 2 h in run 1 (Figure 6.2), or until about 4 h in run 2 (Figure 6.3).

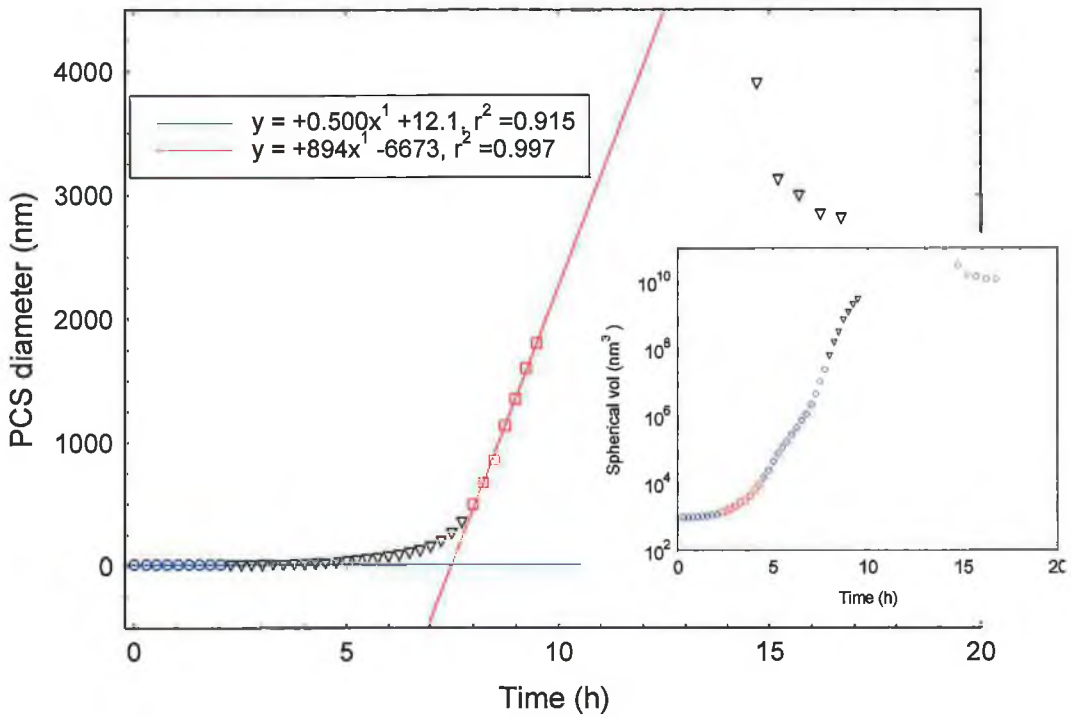

Figure 6.2. PCS data for ME addition of magnetite suspension H5a over silica-C18 showing the increase in Z-average of suspension with time in run 1. The PCS diameter in the Y-axis is converted to the volume and shown as the inset.

The initial linear growth phases in both the runs was followed by a rapid increase and a second linear growth phase, in which rate of growth is almost twice as fast as in case of

the first run. The smallest changes in the Z-average size of the particles are magnified in the volume curve, as volume is proportional to the cube of the radius.

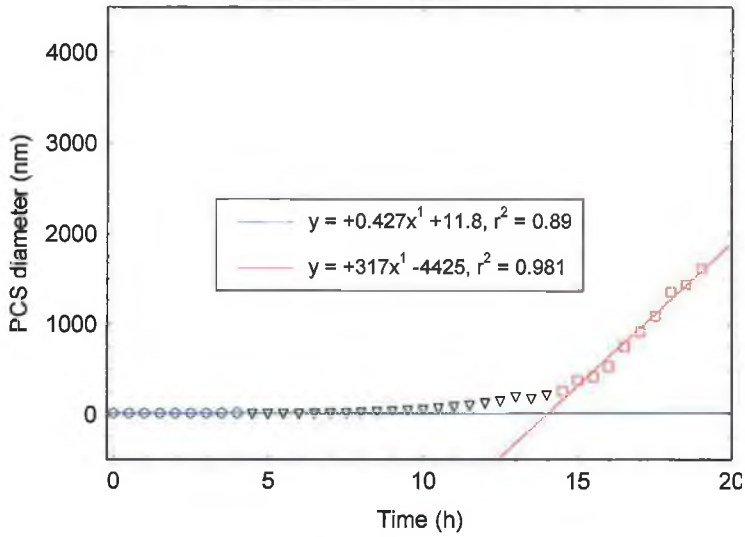

Figure 6.3. PCS data for ME addition of magnetite suspension H5a over silica-C18 substrate in run 2.

The change in polydispersity index and mean count rate data for run 1 and 2 is presented in Figure 6.4 below. The breaks in the data for the first run arose due to protocols on the acquisition PC interrupting the data storage. The polydispersity of the particles grew to a maximum (1.00) in about 7 h during the first run where as the PDI did not exceed ~0.6 during the second run over the course of about 15 h.

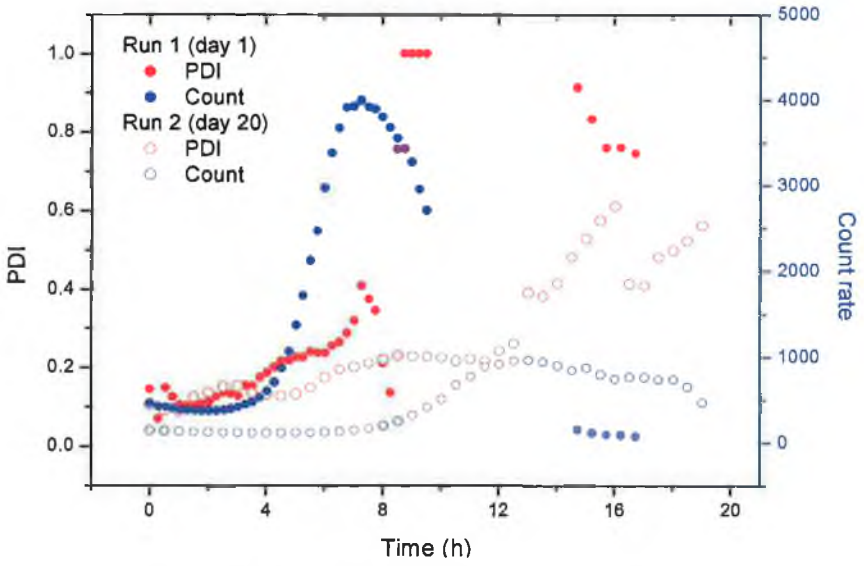

Figure 6.4. The change of polydispersity index and the mean count rates for ME addition of magnetite suspension H5a over silica-C18 (run 1 and 2).

The mean count rates also increased drastically to 4000 kcps in just 7 h in case of the first run. The two runs were performed under identical conditions, as far as possible, using the same magnetite suspension, but 19 days apart. This suggests a change in the properties of the magnetite suspension over time.

The change in light absorbance of a ME magnetite suspension over silica-C18 was monitored over time, the data is presented in Figure 6.5. The absorbance of light was recorded every 30 minute for 2 days, under conditions where the particles grew, when monitored by PCS. The changes in absorbance are synchronised with the growth pattern. There is very little change up to about 7-8 h followed by a sharp fall in absorbance. The rate of change slowed significantly after about 15h and there was very little change in absorbance after 20 h.

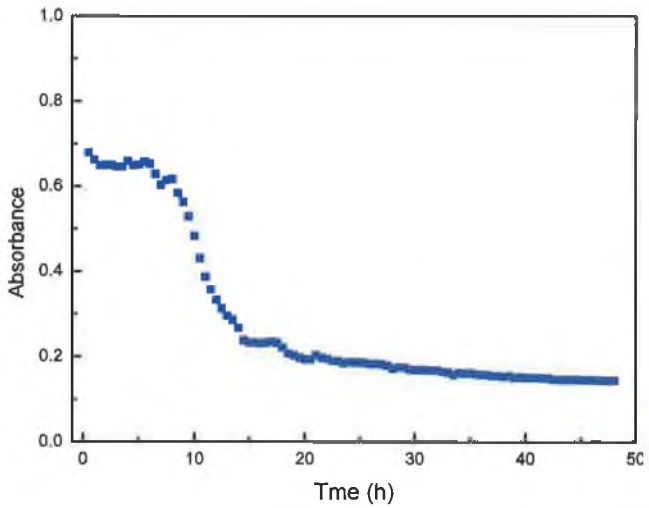

Figure. 6.5. UV absorbance at 475nm over time for a ME experiment with H5a suspension over silica-C18.

6.3.1.2 Suspension H5b

The ME experiment was also performed with an independently synthesised suspension, H5b, of slightly different particle size (12.0 nm) and relaxivity as shown in Figure 1. This experiment was repeated four times, the change in PCS size with time is given in Figure 6.6.

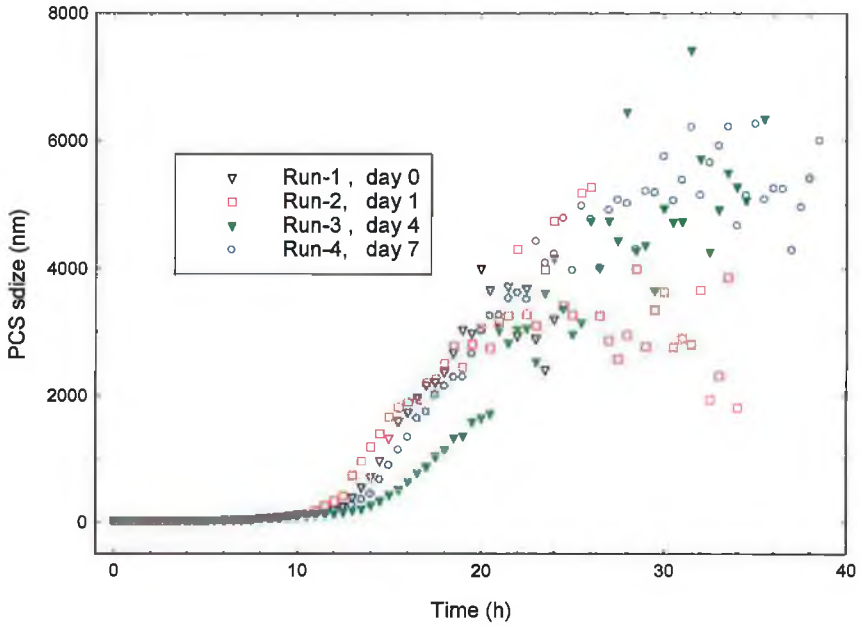

Figure 6.6. Z-average size of H5b of slightly different size (11.8 nm) for ME addition experiment during four consecutive runs

The change in mean counts for all the ME adsorption runs with suspension H5b are given in Figure 6.7. The growth profiles of the particles are very similar for all four repeat experiments performed within 10 days from the date of synthesis of the magnetite suspension (Figure 6.6). The pattern of change in PDI and counts (Figure 6.7, 6.8) is very similar to that observed for suspension H5a. The mean count rate in all the experiments increased steadily until ~12 h, and then decreased to almost the starting value over another 12 h. The variation in the value of the counts between runs is quite significant. However as the scattering intensity is weighted by volume a small change in the number of particles at the upper end of the size distribution, at any given time, will significantly affect the scattering intensity but not the z-average or PDI to as great an extent. The observation of a maximum is consistent with ongoing cluster growth and, as the experiment progresses, with the presence of fewer clusters. This is also apparent from the increase in the scatter of the particle size data after about 20 h.

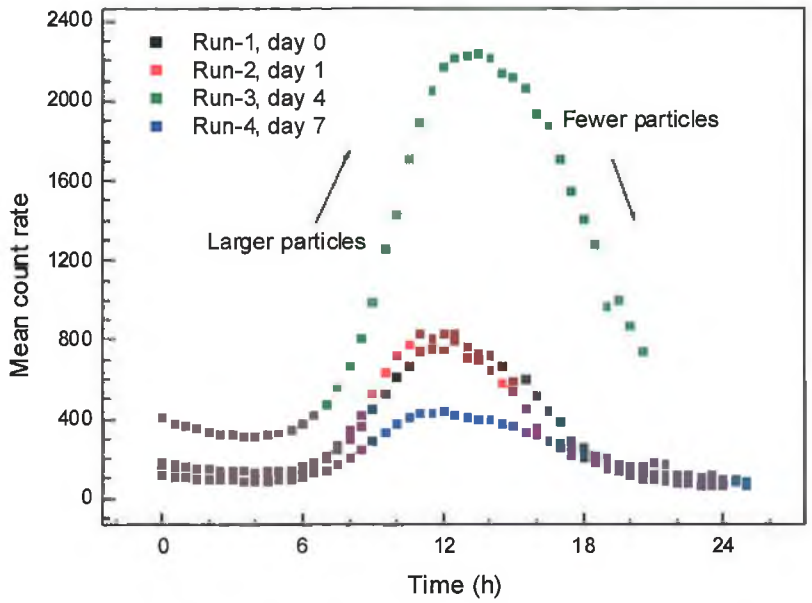

Figure 6.7. The change in the mean count rate with time for 1 monolayer addition of magnetite suspension (H5b) over silica-C18.

The change in polydispersity index with time for is presented in Figure 6.8. As the experiment progressed the PDI increased and the particle size distibution became wider. The mean count rate and the polydispersity index (PDI) show an interesting trend at 12-13 h from the start, when the backscattered intensity is at a maximum. Around this time, an increase in PDI was seen in every experiment in the form of a spike.

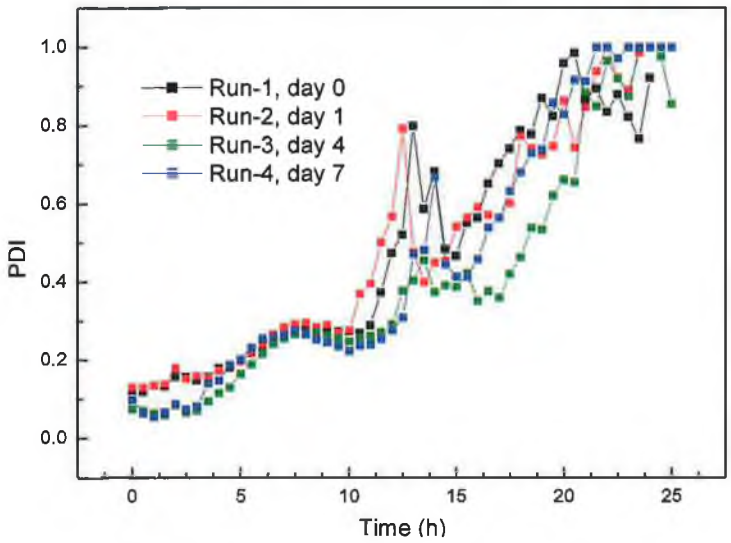

Figure 6.8. The change in PDI with time for ME addition of magnetite suspension (H5b) over silica-C18.

The correlation functions for three selected times are shown in Figure 6.9 below. The quality of data fit is poorer for the later measurements. The PDI is high at ~12 h, but

there is still a good fit to the data, hence the Z-average is a realistic average of the experimental distribution. The counts are highest in this region. But after about 24 h the counts decrease to a small number. The fit in blue is only partly through the data points after 48 h, hence the polydispersity index is 1.00, and the Z-average is a less reliable measure. The PCS software for all the ME experiments crashed, due to low scattering intensity, after 25-35 h.

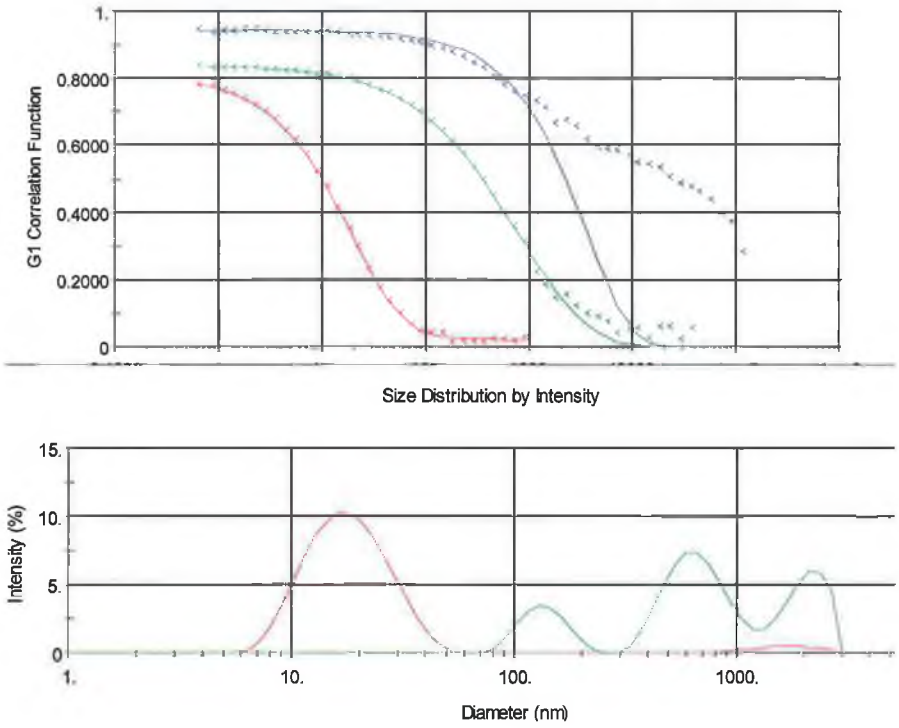

Figure 6.9. The PCS correlation data fits and the intensity size distribution for sample H5b in ME experiment over silica-C18 after 5h (—), 13 h (—) and at the end of the experiment 48 h (—). The intensity distribution for the 48 h (—) data is zero in the range shown; larger particles only present.

6.3.2 Bilayer equivalent adsorption

The PCS data obtained for a bilayer equivalent (BE) adsorption of magnetite suspension H5a onto silica-C18, during run 1 and run 2 are presented in Figure 6.10. The Z-average and PDI showed very similar behaviour to the ME experiments. There was a short linear growth phase up to about 4-6 h for both the runs, which were carried out with a gap of 16 days using the same nanoparticle suspension. In contrast to the ME experiments, the BE suspensions follow two linear rapid growth phases. The first begins after ~ 15 h and continues until 35 h in run 1 and up to ~ 40 h in case of run 2. As was seen in the ME

experiments, the rate of growth is much faster in fresh samples. The second linear growth phase showed almost identical growth rates, for both runs, of ~0.25 nm/h.

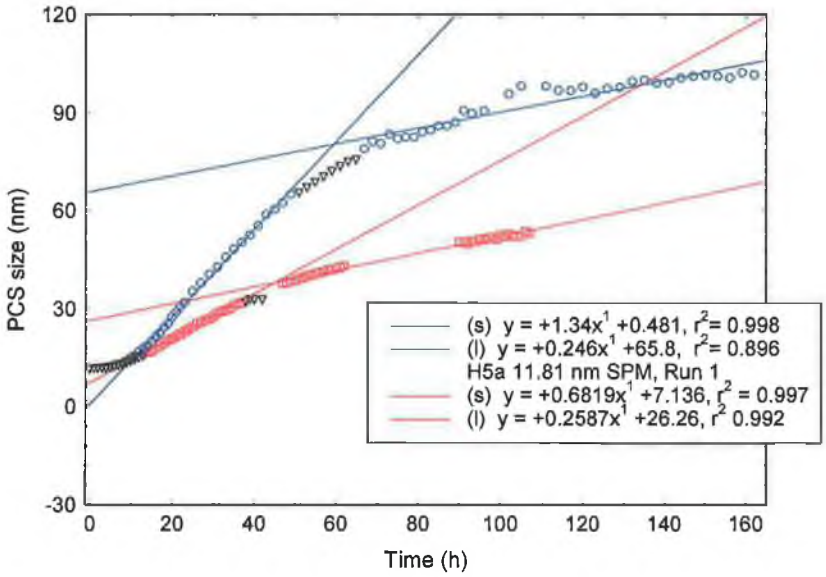

Figure 6.10. PCS data for suspension H5a for BE addition over silica-C18 showing the increase in Z-average of suspension with time for run 1 (—), and for run 2 (—). The parameters for the linear fits to the short (s) and long (l) time data are included for each run.

It is interesting to note that in the ME experiment the PCS size increased over 1500 nm in all cases, whereas in case of the BE experiments the growth was limited to about 100 nm. This phase was followed after 50-60 h by a phase with very slow growth. There are breaks in the data in Figure 6.10, run 2 where the PCS spectrometer was being used for other experiments. The cuvette was carefully removed and kept in a constant temperature bath at 25°C during these periods. On restarting the experiment the position of the cuvette and laser attenuation were automatically adjusted, so there are discontinuities in the counts in Figure 6.11. The fact that the growth of the clusters still lies along the same straight line after the interruption is interesting, it demonstrates that moving the cuvette did not upset the experiment and that the laser light in the PCS experiment does not have any effect on the nanocluster growth.

The change in PDI and count rate in the BE adsorption experiment in sample H5a are shown in Figure 6.11. As was observed for the ME experiment (Figure 6.4) the mean count rate increased continuously for the first 20-40 h to about 500 kcps and then decreased for both runs.

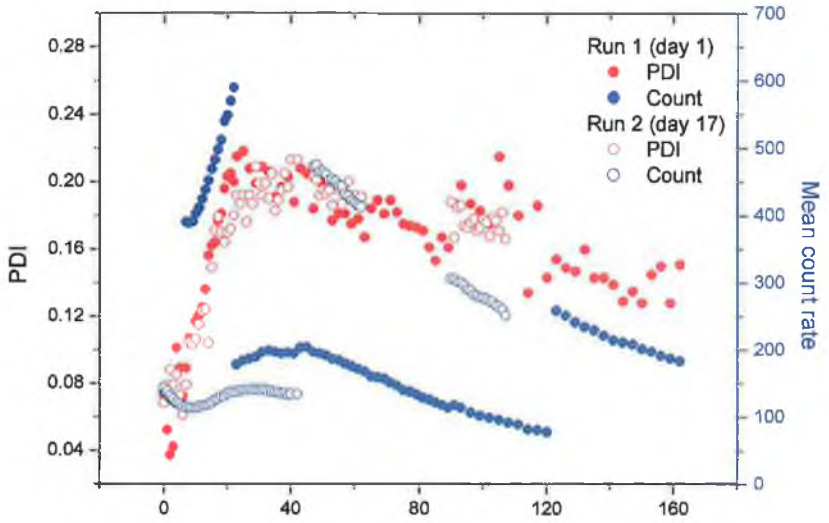

Figure 6.11. The polydispersity index (PDI) and mean count rate in BE experiment with H5a.

The fit to the time correlation data and the resulting size intensity distributions for the BE experiment, with sample H5a, at three selected times is given in Figure 6.12 below. The fits for the BE experiments are of better quality, with lower PDI values, than the ME experiments, in all cases the cumulants fit passes through the data. The cluster size distributions are not as broad during the BE experiments.

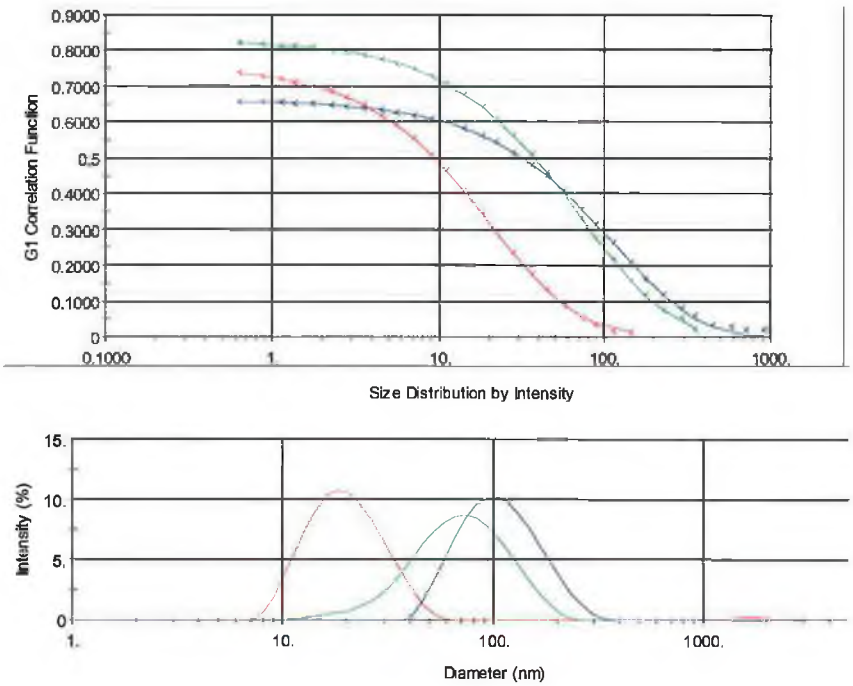

Figure 6.12. The PCS data fit and intensity size distribution for suspension H5a over porous silica-C18 substrate from the first run of the BE experiment, after 14 h (—), 44 h (—) and 120 h (—).

The data for the growth of the clusters from different preparations in the BE experiment is presented in Figure 6.13. In general the hydrodynamic diameter (PCS size) increases up to about 50 h, after which there is some reduction in the growth rate. The trend of an increase in count rate time up to about 40 h, followed by a decrease was again observed. The counts were found to increase till about 40 h in all the runs in BE addition.

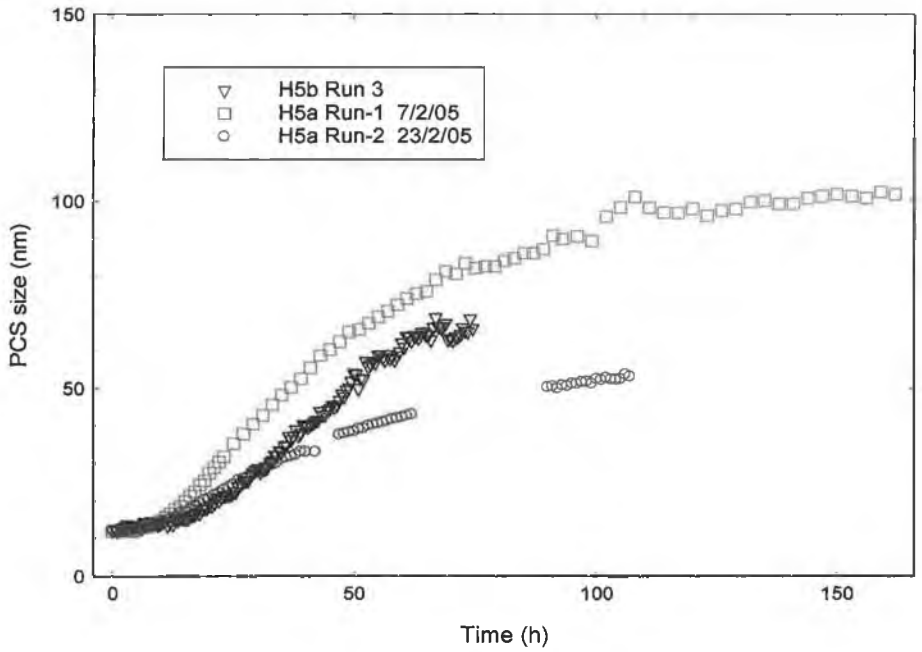

Figure 6.13. Z-average data with time for three runs for the BE experiment. (□) H5a run 1, (○) H5a run 2 and (∇) H5b run 3.

The change in light absorbance of a BE magnetite suspension over silica-C18 was monitored over time, the data is presented in Figure 6.15. As the experiment proceeded over 120 h the absorbance decreased, in addition, the rate of decrease gradually diminishes. There are no discontinuities in the curve.

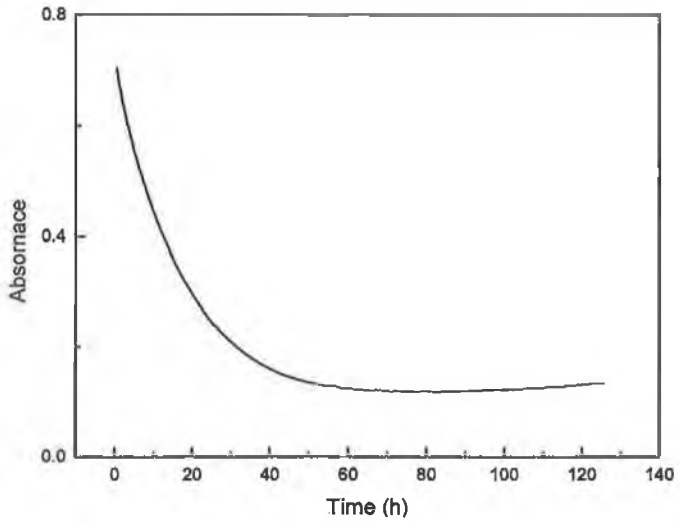

Figure 6.14. UV absorbance at 475 nm over time for a BE experiment with H5b suspension over silica-C18.

6.3.3 Further experiments

An experiment was performed where a sample of oleic acid coated nanoparticles in heptane, was placed over untreated silica, instead of silica-C18. It was found that there is no clustering or adsorption in this case.

An experiment was performed where a sample of oleic acid coated nanoparticles in heptane, was placed over anionic silica-CN, instead of silica-C18. It was found that there is rapid cluster growth into the μm range within 3 hours, see Figure 6.15. The PCS software crashed after 4 h, due to low scattering intensity. The later time points were run the next day after re-optimising the PCS spectrometer.

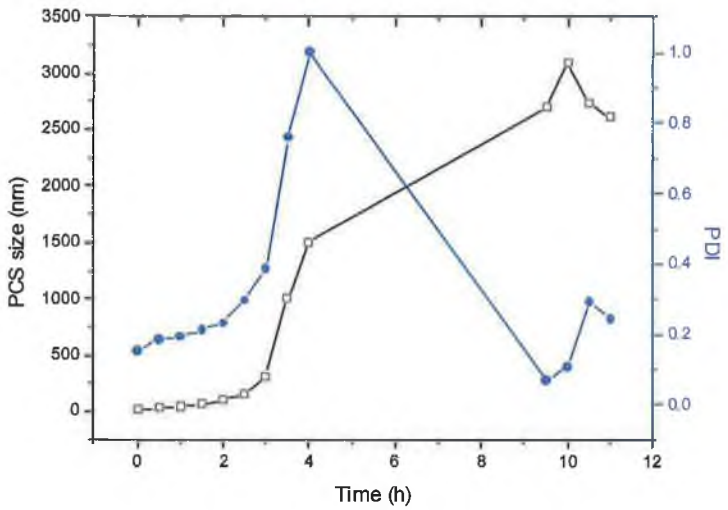

Figure 6.15. PCS data for ME adsorption of magnetite suspension onto silica-CN substrate. The Z-average size is indicated with a (□), the PDI with (●).

A blank experiment was run using same quantity of silica-C18 substrate (50 mg) with pure heptane placed over it. PCS measurements were performed on the suspension after shaking it. The PCS data initially indicated particles of 82 μm size. This is due to the silica settling to the bottom of the cuvette. At no point over the following days were particles detectable. A cuvette was prepared containing 5 mM oleic acid in heptane over same quantity of silica-C18. This suspension also produced no suspended particles over two days, the PCS measurement crashed on each occasion.

A series of adsorption experiments were performed where samples of oleic acid coated nanoparticles in heptane, were placed over silica-C18 and an aliquot of the solution removed at a given time, at which point the experiment was stopped. The iron content in the aliquots was then determined, the data is presented in Table 6.2. For the ME experiments the iron concentration dropped to a residual level after a few days. The concentration of iron in case of the BE experiments indicate a rapid decrease initially, the final concentration is close to that in the ME experiment. After 3 days the suspensions are almost stripped of iron nanoparticles, which have been adsorbed onto the silica-C18. The physical appearances of the sample confirms this, the white silica-C18 substrate slowly becomes chocolate-brown.

Table 6.2. Iron oxide concentration in different test suspensions after adsorption

Treatment details	Starting concentration of Fe (mM)	Time after which sample removed for estimation (h)	Fe concentration (mM)
ME	1.78	> 72	0.029
BE	1.78	12	0.62
BE	1.78	24	0.19
BE	1.78	96	0.06

In a further experiment, two portions of 5 mM of oleic acid in heptane were placed over 50 mg silica-C18 in two quartz cuvettes. The volume of the suspensions was such that the oleic acid would form a monolayer over silica-C18. The surface adsorption of oleic acid over silica-C18 was monitored analytically over time. One 0.5 ml aliquot was taken from the first cuvette after 5 h, and from the second cuvette after 20 h. The amount of oleic acid in the suspensions was determined using methods described in Chapter 2, the results are given in Table 6.3 below.

Table 6.3. The gas chromatographic analysis of data for oleic acid in heptane in blank experiment over silica-C18

Time sample taken (h)	Concentration of oleic acid (mM)
0	5
5	0.74
20	0.72

Clearly oleic acid adsorbs onto the surface of silica-C18. It is known that oleic acid adsorbs onto untreated silica [211], with coordination through the carboxylate group. Adsorption of oleic acid onto silica-C18 is not surprising, the presence of the C18 phase on a large fraction of the silica surface renders it more hydrophobic.

During the characterisation of the non-aqueous magnetic fluids, the samples, with typical [Fe]=30-80 mM were diluted with heptane, the particle size was stable after dilution above ×5 and to further dilution to ×100. A second sample of oleic acid coated nanoparticles in heptane, was diluted ×10 with a 5 mM oleic acid solution in heptane, and monitored by PCS. Once again, the particle size was unchanged, indicating the stability of the chemisorbed layer.

A sample of oleic acid coated nanoparticles in heptane, [Fe] = 32 mM, was diluted with heptane and monitored by PCS, the particle size was unchanged within the measurable range. A second sample of oleic acid coated nanoparticles in heptane, was diluted with a 5 mM oleic acid solution in heptane, (Fe concentration 87 mM) and monitored by PCS. Again, the particle size was unchanged.

A sample was prepared for high field ^{1}H NMR by diluting the upper liquid from the second run of the BE experiment by 1:1. 1.7 ml of this suspension was dried by purging nitrogen in a 20 ml round bottom flask. The dried mass was then dissolved in 0.7 ml $CDCl_3$ and placed in a 5 mm NMR tube. A 6.24 mM TSP solution was used as an internal standard. The NMR spectra is shown in Figure 6.16, it indicates the presence of trace quantites of oleic acid.

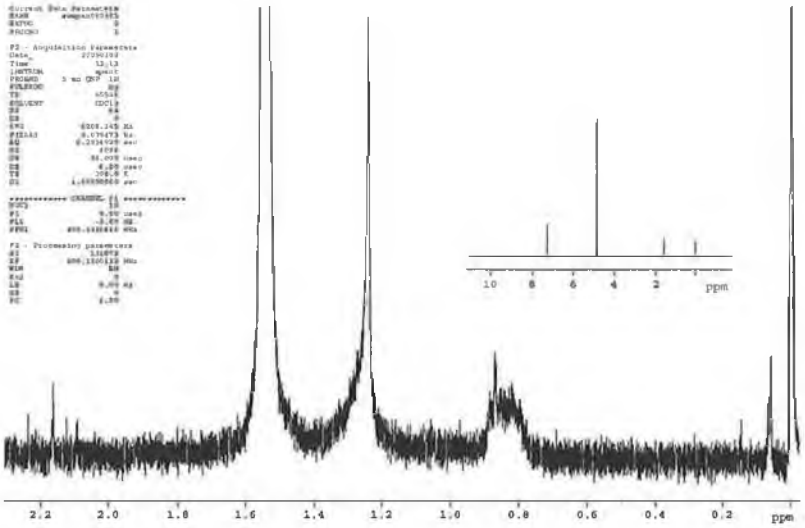

Figure 6.16. High resolution (400 MHz) ^{1}H NMR spectrum, in $CDCl_3$, of the BE suspension, with 6.24 mM TSP solution as the internal standard.

6.3.4 Scanning electron microscopy

Samples for electron microscopy were prepared by spreading a drop of liquid on an SEM stub and allowing it to dry. The liquid was taken from the bottom of a cuvette, using a glass pipette, once the PCS measurement had ended. An 'uncoated' silica-C18 sample was prepared by splashing a pinch of powder on the tip of a spatula onto an aluminium SEM stub fixed with conducting carbon tape. SEM images of the silica-C18 particles under low magnification indicated that the particles in the range of 25-50 μm; with a few

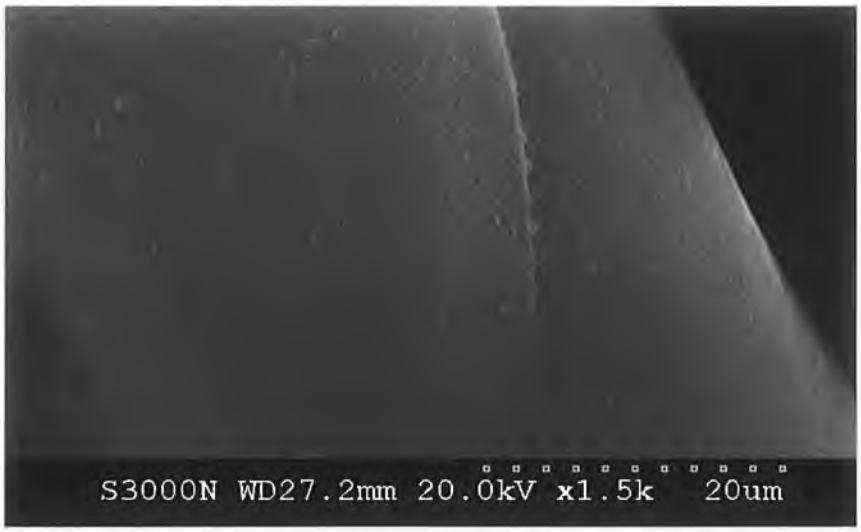

Figure 6.17. Scanning Electron Microscope image of fresh silica-C18 surface

larger particles of up to 100 μm. The SEM image in Figure 6.17 gives an insight of the fine morphology of the crystalline silica-C18 surface with very fine tiny white amorphous inclusions. Higher resolution images show the inclusions are in the size range from 50-200 nm. The micrographs of most of the regions of monolayer treated magnetite suspension indicated no coating of nanoparticles on the silica-C18 surface.

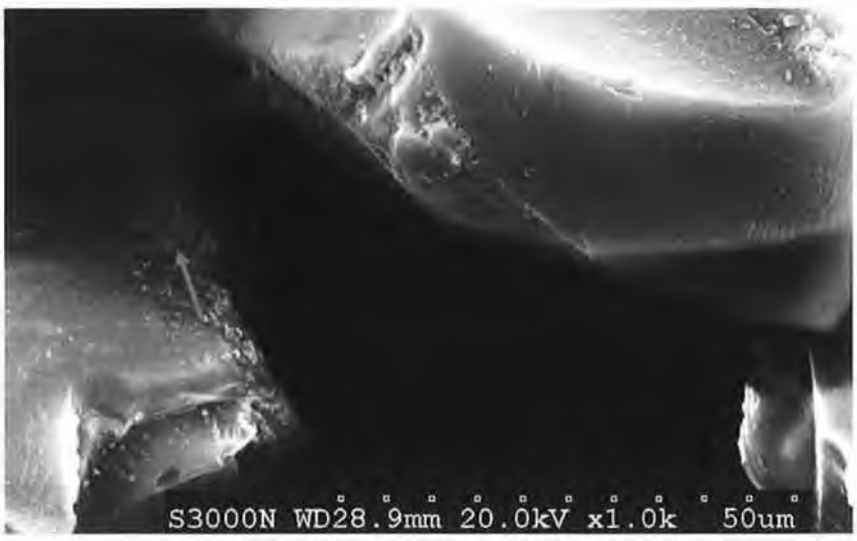

Figure 6.18a. Electron micrograph of coated silica-C18 particles from a ME experiment.

Magnetite nanoparticles were found to be deposited as large aggregates along edges, particularly in the vicinity of neighbouring silica particles. The green arrow in Figure 6.18a indicates one of such few regions of nanoparticle deposits, which was selected for

the image shown in Figure 6.18b. The magnetic particle clusters are as big as 100-200 nm.

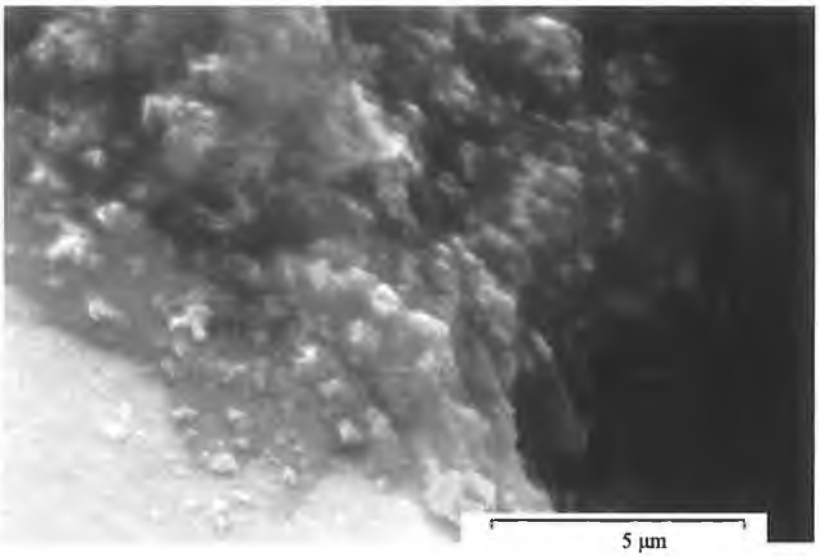

Figure 6.18b. Magnified image of the region indicated by the green arrow in Figure 6.18a.

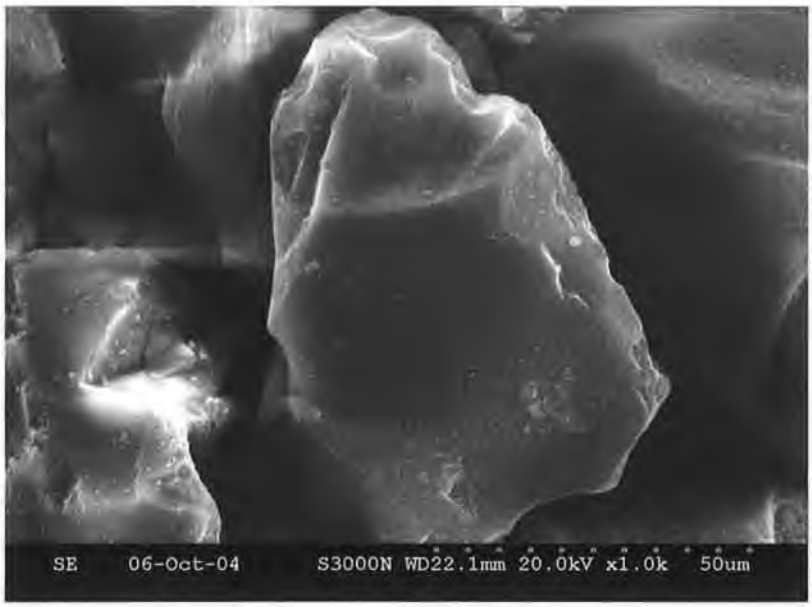

Figure 6.19. Electron micrograph of coated silica-C18 particles from a BE experiment.

There is no indication of any magnetite particle deposits on the flatter surfaces or in the junction between two particles, Figure 6.19. Furthermore AFM studies did not provide any evidence of the presence of nanoparticles on the flatter surfaces. Thus the ME and BE designations refer in effect to high and low magnetite concentration samples.

6.4 Discussion

NMRD and PCS measurements confirm that suspensions H5a and H5b are very stable even after couple of months from the date of synthesis. It was very clear by visual observation that the suspensions placed over silica-C18 were being depleted of iron oxide with time. The adsorption is confirmed by absorbance measurements and by iron determination.

For the ME adsorption experiments the Z-average cluster size increased slowly in a linear fashion for the first few hours. This was followed by a transitional phase of faster growth, up to around 12 h. This phase was associated with an increase in the backscattered light intensity and an increase in the PDI to around 0.2. At this time the clusters are in the region of 100nm diameter. There then followed a phase of very rapid linear growth (of the order of 100 nm/h) that resulted in clusters in the μm range within a few hours. This phase was associated with a decrease in scattered light and an increase in the PDI up to the maximum value of 1.0. The data acquisition invariably stopped, due to low backscattered light intensity, within 24 hours.

For the BE adsorption experiments, the cluster growth was generally slower, and was usually observed to occur in three stages. It started with a brief phase of slow linear growth, similar to the ME experiments, this was followed by another phase of linear growth at a faster rate (c. 0.5nm/h) and ended with a phase of slower linear growth (c. 0.25nm/h) in most cases. There were some experiments where growth continued more rapidly and in an anomalous fashion. As in the ME experiment the backscattered intensity increased, until the transition to the slower growth phase at about 40-60 h, after which it began to decrease again.

There are some common features to the ME and BE experiments, there is an induction phase during which there is little change in the particle size, after which the cluster growth accelerates significantly. The backscattered light intensity grows to a maximum in both cases before decreasing as the iron concentration falls towards zero. There are also significant differences, for the BE experiments the growth is slower and the clusters that remain in suspension do not grow to be as large. The growing clusters are also far more monodisperse for the BE experiment. For the BE experiments if there is an induction phase, it is much shorter than for the ME experiments.

There is one report in the literature from van Ewijk and Philipse [212] of anomalous attraction between fatty acid coated magnetite nanoparticles and a stable colloid of octadecanol coated silica spheres of 420 nm, in apolar solvents. The authors present clear evidence that the nanoparticles gradually coat the silica particles, over hundreds of hours. The adsorption is too slow to be diffusion limited. The slow kinetics could arise due to repulsive interactions of the order of $20k_BT$, or to a slow chemical or physical process preceding adsorption. The main contribution of the paper is in discussing all the possible mechanisms. Calculations confirm that the barrier far is too high to be a van der Waals interaction, but that it is consistent with a charge separation process. However as the adsorption occurs in apolar solvents and given the high surface coverage obtained, it is argued that nanoparticles of opposite charge must be adsorbed, leading to a charge neutral silica sphere. It is also noted that the process is usually irreversible, but that desorption occurs on transfer to a higher dielectric constant solvent. Finally, the authors speculate about whether the adsorption desorption processes are at equilibrium.

The observations of the ME and BE experiments can be rationalised using the mechanism proposed by van Ewijk and Philipse. We propose that during the induction phase the nanoparticles diffuse close to the silica surface. The majority of the particles are repelled, but those that encounter an edge may exchange a proton, or a hydroxyl group with the surface and are held by coulombic attraction. Our data strongly suggests that some of these particles subsequently desorb. The monolayer coating of the desorbed nanoparticle is disrupted, some of the oleic acid coating is now bound to the silica-C18, resulting in activated nanoparticles in suspension. It is not possible to speculate as to how long the particle remains on the surface before desorbing, indeed they may be adsorbed for a short time, but it is highly unlikely that the nanoparticles desorb as a charged entity.

The nature of the adsorption sites on the silica surface remains unclear, it is apparent that a monolayer is not formed over the surface and that the nanoparticles build up in clusters along edges of the silica particles. The SEM images suggest that the edges tend to face neighbouring silica particles, but this may arise as the particles dry on the SEM stub. It might be anticipated that the presence of impurities, such as aluminium oxide, in the silica may be responsible for the surface activity. However no adsorption is observed for untreated silica, but very rapid adsorption is observed for silica-CN. It should also be

pointed out that while 11 nm magnetite particles will diffuse easily through the gaps between the silica particles, it is unlikely that the larger clusters will be able to do so.

There is another possibility for generating activated nanoparticles, without direct intervention of the silica surface. As oleic acid adosrbs onto silica-C18, if there was an equilibrium between the chemisorbed oleate groups on the nanoparticles and the bulk, the silica would disrupt this. However, this possibility can be discounted as chemisorbed oleate is strongly bonded to the magnetite surface, and there are no H^+ and OH^- groups available in heptane solution to maintain the charge neutrality of the magnetite nanoparticle and desorbing oleate group. Furthermore, it is not possible to alter the stability of a nanoparticle suspension in heptane by dilution with heptane or oleic acid solution.

At the end of the induction phase the population of surface activated nanoparticles in suspension exceeds a critical value. The duration of the induction phase varies somewhat, which may be related to the low probability of establishing nanoparticle deposits on the silica surface. In the ME experiments there is then aggregation between surface activated nanoparticles resulting in the growth of clusters. As the magnetite content is relatively low, there remains silica surface capacity for generating more surface activated nanoparticles. There is subsequently a gradual transition to a later phase of very rapid cluster growth, Figure 6.6, which probably arises due to the aggregation of clusters. At some point the growing clusters precipitate due to gravity, Figure 6.20.

In the BE experiments the cluster growth is slower and more controlled. The magnetite content is relatively high, so there is less available silica surface capacity for generating surface activated nanoparticles, which are therefore at lower concentration throughout. Cluster growth is due to the addition of individual nanoparticles to the growing clusters. There is a strong tendency for all the clusters in the population to grow together, which suggests that the clusters at the upper end of the distribution are somewhat less reactive. There is eventually a transition to a phase of slower cluster growth, Figure 6.10, which may be due to the complete depletion of the original 11 nm particles from the suspension. In Figure 6.12 the curve at 44 h still contains some nanoparticles, this corresponds to the time at which the initial growth begins to slow.

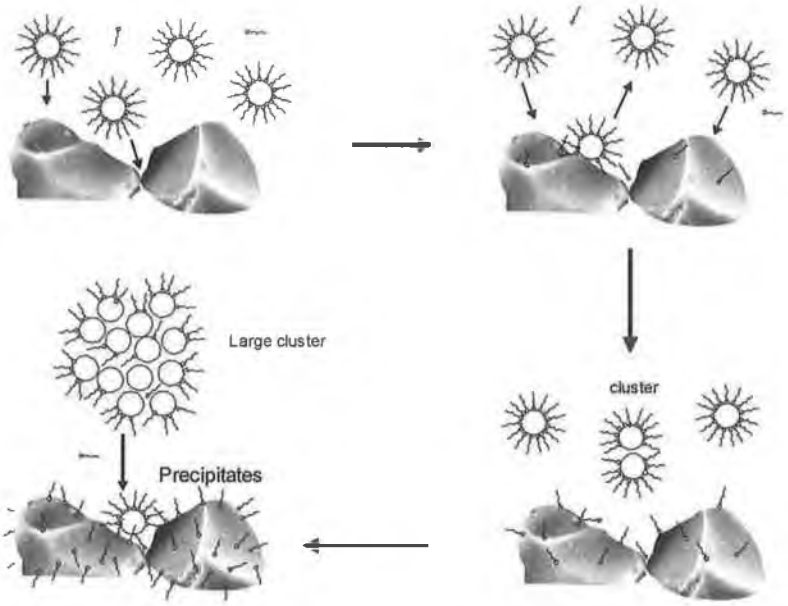

Figure 6.20. Magnetite particles losing surfactant molecules on desorption from the silica surface, leading to the growth of nanoclusters, with eventual precipitation.

6.5 Conclusions

The adsorption of oleic acid coated magnetic nanoparticles from heptane suspension onto silica-C18 has been observed to occur while the remaining suspended particles continuously aggregate into clusters. The clusters can grow into the micron size range over a period of days. The rate of adsorption is orders of magnitude slower than is expected for a diffusion controlled process. This indicates that there is a significant energy barrier reducing the interaction of the nanoparticles with the silica surface, or that there is another process preceding adsorption. The proposed mechanism for nanocluster growth is desorptive loss of temporarily adsorbed nanoparticles from the silica surface. This results in surface activated nanoparticles in suspension, for which the oleic acid coating has been partially removed. A small population of reactive nanoparticles are stabilised by interacting with other desorbed particles, mediating growth of clusters into the micron range, or until they bind irreversibly with the silica substrate.

Chapter 7

Overall conclusions

Overall conclusions and further work

The suspension of uncoated iron oxide nanoparticles in water has been successfully demonstrated, though the amount suspendable is small. The uncoated nanoparticles can be suspended at higher concentration and over longer periods when surfacted with sodium oleate. The methods of application used include wet grinding the magnetite in an agate mortar and ultrasonication in presence of the surfactant at 50°C. The resulting suspensions lose material by precipitation during the initial weeks, when the suspension is little turbid. Greater stability is attained after a few months of ageing and is associated with the suspension becoming translucent. At this time the concentration of iron remaining in suspension is in the millimolar range. These aqueous suspensions contain non-superparamagnetic clusters of 80-170 nm size. They are stable in a narrow pH and temperature range, and against dilution with water and surfactant solutions. The suspensions have relaxivity values at, or slightly above, that expected for superparamagnetic suspensions in the clinical MRI range, while they very high relaxivity at lower field.

It is also possible to prepare very stable suspensions from single and double stranded DNA coated magnetite suspensions. Single stranded DNA coated crystals form non-superparamagnetic clusters in a manner similar to the fatty acid suspensions, although the DNA suspensions show even higher low-field relaxivity. The double stranded DNA stabilised material exhibits behaviour consistent with two magnetic phases, some of the magnetite is superparamagnetic in nature, the rest is magnetically blocked.

Magnetic nanoparticles, coated *in situ* with saturated fatty acids, have been produced by modifications of the ammonia coprecipitation method. Nanoparticles could be synthesised with a reproducible core size of about 11 nm. These particles can be phase transferred easily from aqueous to heptane suspension, or can be stabilised in water by the addition of a second surfactant layer. The heptane and aqueous suspensions of ammonia precipitated nanoparticles are found to be stable for over a year. NMRD and PCS analysis showed that the aqueous suspensions are superparamagnetic clusters, which are stable to changes in pH and temperature. The use of surfactants of different chain lengths produced moderate effects on the relaxivity of the suspensions. It was found that saturated acids with chains of more than 16 carbons were found not to be effective at coating magnetite at higher ionic strength. Decanoic and dodecanoic acids were found to

be the most effective fatty acids tested for producing manolayer stabilised magnetite suspensions in heptane.

It is possible to synthesise very small magnetic nanoparticles in the size range ~4 nm by a slight modification of a published method. This involves the reflux of an iron precursor at 265°C in diphenyl ether. The fine nanocrystallites are of reproducible size and are coated with a surfactant monolayer. NMR data for the heptane suspensions can be interpreted using superparamagnetic relaxation theory. This indicates that the low and variable relaxivity observed is largely due to significant magnetocrystalline anisotropy, perhaps associated with shape distortions. It is possible to stabilise the nanoparticles from the non-aqueous preparation in water by the application of a second physisorbed fatty acid layer. However, the rate of success is very low.

The interaction of oleic acid coated magnetic nanoparticles from heptane suspension onto alkyl chain grafted silica has been studied. Photon correlation spectroscopy revealed that when such suspensions are kept over silica, the magnetic particles in suspension continuously aggregate into clusters. The clusters can grow into the micron size range over a period of hours to days, depending on the availability of coated particles. The rate of adsorption is orders of magnitude slower than is expected for a diffusion controlled process. We propose that nanocluster growth arises due to desorptive loss of nanoparticles from the silica surface. The desorbed particles are activated as their oleate coating has been partially removed. The reactive nanoparticles are stabilised by interacting with other desorbed particles, mediating growth of clusters into the micron range, or until they bind irreversibly with the silica substrate.

The limited time and vastness of the area left the scope of much more to do in future. The most important work which could be done as a direct extension of this thesis, is a thorough study of the structure and detailed morphology of the large aqueous magnetic clusters. In particular, it would be interesting to investigate the differences between the blocked and superparamagnetic clusters. As the nanoclusters are likely to be flexible, Cryo-TEM may be a suitable technique. The low field relaxivity is interesting, further investigations into the detailed causes of this effect could be interesting, again Cryo-TEM studies may help here. The work could be extended to testing some of the more stable aqueous suspensions in animals under MRI conditions. There are some field-cycling MRI scanners available in the UK.

References

1. Bloch, F., Nuclear induction, *Physical Review* 1946, 70(7-8), 460-474.
2. Bloch, F., Hansen, W. W. and Packard, M., The nuclear induction experiment, *Physical Review* 1946, 70(7-8), 474-485.
3. Purcell, E. M., Spontaneous Emission Probabilities at Radio Frequencies, *Physical Review* 1946, 69(11-1), 681-681.
4. Purcell, E. M., Torrey, H. C. and Pound, R. V., Resonance Absorption by Nuclear Magnetic Moments in a Solid, *Physical Review* 1946, 69(1-2), 37-38.
5. Proctor, W. G. and Yu, F. C., The Dependence of a Nuclear Magnetic Resonance Frequency Upon Chemical Compound, *Physical Review* 1950, 77(5), 717-717.
6. Dickinson, W. C., The Time Average Magnetic Field at the Nucleus in Nuclear Magnetic Resonance Experiments, *Physical Review* 1951, 81(5), 717-731.
7. Pauli, W., Pauli exclusion principle, *Naturwiss* 1924, 12, 741.
8. Levitt, M. H., in *Spin dynamics: basics of nuclear magnetic resonance*, Chichester, John Wiley & Sons: New York, 2001.
9. Kimmich, R. and Anoardo, E., Field-cycling NMR relaxometry, *Progress in Nuclear Magnetic Resonance Spectroscopy* 2004, 44(3-4), 257-320.
10. Halle, B., Johannesson, H. and Venu, K., Model-free analysis of stretched relaxation dispersions, *Journal of Magnetic Resonance* 1998, 135(1), 1-13.
11. Lauterbur, P. C., Image Formation by Induced Local Interactions - Examples Employing Nuclear Magnetic-Resonance, *Nature* 1973, 242(5394), 190-191.
12. Muller, R. N., Roch, A., Colet, J.-M., Quakssim, A. and Gillis, P., in *The Chemistry of Contrast Agents in Medical Magnetic Resonance, Imaging*; (Ed. A. E. Merbach, A. E., Toth, E.), John Wiley and Sons Publishers, 2001.
13. Cerofolini, E., Landi, A., Desantis, G., Maiorana, A., Canossi, G. and Romagnoli, R., MR of Benign Peripheral-Nerve Sheath Tumors, *Journal of Computer Assisted Tomography* 1991, 15(4), 593-597.
14. Friebolin, H., in *Basic One- and Two-Dimensional NMR spectroscopy*, VCH: Germany, 1993.
15. Runge, V. M., Clanton, J. A., Herzer, W. A., Gibbs, S. J., Price, A. C., Partain, C. L. and James, A. E., Intravascular Contrast Agents Suitable for Magnetic-Resonance Imaging, *Radiology* 1984, 153(1), 171-176.

16. [online], http://www.irm.umn.edu/hg2m/hg2m_b/hg2m_b.html; (Accessed 19 October 2004)

17. Kittel, C., in *Introduction to Solid State Physics*, Wiley: New York, 1976.

18. Sorensen, C. M., in *Nanoscale Materials in Chemistry*; (Ed. Klabunde, K. J.), John Wiley and Sons, Inc.: New York, 2001.

19. Elliott, S. R., in *The Physics and Chemistry of Solids*, John Wiley & Sons: New York, 1998.

20. Hoon, H. R., An Introduction to Environmental Magnetism & Measurements Techniques, [online], http://www.egs.mmu.ac.uk/users/shoon/pers_page/envmagn_tables_anal/Intro-Env-Magn.pdf, (Accessed 15 December 2004),

21. Hochepied, J. F., Magnetic nanoparticles and information storage, *Online journal of Nanotechnologies* 2000, 1(1), 1-4.

22. Wells, A. F., in *Structural Inorganic Chemistry, 5th ed.*, Oxford University Press: Oxford, 1991.

23. Cornell, R. M. and Schertmann, U., in *The Iron Oxides: Structure, Properties, Reactions, Occurrence and Uses*, VCH Publishers: Weinheim, 1996.

24. Sun, S. H. and Zeng, H., Size-controlled synthesis of magnetite nanoparticies, *Journal of the American Chemical Society* 2002, 124(28), 8204-8205.

25. Gazeau, F., Bacri, J. C., Gendron, F., Perzynski, R., Raikher, Y. L., Stepanov, V. I. and Dubois, E., Magnetic resonance of ferrite nanoparticles: evidence of surface effects, *Journal of Magnetism and Magnetic Materials* 1998, 186(1-2), 175-187.

26. Cox, P. A., in *Transition Metal Oxides*, Oxford University Press: Oxford, 1992.

27. Coey, J. M. D., Berkowitz, A. E., Balcells, L., Putris, F. F. and Parker, F. T., Magnetoresistance of magnetite, *Applied Physics Letters* 1998, 72(6), 734-736.

28. Jolivet, J. P., Chaneac, C. and Tronc, E., Iron oxide chemistry. From molecular clusters to extended solid networks, *Chemical Communications* 2004(5), 481-487.

29. Feltin, N. and Pileni, M. P., New technique for synthesizing iron ferrite magnetic nanosized particles, *Langmuir* 1997, 13(15), 3927-3933.

30. Qiu, X. P., Synthesis and characterisation of magnetic nanoparticles, *Chinese Journal of Chemistry* 2000, 18(6), 834-837.

31. Dana, J. D. and Dana, E. S., in *The System of Mineralogy, 8th Edn.,*; (Ed. Gaines, R. V., Catherine, H., Skinner, W., Foord, E. E., Mason, B., Rosenzweig, A.), John Wiley & Sons: New York, 1997.

32. Cho, Y., Matsuura, K., Valanoor, N. and Ramesh, R., Direct domain wall thickness measurement using scanning nonlinear dielectric microscopy, *Ferroelectrics* 2003, 292, 171-180.

33. Smit, J. and Wijn, H. P. J., in *Ferrites*, John Wiley & Sons: New York, 1959.

34. Ozaki, M., in *Fine Particles: Synthesis, Characterization, and Mechanisms of Growth*; Vol. 92 (Sugimoto, T.), Marcel Dekker, Inc.: New York, 2000.

35. Wohlfarth, E. P., Magnetic-Properties of Single Domain Ferromagnetic Particles, *Journal of Magnetism and Magnetic Materials* 1983, 39(1-2), 39-44.

36. LesliePelecky, D. L. and Rieke, R. D., Magnetic properties of nanostructured materials, *Chemistry of Materials* 1996, 8(8), 1770-1783.

37. Skumryev, V., Stoyanov, S., Zhang, Y., Hadjipanayis, G., Givord, D. and Nogues, J., Beating the superparamagnetic limit with exchange bias, *Nature* 2003, 423(6942), 850-853.

38. Morales, M. P., Andres-Verges, M., Veintemillas-Verdaguer, S., Montero, M. I. and Serna, C. J., Structural effects on the magnetic properties of gamma-Fe_2O_3 nanoparticles, *Journal of Magnetism and Magnetic Materials* 1999, 203, 146-148.

39. Popplewell, J. and Sakhnini, L., The Dependence of the Physical and Magnetic-Properties of Magnetic Fluids on Particle-Size, *Journal of Magnetism and Magnetic Materials* 1995, 149(1-2), 72-78.

40. Wang, Q., Shi, J. L., Chen, L. D. and Yan, D. S., *Synthesis of nanocrystalline magnetite (Fe_3O_4) films by self-reduction sol-gel route*, in Functionally Graded Materials VII, 2003, p. 569-572.

41. Kodama, R. H. and Berkowitz, A. E., Atomic-scale magnetic modeling of oxide nanoparticles, *Physical Review B* 1999, 59(9), 6321-6336.

42. Kotitz, R., Fannin, P. C. and Trahms, L., Time-Domain Study of Brownian and Neel Relaxation in Ferrofluids, *Journal of Magnetism and Magnetic Materials* 1995, 149(1-2), 42-46.

43. Bean, C. P., Hysteresis loops of mixtures of ferromagnetic micropowders, *Journal of Applied Physics* 1955, 26(11), 1381-1383.

44. Kodama, R. H., Magnetic nanoparticles, *Journal of Magnetism and Magnetic Materials* 1999, 200(1-3), 359-372.

45. Kodama, R. H., Berkowitz, A. E., McNiff, E. J. and Foner, S., Surface spin disorder in $NiFe_2O_4$ nanoparticles, *Physical Review Letters* 1996, 77(2), 394-397.

46. Gazeau, F., Dubois, E., Hennion, M., Perzynski, R. and Raikher, Y., Quasi-elastic neutron scattering on gamma-Fe_2O_3 nanoparticles, *Europhysics Letters* 1997, 40(5), 575-580.

47. Bellouard, C., Mirebeau, I. and Hennion, M., Magnetic correlations of fine ferromagnetic particles studied by small-angle neutron scattering, *Physical Review B* 1996, 53(9), 5570-5578.

48. Dresco, P. A., Zaitsev, V. S., Gambino, R. J. and Chu, B., Preparation and properties of magnetite and polymer magnetite nanoparticles, *Langmuir* 1999, 15(6), 1945-1951.

49. Odenbach, S., Ferrofluids - magnetically controlled suspensions, *Colloids and Surfaces a-Physicochemical and Engineering Aspects* 2003, 217(1-3), 171-178.

50. Rosensweig, R. E., in *Ferrohydrodynamics*, Cambridge University Press: Cambridge, 1985.

51. Matijevic, E., Preparation and Properties of Uniform Size Colloids, *Chemistry of Materials* 1993, 5(4), 412-426.

52. Jolivet, J. P., in *Metal Oxide Chemistry and Synthesis: From solution to solid state*, Wiley: Chichester, 2000.

53. Cornell, R. M. and Schertmann, U., in *Iron Oxides in the Laboratory; Preparation and Characterisation*, VCH: Weinheim, 1991.

54. Lefebure, S., Menager, C., Cabuil, V., Assenheimer, M., Gallet, F. and Flament, C., Langmuir monolayers of monodispersed magnetic nanoparticles coated with a surfactant, *Journal of Physical Chemistry B* 1998, 102(15), 2733-2738.

55. Kim, D. K., Zhang, Y., Voit, W., Rao, K. V. and Muhammed, M., Synthesis and characterization of surfactant-coated superparamagnetic monodispersed iron oxide nanoparticles, *Journal of Magnetism and Magnetic Materials* 2001, 225(1-2), 30-36.

56. Jolivet, J. P., Froidefond, C., Pottier, A., Chaneac, C., Cassaignon, S., Tronc, E. and Euzen, P., Size tailoring of oxide nanoparticles by precipitation in aqueous medium. A semi-quantitative modelling, *Journal of Materials Chemistry* 2004, 14(21), 3281-3288.

57. Bacri, J. C., Perzynski, R., Salin, D., Cabuil, V. and Massart, R., Ionic Ferrofluids - a Crossing of Chemistry and Physics, *Journal of Magnetism and Magnetic Materials* 1990, 85(1-3), 27-32.

58. Wooding, A., Kilner, M. and Lambrick, D. B., Studies of the Double Surfactant Layer Stabilization of Water-Based Magnetic Fluids, *Journal of Colloid and Interface Science* 1991, 144(1), 236-242.

59. Wooding, A., Kilner, M. and Lambrick, D. B., Stripped Magnetic Particles - Applications of the Double Surfactant Layer Principle in the Preparation of Water-Based Magnetic Fluids, *Journal of Colloid and Interface Science* 1992, 149(1), 98-104.

60. Shen, L. F., Stachowiak, A., Fateen, S. E. K., Laibinis, P. E. and Hatton, T. A., Structure of alkanoic acid stabilized magnetic fluids. A small-angle neutron and light scattering analysis, *Langmuir* 2001, 17(2), 288-299.

61. Fertman, V. E., in *Magnetic Fluids Guidebook: Properties and Applications*, Hemisphere Publishing Corporation: New York, 1990.

62. Napper, D. H., in *Polymeric Stabilisation of Colloidal Dispersions*, Academic Press: London, 1983.

63. Bica, D., Vekas, L. and Rasa, M., Preparation and magnetic properties of concentrated magnetic fluids on alcohol and water carrier liquids, *Journal of Magnetism and Magnetic Materials* 2002, 252(1-3), 10-12.

64. Khalafalla, S. E. and Reimers, G. W., Preparation of Dilution-Stable Aqueous Magnetic Fluids, *Ieee Transactions on Magnetics* 1980, 16(2), 178-183.

65. Shen, L. F., Laibinis, P. E. and Hatton, T. A., Bilayer surfactant stabilized magnetic fluids: Synthesis and interactions at interfaces, *Langmuir* 1999, 15(2), 447-453.

66. Shen, L. F., Laibinis, P. E. and Hatton, T. A., Aqueous magnetic fluids stabilized by surfactant bilayers, *Journal of Magnetism and Magnetic Materials* 1999, 194(1-3), 37-44.

67. Shen, L. F., Stachowiak, A., Hatton, T. A. and Laibinis, P. E., Polymerization of olefin-terminated surfactant bilayers on magnetic fluid nanoparticles, *Langmuir* 2000, 16(25), 9907-9911.

68. Tadmor, R., Rosensweig, R. E., Frey, J. and Klein, J., Resolving the puzzle of ferrofluid dispersants, *Langmuir* 2000, 16(24), 9117-9120.

69. Sahoo, Y., Pizem, H., Fried, T., Golodnitsky, D., Burstein, L., Sukenik, C. N. and Markovich, G., Alkyl phosphonate/phosphate coating on magnetite nanoparticles: A comparison with fatty acids, *Langmuir* 2001, 17(25), 7907-7911.

70. Shinoda, K., Jeyadevan, B., Kasai, M., Nakatani, I., Oka, H. and Tohji, K., Characterization of inherent clusters in water-based magnetite magnetic fluid, *Journal of Magnetism and Magnetic Materials* 2002, 252(1-3), 141-143.

71. Avdeev, M., Balasoiu, M., Torok, G., Bica, D., Rosta, L., Aksenov, V. L. and Vekas, L., SANS study of particle concentration influence on ferrofluid nanostructure, *Journal of Magnetism and Magnetic Materials* 2002, 252(1-3), 86-88.

72. Lo, B. and Waite, T. D., Structure of hydrous ferric oxide aggregates, *Journal of Colloid and Interface Science* 2000, 222(1), 83-89.

73. Du, Y. B. and Tong, P., Light scattering properties of paramagnetic particles, *Journal of Chemical Physics* 1997, 107(2), 355-362.

74. Papell, S. S.; *Low viscosity magnetic fluid obtained by the colloidal suspensions of magnetic particles*, US Patent No. 3 215 572, 1964

75. Elmore, W. C., The Magnetization of Ferromagnetic Colloids, *Physical Review* 1938, 54, 1092-1095.

76. Pardoe, H., Chua-anusorn, W., St Pierre, T. G. and Dobson, J., Structural and magnetic properties of nanoscale iron oxide particles synthesized in the presence of dextran or polyvinyl alcohol, *Journal of Magnetism and Magnetic Materials* 2001, 225(1-2), 41-46.

77. Blesa, M. A. and Matijevic, E., Phase-transformations of iron-oxides, oxohydroxides, and hydrous oxides in aqueous-media, *Advances in Colloid and Interface Science* 1989, 29(3-4), 173-221.

78. Farley, K. J., Dzombak, D. A. and Morel, F. M. M., A Surface Precipitation Model for the Sorption of Cations on Metal-Oxides, *Journal of Colloid and Interface Science* 1985, 106(1), 226-242.

79. Dufour, J., Marron, J. O., Negro, C., Latorre, R., Formoso, A. and Lopez-Mateos, F., Mechanism and kinetic control of the oxyprecipitation of sulphuric liquors from steel pickling, *Chemical Engineering Journal* 1997, 68(2-3), 173-187.

80. Vayssieres, L., Chaneac, C., Tronc, E. and Jolivet, J. P., Size tailoring of magnetite particles formed by aqueous precipitation: An example of thermodynamic stability of nanometric oxide particles, *Journal of Colloid and Interface Science* 1998, 205(2), 205-212.

81. Kim, D. K., Zhang, Y., Voit, W., Kao, K. V., Kehr, J., Bjelke, B. and Muhammed, M., Superparamagnetic iron oxide nanoparticles for bio-medical applications, *Scripta Materialia* 2001, 44(8-9), 1713-1717.

82. Bee, A., Massart, R. and Neveu, S., Synthesis of very fine maghemite particles, *Journal of Magnetism and Magnetic Materials* 1995, 149(1-2), 6-9.

83. Sugimoto, T., Preparation of Monodispersed Colloidal Particles, *Advances in Colloid and Interface Science* 1987, 28(1), 65-108.

84. Wu, K. T., Kuo, P. C., Yao, Y. D. and Tsai, E. H., Magnetic and optical properties of Fe_3O_4 nanoparticle ferrofluids prepared by coprecipitation technique, *Ieee Transactions on Magnetics* 2001, 37(4), 2651-2653.

85. Gribanov, N. M., Bibik, E. E., Buzunov, O. V. and Naumov, V. N., Physicochemical Regularities of Obtaining Highly Dispersed Magnetite by the Method of Chemical Condensation, *Journal of Magnetism and Magnetic Materials* 1990, 85(1-3), 7-10.

86. Bizdoaca, E. L., Spasova, M., Farle, M., Hilgendorff, M. and Caruso, F., Magnetically directed self-assembly of submicron spheres with a Fe_3O_4 nanoparticle shell, *Journal of Magnetism and Magnetic Materials* 2002, 240(1-3), 44-46.

87. Fu, L., Dravid, V. P. and Johnson, D. L., Self-assembled (SA) bilayer molecular coating on magnetic nanoparticles, *Applied Surface Science* 2001, 181(1-2), 173-178.

88. Goetze, T., Gansau, C., Buske, N., Roeder, M., Gornert, P. and Bahr, M., Biocompatible magnetic core/shell nanoparticles, *Journal of Magnetism and Magnetic Materials* 2002, 252(1-3), 399-402.

89. Deng, J. G., Ding, X. B., Zhang, W. C., Peng, Y. X., Wang, J. H., Long, X. P., Li, P. and Chan, A. S. C., Magnetic and conducting Fe_3O_4-cross-linked polyaniline nanoparticles with core-shell structure, *Polymer* 2002, 43(8), 2179-2184.

90. Domingo, C., Rodriguezclemente, R. and Blesa, M. A., The Pathways to Spinel Iron-Oxides by Oxidation of Iron (II) in Basic-Media, *Materials Research Bulletin* 1991, 26(1), 47-55.

91. Strable, E., Bulte, J. W. M., Moskowitz, B., Vivekanandan, K., Allen, M. and Douglas, T., Synthesis and characterization of soluble iron oxide-dendrimer composites, *Chemistry of Materials* 2001, 13(6), 2201-2209.

92. Yu, L. Q., Zheng, L. J. and Yang, J. X., Study of preparation and properties on magnetization and stability for ferromagnetic fluids, *Materials Chemistry and Physics* 2000, 66(1), 6-9.

93. Qu, S. C., Yang, H. B., Ren, D. W., Kan, S. H., Zou, G. T., Li, D. M. and Li, M. H., Magnetite nanoparticles prepared by precipitation from partially reduced

ferric chloride aqueous solutions, *Journal of Colloid and Interface Science* 1999, 215(1), 190-192.

94. Lee, Y., Lee, J., Bae, C. J., Park, J. G., Noh, H. J., Park, J. H. and Hyeon, T., Large-scale synthesis of uniform and crystalline magnetite nanoparticles using reverse micelles as nanoreactors under reflux conditions, *Advanced Functional Materials* 2005, 15(3), 503-509.

95. Liu, Z. L., Wang, X., Yao, K. L., Du, G. H., Lu, Q. H., Ding, Z. H., Tao, J., Ning, Q., Luo, X. P., Tian, D. Y. and Xi, D., Synthesis of magnetite nanoparticles in W/O microemulsion, *Journal of Materials Science* 2004, 39(7), 2633-2636.

96. LopezPerez, J. A., LopezQuintela, M. A., Mira, J. and Rivas, J., Preparation of magnetic fluids with particles obtained in microemulsions, *Ieee Transactions on Magnetics* 1997, 33(5), 4359-4362.

97. Montagne, F., Mondain-Monval, O., Pichot, C., Mozzanega, H. and Elaissari, A., Preparation and characterization of narrow sized (o/w) magnetic emulsion, *Journal of Magnetism and Magnetic Materials* 2002, 250(1-3), 302-312.

98. Yaacob, II, Nunes, A. C. and Bose, A., Magnetic Nanoparticles Produced in Spontaneous Cationic-Anionic Vesicles - Room-Temperature Synthesis and Characterization, *Journal of Colloid and Interface Science* 1995, 171(1), 73-84.

99. De Cuyper, M., Muller, P., Lueken, H. and Hodenius, M., Synthesis of magnetic Fe_3O_4 particles covered with a modifiable phospholipid coat, *Journal of Physics-Condensed Matter* 2003, 15(15), S1425-S1436.

100. Lee, J., Isobe, T. and Senna, M., Preparation of ultrafine Fe_3O_4 particles by precipitation in the presence of PVA at high pH, *Journal of Colloid and Interface Science* 1996, 177(2), 490-494.

101. Tronc, E. and Jolivet, J. P., Surface Effects on Magnetically Coupled Gamma-Fe_2O_3 Colloids, *Hyperfine Interactions* 1986, 28(1-4), 525-528.

102. Tronc, E. and Jolivet, J. P., *Dispersions of gamma-Fe_2O_3 nanoparticles. Mossbauer spectroscopic studies of the superparamagnetic relaxation*, in Synthesis and Properties of Mechanically Alloyed and Nanocrystalline Materials, Pts 1 and 2 - Ismanam-96, 1997, p. 659-667.

103. Sugimoto, T. and Matijevic, E., Formation of Uniform Spherical Magnetite Particles by Crystallization from Ferrous Hydroxide Gels, *Journal of Colloid and Interface Science* 1980, 74(1), 227-243.

104. Das, D. and Das, P. K., Improving the lipase activity profile in cationic water-in-oil microemulsions of hydroxylated surfactants, *Langmuir* 2003, 19(22), 9114-9119.

105. Deng, Y., Wang, L., Yang, W., Fu, S. and Elaissari, A., Preparation of magnetic polymeric particles via inverse microemulsion polymerization process, *Journal of Magnetism and Magnetic Materials* 2003, 257(1), 69-78.

106. Liz, L., Quintela, M. A. L., Mira, J. and Rivas, J., Preparation of Colloidal Fe_3O_4 Ultrafine Particles in Microemulsions, *Journal of Materials Science* 1994, 29(14), 3797-3801.

107. Betancourt-Galindo, R., Saldivar, R., Rodriguez-Fernandez, O. S. and Ramos-de Valle, L. F., Preparation and characterisation of magnetic latexes using styrene monomer, *Polymer Bulletin* 2004, 51(5-6), 395-402.

108. Lee, K. M., Sorensen, C. M., Klabunde, K. J. and Hadjipanayis, G. C., Synthesis and Characterization of Stable Colloidal Fe_3O_4 Particles in Water-in-Oil Microemulsions, *IEEE Transactions on Magnetics* 1992, 28(5), 3180-3182.

109. Yaacob, II, Nunes, A. C., Bose, A. and Shah, D. O., Synthesis and Characterization of Magnetic Nanoparticles in Spontaneously Generated Vesicles, *Journal of Colloid and Interface Science* 1994, 168(2), 289-301.

110. Santra, S., Tapec, R., Theodoropoulou, N., Dobson, J., Hebard, A. and Tan, W. H., Synthesis and characterization of silica-coated iron oxide nanoparticles in microemulsion: The effect of nonionic surfactants, *Langmuir* 2001, 17(10), 2900-2906.

111. De Cuyper, M. and Joniau, M., Magnetoliposomes - Formation and Structural Characterization, *European Biophysics Journal with Biophysics Letters* 1988, 15(5), 311-319.

112. Menager, C. and Cabuil, V., Synthesis of Magnetic Ddab Vesicles, *Colloid and Polymer Science* 1994, 272(10), 1295-1299.

113. Sapieszko, R. S. and Matijevic, E., Preparation of Well-Defined Colloidal Particles by Thermal-Decomposition of Metal-Chelates .1. Iron-Oxides, *Journal of Colloid and Interface Science* 1980, 74(2), 405-422.

114. Vijayakumar, R., Koltypin, Y., Felner, I. and Gedanken, A., Sonochemical synthesis and characterization of pure nanometer-sized Fe_3O_4 particles, *Materials Science and Engineering a-Structural Materials Properties Microstructure and Processing* 2000, 286(1), 101-105.

115. Rockenberger, J., Scher, E. C. and Alivisatos, A. P., A new nonhydrolytic single-precursor approach to surfactant-capped nanocrystals of transition metal oxides, *Journal of the American Chemical Society* 1999, 121(49), 11595-11596.

116. Prozorov, T., Prozorov, R., Shafi, K. and Gedanken, A., Self-organization in ferrofluids prepared by sonochemical radiation method, *Nanostructured Materials* 1999, 12(5-8), 669-672.

117. Biddlecombe, G. B., Gun'ko, Y. K., Kelly, J. M., Pillai, S. C., Coey, J. M. D., Venkatesan, M. and Douvalis, A. P., Preparation of magnetic nanoparticles and their assemblies using a new Fe(II) alkoxide precursor, *Journal of Materials Chemistry* 2001, 11(12), 2937-2939.

118. Hyeon, T., Lee, S. S., Park, J., Chung, Y. and Bin Na, H., Synthesis of highly crystalline and monodisperse maghemite nanocrystallites without a size-selection process, *Journal of the American Chemical Society* 2001, 123(51), 12798-12801.

119. Raj, K., Moskowitz, B. and Casciari, R., Advances in Ferrofluid Technology, *Journal of Magnetism and Magnetic Materials* 1995, 149(1-2), 174-180.

120. Molday, R. S. and Mackenzie, D., Immunospecific Ferromagnetic Iron-Dextran Reagents for the Labeling and Magnetic Separation of Cells, *Journal of Immunological Methods* 1982, 52(3), 353-367.

121. Jung, C. W. and Jacobs, P., Physical and Chemical-Properties of Superparamagnetic Iron-Oxide MR Contrast Agents - Ferumoxides, Ferumoxtran, Ferumoxsil, *Magnetic Resonance Imaging* 1995, 13(5), 661-674.

122. Raj, K. and Moskowitz, R., Commercial Applications of Ferrofluids, *Journal of Magnetism and Magnetic Materials* 1990, 85(1-3), 233-245.

123. Perez-Castillejos, R., Plaza, J. A., Esteve, J., Losantos, P., Acero, M. C., Cane, C. and Serra-Mestres, F., The use of ferrofluids in micromechanics, *Sensors and Actuators a-Physical* 2000, 84(1-2), 176-180.

124. Hoffmann, B. and Kohler, W., Reversible light-induced cluster formation of magnetic colloids, *Journal of Magnetism and Magnetic Materials* 2003, 262(2), 289-293.

125. Hong, C. Y. R., Hong, H. E., Yang, H. C. and Yeung, W. B.; US Patent No. 5 948 321, 1999

126. Ao, R., Kummerl, L. and Haarer, D., Present limits of data-storage using dye molecules in solid matrices, *Advanced Materials* 1995, 7(5), 495-98.

127. Mallinson, J. C., in *The Foundations of Magnetic Recording*, Academic Press: Berkeley, 1987.

128. Bradley, F. N., in *Materials for Magnetic Functions*, Hayden Book Company: New York, 1976.

129. Gaur, N. K., Klotz, S. A. and Henderson, R. L., Overexpression of the Candida albicans ALA1 gene in Saccharomyces cerevisiae results in aggregation following attachment of yeast cells to extracellular matrix proteins, adherence properties similar to those of Candida albicans, *Infection and Immunity* 1999, 67(11), 6040-6047.

130. Oswald, P., Clement, O., Chambon, C., SchoumanClaeys, E. and Frija, G., Liver positive enhancement after injection of superparamagnetic nanoparticles: Respective role of circulating and uptaken particles, *Magnetic Resonance Imaging* 1997, 15(9), 1025-1031.

131. Jordan, A., Scholz, R., Wust, P., Fahling, H. and Felix, R., Magnetic fluid hyperthermia (MFH): Cancer treatment with AC magnetic field induced excitation of biocompatible superparamagnetic nanoparticles, *Journal of Magnetism and Magnetic Materials* 1999, 201, 413-419.

132. Nielsen, O. S., Horsman, M. and Overgaard, J., A future for hyperthermia in cancer treatment?, *European Journal of Cancer* 2001, 37(13), 1587-1589.

133. van der Zee, J., Heating the patient: a promising approach?, *Annals of Oncology* 2002, 13(8), 1173-1184.

134. Hildebrandt, B., Wust, P., Ahlers, O., Dieing, A., Sreenivasa, G., Kerner, T., Felix, R. and Riess, H., The cellular and molecular basis of hyperthermia, *Critical Reviews in Oncology Hematology* 2002, 43(1), 33-56.

135. Overgaard, K. and Overgaard, J., Investigations on Possibility of a Thermic Tumor Therapy .1. Short-Wave Treatment of a Transplanted Isologous Mouse Mammary-Carcinoma, *European Journal of Cancer* 1972, 8(1), 65-78.

136. Moroz, P., Jones, S. K. and Gray, B. N., Status of hyperthermia in the treatment of advanced liver cancer, *Journal of Surgical Oncology* 2001, 77(4), 259-269.

137. Dubois, J. B., Hyperthermia for the Treatment of Cancer, *Journal De Chirurgie* 1992, 129(4), 227-231.

138. Gel'vich, E. A. and Mazokhin, V. N., Technical aspects of electromagnetic hyperthermia in medicine, *Critical Reviews in Biomedical Engineering* 2001, 29(1), 77-97.

139. Andrä, W., in *Magnetism in Medicine: A Handbook*; (Ed. Andrä, W., Nowak, H.), Wiley-VCH: Berlin, 1998.

140. Hill, D. A., Further-Studies of Human Whole-Body Radiofrequency Absorption Rates, *Bioelectromagnetics* 1985, 6(1), 33-40.

141. Bonnemain, B., Superparamagnetic agents in magnetic resonance imaging: Physicochemical characteristics and clinical applications - A review, *Journal of Drug Targeting* 1998, 6(3), 167-174.

142. Bomati-Miguel, O., Morales, M. P., Tartaj, P., Ruiz-Cabello, J., Bonville, P., Santos, M., Zhao, X. Q. and Veintemillas-Verdaguer, S., Fe-based nanoparticulate metallic alloys as contrast agents for magnetic resonance imaging, *Biomaterials* 2005, 26(28), 5695-5703.

143. Hahn, P. F., Stark, D. D., Lewis, J. M., Saini, S., Elizondo, G., Weissleder, R., Fretz, C. J. and Ferrucci, J. T., 1st Clinical-Trial of a New Superparamagnetic Iron-Oxide for Use as an Oral Gastrointestinal Contrast Agent in MR Imaging, *Radiology* 1990, 175(3), 695-700.

144. Stark, D. D., Fahlvik, A. K. and Klaveness, J., Abdominal Imaging, *JMRI-Journal of Magnetic Resonance Imaging* 1993, 3(1), 285-295.

145. Forsting, M., Reith, W., Dorfler, A., Vonkummer, R., Hacke, W. and Sartor, K., MRI in Acute Cerebral-Ischemia - Perfusion Imaging with Superparamagnetic Iron-Oxide in a Rat Model, *Neuroradiology* 1994, 36(1), 23-26.

146. Hahn, P. F., Stark, D. D., Saini, S., Lewis, J. M., Wittenberg, J. and Ferrucci, J. T., Ferrite Particles for Bowel Contrast in MR Imaging - Design Issues and Feasibility Studies, *Radiology* 1987, 164(1), 37-41.

147. Freed, J. H., Dynamic Effects of Pair Correlation-Functions on Spin Relaxation by Translational Diffusion in Liquids .2. Finite Jumps and Independent T1 Processes, *Journal of Chemical Physics* 1978, 68(9), 4034-4037.

148. Gueron, M., Nuclear-Relaxation in Macromolecules by Paramagnetic-Ions - Novel Mechanism, *Journal of Magnetic Resonance* 1975, 19(1), 58-66.

149. Grant, D., Toft, K. G., Martinsen, I. and Atzpodien, E., Tissue distribution and general safety of MnDPDP in male beagle dogs: with or without total common bile duct obstruction, *Acta Radiologica* 1997, 38(4), 732-739.

150. Lauffer, R. B., Paramagnetic Metal-Complexes as Water Proton Relaxation Agents for NMR Imaging - Theory and Design, *Chemical Reviews* 1987, 87(5), 901-927.

151. Koenig, S. H. and Kellar, K. E., Theory of 1/T-1 and 1/T-2 NMRD Profiles of Solutions of Magnetic Nanoparticles, *Magnetic Resonance in Medicine* 1995, 34(2), 227-233.

152. Roch, A., Muller, R. N. and Gillis, P., Theory of proton relaxation induced by superparamagnetic particles, *Journal of Chemical Physics* 1999, 110(11), 5403-5411.

153. Kimmich, R. and Bachus, R., NMR Field-Cycling Relaxation Spectroscopy, Transverse Nmr Relaxation, Self-Diffusion and Zero-Shear Viscosity - Defect Diffusion and Reptation in Non-Glassy Amorphous Polymers, *Colloid and Polymer Science* 1982, 260(10), 911-936.

154. Noack, F., NMR Field-Cycling Spectroscopy - Principles and Applications, *Progress in Nuclear Magnetic Resonance Spectroscopy* 1986, 18, 171-276.

155. Koenig, S. H. and Brown, R. D., Field-Cycling Relaxometry of Protein Solutions and Tissue - Implications for MRI, *Progress in Nuclear Magnetic Resonance Spectroscopy* 1990, 22, 487-567.

156. Abragam, A. and Proctor, W. G., Spin temperature, *Physical Review* 1958, 109(5), 1441-1458.

157. Schumacher, R. T., Dynamics of Interacting Spin Systems, *Physical Review* 1958, 1(3), 837-842.

158. Pershan, P. S., Cross Relaxation in LIF, *Physical Review* 1960, 117(1), 109-116.

159. Hebel, L. C. and Slichter, C. P., Nuclear Relaxation in Superconducting Aluminum, *Physical Review* 1957, 107(3), 901-902.

160. Hebel, L. C. and Slichter, C. P., Nuclear Spin Relaxation in Normal and Superconducting Aluminum, *Physical Review* 1959, 113(6), 1504-1519.

161. Anderson, A. G. and Redfield, A. G., Nuclear spin-lattice relaxation in metals, *Physical Review* 1959, 116(3), 583-591.

162. Koenig, S. H., Brown and Noack, F., [online], http://www.stelar.it/What_is_FFC.htm, (Accessed 24 July 2005),

163. [online], http://www.stelar.it/the_history_of_field_cycling.htm; (Accessed 17 December 2005)

164. Satheesh, V., Galkin, A., Sykora, S. and Ferrante, G., Technical issues of fast field cycling NMR relaxometry, 2001,

165. Halle, B., Denisov, V. P. and Venu, K., in *Biological Magnetic Resonance*; (Ed. Krishna, N. R., Berliner, L. J.), Kluwer/Plenum: New York, 1999.

166. de la Torre, J. G., Carrasco, B. and Huertas, M. L., Hydrodynamic coefficients and other solution properties (including NMR relaxation) of globular proteins

predicted from atomic level structures, *Biophysical Journal* 2000, 78(1), 401A-401A.

167. Brink, D. M. and Satchler, G. R., in *Angular Momentum, 2nd ed.*, Clarendon Press: Oxford, 1968.

168. Seitter, R. O. and Kimmich, R., in *Magnetic Resonance Relaxometers: Encyclopedia of Spectroscopy and Spectrometry*; (Eds. Lindon, J. C., Tranter, G. E., Holmes, J. L.), Academic Press: London, 1999.

169. Abragam, A., in *The Principles of Nuclear Magnetism*, Clarendon Press: Oxford, 1961.

170. Fukushima, E. and Roeder, S. B. W., in *Experimental Pulse NMR*, Addison-Wesley: Massachusetts, 1981.

171. Sitnikov, R., Furo, I., Henriksson, U. and Toth, F., Nuclear magnetic resonance spectrometer with a frequency range extended below the megahertz region, *Review of Scientific Instruments* 2000, 71(2), 450-457.

172. Murray, E. and Brougham, D. F., NMRD of polyaniline-based conducting polymers, *Synthetic Metals* 2005, 155(3), 681-683.

173. Okuyama, K., in *Nanoparticle Technology*: Kagaku Kogyo, 65, 2001.

174. Pecora, R., Doppler Shifts in Light Scattering from Pure Liquids + Polymer Solutions, *Journal of Chemical Physics* 1964, 40(6), 1604-1614.

175. Cummins, H. Z., Yeh, Y. and Knable, N., Observation of Diffusion Broadening of Rayleigh Scattered Light, *Physical Review Letters* 1964, 12(6), 150-153.

176. Cummins, H. Z. and Pike, E. R., eds., in *Photon Correlation and Light-Beating Spectroscopy*, Plenum Press: New York, 1974.

177. Pecora, R., ed., in *Dynamic Light Scattering, Applications of Photon Correlation Spectroscopy*, Plenum Press: New York, 1985.

178. Berne, J. B. and Pecora, R., in *Dynamic light scattering*, Dover Publications Inc.: New York, USA, 2000.

179. Müller, F., Polke, R., Schäfer, M. and Scholz, N. *Mutual Benefits of Particle System Characterisation and Modelling*. in *PARTEC*. 2001.

180. Jennings, B. R. and Parslow, K. *Particle size measurement: the equivalent spherical diameter*. in *Proc. R. Soc. Lond. A*. 1988. London.

181. Comberg, U. and Wriedt, T., Comparison of scattering calculations for aggregated particles based on different models, *Journal of Quantitative Spectroscopy & Radiative Transfer* 1999, 63(2-6), 149-162.

182. Wriedt, T., A review of elastic light scattering theories, *Particle & Particle Systems Characterization* 1998, 15(2), 67-74.

183. ISO standard document 13321:1996 E.

184. Walsh, A., The Application of Atomic Absorption Spectra to Chemical Analysis, *Spectrochimica Acta* 1955, 7(2), 108-117.

185. Singh, N., Ramachandran, R. D. and Sarkar, A. K., Quantitative estimation of constituents in fly ash by lithium tetraborate fusion, *International Journal of Environmental Analytical Chemistry* 2003, 83(10), 891-896.

186. Ye, F. Q., Martin, W. R. W. and Allen, P. S., Estimation of the iron concentration in excised gray matter by means of proton relaxation measurements, *Magnetic Resonance in Medicine* 1996, 35(3), 285-289.

187. Chan, S., Gerson, B., Reitz, R. E. and Sadjadi, S. A., Technical and clinical aspects of spectrometric analysis of trace elements in clinical samples, *Clinics in Laboratory Medicine* 1998, 18(4), 615-+.

188. Metcalfe, L. D. and Schmitz, A. A., Rapid Preparation of Fatty Acid Esters for Gas Chromatographic Analysis, *Analytical Chemistry* 1961, 33(3), 363-&.

189. Brondz, I., Development of fatty acid analysis by high-performance liquid chromatography, gas chromatography, and related techniques, *Analytica Chimica Acta* 2002, 465(1-2), 1-37.

190. Supplied by Dr. Yurii Gunko, project partner, Trinity College, Dublin;

191. Byrne, S. J., Corr, S. A., Gun'ko, Y. K., Kelly, J. M., Brougham, D. F. and Ghosh, S., Magnetic nanoparticle assemblies on denatured DNA show unusual magnetic relaxivity and potential applications for MRI, *Chemical Communications* 2004(22), 2560-2561.

192. Shen, J. C., Ebner, A. D. and Ritter, J. A., Points of zero charge and intrinsic equilibrium constants of silica-magnetite composite oxides, *Journal of Colloid and Interface Science* 1999, 214(2), 333-343.

193. Hanus, L. H. and Ploehn, H. J., Conversion of intensity-averaged photon correlation spectroscopy measurements to number-averaged particle size distributions. 1. Theoretical development, *Langmuir* 1999, 15(9), 3091-3100.

194. Seeman, N. C., DNA in a material world, *Nature* 2003, 421(6921), 427-431.

195. Ouakssim, A., Roch, A., Pierart, C. and Muller, R. N., Characterization of polydisperse superparamagnetic particles by nuclear magnetic relaxation dispersion (NMRD) profiles, *Journal of Magnetism and Magnetic Materials* 2002, 252(1-3), 49-52.

196. Korb, J. P. and Bryant, R. G., The physical basis for the magnetic field dependence of proton spin-lattice relaxation rates in proteins, *Journal of Chemical Physics* 2001, 115(23), 10964-10974.

197. Gossuin, Y., Roch, A., Lo Bue, F., Muller, R. N. and Gillis, P., Nuclear magnetic relaxation dispersion of ferritin and ferritin-like magnetic particle solutions: A pH-effect study, *Magnetic Resonance in Medicine* 2001, 46(3), 476-481.

198. Meriles, C. A., Sakellariou, D., Heise, H., Moule, A. J. and Pines, A., Approach to high-resolution ex situ NMR spectroscopy, *Science* 2001, 293(5527), 82-85.

199. Liu, X. Q., Xing, J. M., Guan, Y. P., Shan, G. B. and Liu, H. Z., Synthesis of amino-silane modified superparamagnetic silica supports and their use for protein immobilization, *Colloids and Surfaces a-Physicochemical and Engineering Aspects* 2004, 238(1-3), 127-131.

200. [online], http://www.chem.sc.edu/faculty/handy/334Notes/Chapter16.doc; (Accessed 9 November 2005)

201. [online], http://www.chem.sc.edu/people/documents/murphy/SCCC104labmanual2.pdf; (accessed September 3, 2005)

202. Kanicky, J. R. and Shah, D. O., Effect of degree, type, and position of unsaturation on the pK(a) of long-chain fatty acids, *Journal of Colloid and Interface Science* 2002, 256(1), 201-207.

203. Soderman, O., Ginley, M., Henriksson, U., Malmvik, A. C. and Johansson, L. B. A., Interpretation of Frequency-Dependent Nuclear-Magnetic-Resonance Relaxation Data from Micelles Formed in the 6-(Dimethyleicosylammonio)Hexanoate Water-System, *Journal of the Chemical Society-Faraday Transactions* 1990, 86(9), 1555-1559.

204. Hrianca, I., Caizer, C. and Schlett, Z., Dynamic magnetic behavior of Fe_3O_4 colloidal nanoparticles, *Journal of Applied Physics* 2002, 92(4), 2125-2132.

205. Bersani, D., Lottici, P. P. and Montenero, A., Micro-Raman investigation of iron oxide films and powders produced by sol-gel syntheses, *Journal of Raman Spectroscopy* 1999, 30(5), 355-360.

206. deFaria, D. L. A., Silva, S. V. and deOliveira, M. T., Raman microspectroscopy of some iron oxides and oxyhydroxides, *Journal of Raman Spectroscopy* 1997, 28(11), 873-878.

207. Thibeau, R. J., Brown, C. W. and Heidersbach, R. H., Raman-Spectra of Possible Corrosion Products of Iron, *Applied Spectroscopy* 1978, 32(6), 532-535.

208. Sousa, M. H., Tourinho, F. A. and Rubim, J. C., Use of Raman micro-spectroscopy in the characterization of M(II)Fe_2O_4 (M = Fe, Zn) electric double layer ferrofluids, *Journal of Raman Spectroscopy* 2000, 31(3), 185-191.

209. Lee, S. H., Lee, H. and Pak, H., Molecular dynamics simulation of liquid alkanes .2. Dynamic properties of normal alkanes: n-butane to n-heptadecane, *Bulletin of the Korean Chemical Society* 1997, 18(5), 478-484.

210. Chin, C. J., Yiacoumi, S. and Tsouris, C., Probing DLVO forces using interparticle magnetic forces: Transition from secondary-minimum to primary-minimum aggregation, *Langmuir* 2001, 17(20), 6065-6071.

211. Blyholder, G., Adhikar, C. and Proctor, A., Structure and Orientation of Oleic-Acid Adsorbed onto Silica-Gel, *Colloids and Surfaces a-Physicochemical and Engineering Aspects* 1995, 105(1), 151-158.

212. van Ewijk, G. A. and Philipse, A. P., Anomalous attraction between colloidal magnetite and silica spheres in apolar solvents, *Langmuir* 2001, 17(23), 7204-7209.

Chapter 8

Appendices

List of publications and presentations

8.1 Publications

1. Stephen Byrne, Serena Corr, Yurii Gun'ko, John M. Kelly, Dermot F. Brougham and Swapankumar Ghosh, Magnetic nanoparticle assemblies on denatured DNA show unusual magnetic relaxivity and potential applications for MRI, *Chemical Communication* 2004, 22, 2560-2561.

COMMUNICATION

ChemComm
www.rsc.org/chemcomm

Magnetic nanoparticle assemblies on denatured DNA show unusual magnetic relaxivity and potential applications for MRI†

Stephen J. Byrne,[a] Serena A. Corr,[a] Yurii K. Gun'ko,*[a] John M. Kelly,*[a] Dermot F. Brougham*[b] and Swapankumar Ghosh[b]

[a] *The Department of Chemistry, Trinity College, University of Dublin, Dublin 2, Ireland. E-mail: igounko@tcd.ie*

[b] *National Institute for Cellular Biotechnology, School of Chemical Sciences, Dublin City University, Dublin 9, Ireland*

Received (in Cambridge, UK) 25th June 2004, Accepted 18th August 2004
First published as an Advance Article on the web 27th September 2004

Denatured (substantially single-stranded) herring sperm DNA acts as a template for the preparation of magnetic nanowires, forming stable aqueous suspensions, which exhibit unprecedentedly high relaxivity at low field, suggesting that the material may be a potentially useful reagent for MRI.

The preparation of uniformly dispersed colloidal ferrofluids of particle sizes in the range of 10 nm continues to be of interest for many areas of technology including the biosciences.[1] Particles of this size are referred to as "superparamagnetic", as each particle possesses a constant magnetic dipole moment proportional to its size, is attracted to a magnetic field, but retains no residual magnetism after the field is removed.[2] This aspect of the particles' magnetism is important for their use as MRI contrast agents, where signal intensity relies on the effect of the magnetic particles on the NMR signal of water in the tissues being imaged.[3] While there are some obstacles to the clinical application of colloids, materials with high relaxivity at low field will become important with the advent of low-field MRI.[4] One approach to obtaining such materials is to prepare conjugates with biomolecules. As a consequence of its nanometre-sized cross-section, functional groups, and regular structure, DNA can be used to construct assemblies of nanoparticles.[5–8] Indeed previously Mornet *et al.* have reported the association of magnetite nanoparticles with double stranded DNA,[9] while the use of DNA-modified magnetic nanoparticles as recognition devices has been studied.[10] In this paper, we report that the use of denatured DNA as both a surfactant and a template allows the preparation and organisation of magnetite nanoparticles, yielding materials with a remarkably high relaxivity at low field.

Magnetite nanoparticles were prepared by reacting a mixture of ferrous and ferric chlorides (2 : 1 molar ratio; 2×10^{-2} mol dm^{-3} and 1×10^{-2} mol dm^{-3} respectively) with ammonia in a degassed aqueous solution at room temperature[11] containing herring sperm-DNA (hs-DNA), either natural (double-stranded) or after heat-induced denaturation (substantially single-stranded) [1.7×10^{-3} mol dm^{-3} nucleotide].‡ This controlled precipitation method leads to the formation of magnetite nanoparticles (as shown by XRD, IR and Raman spectroscopy†). Transmission electron microscopy (TEM) revealed that in each case the Fe_3O_4 nanoparticles have a size of 9.0 ± 2 nm (estimated for a sample of 100 particles). TEM also demonstrated that denatured hs-DNA–magnetite nanocomposites (Fig. 1(a)) were comprised of randomly distributed chains whereas by contrast, in the double-stranded DNA–magnetite samples the chains are much more entangled (Fig. 1(c)).

To test whether these materials could be further aligned by exposure to a magnetic field, 20 μL samples of the denatured or double-stranded DNA nanocomposites dispersed in deoxygenated water were placed on copper TEM grids and then introduced perpendicular to a magnetic field of 7 T for 30 minutes. These were then removed and allowed to dry in air at room temperature (~18 hours). TEM showed that this treatment caused the single-stranded DNA sample to align in an end-to-end fashion, forming ordered ropes of many microns long (Fig. 1(b)) (each rope appears to be composed of bundles of smaller chains of magnetite arranged on the DNA template). By contrast, TEM shows that the magnetic field has very little effect for either the duplex-DNA nanocomposites (Fig. 1(d)) or the nanoparticles prepared by controlled precipitation in the absence of DNA.† This markedly differing behaviour of the duplex and denatured DNA may be attributed to a more efficient binding of the magnetic nanoparticles to the phosphate backbone of the single-stranded DNA. This was confirmed by IR studies as a band attributable to a Fe–O–P stretch is observed at 1157 cm^{-1}.[12]

The effect of these nanoparticle composites on the water proton spin–lattice relaxation time T_1 has been measured by NMR dispersion (NMRD), allowing the determination of the frequency dependence of the relaxivity r_1 *via* eqn. (1) {where $T_{1(water)}$ is the native relaxation time of the supporting fluid (water) and r_1 is independent of the concentration of the magnetic fluid}.[3a]

$$R_{1(obs)} = \frac{1}{T_{1(obs)}} = \frac{1}{T_{1(water)}} + \frac{1}{T_{1(para)}} = \frac{1}{T_{1(diam)}} + r_1[\mathrm{Fe}] \qquad (1)$$

For complex particulate systems, it has been established that the contributions to the overall relaxivity from magnetic material in different components of the suspension is often additive.[13] In such

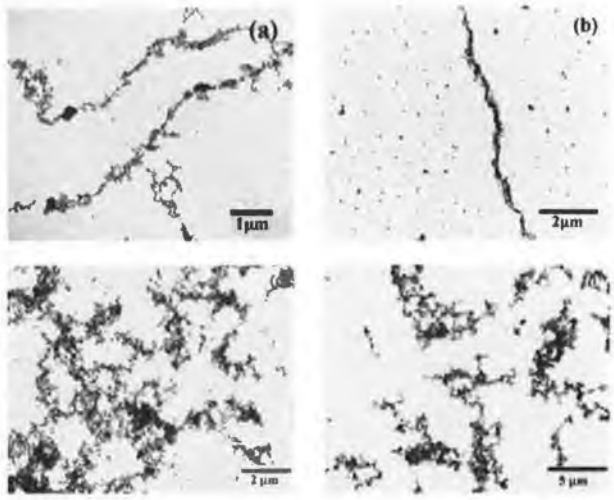

Fig. 1 Representative TEM images of denatured hs-DNA-magnetite nanocomposites (a) without and (b) with subjection to a magnetic field of 7 T; (c) double-stranded hs-DNA–magnetite nanocomposites without and (d) with subjection to a magnetic field of 7 T (see ESI for further TEM images†).

† Electronic supplementary information (ESI) available: NMRD experimental details, TEM images, XRD data, IR and Raman spectra. See http://www.rsc.org/suppdata/cc/b4/b409603g/

DOI: 10.1039/b409603g

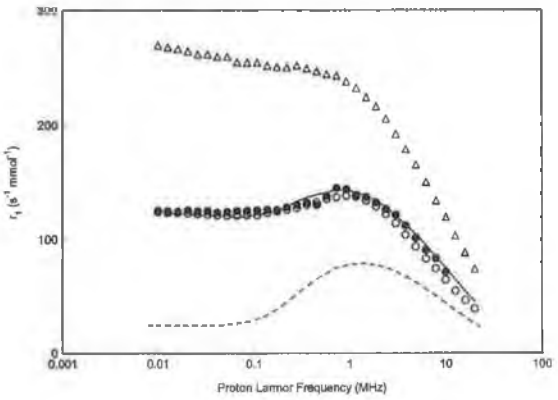

Fig. 2 NMRD relaxation curve recorded at a measuring frequency of 9.25 MHz for (a) (Δ) denatured hs-DNA–magnetite nanocomposites; (b) (●) double-stranded hs-DNA–magnetite nanocomposites; (c) (——) simulated curve for a two component system (see text below); (d) (– – –) simulated curve for a distribution of superparamagnetic particles of magnetite of diameter 9 ± 2 nm and (e) (○) double-stranded salmon sperm-DNA–magnetite nanocomposites. All measurements were carried out at 25 ± 1 °C. All measured NMRD curves were stable; errors in r_1 are 1%, with repeat preparations giving the same r_1 to 3%.

cases the paramagnetic contribution to the relaxivity is given by eqn. (2):

$$r_1 = \sum_i x_i r_{1i} \qquad (2)$$

(x_i is the mole fraction of Fe in component i, with relaxivity r_{1i}.)

The NMRD curves obtained for both DNA composites differ dramatically from that expected for a purely superparamagnetic magnetite sample, which can be successfully predicted by the theory[3a,b] developed previously for dispersed magnetite suspensions (Fig. 2(d)). In particular the relaxivity at low field in both cases, but especially for the single-stranded sample, is extraordinarily high. The denatured DNA nanocomposites (Fig. 2(a)) show an unusual dual power law dependence of T_1 on frequency, which is not consistent with the predictions of outer sphere theory.[14] We propose that the behaviour of the two different DNA-stabilised systems (Figs. 2(a) and 2(b)) can be explained on the basis that the denatured DNA material is composed of 'magnetically aggregated' particles of relaxivity r_{1agg} while the double-stranded DNA composite also contains 'magnetically dispersed' superparamagnetic particles. The solid curve (Fig. 2(c)) is a fit to the data for the double-stranded hs-DNA sample (Fig. 2(b)) based on eqn. (2). We assume a two-phase system, using r_{1spm} taken from the simulated NMRD response (Fig. 2(d)) and r_{1agg} from the denatured DNA nanocomposites and further postulating that the relaxation due to the dispersed and aggregated populations is additive ($x_{spm} = 0.59$ and $x_{agg} = 0.41$). The materials therefore have a larger local magnetic moment, consistent with improved magnetic ordering and higher relaxivity. The differing behaviour of the two types of DNA samples may be attributed to the greater binding efficiency of the single-stranded segments of the denatured DNA which results in higher concentration of the magnetite particles. Also included (Fig. 2(e)) are data for an analogously prepared double-stranded salmon-sperm-DNA–magnetite nanocomposite, which exhibits very similar two-phase behaviour. For this sample the r_1 maximum due to the superparamagnetic fraction is more apparent.

In summary, we have successfully prepared long-range ordered chains of denatured hs-DNA–magnetite nanocomposites. TEM analysis and spectroscopy results are consistent with magnetite nanoparticles bound to the DNA phosphate groups, acting as a cross linker between strands, thereby increasing the chain length to micron size. It is found that, in contrast to the behaviour with duplex DNA, the denatured hs-DNA–magnetite nanocomposites can be aligned in a magnetic field. The denatured DNA composites also exhibit an unprecedented dual power law dependence of the water T_1 on frequency and a remarkably high relaxivity at low field. This suggests that such materials might be potentially useful for low field MRI.[4] Future work will include a study of these particles bound to synthetic DNA of defined sequence and varying length and a detailed examination of the causes of the very high relaxivity.

We thank Dr John O'Brien for assistance with magnetic field trials, Sean Quilty of Particular Sciences Ltd. for performing PCS measurements, Dr Alain Roch and Prof. Robert Muller for helpful discussions. This work is supported by the Enterprise Ireland Research Innovation Fund (IF-2001-364) and HEA PRTLI programme.

Notes and references

‡ *Experimental procedure:* the sodium salt of herring sperm (hs) DNA (0.06 g in 100 mL autoclaved water) purchased from Aldrich was denatured by boiling to 100 °C. The extent of denaturation was monitored *via* the UV absorbance of the DNA solutions. Both double-stranded and denatured DNA solutions were added directly to a solution of ferric and ferrous salts in autoclaved water [$FeCl_3$, 2×10^{-2} mol dm^{-3}; $FeCl_2$, 1×10^{-2} mol dm^{-3}]. The magnetite nanoparticles are formed *via* addition of ammonia solution until a pH of 9 is reached. The resultant magnetic precipitate was then washed several times with autoclaved, double distilled water and dried once a neutral pH was achieved.

1 (*a*) B. M. Berkovsky, V. F. Medvedev and M. S. Krokov, *Magnetic fluids: Engineering Applications*, Oxford University Press, Oxford, 1993; (*b*) B. Bonnemain, *J. Drug Targeting*, 1998, **6**, 167; (*c*) A. Wooding, M. Kilner and D. B. Lambrick, *J. Colloid Interface Sci.*, 1991, **144**, 236; (*d*) K. Butter, P. H. H. Bomans, P. M. Frederik, G. J. Vroege and A. Philipse, *Nat. Mater.*, 2003, **2**, 88.
2 H. E. Horng, C.-Y. Hong, S. Y. Yang and H. C. Yang, *J. Phys. Chem. Solids*, 2001, **62**, 1749.
3 (*a*) R. N. Muller, A. Roch, J.-M. Colet, A. Ouakssim and P. Gillis, *The Chemistry of Contrast Agents in Medical Magnetic Resonance Imaging*, ed. A. E. Merbach and E. Toth, John Wiley and Sons Publishers, New York, 2001, p. 417; (*b*) A. Roch, R. Muller and P. Gillis, *J. Chem. Phys.*, 1999, **110**, 5403; (*c*) D. K. Kim, Y. Zhang, J. Kehr, T. Klason, B. Bjelke and M. Muhammed, *J. Magn. Magn. Mater.*, 2001, **225**, 256.
4 (*a*) G. Navon, Y. Q. Song, T. Room, S. Appelt, R. E. Taylor and A. Pines, *Science*, 1996, **271**, 1848; (*b*) C. H. Tseng, G. P. Wong, V. R. Pomerpy, R. W. Mair, D. P. Hinton, D. Hoffmann, R. E. Stoner, F. W. Hersman, D. G. Cory and R. L. Walsworth, *Phys. Rev. Lett.*, 1998, **81**, 3785.
5 N. C. Seeman, *Nature*, 2003, **421**, 427.
6 H. Yan, T. H. LaBean, L. Feng and J. H. Reif, *Proc. Natl. Acad. Sci. U. S. A.*, 2003, **100**, 8103.
7 M. G. Warner and J. E. Hutchison, *Nat. Mater.*, 2003, **2**, 272.
8 (*a*) J.-M. Nam, C. S. Thaxton and C. A. Mirkin, *Science*, 2003, **301**, 1884; (*b*) J.-M. Nam, S.-J. Park and C. A. Mirkin, *J. Am. Chem. Soc.*, 2002, **124**, 3820.
9 S. Mornet, A. Vekris, J. Bonnet, E. Duguet, F. Grasset, J.-H. Choy and J. Portier, *Mater. Lett.*, 2000, **42**, 183.
10 L. Josephson, J. M. Perez and R. Weissleder, *Angew. Chem., Int. Ed.*, 2001, **40**, 3204.
11 (*a*) R. Massart, *IEEE Trans. Magn.*, 1981, **17**, 1247; (*b*) X.-P. Qiu, *Chin. J. Chem.*, 2000, **18**, 834.
12 K. V. P. M. Shafi, A. Ulman, X. Yan, N.-L. Yang, C. Estournès, H. White and M. Rafailovich, *Langmuir*, 2001, **17**, 5093.
13 A. Ouakssim, A. Roch, C. Pierart and R. N. Muller, *J. Magn. Magn. Mater.*, 2002, **252**, 49.
14 J. H. Freed, *J. Chem. Phys.*, 1978, **68**, 4034.

8.2 Presentations

1. Magnetic Nanoparticle Assemblies, Swapankumar Ghosh*, Dermot F. Brougham, Serena Corr, Yurii Goun'ko, a talk given at the 57th Irish Universities Chemistry Research Colloquium, Maynooth, Ireland, 22-24 June 2005.
2. The Development of New Magnetic Nanocomposites and Magnetic Fluids, Serena A. Corr*, Yurii K. Gun'ko, Stephen J. Byrne, John M. Kelly, Swapankumar Ghosh, Dermot F. Brougham, 28th Annual Symposium of the Microscopical Society of Ireland, 1-3 September 2004, Trinity College Dublin, Ireland.

8.3 Posters

1. "Surface coating and stability of magnetic nanoparticles", Swapankumar Ghosh, Gareth Cooke, Serena Corr, Yurii Goun'ko, and Dermot Brougham, Presented at the 10th Chianti Workshop on Magnetic Resonance, Nuclear and Electron Relaxation - The Neon Jubilee Edition - San Miniato (Pisa), Italy, May 25-30, 2003, proceedings, pp 60.
2. Magnetic nanoparticle assemblies show unusual magnetic relaxivity and potential applications for MRI, Swapankumar Ghosh and Dermot F. Brougham, International Conference on Magnetic Resonance in Biological Systems (ICMRBS), Hyderabad, India, 16-21 Jan 2005.
3. New Two-in-One Magnetic-Fluorescent Nanocomposite Materials, Serena A. Corra, Yurii K. Gun'ko, Aisling O' Byrne, Séverine Chapuis, Noemie van Garderen, Swapankumar Ghosh, and Dermot F. Brougham, BioNano 3: An International Conference on BioNanotechnology Research, 19-21 September 2005, University of Sussex, Brighton, UK.

8.4 Magnetite addition of 3.5 equivalents

Sample H5, Z-average 11.5 nm, 3.5 monolayer equivalents over 50mg silica-C18 in heptane. [Fe] = 3.48 mM. Total volume 0.8 ml. The PCS data is shown in Figure 8.1.

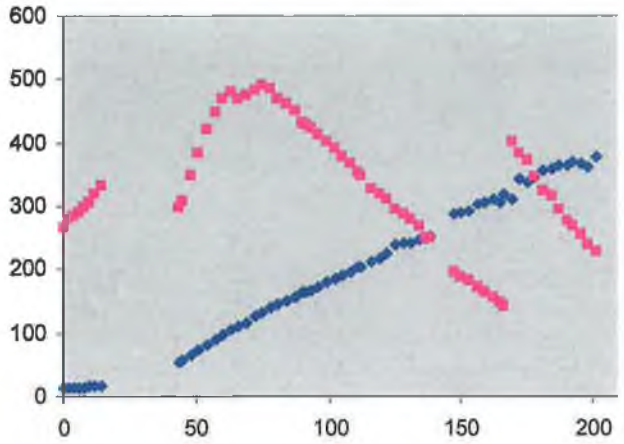

Figure 8.1. Z-average (■) and mean counts (■) for the 3.5 equivalent addition of magnetite suspension on silica.

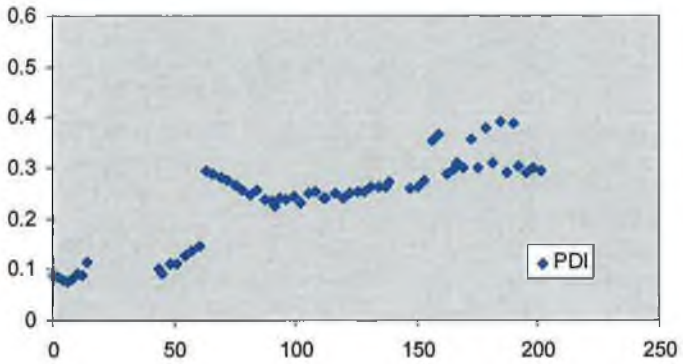

Figure 8.2. The polidispersity index for the 3.5 equivalent addition magnetite suspension on silica

As is normally the case the backscattered intensity went through a maximum. It can be seen that the growth is linear after the induction period, with a rate of growth almost equal to the BE experiment (despite the higher Fe concentration. However the growth does not slow down with time. It is possible to fit all of the later time data with a single line. This suggests that for the BE experiment the reduction in growth rate is due to the absence of smaller particles. It is interesting to note that the growth can be extended to

larger clusters, although the monodispersity is not significantly improved over the BE experiment, at least at this concentration, and it does not decrease in the later stages.

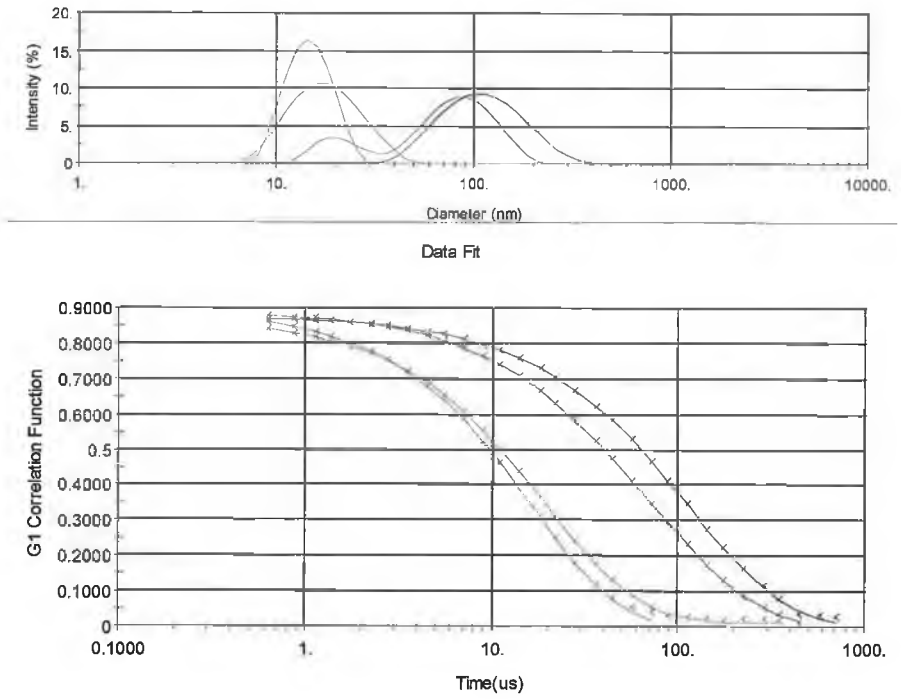

Figure 8.3. 3.5 equivalents (—) 1h, (—) 15h, (—) 44h, (—) 57h

Table 8.1. Time required for different equivalent silica experiments to reach maximum counts and Z-average at max.

Layers	Time to counts max (h)	Z-average(PDI) at max nm
1	~14	1000+ (0.4)
2	30-40	55 (0.2)
3.5	75	140 (0.2)

8.5 Stoichiometry of magnetite nanoparticles

pi	3.14159			
Avogardo (mol-1)	6.02E+23			
		magnetite	oleate	heptane
density (g/cm^3)		5.18	0.891	0.684
footprint (A^2)			21.5	
footprint (m^2)			2.15E-19	
mass (g/mol)		231.55	282.47	
length (m)			1.20E-09	
molar vol (m^3/mol)		4.47E-05	3.17E-04	

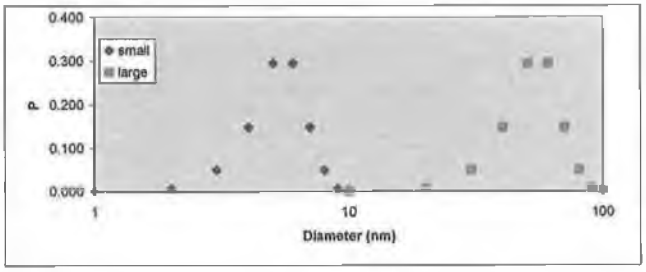

Nanoparticle

P	core	core rad	core vol	core mass	SA	oleate/core	Fe3O4/core	coating mass	coated mass	coated vol	fract mass	fract vol	particles in 1 mL with [Fe]=10mM
	(nm)	(m)	(m3)	(g)	(m2)			(g)	(g)	(m3)	(g)	(m3)	
0.000	1	5.00E-10	5.24E-28	2.71E-21	3.14E-18	15	7	6.85E-21	9.67E-21	2.06E-26	3.02E-24	6.49E-30	8.54E+17
0.007	2	1.00E-09	4.19E-27	2.17E-20	1.26E-17	58	56	2.74E-20	4.91E-20	4.48E-26	3.41E-22	3.10E-28	1.07E+17
0.049	3	1.50E-09	1.41E-26	7.32E-20	2.83E-17	132	190	6.17E-20	1.35E-19	8.24E-26	6.63E-21	4.05E-27	3.16E+16
0.147	4	2.00E-09	3.35E-26	1.74E-19	5.03E-17	234	451	1.10E-19	2.83E-19	1.37E-25	4.17E-20	2.02E-26	1.33E+16
0.296	5	2.50E-09	6.54E-26	3.39E-19	7.85E-17	365	882	1.71E-19	5.10E-19	2.12E-26	1.50E-19	6.26E-26	6.83E+15
0.295	6	3.00E-09	1.13E-25	5.86E-19	1.13E-16	526	1524	2.47E-19	8.33E-19	3.10E-25	2.45E-19	9.15E-26	3.95E+15
0.147	7	3.50E-09	1.80E-25	9.30E-19	1.54E-16	716	2420	3.36E-19	1.27E-18	4.35E-25	1.87E-19	6.41E-26	2.49E+15
0.049	8	4.00E-09	2.68E-25	1.39E-18	2.01E-16	935	3612	4.39E-19	1.83E-18	5.69E-25	8.98E-20	2.89E-26	1.67E+15
0.007	9	4.50E-09	3.82E-25	1.98E-18	2.54E-16	1184	6142	5.56E-19	2.53E-18	7.76E-25	1.76E-20	6.36E-27	1.17E+15
0.003	10	5.00E-09	5.24E-25	2.71E-18	3.14E-16	1461	7054	6.85E-19	3.40E-18	9.98E-25	1.07E-20	3.15E-27	8.54E+14
										Mass av	7.48E-19	2.60E-25	
										Weight av			
0.000	10	5.00E-09	5.24E-25	2.71E-18	3.14E-16	1461	7054	6.85E-19	3.40E-18	9.98E-25	1.07E-21	3.15E-28	8.54E+14
0.007	20	1.00E-08	4.19E-24	2.17E-17	1.26E-15	5845	56432	2.74E-18	2.44E-17	5.98E-24	1.70E-19	4.08E-26	1.07E+14
0.049	30	1.50E-08	1.41E-23	7.32E-17	2.83E-15	13151	190457	6.17E-18	7.94E-17	1.78E-23	3.80E-18	8.75E-25	3.16E+13
0.147	40	2.00E-08	3.35E-23	1.74E-16	5.03E-15	23379	451454	1.10E-17	1.85E-16	3.99E-23	2.72E-17	5.88E-24	1.33E+13
0.295	50	2.50E-08	6.54E-23	3.39E-16	7.85E-15	36530	881747	1.71E-17	3.56E-16	7.53E-23	1.05E-16	2.22E-23	6.83E+12
0.295	60	3.00E-08	1.13E-22	5.86E-16	1.13E-14	52603	1523659	2.47E-17	6.11E-16	1.27E-22	1.80E-16	3.76E-23	3.95E+12
0.147	70	3.50E-08	1.80E-22	9.30E-16	1.54E-14	71599	2419613	3.36E-17	9.64E-16	1.99E-22	1.42E-16	2.93E-23	2.49E+12
0.049	80	4.00E-08	2.68E-22	1.39E-15	2.01E-14	93517	3611635	4.39E-17	1.43E-15	2.93E-22	7.04E-17	1.44E-23	1.67E+12
0.007	90	4.50E-08	3.82E-22	1.98E-15	2.54E-14	118356	5142347	5.55E-17	2.03E-15	4.13E-22	1.41E-17	2.87E-24	1.17E+12
0.003	100	5.00E-08	5.24E-22	2.71E-15	3.14E-14	148120	7053974	6.85E-17	2.78E-15	5.62E-22	8.77E-18	1.77E-24	8.54E+11
										Mass av	5.52E-16	1.15E-22	